ATMOSPHERIC INTERACTIONS DURING GLOBAL DEPOSITION OF CHICXULUB IMPACT EJECTA

by

Tamara Joan Goldin

A Dissertation Submitted to the Faculty of the

DEPARTMENT OF GEOSCIENCES

In Partial Fulfillment of the Requirements
For the Degree of

DOCTOR OF PHILOSOPHY

In the Graduate College

THE UNIVERSITY OF ARIZONA

2008

THE UNIVERSITY OF ARIZONA
GRADUATE COLLEGE

As members of the Dissertation Committee, we certify that we have read the dissertation prepared by Tamara Goldin

entitled Atmospheric Interactions during Global Deposition of Chicxulub Impact Ejecta

and recommend that it be accepted as fulfilling the dissertation requirement for the Degree of Doctor of Philosophy

_____ Date: 11/18/08
H. Jay Melosh

_____ Date: 11/18/08
Clement G. Chase

_____ Date: 11/18/08
Randall M. Richardson

_____ Date: 11/18/08
Elisabetta Pierazzo

Final approval and acceptance of this dissertation is contingent upon the candidate's submission of the final copies of the dissertation to the Graduate College.

I hereby certify that I have read this dissertation prepared under my direction and recommend that it be accepted as fulfilling the dissertation requirement.

_____ Date: 11/18/08
Dissertation Director: H. Jay Melosh

STATEMENT BY AUTHOR

This dissertation has been submitted in partial fulfillment of requirements for an advanced degree at the University of Arizona and is deposited in the University Library to be made available to borrowers under rules of the Library.

Brief quotations from this dissertation are allowable without special permission, provided that accurate acknowledgment of source is made. Requests for permission for extended quotation from or reproduction of this manuscript in whole or in part may be granted by the head of the major department or the Dean of the Graduate College when in his or her judgment the proposed use of the material is in the interests of scholarship. In all other instances, however, permission must be obtained from the author.

SIGNED: Tamara J. Goldin

ACKNOWLEDGEMENTS

Although the last few months of my graduate studies have felt analogous to being trapped alone in a cave with only a laptop, a stack of references, and a really bad FORTRAN-induced headache, completing this dissertation was not a solitarily drudge to the finish line. Most of the journey was more like the Wizard of Oz where Dorothy is a geologist swept away into an unknown land of computer modeling and thermal radiation physics and where the yellow brick road is iridium-enriched. It's a little too hot for tin men in Tucson, but many people along my road helped me to complete this project and preserve my sanity even when the wicked witch of debugging came a knocking.

First and foremost, I would like to thank Jay Melosh, who served as not only my advisor, mentor and teacher, but also as my close collaborator for much of this project. We spent many hours discussing how to most efficiently fry dinosaurs to a crisp and conspiring in other forms of geologic violence. I was at times worried that the nitty-gritty of this project was way out of my league, but somehow Jay succeeded in converting me into a marginally-decent computer programmer and preventing me from throwing the computer out the window when nothing was working and I had no clue how to fix it. For a modeler with an unfortunate lack of fieldwork in exotic places, I sure spent a lot of time off in exotic places and I thank Jay for those opportunities. In particular I am very grateful that I got to tag along with Jay for a year of "sabbatical" in Germany. Jay also made sure that I never went too long without seeing an actual impact crater. My impact studies took me to the Mexican waters over Chicxulub, the Vredefort Dome and Tswaing Crater in South Africa, the Lockne structure in Sweden, the Charlevoix structure in Quebec, the Sierra Madera and Odessa craters in western Texas, Decaturville and Crooked Creek in Missouri, Meteor Crater in Arizona, the Ries Crater in Germany, and the K-Pg boundary in all its extraterrestrial glory.

A big chocolate scoop of thanks to:

-Gareth Collins and Kai Wünnemann who taught me the ropes of hydrocode modeling, guided me through my first two years, and continue to assist me in cratering fun.
-Betty Pierazzo, Gordon "Oz" Osinski, Gwen Barnes, Abby Sheffer, Jim Richardson, Zibi Turtle, Diana Smith, Lissa Ong, and the other impact fanatics who passed through the Meloshian universe at one time or another.
-Committee members past and present, Clem Chase, Randy Richardson, Betty Pierazzo, Adam Showman, and Roy Johnson for keeping me on track and reading my thesis
-David Rubie and the folks at the Bayerisches Geoinstitut in Bayreuth for hosting me
-The fellow survivors of the 2005 Chicxulub Seismic Experiment (and the R/V Maurice Ewing for not sinking despite getting a little dinged up…)
-Nancye Dawers and the Tulane geology department for providing a great foundation
-Daniel Horton for sharing rocks, stories, and the world with me for all these years
-The lil' rascals of Mabel St & Norton St and those who kept the music going even when I lost the beat
-Mom, Dad, Daniel, Micki, NOLA, the A's, and all that jazz
-The element iridium, without which I would not be writing this thesis at all

DEDICATION

To the Old Bear,

STANLEY VAL GOLDIN,

master of clever solutions to curious problems,

raked leaves, the weather, blueprints, and latkes

who taught me that the Earth is a jungle waiting to be explored.

TABLE OF CONTENTS

TABLE OF CONTENTS - *Continued*

TABLE OF CONTENTS - *Continued*

LIST OF FIGURES

LIST OF FIGURES - *Continued*

LIST OF FIGURES - *Continued*

LIST OF FIGURES - *Continued*

LIST OF FIGURES - *Continued*

LIST OF FIGURES - *Continued*

LIST OF FIGURES - *Continued*

LIST OF TABLES

ABSTRACT

Atmospheric interactions affected both the mechanics of impact ejecta deposition and the environmental effects from the catastrophic Chicxulub impact at the Cretaceous-Paleogene (K-Pg) boundary. Hypervelocity reentry and subsequent sedimentation of Chicxulub impact spherules through the Earth's atmosphere was modeled using the KFIX-LPL two-phase flow code, which includes thermal radiation and operates at the necessary range of flow regimes and velocities. Spherules were injected into a model mesh approximating a two-dimensional slice of atmosphere at rates based on ballistic models of impact plume expansion. The spherules decelerate due to drag, compressing the upper atmosphere and reaching terminal velocity at ~70 km in altitude. A band of spherules accumulates at this altitude, below which is compressed cool air and above which is hot (>3000 K) relatively-empty atmosphere.

Eventually the spherule-laden air becomes unstable and density currents form, transporting the spherules through the lower atmosphere collectively as plumes rather than individually at terminal velocity. This has implications for the depositional style and sedimentation rate of the global K-Pg boundary layer. Vertical density current formation in both incompressible (water) and compressible (air) fluids is evaluated numerically via KFIX-LPL simulations and analytically using new instability criteria. Models of density current formation due to particulate loading of water are compared to tephra fall experiments in order to validate the model instabilities.

The impact spherules themselves obtain peak temperatures of 1300-1600 K and efficiently radiate that heat as thermal radiation. However, the downward thermal radiation emitted from decelerating spherules is increasingly blocked by previously-entered spherules settling lower in the atmosphere. This self-shielding effect strengthens with time as the settling spherule cloud thickens and becomes increasingly opaque, limiting both the magnitude and duration of the thermal pulse at the ground. For a nominal Chicxulub reentry model, the surface irradiance peaks at 6 kW/m^2 and is above normal solar fluxes for ~25 minutes. Although biologic effects are still likely, self-shielding by spherules may have prevented the global wildfires previously postulated. However, submicron dust may act as a hot opaque cap in the upper atmosphere, potentially increasing the thermal pulse beyond the threshold for forest ignition.

CHAPTER 1

INTRODUCTION

The 3-mm thick global layer at the Cretaceous-Paleogene (K-Pg[1]) boundary with a peculiar geochemical signature represents a mere blink of the eye in the 4 billion-year-old rock record. If you stand at an outcrop, the stratigraphy of which spans the end of the Cretaceous and beginning of the Paleogene, you may see cycles of deposition and erosion, regression and transgression of the seas, changing wind and wave directions, a succession of fossil assemblages, uplift, and tectonic deformation. In those strata, representing millions of years of geologic history, you might not even notice the thin anomalous layer at the junction between the fossil-rich Cretaceous and the barren Paleogene rocks. In fact, no one noticed anything unusual about the deposit until Walter Alvarez and colleagues decided to measure the iridium concentration of the layer in Gubbio, Italy and discovered an extraterrestrial signature (Alvarez et al., 1980).

Since the Alvarez impact hypothesis for the end-Cretaceous mass extinctions was first proposed and the uniformitarian paradigm revised, the K-Pg impact ejecta layer has been identified and studied at >200 sites worldwide. More than a by-product of the Chicxulub impact event on the Yucatán peninsula, the thin global deposit of sub-millimeter sized particles reveals information about the global biologic upheaval that took place 65 million years ago. Packed into a mere 3 mm of the stratigraphic column is a story of meteorite impact, environmental catastrophe, and sedimentology at its most

[1] Historically known as the K-T boundary for the now-obsolete Tertiary period.

extreme. I seek to understand the deposition of the Chicxulub impact ejecta around the globe and the role that this deposition played in the end-Cretaceous mass extinctions.

Although ejecta deposits from impacts onto airless bodies, such as the moon, are fairly well understood by ballistic models (Melosh, 1989; Oberbeck, 1975; Oberbeck et al., 1975), those on planets with atmospheres, such as the Earth, are more complex. Interactions between falling impact ejecta and the atmosphere must be considered to understand the mechanics of the K-Pg boundary layer deposition and also any alteration of the atmosphere, which has important implications for the environmental consequences of ejecta reentry. Although simplified models of ejecta-atmosphere interactions during the descent of K-Pg ejecta spherules have been considered in several previous studies (Kring and Durda, 2002; Melosh et al., 1990; Toon et al., 1997), until now no numerical model has been able to address the complex exchanges of mass, momentum, and energy that occur during the descent of ejecta through the Earth's atmosphere. Here I present a new numerical model of Chicxulub impact ejecta deposition using a multiphase fluid flow code and examine both the mechanical style of ejecta sedimentation and the environmental effects of ejecta-air interactions, including the first realistic numerical model of thermal radiation transfer to the Earth's surface.

Less than 30 years have passed since the discovery of the K-Pg boundary layer, but in that brief amount of time there has been a spate of research across scientific disciplines seeking to unravel the catastrophic events at the end of the Cretaceous. An overview of K-Pg boundary research is presented in Chapter 2, including the proposed environmental effects of the Chicxulub impact and, in particular, those effects directly related

to ejecta emplacement. I introduce the K-Pg boundary layer and describe the occurrence of the globally distributed impact plume material at both distal localities as well as at localities more proximal to the crater. This is put into the context of impact ejecta theory, including ejection of target and projectile material in an impact plume during the impact event, expansion of the plume and condensation of droplets, and sedimentation—either ballistically on an airless body or non-ballistically on a body with an atmosphere—to form an ejecta deposit. The need for a model including atmospheric effects is evident, for understanding both the deposition and environmental implications of the K-Pg boundary layer and the influence of an atmosphere on ejecta sedimentation in general.

The KFIX-LPL two-phase fluid flow code is presented in Chapter 3. I describe the basic physics behind two-phase flow codes and explain why this numerical method is essential for modeling ejecta-atmosphere interactions. I describe the original KFIX code and discuss the major modifications implemented in our version to suit the problem of impact sedimentation where disperse particles are travelling at high velocities, air density varies across the height of the atmosphere, and there are large rates of energy deposition to the upper atmosphere. Several test problems are also presented in this chapter, which serve to validate KFIX-LPL for use in modeling impact ejecta deposition and other geologic flows.

Chapter 4 presents the KFIX-LPL model for Chicxulub and discusses the deceleration of particles in the atmosphere and changes to the pressure and temperature structure of the atmosphere during spherule reentry. This chapter introduces the mechanics of the basic Chicxulub model in preparation for more detailed discussion about the me-

chanical style of ejecta deposition through the lower atmosphere and thermal radiation from the decelerating spherules in subsequent chapters. The ejecta-atmosphere interactions in our Chicxulub model lead to new hypotheses which explain why the K-Pg boundary layer is so uniform in thickness across distal sites despite the seemingly heterogeneous nature of ejecta dispersal in the impact plume, and also why shocked quartz is found in distal deposits of high velocity ejecta, despite the fact that shock features would not survive transport at such velocities.

The question of whether the global Chicxulub ejecta settled through the atmosphere individually as a rain of particles or whether they were incorporated into density currents leading to a faster and more turbulent transport of ejecta to the Earth's surface is addressed in Chapter 5. Extending beyond Chicxulub, this chapter is a comprehensive discussion of viscous and turbulent vertical density current formation in geologic flows, where a layer containing a mixture of fine particles and a fluid overlies a compressible fluid medium. KFIX-LPL is first used to model a series of tephra fall experiments (Carey, 1997) in water, in which vertical density currents were observed to form. Both the model and experimental results are successfully compared to a new analytical criterion for turbulent instability growth in an incompressible fluid. A model of the more complicated scenario of impact sedimentation through the atmosphere was compared to a new set of analytical criteria for density current onset in a compressible fluid.

Chapters 6 and 7 present extensive studies of thermal radiation transfer during the atmospheric reentry of hypervelocity ejecta. Chapter 6 presents a nominal model for Chicxulub ejecta reentry and shows that self-shielding by spherules settling through the

lower atmosphere reduces the dose of thermal radiation reaching the ground. I discuss the environmental implications of our models for the global wildfire hypothesis (Melosh et al., 1990) and the thermal-sheltering of terrestrial animals hypothesis (Robertson et al., 2004). Chapter 7 presents a more detailed analysis of thermal radiation following ejecta reentry with a series of models in which ejecta input parameters are varied. I show how the rate of ejecta reentry, in addition to the properties of the ejecta particles, affects not only the production of thermal radiation in the upper atmosphere, but also the proportion of thermal energy that is blocked—either by greenhouse species in the air or other ejecta particles—during transport upwards to space and downwards to the Earth's surface.

Each of the chapters in this thesis is written to stand alone. Although this results in some repetition of introductory background material and descriptions of numerical methods, I felt it important to give the reader the option of reading individual chapters or delving into the whole K-Pg ejecta saga. Chapters 4 through 7 represent independent papers which I intend to submit for publication. Chapters 2 and 3 and the appendices provide additional background and technical material for improved understanding of the methodology and scientific context of this work.

This work has been a collaborative effort with Jay Melosh, who contributed several new algorithms, which I incorporated into the KFIX-LPL code, and provided assistance with some of the more difficult physics required to accurately model impact ejecta reentry into the atmosphere. His most substantial contribution is the thermal radiation model, which I then implemented and tested for my KFIX-LPL simulations. New drag and heat transfer functions (see Melosh and Goldin, 2008) for use at the necessary ranges

of velocities and flow regimes, including free molecular flow, as well as an air equation of state adapted to include the effects of ionization in a hot upper atmosphere, were developed primarily by Jay Melosh for use in KFIX-LPL. The instability criterion for compressible flow that I compare with my tephra fall model results is based on Melosh's unpublished response to the Carey (1997) paper on density currents during tephra fall, which was later revisited by Melosh and G. S. Collins in an unsuccessful modeling attempt using the SALE hydrocode. These previous models were unable to replicate density current onset because they lacked treatment of necessary interactions between particles and the fluid medium, which I am able to do with my adapted version of the K-FIX flow code. I successfully replicate the results of the Carey experiments and verify the analytical criteria. The three criteria for instability in a compressible fluid were derived by Melosh. I adapted the criteria for practical use with the KFIX-LPL ejecta models and compared my model simulations with the criteria. In Chapter 6, I discuss the role of submicron dust in the transfer of thermal radiation, which includes the insight of Melosh based on his prior work on SiO_2 condensation from a hot impact plume (Melosh, 2007). I then model the effect of adding dust to the ejecta simulations and assess our dust hypothesis.

I was responsible for adapting K-FIX for use with diffuse geologic flows such as impact sedimentation through air and tephra fall through water. In addition to the algorithms provided by Melosh, I added a number of additional subroutines which are described in Chapter 3. I implemented and tested each modification and conducted all simulations for the modeling results presented in this thesis. For some practical purposes,

I did take advantage of the programming experience of Melosh, who added improved boundary conditions, tracer injection schemes, and PGPLOT plotting into KFIX-LPL, based on similar subroutines within the SALE and TEKTON codes.

The principal results of my research are two-fold. Firstly, my models show that the deposition of Chicxulub ejecta spherules to form the global K-Pg boundary layer did not occur as a rain of particles falling individually at their terminal velocities; instead, the particles fell collectively as vertical density currents under gravity. This has important implications for the time required for deposition of the K-Pg boundary layer and the mechanical style of deposition, which can be tested with geologic observations. Secondly, my calculations of thermal radiation transport during atmospheric reentry of spherules in the upper atmosphere show that the pulse of thermal radiation reaching the surface is limited in both magnitude and duration due to absorption by spherules settling lower in the atmosphere. Unlike previous workers, who assumed that only atmospheric greenhouse gases reduce the downwards thermal radiation (Durda and Kring, 2004; Kring and Durda, 2002; Melosh et al., 1990; Toon et al., 1997), I propose that self-shielding by spherules increasingly blocks the radiation as reentry progresses and, depending on the strength of self-shielding relative to the energy deposition in the upper atmosphere, may prevent extreme thermal damage to the Earth's surficial environment. I present a new assessment of the hypotheses for global wildfires and thermal damage to the terrestrial biosphere following Chicxulub.

This thesis shows that interactions between impact ejecta and the atmosphere alter the mechanics of ejecta deposition and lead to important environmental effects. My

modeling work presents the most detailed numerical model to date of impact ejecta sedimentation through an atmosphere and adds one more chapter to the story of the K-Pg boundary, explaining why the global emplacement of a 3-mm thick deposit was both sedimentologically dramatic and environmentally catastrophic.

CHAPTER 2

THE GLOBAL K-PG BOUNDARY LAYER: FROM IMPACT TO ENVIRONMENTAL CATASTROPHE

2.1 Evidence for Impact at the K-Pg Boundary

The 'Cretaceous/Tertiary Boundary Events Symposium' convened in Copenhagen in September, 1979. The conference was attended by the world's experts on the K-Pg boundary interval, who all sought the cause of the kill-off at the end of the Cretaceous. Many competing hypotheses for the mass extinction trigger were presented and included oceanic events, sea level change, climatic and atmospheric changes, magnetic reversal, and a nearby supernova. However, none of these mechanisms explained the seemingly abrupt extinction, the differential survival patterns observed in the marine and terrestrial fossil record, and other geochemical and sedimentological data gathered across the K-Pg boundary transition. The difficulty in fitting all the data to a single environmental stress and the resulting complex explanations involving multiple simultaneous disturbances led one paper (Vogt and Holden, 1979) to complain that, for the K-Pg extinctions, "data can be dangerous. New data, regardless of reliable source of high quality, have scarcely ruled out any past theory, but have fueled the promulgation of newer and even more outlandish proposals… Somehow there are fields of science where the data become progressively harder as the theories put forth to explain these data become progressively softer."

A group from UC Berkeley, led by the father-son team of Luis and Walter Alvarez, was on the verge of a new hypothesis of catastrophic proportions that would account for the end-Cretaceous mass extinctions and endure the rigorous scientific testing that was to follow. At the symposium, they reported (Alvarez et al., 1979) anomalously high iridium levels in a <1-cm thick clay layer found at the K-Pg boundary in a section near Gubbio, Italy. Lacking a complete explanation at that time, Alvarez et al. posited only that an extraterrestrial source from within the solar system was responsible for the non-terrestrial geochemical signature. Jan Smit (1979), another attendee of the Copenhagen symposium, also noted anomalously high iridium at the K-Pg boundary near Caravaca, Spain, although he was unclear of its significance. In June of the following year, Alvarez et al. (1980) proposed that a large impact was the source of the extraterrestrial material in the K-Pg boundary layer clay and the cause of the mass extinction event. The landmark paper marked the beginning of a massive interdisciplinary effort to unravel the events at the K-Pg boundary and led to a shift in the strictly uniformitarian geologic principles of the time to a paradigm that included the occasional catastrophe of extraterrestrial origins.

Like many great scientific discoveries, the impact hypothesis came about by accident. Sedimentary layers in the Earth's stratigraphy record a continuous history of the terrestrial accretion of cosmic dust (i.e. Brownlee, 1985). The platinum group elements (PGEs) are depleted in the Earth's crust compared to chondritic meteorites and average solar system material because they are siderophiles and partition almost completely into metal and sink to the Earth's core during differentiation, leaving only trace amounts in the silicate mantle and crust (Walter and Trønnes, 2004). The low concentra-

tions of PGEs in most sedimentary rocks are thought to result from cosmic dust accretion and a correlation exists between sedimentation rate and iridium concentration (Barker and Anders, 1968). Walter Alvarez and colleagues (1980) measured iridium concentration in the <1-cm thick clay layer at the K-Pg boundary at Gubbio in order to derive the sedimentation rate and thus the time represented by that layer. Surprisingly, in contrast to the iridium levels above and below the layer indicative of normal sedimentation rates, the iridium concentration spiked to more than 30 times greater than background levels within the clay. They also reported an iridium anomaly at the K-Pg boundary at Stevns Klint near Copenhagen, indicating a nonlocal source for the enrichment. Smit (1979) originally interpreted a similar iridium anomaly observed at the K-Pg boundary in Caravaca, Spain as evidence for an abrupt drop in sedimentation rate (but not in cosmic dust accumulation), despite evidence for seemingly continuous sedimentation before and after the boundary. Alvarez et al. (1980) rejected this and proposed that the best interpretation for the iridium anomaly was an abnormal influx of extraterrestrial material following a large meteorite impact event. Based on the iridium content of the boundary clay, it was postulated that a 10-km diameter meteorite struck the Earth 65 million years ago dispersing projectile-enriched material worldwide and causing the end-Cretaceous mass extinctions.

Although the impact hypothesis was heavily criticized, especially by paleontologists who supported more gradual species extinctions (i.e. Keller et al., 1993; Sloan et al., 1986; Ward et al., 1986) across the boundary and by volcanologists who proposed the Deccan Trap flood basalts in India as the cause of the global environmental disturbance (Courtillot et al., 1990; Courtillot, 1990), evidence quickly mounted in favor of meteorite

impact. The iridium anomaly was reported at the K-Pg boundary at terrestrial and marine sites around the world (Alvarez et al., 1984), shocked quartz and other shock metamorphosed mineral grains—the "smoking-gun" for bolide impact—were identified within the iridium-enriched deposit (Bohor et al., 1984; Bohor et al., 1987), and impact spherules containing nickel-rich spinels were described (Glass and Burns, 1988; Kyte and Smit, 1986; Montanari et al., 1983; Smit and Klaver, 1981; Smit and Kyte, 1984). Meanwhile, paleontological evidence for animal extinctions occurring abruptly at the K-Pg boundary layer continued to mount (Huber et al., 2002; Pearson et al., 2001).

Meteorite impact at the K-Pg boundary had been established, but where was the crater? The basaltic composition of the spherules distributed worldwide suggested a oceanic target (Montanari et al., 1983), but shocked quartz and zircon grains accompanying the spherules suggested a granitic source. In addition, altered silicic glassy material found in an anomalous second layer of ejecta below the iridium layer in the western interior of North America and in Haiti suggested a second impact into continental crust (Bohor et al., 1987).

The impact ejecta deposits at the K-Pg boundary continued to yield clues about the location of the source crater. The deposits of ejecta material were thicker in localities closer to North America and a K-Pg-related tsunami deposits were identified ringing the Gulf of Mexico. Several known impact craters were proposed, but these failed to either date to 65 Ma or be large enough to create a global ejecta deposit. Finally, a circular gravity anomaly in the Gulf of Mexico (Lopez-Ramos, 1975; Penfield and Camargo, 1981) led to the discovery of the buried ~180-km diameter Chicxulub impact structure on

the Yucatán peninsula, which was linked to the K-Pg deposits (Hildebrand et al., 1991). The unusual target rock composition (granitic basement rock overlain by a sequence of carbonates and anhydrites), combined with a meteoritic contribution and the way in which material is ejected and transported following an impact event, explain the anomalous composition of the global ejecta deposits and the presence of two compositionally distinct types of ejecta proximal to the crater, as we will show later.

Since Chicxulub's discovery, the structure of the crater and the characteristics of its proximal ejecta deposits have been explored via geophysical studies, bore holes, and field observations. As our ultimate goal is to understand the global environmental effects of the Chicxulub impact event, the ejecta studies presented in this thesis are primarily concerned with the global iridium-bearing ejecta deposit at the K-Pg boundary only. The remainder of this chapter will focus on the global ejecta layer including the properties of the ejecta, its origins from the impact plume, and potential environmental effects of its emplacement. For a detailed description of K-Pg boundary stratigraphy including proximal localities and the geographic distribution of ejecta deposits see Smit (1999), Claeys et al. (2002), and Kiessling and Claeys (2002).

2.2 The Global K-Pg Boundary Ejecta Layer

Impact ejecta material has been recognized around the globe in both continental and marine settings. Distal impact ejecta deposits >7000 km from Chicxulub are fairly uniform in thickness (2-3 mm), particularly at sites largely undisturbed by processes such as bioturbation (Smit, 1999). The site closest to Chicxulub with an undisturbed ejecta layer is Alamedilla, Spain (7,000 km) and the furthest is Woodside Creek, New Zealand (15,000 km) and in both locations the layer is a few millimeters thick (Smit, 1999). In

most sites all but the high-temperature and pressure (shocked) minerals have been altered to clay by diagenetic processes (Smit, 1999) and the layer has been deformed by compaction or reworking of sediments. The deposit is a chronostratigraphic marker bed for the exact location of the K-Pg boundary and lies precisely at the abrupt transition between Cretaceous and Paleogene fossil assemblages. An iridium-bearing deposit of similar thickness is found at sites more proximal to Chicxulub coating the thicker units of terrestrial ejecta material below, which do show an inverse relationship in thickness with distance from the crater.
Figure 1 shows the stratigraphy of the K-Pg boundary interval at Agost, Spain where the 3 mm-thick ejecta layer is filled with altered impact spherules.

In the global K-Pg boundary deposit, the PGE enrichment and spherules bearing Ni-rich spinel crystallites indicate an extraterrestrial (projectile) component and suggest that the material deposited worldwide originated from the impact plume, which contained both target and projectile material and most of the energy of the impact. Because of this, the global K-Pg impact ejecta layer is sometimes referred to as the "fireball layer" or the "magic layer". I think the term "global ejecta layer" suffices as it distinguishes the 3-mm thick layer from the thicker ejecta layers more proximal to Chicxulub which are not distributed globally. The term 'fireball' is somewhat misleading as the layer is not related to a fireball in the nuclear explosion sense. Also, although the iridium signature is anomalous for a sedimentary deposit, there is nothing 'magical' about the layer: today we recognize the deposit as a product of an established geologic process—impact cratering.

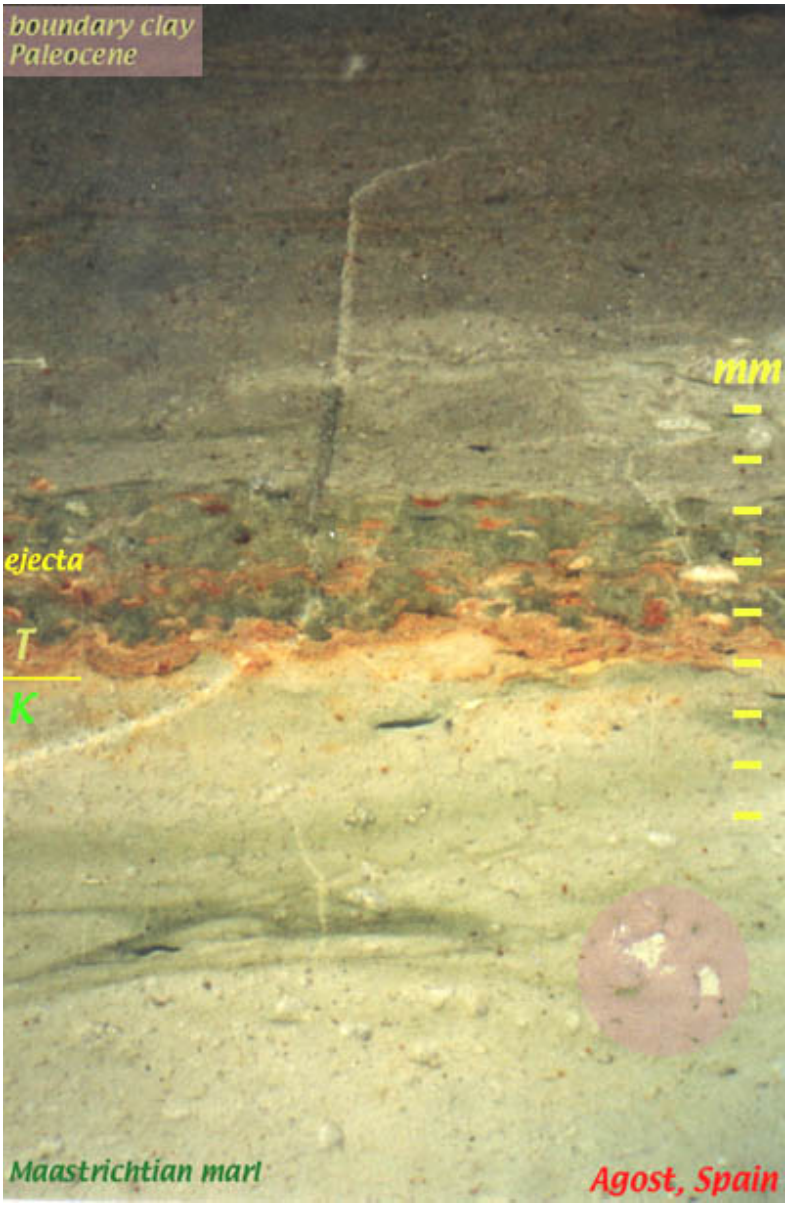

Figure 1. The K-Pg boundary interval at Agost, Spain. The Late Cretaceous marls are filled with fossils such as the large foraminifera in the shaded circle. This is overlain by the 3-mm thick altered ejecta layer containing microkrystites which defines the K-Pg boundary. Above the ejecta layer is the boundary clay which is foraminifera-poor. Image courtesy of Jan Smit.

2.2.1 Geochemistry

Impact ejecta material has been identified at 101 of the 345 known K-Pg boundary sites listed in the KTbase database (Claeys et al., 2002). Of these, 85 sites, representing all depositional environments, contain an iridium anomaly. Other PGEs (Pt, Pd, Os, Ru, Re) are also enriched, as are other elements that are found in higher abundances in chondrites as compared with terrestrial sediments (Ni, Cr, Co) (Claeys et al., 2002). Chondritic enrichments indicate a projectile component within the ejecta. Compared with the heavier ejecta components, such as spherules, in the global deposits that form a well-defined layer, the iridium anomaly is often vertically diffuse due to bioturbation and other post-depositional processes (Claeys et al., 2002; Ebel and Grossman, 2005). This is because iridium, which is mainly found within the altered matrix of the ejecta layer, diffuses more easily than the spinels and spherules (Robin et al., 1991). Although the host of the iridium is not known, it is thought to be associated with some fine dust fraction (Kyte et al., 1990; Schmitz, 1988) of the original ejecta which has since weathered to clay.

2.2.2 Impact Spherules

The global impact ejecta layer is primarily composed of impact spherules (Figure 2) with an average diameter of 250 µm (Smit, 1999) and an average basaltic composition (Montanari et al., 1983). Modeling the deposition of these spherules is the subject of the remaining chapters of this thesis. Although diagenetically altered to clay in most places,

the spherules reveal a relict quench-crystal texture (Smit et al., 1992a) indicating rapidly crystallizing feldspar and mafic silicates (Montanari et al., 1983). Unlike the rest of the spherule, abundant spinel crystals and mafic minerals such as clinopyroxene are relatively unaffected by diagenesis and form a dendritic lattice throughout the cores of the spherules (Figure 3).

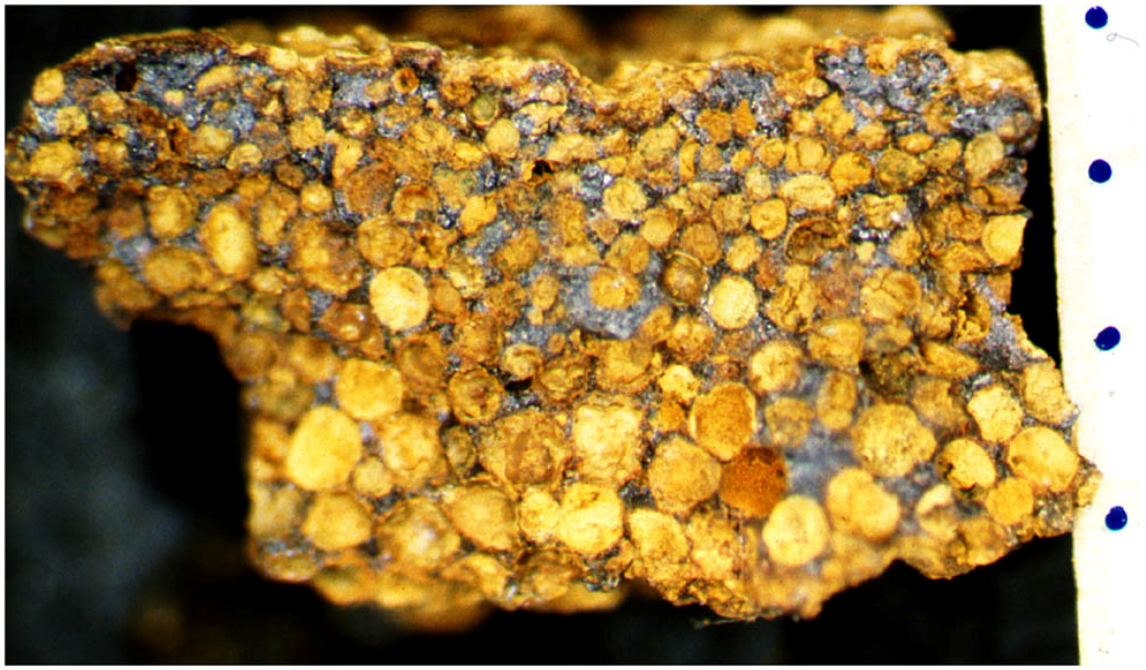

Figure 2. The K-Pg boundary distal ejecta layer from the Republic of Georgia. The layer is composed primarily of impact spherules (microkrystites) which have been diagenetically altered to Goethite. The blue dots indicate 1 mm increments. Photo courtesy of Jan Smit.

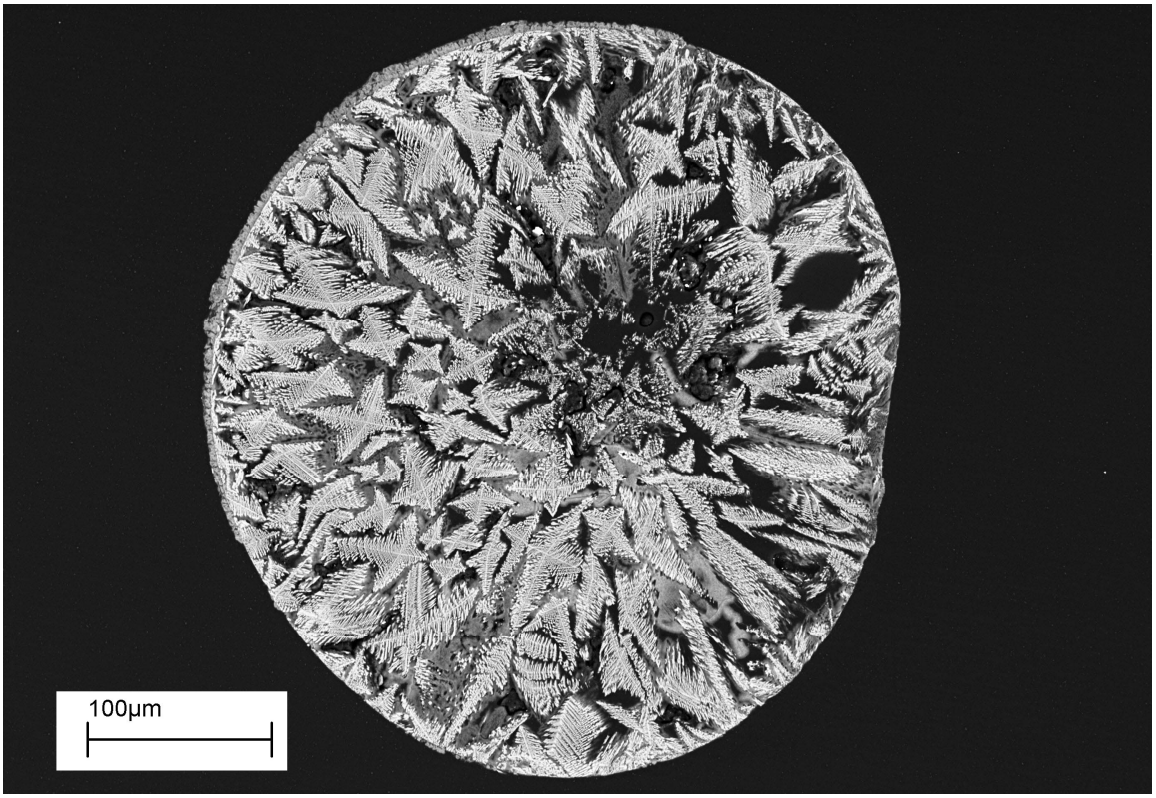

Figure 3. Backscatter image of an impact spherule (microkrystite) from DSDP hole 577. Although largely altered to smectite, the spherule shows a dedritic network of clinopyroxene crystals in the core. Photo courtesy of Frank Kyte.

Due to the presence of mineral crystals, the spherules are classified as *microkrystites* (Glass and Burns, 1988) in order to differentiate them from glassy spherules, *microtektites*, in more proximal K-Pg deposits. This distinction is not always made in the literature and often the two types of spherical ejecta are referred to interchangedly as simply spherules, but, as we will see later when we discuss the formation and transport of impact ejecta from the impact site, the differences between these two types of ejecta are important as they have entirely different origins from the impact cratering process. Microkrystites are basaltic, iridium-enriched, free of SiO_2 glass (lechatelierite), usually

smaller than 500 µm, spherical in shape (no splash structures), and are often found with internal crystallites such as spinel, clinopyroxene or altered sanidine (Glass and Burns, 1988; Smit et al., 1992a). In contrast, microtektites (Figure 4) are andesitic, homogenous in composition, entirely glassy with no primary crystallites or relict grains, iridium-poor, and are on average larger than microkrystites (grading into the larger *tektites*); they also often have a splash form morphology showing flow lines and other evidence for spinning during flight, bubble cavities formed by outgassing, and silica-rich lechatelierite glass (Glass, 1990; Glass and Burns, 1988; Sigurdsson et al., 1991; Simonson and Glass, 2004; Smit et al., 1992a). The spherical shape, primary crystallites, and lack of depletion of volatile elements indicates that the microkrystites survived atmospheric reentry unmelted (Ebel and Grossman, 2005; Greshake et al., 1998), unlike the microtektites/tektites whose morphology reflects aerodynamic deformation in a molten state. There are no transitional forms between microkrystites and microtektites/tektites and they appear to occur in two distinct strewn fields concentric to the Chicxulub crater (Smit, 1999; Smit et al., 1992a): the microkrystites are found only in the 2-3 mm thick global ejecta deposit (with the PGE enrichment and shocked minerals) and the microtektites are found in the lower ejecta layer in North American localities, which has only minor PGE enrichment and few shocked minerals (Bohor and Glass, 1995; Bohor et al., 1987) and are compositionally and morphologically linked to the larger tektites found in Haiti and Mexico (Sigurdsson et al., 1991). Although, the microkrystites show no size dependence in distal localities, the tektites clearly decrease in size at further distances from the crater—another clue to distinct origins for the two types of spherules.

Figure 4. Glassy impact spherule (tektite) from the Beloc, Haiti K-Pg ejecta locality. Note the bubble cavity in the center of the spherule and the lack of crystallites in the completely glassy core. Photo courtesy of Jan Smit.

Both types of impact spherules have experienced substantial diagenetic alteration to clay minerals such as smectite, glauconite, goyazite, goethite and also K-spar and pyrite. The alteration product depends partly on the original composition, but also the local chemistry of the depositional environment (Smit et al., 1992a). For example, many marine spherules alter to smectite and many terrestrial spherules alter to goyazite. Goethite spherules in the global ejecta layer often show no crystalline texture due to extreme alteration or authigenic bacterial activity in anoxic conditions (Smit et al., 1992a). In addition to mineralogical changes, the ejecta layer in many localities has been compacted and deformed by tectonic pressure and the deformed spherules led some early workers to question the impact origin of both the microkrystite and microtektite-containing ejecta layers (Izett, 1987; Izett, 1990).

2.2.3 Spinel

Magnetic spinels are abundant in all extraterrestrial objects, but Ni-rich spinels are not found in normal terrestrial crustal materials (Robin et al., 1992). This indicates that cosmic spinels and terrestrial spinels form from different initial compositions, temperatures, and oxygen fugacities (Robin et al., 1992). Thus, the abundance of magnetic nickel-rich spinels in the K-Pg microkrystites are unusual and indicate an "exceptional accretionary cosmic event" (Robin et al., 1992).

The K-Pg spinels are commonly skeletal with dendritic textures, reflecting a high temperature phase (>900° C) rapidly crystallized from molten silicate droplets (Kyte and Smit, 1986). The spinels have relatively high Mg, Al, and Ni contents and low Ti and Cr compositions as compared with terrestrial spinels of volcanic and sedimentary origins (Kyte and Smit, 1986). A high Fe_2O_3/FeO ratio indicates oxidizing conditions during crystallization. Several origins for the K-Pg spinels have been proposed including (1) ablation products of meteors (Gayraud et al., 1996; Robin et al., 1992), (2) impact melt droplets (Montanari et al., 1983), and (3) liquid condensates from the impact plume (Kyte and Smit, 1986). Models show that the unique chemistry of the K-Pg spinels are likely due to condensation from a hot impact plume containing a mixture of Chicxulub target rock and projectile material (Ebel and Grossman, 1999; Ebel and Grossman, 2005; Siret and Robin, 2003). The heterogeneous differences in composition between spherules may be explained if they originate from different regions of compositionally heterogeneous plume and quench at different temperatures (Ebel and Grossman, 2005).

There is some argument about whether atmospheric entrainment or ablation is required to achieve the oxidized and Ni-rich composition of the spinels (Ebel and Grossman, 2005; Siret and Robin, 2003). Less oxidized spinels in Archean spherule layers, from a time when the Earth's atmosphere was less oxygenated, support atmospheric involvement (Byerly and Lowe, 1994), although there was also less continental crust in the Archean and the compositional differences may be explained by impacts into oceanic target rocks (Simonson and Harnik, 2000) as compared with the unusual carbonate platform rocks at Chicxulub where carbonate and anhydrite units lead to an unusually high oxygen fugacity of the impact plume (Ebel and Grossman, 2005).

2.2.4 Shocked Minerals

Shocked mineral grains, including quartz and zircons, from the granitic basement rock at Chicxulub are abundant in the Ir-enriched global impact ejecta layer (Bohor et al., 1984; Bohor et al., 1987). The quartz grains are large (>500 µm) in the western interior of North America, but <300 µm in the Pacific Ocean and <100 µm and rare in Europe (Claeys et al., 2002). Some workers have suggested a particle size gradation that may be inversely related to distance from the impact (Bohor et al., 1987; Croskell et al., 2002); other workers have noted the apparent pattern of higher abundances and mean grain sizes to the west of Chicxulub and suggested that either the Earth's rotation or an oblique impact (<30°) from the southeast to the northwest (Schultz and D'Hondt, 1996) is respon-

sible. However, it is unclear if these trends are simply a sampling bias, as evidenced from large quartz grains found in a single K-Pg locality in Brazil (Claeys et al., 2002).

Although shock metamorphism is expected from and is a diagnostic indicator of meteorite impact, the occurrence of shocked quartz in the Chicxulub ejecta deposits is enigmatic for several reasons (Alvarez et al., 1995): (1) In North America where there are two ejecta layers—the lower representing the thinning edge of the ejecta curtain and the upper equivalent to the global iridium-enriched deposit—the shocked quartz grains are abundant in the upper layer but only a few grains are found in the lower layer (and these may be due to bioturbation) despite the fact that the upper layer represent the high energy material that has been vaporized and melted, processes that would destroy shocked quartz: (2) There is an apparent asymmetry in the distribution of grain size and abundance in relation to Chicxulub despite the fact that no such trend is seen in the associated microkrystite spherules, iridium content, or layer thickness. (3) Shocked quartz is found even in the most distal localities despite the fact that the velocities required to reach these distances ballistically far exceed those of shocked quartz ejection from the impact site where planar deformation occurs at shock pressures of ~10 GPa (French, 1998), which is associated with ejection velocities <4 km/s. In addition, recent modeling work suggests that the distal ejecta is derived from the sedimentary target rock units, not the underlying granitic basement, which is the presumed source of the quartz and zircon grains (Artemieva and Morgan, 2008). How the shocked mineral grains became entrained in the impact plume material and spread around the globe without annealing is still a matter of

debate. The models presented in Chapter 4 shed some light on the shocked quartz mystery and suggest that atmospheric interactions may explain this anomaly.

2.3 Emplacement of Global Chicxulub Ejecta

The journey of impact ejecta begins with the impact itself. The modeling work presented in this thesis is primarily concerned with the final deposition of the ejecta through the atmosphere, but it is important to explain how the ejecta arrives to the top of the atmosphere from a large impact to understand the impact parameters used in the model. The following is a brief overview of impact cratering theory, with particular focus on ejecta formation and transport. For a more complete description see the comprehensive impact cratering manuals of Melosh (1989) and French (1998).

2.3.1 Cratering Theory

Crater formation can be divided into three general stages (Melosh, 1989) from the time of impact to the time when target deformation ceases and a final crater is obtained:

(1) Contact and Compression

The projectile contacts the surface, decelerates as the target resists its penetration, and transfers its kinetic energy to the target creating a shock wave. This stage ends once the projectile has unloaded from high pressure and the shock wave and the subsequent

rarefaction wave have traversed the projectile. High temperatures, pressures, and velocities are produced in the target within a region comparable to the projectile size.

(2) Excavation

As a hemispherical shock wave expands and propagates through the target, it initiates a subsonic excavation flow that causes the crater to open (Figure 5). Excavation flow velocities are highest near the impact site and decrease with distance. The material in the excavation flow follows streamlines. Ejecta following streamlines which intersect with the surface are ejected and those following streamlines which do no are simply displaced downwards and outwards. The streamlines cross pressure contours, which means that the material ejected from any location contains a mixture of shock levels. Because material closer to the impact point is ejected at faster velocities than ejecta formed further out, the resulting *ejecta curtain* is an inverted cone that grows outward as the crater grows. The ejecta in the ejecta curtain travels on ballistic trajectories and is eventually deposited to form an *ejecta blanket* which decreases in thickness with increasing distance from the crater. The ejecta with the highest velocities is transported the farthest and has a smaller mean size.

Some of the earliest and highest velocity ejecta to leave the impact site are not part of the subsonic excavation flow and ejecta curtain. A significant volume of material, including the projectile as well as target rock, is vaporized to form an expanding *impact plume* consisting of vaporized and melted ejecta material travelling at supersonic speeds and containing a significant fraction of the impact energy. Although the initial stages of plume growth are complicated, once the impact plume has expanded to several times the

projectile diameter plume expansion can be approximated as an adiabatically expanding hemisphere of hot gas (Figure 6). The expansion velocity increases linearly from the center of the plume to the edge. As the plume cools, it begins to condense to form spherical droplets. A model of spherical droplet formation has been presented by Melosh and Vickery (1991) in which the characteristic droplet radius of the resulting spherules is a function of impactor size. More work is still needed to explain the details of impact plume expansion and chemistry and heterogeneities within the plume. The models presented here assume a homogenous, hemispherical, adiabatically expanding plume.

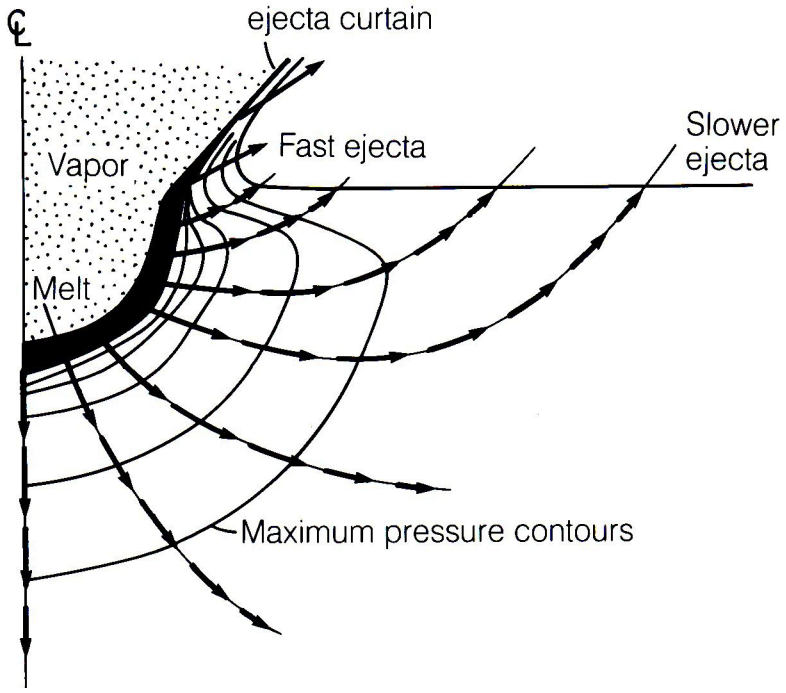

Figure 5. Geometry of the excavation flow field. The arrows show the movement of excavated target rock along streamlines, which cross pressure contours. Some streamlines intersect the surface and release ejecta on ballistic trajectories. This ejecta forms an expanding ejecta curtain with an inverted cone morphology. The impactor and some target rock is vaporized near the point of impact to form the impact plume. From Melosh (1989).

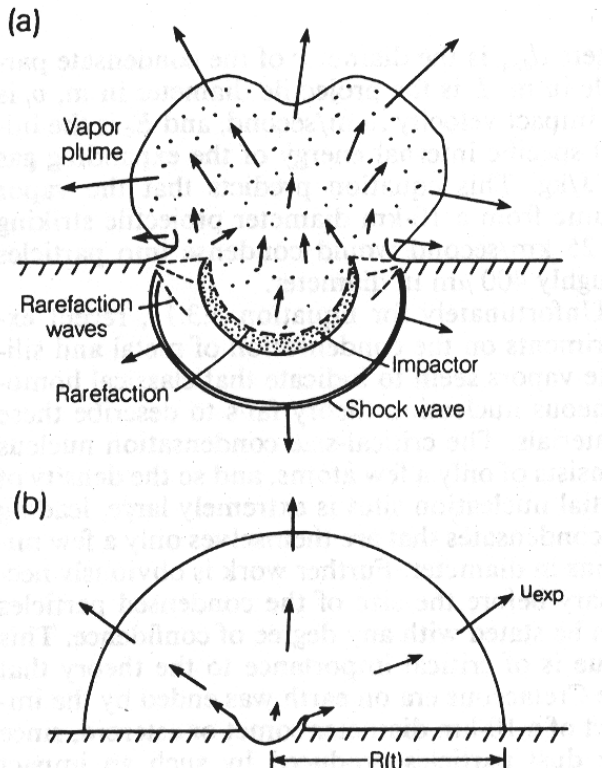

Figure 6. Expansion of the impact plume during the early stages of an impact. (a) Initially, the vapor flow pattern is complex because the plume is composed of a mixture of components shocked to different pressures and temperatures. (b) Once the impact plume has expanded to several times the projectile diameter, the flow is nearly hemispherical and has accelerated to much higher velocities than the ejecta curtain. From Melosh (1989).

There are two major types of ejecta deposits: ejecta curtain deposits (the ejecta blanket) and impact plume deposits. Due to their different origins in the impact cratering process, the ejecta curtain material contains only melted or fragmented target rock, is ejected at subsonic velocities, and is deposited with thicknesses inversely related to distance from the crater. In contrast, the impact plume deposits contains both projectile and

target material that has been melted or vaporized, travels at supersonic velocities, and does not have the same organized velocity structure. In addition, the condensed droplets from the impact plume are smaller than those from the ejecta curtain and are controlled by impactor size, not distance from the impact site.

The global K-Pg impact layer is thought to be ejecta from the impact plume, due to its meteoritic geochemistry, spinel-containing spherules (microkrystites), and global distribution. The ejecta curtain material is not able to travel globally. The microtektite- and tektite- bearing layer consisting of target material only (no extraterrestrial component) is thought to be from the ejecta curtain, which is consistent with lower observed shock levels and thickening of this layer from 0.5 cm in Montana to ~1 cm in New Mexico to the thick ejecta blanket deposits in Mexico (Smit, 1999).

(3) Modification

At the end of the excavation stage, a transient crater is obtained which represents the maximum depth to diameter ratio attained during crater formation. However, the transient crater is short-lived and soon collapses under gravity to form the final crater. The details of the modification stage and the final crater morphology depend on the size of the impact, gravity, and target properties. Smaller craters, such as Meteor Crater, are simple bowl-shaped craters where as larger craters, such as Chicxulub, have complex morphologies. We are only concerned with ejecta in this study, not the formation of the crater itself, and therefore not concerned with this stage of impact cratering.

2.4 Mass Extinction and Environmental Perturbations at the end of the Cretaceous

Mass extinctions have punctuated the history of life (Jablonski, 1996). A mass extinction is defined by Jablonski (1986) as an extinction event that is extreme in duration, magnitude, and breadth. A mass extinction is relatively sudden and short-lived, marked by a substantial increase in extinction rates above normal background levels, and effects a variety of organisms across multiple taxonomic groups (Flessa, 1990). Mass extinctions recorded in the Earth's fossil record were accompanied by 25% to >90% loss of species (Raup and Sepkoski, 1984; Sepkoski, 1993). The pervasive environmental, taxonomic, and geographic extent of these events suggests that physical forcing factors are involved (Jablonski, 1996). Proposed causes of such global environmental perturbations include sea level change, volcanism, oceanic anoxic events, solar cycles, and, as proposed for the end-Cretaceous mass extinction, large meteorite impact.

The K-Pg boundary event was the first major extinction recognized (Ryder, 1996), and its discovery in the early 19th century following the advent of fossil-based stratigraphy was partly due to the abrupt nature of the transition. Cuvier and Brongniart (1811), working in the Paris Basin, noted the lack of a transition between the Cretaceous chalk and the overlying clay and surmised, based on sedimentological evidence that a separation in time divided the two distinct units. A few years layer, d'Halloy (1822) classified these units into two geologic formations, the "cretaceous" and "mastozootic" (a precursor to the former "Tertiary" and current "Paleogene" terminology), based on both lithologic and faunal change at the boundary. Interestingly, the recognition of the sharp

boundary corresponding to the modern K-Pg boundary preceded our modern understanding of mass extinctions and even dinosaurs, which were not formally named until the 1940s (Ryder, 1996). Initially, the abrupt transition was explained as a depositional hiatus. Even Darwin (1859) surmised that the apparent sudden extinction of the ammonites and other groups was due to a time gap between the two formations. However, as paleontology and biostratigraphy work on the geologic interval progressed, the global and abrupt nature of microfaunal and macrofaunal changes at the K-Pg boundary became clear. In addition to the K-Pg boundary, other global biotic turnovers were identified in the stratigraphic record and today five major mass extinctions are recognized in the Phanerozoic: Late Ordovician, Late Devonian, Late Permian, Late Triassic, and Late Cretaceous. Of these, only the end-Cretaceous mass extinction is distinctly abrupt and distinctly associated with impact materials lying precisely at the lithologic and biologic boundary.

Despite the abruptness of the K-Pg boundary, both sedimentologically in the sharp lithologic transition from fossil-rich Cretaceous rocks to a fossil-poor clay and paleontologically particularly in the microfossil record, and the lack of transition units, a non-abrupt mechanism in line with the uniformitarian paradigm of the time was favored. Workers continued to argue that the discrepancy was due to a long depositional hiatus between the Cretaceous and Paleogene rocks (Hay, 1960; Rainwater, 1960). Even today, after the widespread acceptance of the Chicxulub impact at the K-Pg boundary, some workers continue to argue that the extinction was gradual and unrelated to the impact

event (Kauffman, 1988; Keller, 1988; Keller et al., 1993; Sloan et al., 1986; Ward et al., 1986).

Part of the problem with interpreting the abruptness of a mass extinction is that biases exist in the fossil record. At any given site, both fossil and sediment accumulation are discontinuous, environmental change occurs continually over a range of geographic and temporal scales, and reworking and mixing of sediments can occur over substantial vertical distances distorting the geologic record (Jablonski, 1996). A stratigraphic gap due to depositional hiatus produces an artificially abrupt extinction, just as smaller breaks in deposition can lead to interpretations of an artificially gradual or stepped transition (Birkelund and Hakansson, 1982; Raup, 1989; Signor and Lipps, 1982). The fossil record is always incomplete and, due to sampling bias, does not represent the abundances and ranges of species accurately. The last sample occurrence of some rarer species will occur below the biohorizon where the species actually goes extinct and the apparent range of the taxon will be artificially truncated and cause a mass extinction to appear gradual. This is known as the Signor-Lipps effect (Signor and Lipps, 1982) and, when applied to the K-Pg boundary, predicts that an abrupt extinction event can cause the observed gradual stepwise decline in species diversity at the boundary (Koch, 1991). The Signor-Lipps effect precludes the unequivocal determination of whether an extinction is gradual or abrupt from taxonomy. Statistical analysis of the fossil record can be used to measure the robustness of paleontological patterns and assess extinction intensities (Sepkoski and Koch, 1996). For example, such analyses convinced an initially skeptical

Marshall and Ward (1996) that the ammonites suffered an abrupt extinction at the K-Pg boundary.

The revolutionary hypothesis of the Berkeley group (Alvarez et al., 1980) was controversial when it was first proposed and continues to stir debate. Biostratigraphic and statistical studies continue to strengthen the argument for an abrupt mass extinction at the K-Pg boundary and the evidence in favor of the impact hypothesis continues to mount. Far more than a dinosaur killer, the mass extinction at the K-Pg boundary extinguished ~47% of the genera and 76% of the species living at the end of the Cretaceous (Jablonski, 1991). These include both marine and nonmarine species, macrofauna and microfauna, fauna and flora. Not all species suffered equally and the selectivity of the extinction event yields clues to its causes. I will mention a few interesting examples that illustrate the abrupt and global nature of the extinctions and also the differential survival patterns that the impact-induced environmental perturbations discussed later in this chapter can explain:

(1) Marine microfossils are the most useful organisms for studying extinction intensities due to their large abundances in small samples (Ward, 1990). Among the organisms most devastated by the K-Pg extinction event were marine plankton. Planktonic foraminifera experienced >97% species level extinctions (Thierstein, 1982), whereas benthic foraminifera experienced only ~10% faunal changes across the K-Pg boundary (Culver, 2003; Kaiho, 1992; Thomas, 1990). However, in shallower water (200-1000 m), survivorship decreases (Smit et al., 1997).

(2) Despite the devastation of plankton species, deep-sea, near shore, and brackish-water fish species survived the K-Pg boundary relatively unscathed (Cavin, 2001). Sheehan and Fastovsky (1992) inferred 10% extinction for freshwater vertebrates, and most fish and other species such as crocodiles survived.

(3) Land vertebrates were not so lucky and survivorship has been estimated at between 12% (Sheehan and Fastovsky, 1992) and 64% (Archibald and Bryant, 1990). Compared to marine microfossils, the terrestrial vertebrate fossil record is not very complete and there are fewer known nonmarine K-Pg sites (mostly in North America). The most famous of the K-Pg extinction casualties, dinosaurs, represent only a small percentage of vertebrate species and have a spotty fossil record that suffers from the Signor-Lipps effect (Pierazzo, 1997). In general, large vertebrates such as dinosaurs faired worse than smaller vertebrates such as mammals.

(4) There is evidence for a massive turnover in terrestrial plant assemblages across the K-Pg boundary. Tropical forests filled with abundant species proliferated through the Late Cretaceous, but vanish at the K-Pg boundary. In North American localities this is seen as an abrupt attenuation of the diversity and abundance of pollen grains from flowering flora typical of Cretaceous assemblages (Nichols, 2007; Nichols and Fleming, 1990; Spicer and Shackleton, 1989). Above the K-Pg boundary a dramatic increase in fern spores ("fern spike") is seen (Tschudy et al., 1984), after which the proportion of spores gener-

ally declines and pollen increases in abundance and diversity to characteristic Paleogene flora assemblages (Tschudy and Tschudy, 1986). The plant record supports an abrupt and catastrophic terminal Cretaceous event marked by the abrupt disappearance of most dominant taxa and nearly all angiosperms (Johnson and Hickey, 1990; Nichols and Fleming, 1990). Initial work suggested megafloral extinctions were comparatively minor in the tropics and the southern hemisphere (Johnson and Hickey, 1990; Nichols and Fleming, 1990), but a similar fern spike has been observed in the southern hemisphere in New Zealand (Vajda et al., 2001) indicating that the devastation of forests was a truly global event. A fungal spike has also been reported between the diverse Late Cretaceous flora and the low-diversity early Paleogene fern-dominated assemblages, coincident with the K-Pg ejecta layer (Vajda and McLoughlin, 2004).

Despite the growing consensus that the Chicxulub impact was responsible for the end-Cretaceous mass extinction, many questions remain about how exactly the impact led to the mass extinctions. The global extent of the extinctions and the K-Pg boundary ejecta layer is no coincidence: several proposed impact-induced environmental perturbations are directly linked to deposition of impact plume material into the upper atmosphere. These include effects from enhanced levels of dust, aerosols, and water in the atmosphere, acid rain from injection of nitrogen and sulfur compounds, long term effects due to enhancements in greenhouse gases such as CO_2, and ejecta-triggered ignition of forest fires. For additional information beyond the overview presented here, see Toon et al. (1997), Kring (2003), and Pierazzo et al. (2003).

2.4.1 Dust

In their initial proposal of an end-Cretaceous impact event, Alvarez et al. (1980) surmised that the iridium-enriched boundary layer deposit was once a large quantity of dust which was globally distributed in the atmosphere following Chicxulub blocking the sun, suppressing photosynthesis, and leading to the collapse of the food chain. Although subsequent studies of the heavily altered ejecta layer revealed that the layer is composed primarily of larger microkrystite spherules and shocked mineral grains (Smit, 1999), there is still some quantity of dust and there have been multiple attempts to assess the magnitude of this environmental disturbance and the length and severity of the "impact winter" following Chicxulub (Covey et al., 1990; Covey et al., 1994; Pollack et al., 1983; Toon et al., 1982; Toon et al., 1997). Submicron dust can originate either from condensation of impact plume materials or from pulverized target rock ejected in the ejecta curtain (Toon et al., 1997). Only the former is expected to be globally distributed and is the focus of the remainder of this discussion.

Early studies assumed that the bulk of the boundary layer, which is today heavily altered to clay, was submicron dust (Alvarez et al., 1980; Toon et al., 1982). When the spherules are considered, if all the void spaces between spherules were originally filled with dust, the layer would be <50% dust. Toon et al. (1997) calculate that >10% of the global K-Pg boundary ejecta layer is submicron dust. However, Pope (2002) argues, based on vapor condensation models (O'Keefe and Ahrens, 1982) that predict conden-

sates several hundred micrometers in size, that vapor condensates from Chicxulub's impact plume would produce minimal submicron particles. In this case, submicron dust would compose <1% of the global K-Pg deposits and have insignificant environmental effects. Microphysical simulations of a dust cloud in the stratosphere by Toon et al. (1982) predict that the dust particles fall out of the atmosphere in less than 6 months, which is consistent with measurements of Pinatubo tephra in the atmosphere from the 1991 eruptions (Pueschel et al., 1994). In a dust cloud consisting of as little as 1% of the K-Pg boundary layer, coagulation of dust to form larger particles would be significant and lead to more rapid sedimentation (Toon et al., 1982). Condensation of water vapor (also injected by the impact plume into the upper atmosphere) into faster-settling ice crystals would also sweep away some of the dust (Toon et al., 1997), although the efficiency of this process is unknown.

A cloud of dust in the upper atmosphere acts to limit the radiative transfer of solar energy to the surface and depends on the optical depth of the dust layer. The transmission of sunlight can be approximated by an exponential function of the dust layer's optical depth (Toon et al., 1997). For a Chicxulub-sized impact, even if using conservative estimates of dust (~10% of the boundary layer), the loss of sunlight is sufficient to prevent photosynthesis and vision following the impact event (Toon et al., 1982; Toon et al., 1997). Using an atmospheric general circulation model (GCM), Covey et al. (1994) modeled a dust layer from a Chicxulub-sized impact and found that the land surface temperature was depressed for one year despite the gradual removal of dust. In addition there was a 90% decrease in precipitation for several months. The temperature decrease

and timescale was comparable to those found by Luder et al. (2002), although they calculated only a 50% decrease in precipitation. Unless the amount of dust is being overestimated (Pope, 2002), an impact-generated dust cloud from Chicxulub could have depressed surface temperatures for a year or more. Despite the fact that the dust likely fell out of the atmosphere over several months, the climatic feedbacks are complex and operate over a longer timescale.

2.4.2 Sulfate Aerosols

The Chicxulub impact occurred into unique target rock stratigraphy of carbonates and anhydrites overlying granitic basement rock (Lopez-Ramos, 1975; Ward et al., 1995). Chicxulub lies in an evaporate terrain rich in calcium sulfate deposits, which would have contributed significant sulfur to the impact plume (Brett, 1992; Sigurdsson et al., 1991; Sigurdsson et al., 1992). Asteroids and comets also contain sulfur: a carbonaceous chondrite, which is thought to be the Chicxulub projectile composition, contains 6% sulfur by weight (Anders and Grevesse, 1989). Experimental evidence suggests that a Chicxulub-sized impact into evaporite may generate as much SO_2 as the ejecta in the K-Pg boundary layer or 5 times more than the 1991 Pinatubo eruption (Sigurdsson et al., 1991; Sigurdsson et al., 1992). The climatic effects of such a sulfur injection into the upper atmosphere can be investigated via analogy with volcanic eruptions. The results from the Pierazzo et al (1998) model is two orders of magnitude larger than any recorded

volcanic eruption and, because increasing SO_2 leads to longer decay times, would have devastating environmental effects (Pierazzo et al., 1998; Pope et al., 1997).

Sulfur-bearing gases from the impact plume react with water vapor to form sulfate aerosols, both within the plume and in the stratosphere (Pierazzo et al., 2003). Like sub-micron silicate dust, sulfate aerosols that condensed from the sulfur-enriched impact plume would block sunlight leading to darkening and cooling of the Earth's surface. Unlike the silicate dust, aerosols would remain in the atmosphere for a longer period of time, extending the timescale of cooling. Pope et al. (1994) calculate a 6-9 month black-out with freezing temperatures and disruption of photosynthesis. The first 3-6 months is due to both silicate dust and aerosols, after which the silicate dust has fallen out of the atmosphere and only the aerosols remain. In the long term, the blackout leads to a 10-20% decrease in solar transmission for 8-13 years, which is the equivalent to the solar forcing of a cloudy day. In the short term, radiative forcing of -300 W/m^2 would dominate over an impact-induced greenhouse effect (~+10 W/m^2). Modeling by Pierazzo et al. (2003) predict a similar radiative forcing of -100 W/m^2 for three years. If there were no other feedback, such a forcing would lead to 100°C cooling, but fortunately the oceans are able to act as a buffer for several years. Even so, models of short-term impact-induced oceanic cooling suggest significant cooling of the ocean surface over a period of <14 years (Covey et al., 1994) and Pollack et al. (1983) also predict a ~15 year timescale for cooling. Although this is less than the timescale of ocean column mixing and the deep ocean likely did not experience any cooling (Luder et al., 2002), the ocean surface was likely near freezing for a few years (Pope et al., 1997).

2.4.3 Water Injection

Emiliani et al. (1981) first suggested that a massive injection of water vapor into the upper atmosphere resulted from the impact at the K-Pg boundary. Now that the location and target characteristics of the impact are known, a more precise estimate of water injections can be made (Toon et al., 1997). Assuming that 50 m of water covered the Chicxulub impact site on the carbonate platform of the Yucatán peninsula, Pope et al. (1994) estimated water injections ranging from the ambient amount in the upper atmosphere to 50 times this amount. Water vapor is an important greenhouse gas and increasing the upper atmospheric humidity 25 times above ambient would lead to an 8°C increase in surface temperature (Manabe and Wetherald, 1967). Portions of the impact-generated water vapor cloud may be cold enough to form ice and fall downwards and evaporate to humidify lower levels in the atmosphere (Toon et al., 1997) and part of the cloud may photolyze to O and H and result in a loss of H_2O vapor. Impact-induced water injection is thus an important source of free radicals that can participate in ozone chemistry (Toon et al., 1997). Although there is still uncertainty concerning the amount of water ejected during the Chicxulub impact, models (Pierazzo, 2005) indicate that the water vapor injected into the upper atmosphere by a Chicxulub-sized impact is greater than triple the quantity that the middle atmosphere can hold in saturation and the excess will fall out following cooling. However, if the upper atmosphere is heated, which our mod-

els show, this would change the ability of the atmosphere to hold water in the vapor phase and prolong the greenhouse effect.

2.4.4 Acid Rain

Two types of impact-induced acid rain following Chicxulub have been proposed: nitric acid rain (Lewis et al., 1982; Prinn and Fegley, 1987) and sulfuric acid rain (Lewis et al., 1982). Both are caused by interactions between impact plume material and the upper atmosphere (Toon et al., 1997): (1) impact-produced shockwaves in the air convert N_2 and O_2 to NO and (2) impact into a sulfate- or carbonate-rich target, such as Chicxulub, forms SO_2 and CO_2. In addition, fires produce nitrogen oxides and other chemicals that may later form acid rain (Toon et al., 1997).

There are four major paths of NO formation from atmospheric N_2 and O_2 (Zahnle, 1990): (1) NO is produced by the shockwave as the meteorite passes through the atmosphere prior to impact (Prinn and Fegley, 1987; Turco et al., 1982). (2) NO is produced by the shockwave as the ejecta plume expands upwards through the atmosphere (Prinn and Fegley, 1987). (3) NO is produced as ejecta reenters the upper atmosphere at hypersonic speeds creating a local shock wave (O'Keefe and Ahrens, 1982). (4) Radiative heating of the atmosphere >1500 K would cause chemical reactions favorable to NO production (Sleep et al., 1989). However, Toon et al. (1997) suggest that it is difficult to produce enough nitric acid rain by an impact to cause serious global effects because energy deposition from the impact plume is at high altitudes where there are few air molecules and

the air cools more slowly following global shock by an impact than an isolated shock event such as a lightning bolt. Global amounts of nitric acid rain were likely similar to those currently experienced in the United States and Europe (Toon et al., 1997) and, acidifying at most 1% of the ocean's surface waters, not a major end-Cretaceous killer.

The argument for sulfuric acid rain is stronger because of the support for an abundance of sulfate aerosols in the atmosphere following Chicxulub, as discussed above. Sulfate aerosols react with water vapor to form sulfuric acid, diffuse into the troposphere, and fall out as sulfuric acid rain. The environmental effects of this depend on the amount of acid rain produced in the atmosphere and how long it takes to rain out, as well as the buffering capacity of the environment and the sensitivity of organisms. Sulfate injections predicted by Sigurdsson (1992) could have caused global acidification of the oceans via acid rain (D'Hondt et al., 1994). However, these early experimental results may be overestimated by an order of two magnitudes (Brett, 1992; Pope et al., 1994) and would not lead to acidification of the oceans. Such smaller estimates are supported by modeling efforts (Chen et al., 1994; Ivanov et al., 1996; Pierazzo et al., 1998).

2.4.5 CO_2 Enhancement

The carbonate target rock at Chicxulub resulted in the injection of some quantity of CO_2 into the upper atmosphere, which would have enhanced the greenhouse effect to some degree. Modeling work (Ivanov et al., 1996; Pierazzo et al., 1998) suggests a <40% increase above end-Cretaceous background levels, although other models (Takata and

Ahrens, 1994) suggest 1-2 orders of magnitude more CO_2. The discrepancy is due to differences in the modelers' equations of state for calcite which determine how much degassing occurs at a given shock pressure. Pope et al. (1994) calculated a maximum climate forcing from CO_2 enhancement of +8 W/m^2 , which is equivalent to 4°C surface warming and Pope et al. (1997) predicted even less (<2°C). This is insignificant combined with the cooling effect of aerosols and dust (-300 W/m^2) due to vaporization of sulfates. However, in the long term—after the cooling due to aerosols has faded—impact-induced warming may occur and would agree with oxygen isotope studies of early Paleogene marine organisms (Hsu et al., 1982) consistent with a warming event.

2.4.6 Fires

Soot has been identified at the K-Pg boundary at sites around the world (Wolbach et al., 1990; Wolbach et al., 1985). Carbonized plant debris (Smit et al., 1992b) and fusinite (Tschudy et al., 1984) have been identified at the K-Pg boundary and attributed to fires. Measured carbon isotope shifts are also consistent with massive fires (Ivany and Salawitch, 1993), suggesting a large fraction of the Cretaceous biomass burned following Chicxulub. Large-scale fires have several environmental consequences: (1) Fires directly kill biomass by burning or by thermal damage. (2) Fires produce smoke which would increase the dust opacity and augment surface cooling, potentially causing similar magnitude of cooling as silicate dust (Toon et al., 1997). (3) Fires produce pyrotoxins (Crutzen and Birks, 1982) and would lead to enhanced CO_2.

There are several ways that an impact can ignite the forests (Toon et al., 1997): As the meteorite enters the atmosphere and ablates it can produce fires on a local scale. Thermal radiation from the rising impact plume can ignite fires on a regional scale. Finally, thermal radiation from the global reentry of ejecta spherules may be sufficient to ignite wildfires on a global scale (Melosh et al., 1990). This latter effect is the focus of Chapters 6 and 7, where thermal radiation from the reentering ejecta is explored in detail.

2.5 Motivation

Unlike impacts onto airless bodies where ejecta deposition from both the ejecta curtain and impact plume can be treated as purely ballistic processes, the Earth has an atmosphere and atmospheric interactions must be considered in any model for Chicxulub ejecta sedimentation. This is particularly true for the impact plume ejecta because, travelling at supersonic velocities, these particles deposit a large quantity of energy into the upper atmosphere. A numerical model is needed to model the atmospheric effects of impact plume ejecta deposition and understand (1) the mechanical style of deposition of the global K-Pg boundary layer and (2) the resulting environmental effects of atmospheric ejecta reentry and descent through the atmosphere.

CHAPTER 3

THE KFIX-LPL TWO-FLUID HYDRODYNAMICS CODE

3.1 Introduction

Two-phase fluid flows are common in both natural and man-made environments. Bubbles rising in a pot of boiling water or a carbonated beverage, raindrops falling through air, and foaming ocean waves are common examples. Development of mathematical models has been historically motivated by the occurrence of two-phase fluid flows in a variety of industrial contexts such as water and steam circulating in a nuclear reactor, gas and air reacting in a car engine, and oil mixing with water in a borehole. Such numerical tools can be applied to two-phase geologic flows which include mixtures of rocks and gas in pyroclastic surges, sediment transport in rivers, turbidites on the ocean floor, tephra fallout though the atmosphere, water and sediment in lahars, sandstorms, fluidized beds, crystal settling through a magma chamber, separation of melt from partially molten rock, and iron/silicate separation during planetary core formation. Although the mechanical details of each flow differ, the macroscopic properties of a two-phase flow can be described with models involving similar physics. Similar numerical approaches can be applied to a wide range of two-phase fluid flows, including disperse flows involving hypersonic velocities. Although in some ways an extreme example of two-phase flow, the same numerical methods that model boiling water can be applied to impact ejecta reentry and sedimentation through the Earth's atmosphere.

Whether the flow involves two immiscible liquids, a liquid and a solid, a liquid and a vapor, or a vapor and a solid, common to all two-phase flows are discernible interfaces separating the phases (Liles, 1981). As the two phases interact across these interfaces, they can exchange mass, momentum, and energy. Modeling these interactions is complex and depends on the relative concentrations of the phases and the general pattern of the flow. For example, the flow of disperse spherical vapor bubbles rising in a bottle of soda behaves differently from the flow that results when one drinks from an inverted soda bottle and air replaces the liquid as a series of vapor slugs.

Analysis of two-phase flow starts with the fundamental conservation equations of mass, momentum, and energy. These can be expressed as instantaneous field equations at every point in space; however, an exact solution of these equations is computationally expensive given the complexities of the interfaces at the microscopic level. However, a macroscopic description of the flow is often sufficient, and the local, instantaneous field equations can be averaged either in time or space to yield an accurate solution (Liles, 1981). Because the two phases may move relative to each other and exchange mass (via phase changes or chemical reactions), momentum, and heat, more than one set of field variables is required to describe two-phase flow dynamics (Harlow and Amsden, 1975). A typical two-phase fluid flow model, where each phase is treated as a continuum, begins with six field equations expressing the mass, momentum, and energy of each phase averaged over, for example, a cell of finite dimensions. The interfaces separating the phases are assumed to have no thickness and can only exchange between phases—but not store—mass, momentum, and energy. The field equations are then used to determine the

fluxes of mass, momentum, and energy between phases. A complete analysis involves constitutive equations, in which each phase is again treated separately, to describe the thermodynamic properties of the two phases and the interactions between them. Constitutive equations serve to compute the stresses for both phases and the manner of material interaction across an interface using material properties of the phases and geometric properties of the interface (Drew, 1983). Constitutive equations, which vary depending on the phases involved and the nature of the flow, describe the interfacial exchange of mass (e.g. evaporation and condensation), momentum (e.g. drag forces), and energy (e.g. conductive or frictional heat transfer). In addition, interactions with the medium containing the flow (its boundaries), such as a pipe in a nuclear reactor or a soda bottle, must be considered. A basic mathematical model of two-phase flow includes six coupled partial-differential equations expressing the conservation principles and numerous constitutive relations.

Even the simplest flows are thus quite complex to model without a numerical computer simulation. The six fundamental partial differential equations can be approximated by algebraic equations that a computer can solve using finite distance intervals (cells) and finite time intervals (time step). In a properly constructed numerical scheme, as the cell size and time step are decreased, the numerical result approaches the exact solution to the original differential equations and so the stability and accuracy of the calculation depend on the choice of these parameters (Liles, 1981).

The KACHINA code (Amsden and Harlow, 1975) was developed at the Los Alamos Scientific Laboratory for application to two-phase fluid flow problems. It is an

eulerian program which employs an implicit, multifield solution method to solve a finite-difference representation of the partial differential equations using a pressure iteration solver. The computing technique used by KACHINA is described in detail by Harlow and Amsden (1975) and Travis et al. (1975), but basically includes implicit treatments of mass convection and equations of state where flow speeds can range from subsonic to supersonic and phases are implicitly coupled over an eulerian mesh of finite cells. KACHINA was supplanted by the K-FIX code (Rivard and Torrey, 1978), in which improvements include the implicit coupling of phase transitions and interfacial heat transfer to the fluid dynamics in the pressure iteration. The resulting finite-difference representations of the partial differential equations are **f**ully **i**mplicit in the e**x**change ('FIX') of mass, momentum and energy.

3.2 The Original K-FIX Code

A complete description of K-FIX can be found in its manual and supplemental material (Rivard and Torrey, 1978). In K-FIX, the field equations for each phase are coupled through the exchange of mass, momentum, and energy and through the condition of pressure equilibrium between phases. Each phase has its own set of field equations which include the effects of phase changes, interfacial friction, and thermal gradients on mass, momentum, and energy transfer. The equation of state for each phase is defined, in which pressure P and internal energy I are the independent variables used to determine density ρ and temperature T. Viscous stresses are also defined.

The partial differential equations are written in finite-difference form so that they can be solved numerically and solutions are obtained in either plane, cylindrical, or spherical geometry. Each computational cell has some volume fraction θ (or 1- θ) of each phase such that the microscopic density ρ' is defined as

$$\rho_g' = \theta\rho_g \qquad [3.1]$$

$$\rho_l' = (1-\theta)\rho_l \qquad [3.2]$$

where ρ_x is the microscopic density of the phase x and l and g denote liquid and gas phases. The velocity components for each phase are centered on the cell boundaries in the staggered grid configuration (see Patankar, 1980, p.118) and most other variables (density, volume fraction, pressure, internal energy, viscosity, etc.) represent cell-centered quantities (

Figure **7**).

The finite difference equations are solved by a point relaxation technique which computes a new cell pressure and iterates, adjusting the pressure nonlinearly as a function of the deviation from mass balance, until the convergence criterion is met in all cells. The convergence criterion we use is 10^{-12} ρ_g', which maintains energy conservation throughout our ejecta simulations. Determining to what decimal place convergence is required depends on the time step and the total number of computational cycles in a simulation. During each iteration, a pressure solution meeting the convergence criterion is determined for each cell and the densities, volume fractions, and mass fluxes are updated. This is repeated iteratively until all cells meet the convergence criterion simultaneously. The pressure iteration solves the mass and momentum equations for the two

phases and yields a partial solution for the energy equations. After convergence, a final solution for the energy equations is obtained.

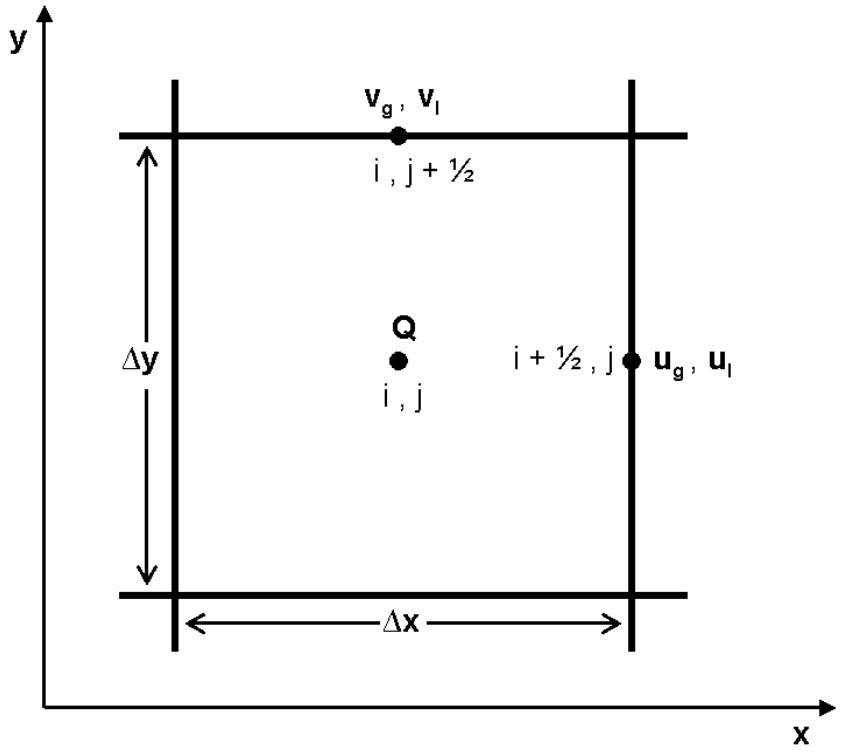

Figure 7. A typical computational cell of indices (i,j) in K-FIX showing the relative spatial locations of the variables used in the finite-difference equations. The velocity components for each phase are centered on the top and right cell boundaries and Q represents all other variables, which are cell-centered. Based on Rivard and Torrey (1978).

K-FIX includes several boundary conditions for the perimeter of the computing mesh: fixed, free-slip, inflow, and outflow. The boundary conditions are enforced using a single row of fictitious 'boundary cells' on each side of the mesh that can exchange mass, momentum, and energy with the adjacent 'active cells' according to the boundary

conditions. Fixed boundaries are no-slip rigid walls, where the velocities of both phases at the boundary is zero. This is achieved by setting the tangential velocities of the fictitious boundary cells equal to those of the adjacent computational cells but in opposite directions. In contrast, the phases slide freely with no reduction in velocity across a free-slip boundary, which is implemented in K-FIX by setting the tangential velocity in a boundary cell equal in direction and magnitude to the adjacent computational cell. Inflow can be prescribed (phase velocities of inflow boundary cells are set by the user) along the bottom and left mesh boundaries and continuative outflow is possible along the top and right mesh boundaries, for which the boundary cells have identical normal velocities as the adjacent computational cells.

3.3 Modifications in KFIX-LPL

KFIX-LPL is a modified version of the original K-FIX code that has been adapted for use in impact ejecta-atmosphere studies. The basic finite-difference equations and the iterative pressure solution are (mostly) unaltered, but constitutive relations have been implemented to describe the air and ejecta phases and the interaction between them. The following common variables (in cgs units[2]) are used where *g* denotes the gas phase (air) and *l* denotes the liquid phase (impact ejecta spherules):

P	Pressure (dynes/cm^2)
ρ_g, ρ_l	Microscopic density (g/cm^3)

[2] KFIX-LPL simulations presented here were run in cgs units, which is remnant from the original K-FIX code. The code is adaptable for other metric unit systems.

ρ_g', ρ_l'	Macroscopic density (g/cm^3)
T_g, T_l	Temperature (K)
C_g, C_l	Specific heat capacity at constant volume (erg g^{-1} K^{-1})
I_g, I_l	Specific internal energy per unit mass (erg/g)
V_g, V_l	Vertical velocity component (cm/s)
U_g, U_l	Horizontal velocity component (cm/s)
a	Particle radius (cm)
A	Interfacial surface area per unit volume (1/cm)
θ	Volume fraction of gas phase
$1-\theta$	Volume fraction of liquid phase
μ_g, μ_l	Shear viscosity (g cm^{-1} s^{-1})
η_g, η_l	Dynamic viscosity (g cm^{-1} s^{-1})
Δx	Cell dimension (cm), where cells are square
Δt	Computational time step (s)

3.3.1 The Gas Phase (Air)

3.3.1.1 *Equation of State*

Air is assumed to behave like a perfect gas according to the ideal gas law, but the equation of state is extended to high temperature and low pressure regimes encountered in the upper atmosphere during ejecta reentry where ionization of atmospheric gases

occurs. Using approximate fits to the detailed numerical computations of Hansen (1958), the current equation of state is suitable for pressures of 0-10 bars and temperatures of 0 to 6000 K:

$$T_g = \frac{d}{b \cdot \sqrt[3]{18}} - \left(\frac{2}{3}\right)^{1/3} \frac{a}{d} \qquad [3.3]$$

$$C_g = 3.448 \times 10^5 \left(a + bT_g{}^2\right) \qquad [3.4]$$

$$\rho_g = \frac{3.448 \times 10^{-7} P}{z(P,T) T_g} \qquad [3.5]$$

where the intermediate variables *a*, *b*, *c*, and *z* are

$$a = 20.785 \qquad [3.6]$$

$$b = \frac{7.93 \times 10^{-6}}{P^{0.12}} \qquad [3.7]$$

$$c = 2.9 \times 10^{-6} I_g \qquad [3.8]$$

$$z(P,T) = 1 + \frac{4.571 \times 10^{-8} T_g^2}{P^{0.11}} \qquad [3.9]$$

3.3.1.2 *Pressure and Temperature Gradients*

For ejecta reentry simulations, the initial mesh approximates the Earth's atmosphere. We implemented routines to calculate the initial pressure and temperature proper-

ties of the air as a function of altitude. We assume an exponential equilibrium pressure distribution for the Earth's atmosphere such that

$$P = P_o e^{-gh/R'T_g} \qquad [3.10]$$

where P_o is the pressure at sea level, g is gravity, h is altitude (of the cell center), and R' is the specific gas constant for air. The atmosphere is assumed to be initially isothermal with the gas phase in every cell set to 273 K.

The actual structure of the Earth's atmosphere is not so simple. US Standard Atmosphere tables (1976) show (Figure 8) that an isothermal atmosphere with an exponential pressure gradient as a function of altitude only (since T_g is constant) is a decent approximation up to ~100 km in altitude. Above this, however, the thermosphere increases in temperature, reaching 600 K at 150 km altitude. We use the simplified pressure and temperature model instead of relying on tabular data because the atmospheric reentry of impact ejecta quickly alters the structure of the upper atmosphere beyond any natural variations. Compression of the upper atmosphere changes its density structure and the air heats up to several thousand degrees Kelvin during spherule deceleration, far exceeding the normal several hundred degree increase in the thermosphere. All the simulations presented here employ an isothermal initial atmosphere, however future simulations will explore the effects of this assumption.

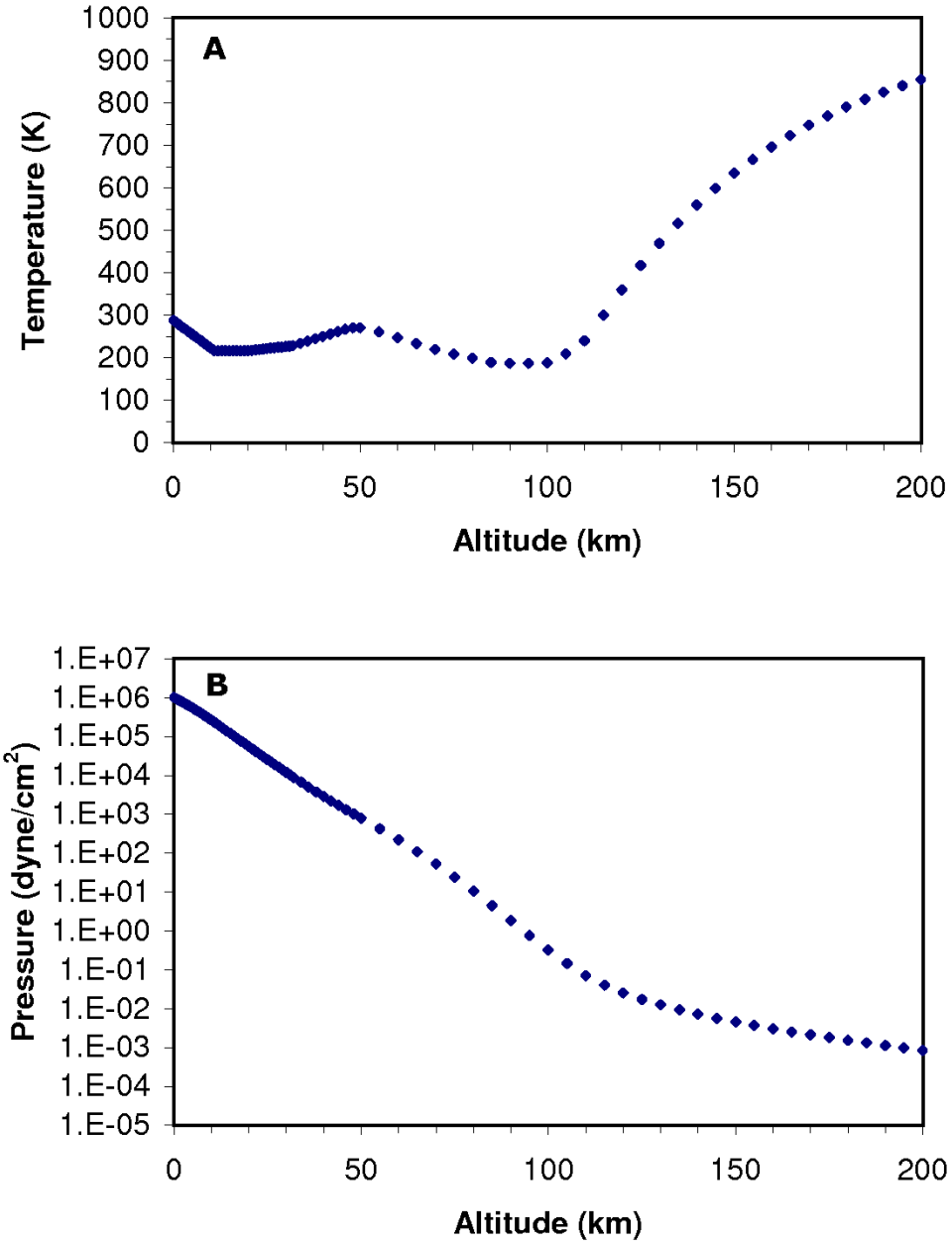

Figure 8. (a) Temperature and (b) pressure of the Earth's atmosphere as a function of altitude according to U.S. Standard Atmosphere (1976) data.

3.3.1.3 *Viscosity*

The shear viscosity of air is adapted from an eddy viscosity approximation by Hirt (2005):

$$\mu_g = 0.03 \rho_g \upsilon_{dif} \Delta x \qquad [3.11]$$

Where υ_{dif} is the variation in gas velocity across the cell. During reentry of Chicxulub ejecta the eddy viscosity in our simulations ranges from 6.5×10^{-5} g cm^{-1} s^{-1} in the upper atmosphere to 0.28 g cm^{-1} s^{-1} near the ground.

The dynamic viscosity of air is approximated based on Capitelli et al. (2000) for T < 10,000 K (Figure 9):

$$\eta_g = 2 \times 10^{-5} T_g^{\,0.7927} \qquad [3.12]$$

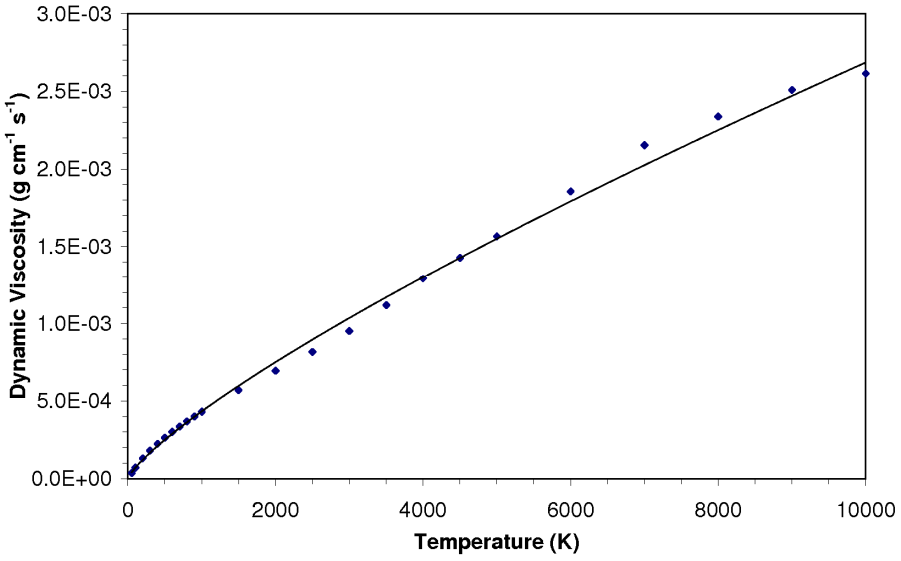

Figure 9. Dynamic viscosity of air as a function of temperature. Blue dots are Capitelli et al. (2000) data points and the line fit to the data is the exponential function used in KFIX-LPL. Air temperatures in the Chicxulub ejecta simulations are <5000 K.

3.3.1.4 *Phase Changes*

No phase changes are permitted at this time. The air remains in the vapor phase and cannot condense. Ionization is considered in the equation of state because high temperatures are experienced in the upper atmosphere during spherule reentry.

3.3.2 The Liquid Phase (Ejecta)

3.3.2.1 *Equation of State*

The ejecta spherule phase is treated as a simple incompressible fluid according to the following equation of state in which the spherules are assumed to have thermodynamic properties and density of average basaltic glass (Bass, 1995; Clauser and Huenges, 1995):

$$C_l = 9.2 \times 10^6 \qquad [3.13]$$

$$\rho_l = 2.777 \qquad [3.14]$$

$$T_l = T_0 + \frac{I_l - I_0}{C_l} \qquad [3.15]$$

where T_0 is the reference temperature (273 K) and I_0 is the internal energy at the reference temperature (2.512×10^9 erg/g).

An actual spherule, if molten, would display some compressibility. However, the incompressible fluid approximation, which assumes constant density at all pressures, is satisfactory for ejecta spherules. The bulk modulus *K*, which describes a substance's resistance to uniform compression, is ~6×10^{11} dynes/cm^2 (~60 GPa) for average basaltic glass (Bass, 1995). The bulk modulus is defined as the pressure increase causing a given relative decrease in volume:

$$K = -V\frac{\partial P}{\partial V} \qquad [3.16]$$

A 250 µm impact spherule decelerates through the upper atmosphere, heats up, and reaches its terminal velocity at ~70 km in altitude. Between 150 km in altitude and 70 km, the pressure increase is ~6.4×10^4 dynes/cm^2 which results in a volume decrease of only ~10^{-5} %. Even if the change in pressure to the ground is considered, at which point there is no possibility of molten spherules, the volume decrease is still only ~10^{-4} %. This volume change is insignificant and the incompressible equation of state is a valid macroscopic approximation for the purposes of the ejecta reentry problem.

3.3.2.2 *Surface Area*

The impact ejecta are modeled as spherical particles with radius *a*. KFIX-LPL does not model individual spherules, but rather a certain volume fraction of the spherule phase dispersed into discrete droplets in each cell. For a given cell volume, the surface area is the total surface area of some number of spherical particles. In other words, it is the total interfacial area between phases in a cell per unit volume:

$$A = \frac{3(1-\theta)}{a} \qquad [3.17]$$

This treatment of the interfacial area assumes low concentration of the liquid phase in dispersed droplets where particles do not share surface area with each other. It is also apparent that this treatment limits all particles in a given cell to a single shape and size.

3.3.2.3 *Viscosity*

The ejecta phase is modeled assuming no shear viscosity. This is adequate because the particles are largely solid and dispersed in the air phase as small droplets at low concentrations.

3.3.2.4 *Phase Changes*

No phase changes are permitted for the ejecta phase at this time. The ejecta spherules are assumed to retain all their mass throughout the simulation. If the particles remain above their melting point for long enough, ablation is significant and this assumption is incorrect.

3.3.3 Particle Injection

Both liquid and gas phases can be injected across an inflow boundary into the computational mesh. The original K-FIX code assumes that the properties and rate of

inflow are constant. KFIX-LPL includes modifications to allow inflow parameters to vary with time. For the impact ejecta simulations, we inject ejecta droplets along with a small mass of air. The mass flux of the liquid phase into the mesh is expressed as a function of time (e.g. a pulse of ejecta reentering the atmosphere from the impact plume) and, based on the microscopic density of the liquid phase and the liquid inflow velocity, this is converted to liquid and gas volume fractions, macroscopic densities, and internal energies in the boundary cell. The air phase has zero (or small) velocity in the inflow boundary cells so as to inject primarily spherules.

Each phase is restricted to a uniform direction of motion, velocity, and particle size in a single computational cell. However, we can vary these parameters in the inflow cells with time which is useful for many geologic problems. Variable particle radii (or the relation of interfacial surface area to liquid volume) are possible only if the different-sized droplets remain in separate cells. We have implemented an advection scheme to advect particle radius with the liquid velocity field as the ejecta particles fall through the atmosphere, although this was not required for the simulations presented here which use only a single spherule size throughout atmospheric reentry of ejecta.

3.3.4 Drag Coefficient

K-FIX defines an interfacial friction function for momentum exchange K_d which depends on the drag coefficient C_d. We initially used the exchange function of Harlow and Amsden (1975, Equation 12), which is valid for disperse spherical particles in uni-

form Stokes or turbulent translation through the vapor phase. Conventional treatments of frictional drag assume that the vapor phase can be treated as a continuum. However, small ejecta particles entering the upper atmosphere at hypersonic velocities are typically much smaller than the mean free path of gas molecules at these altitudes and the particles are in free molecular flow. The Amsden and Harlow (1975) drag expression is not accurate for such flow conditions and overestimates drag forces for the initial spherule descent through the upper atmosphere.

We derived a new drag coefficient function for a sphere at all velocities from the continuum flow limit (Stokes/turbulent) to the semi-continuous regime approaching free-molecular flow (Melosh and Goldin, 2008). It was derived from an expression in the aerospace literature (Crowe, 1967) that describes the motion of small solid particles in hot gases streaming from a rocket nozzle. The new drag coefficient, which is defined in Melosh and Goldin (2008) is a complex function of the Reynolds (*Re*) and Mach (*M*) numbers and includes viscous terms. The drag coefficient is incorporated in a new expression for momentum exchange:

$$K_d = \frac{3\eta(1-\theta)ReC_d(Re,M)}{16\theta a^2} \qquad [3.18]$$

The new drag coefficient is applicable for the ranges of Reynolds numbers (which relate to the flow regime) and Mach numbers (which relate to the flow velocity) experienced by impact ejecta during descent through the Earth's atmosphere.

3.3.5 Heat Transfer

Similarly, a new heat transfer function and friction factor (see Melosh and Goldin, 2008) was derived from existing expressions in the aerospace literature (Carlson and Hoglund, 1964) in order to accommodate the range of flow regimes experienced by impact ejecta during atmospheric descent. The original K-FIX code contains terms that describe frictional heating and heat transfer between liquid and gas phases. K-FIX assigns all frictional heating to the gas and the liquid can only be heated by conduction from the hot gas. However, at the high speeds experienced during ejecta reentry, the gas may heat the liquid directly via compression and friction regardless of temperature gradients and new terms must be added to the energy field equations. Furthermore, frictional heating must be compatible with aerodynamic drag in order to conserve both energy and momentum. The heat transfer function computes the heat exchange between phases as a function of the Nusselt number *Nu*, which represents the ratio of convective to conductive heat transfer. We modified an existing expression for the Nusselt number (Carlson and Hoglund, 1964) to extrapolate correctly to the rarefied gas limit, which is encountered by reentering impact ejecta in the upper atmosphere. The new Nusselt expression (Melosh and Goldin, 2008) is a function of Mach, Prandtl (*Pr*), and Reynolds numbers and is incorporated into the heat transfer function *R* such that

$$R = \frac{3k_g(1-\theta)}{2a^2}Nu \qquad [3.19]$$

where k_g is the thermal conductivity of the gas phase.

We also derived an expression for the heat transfer by friction α which is a function of the Nusselt number, drag coefficient, and "recovery factor" r and represents the fraction of the total energy that is transferred to the particle (see Melosh and Goldin, 2008):

$$\alpha = \frac{8r}{\gamma c_d}\left(\frac{Nu}{\mathrm{Re}\,\mathrm{Pr}}\right) \qquad [3.20]$$

where γ is the ratio of specific heats and $\alpha \leq 1$. Although in most continuum flow regimes $\alpha \approx 0.5$ and frictional heating is split evenly between phases, in the rarefied gas limit $\alpha \approx 0.86$ and most of the frictional heat goes into the particle phase.

3.3.6 Thermal Radiation

A thermal radiative transfer model, which includes optical opacity using a diffusion approximation iterative technique, was developed by H. J. Melosh and implemented within KFIX-LPL. An overview of the thermal radiation model is presented in Chapter 7 and a complete description can be found in Appendix C. The radiation calculation includes special treatment for the mesh boundaries (i.e. how much thermal radiation is permitted to escape vs. be reflected at the boundary) and is coupled to KFIX-LPL at the end of each computational cycle of time interval Δt when the final energies are determined:

$$I_l = I_l - \kappa_l \left(4\sigma T_l^4 - cU\right) \Delta t \qquad [3.21]$$

$$I_g = I_g - \kappa_g \left(4\sigma T_g^4 - cU\right) \Delta t \qquad [3.22]$$

where U (erg/cm^3) is the radiation energy density, κ_g and κ_l (cm^2/g) are the opacities of each phase, c (cm/s) is the speed of light, and σ is the Stefan Boltzmann constant (5.67×10^{-5} erg cm^{-2} K^{-4} s^{-1}). The option for simple black-body thermal radiation, in which particles radiate their heat according to the Stefan-Boltzmann law and all radiated thermal energy is removed from the mesh, has also been incorporated into KFIX-LPL as an alternative. In this case, thermal radiation is not absorbed by either phase and a change in thermal energy (heat loss) occurs only for the liquid phase:

$$I_l = I_l - \left[\frac{A\sigma}{\rho_l^{'}}\left(T_l^4 - T_b^4\right)\right]\Delta t \qquad [3.23]$$

where T_b is the average background temperature. This option is preferable for problems where the opacity of either phase is low and using the full iterative radiation solver is unnecessarily expensive. However, as will be shown in Chapters 6 and 7, the full thermal radiative transfer model with opacities is required for the Chicxulub ejecta atmospheric reentry problem.

3.3.7 Other Practicalities

In addition to the original boundary conditions, periodic boundaries have been added. If one boundary is periodic, then the opposite boundary must be also be periodic. This modification is important for the ejecta reentry problem because we cannot model the entire Earth's atmosphere, but instead just a narrow slice. That narrow slice is not contained by any medium (e.g. rigid walls) and any mass, momentum, or energy of either phase must be allowed to freely exit the sides of the mesh. Since we assume uniform inflow across the top of the mesh, we can conserve mass, momentum and energy by assuming that any flux out of one side of the mesh reenters the opposite side.

Massless tracer particles have been added to track the movement of each phase through the mesh. Tracer particles can be distributed throughout the initial mesh as well as injected across the inflow boundary. The rate at which the tracers are injected is defined by the user. Some tracer particles are designated as history tracer particles and their locations and velocities and other properties at those locations are recorded. Tracer particles also obey periodic boundary conditions.

KFIX-LPL is coupled to the PGPLOT graphics program and plots its output data as vector plots and contour plots according to user preferences. These plots are produced at assigned time intervals while the code runs. The iSALEplot program routines (from the iSALE hydrocode for impact simulations) has also been implemented by G. S. Collins in KFIX-LPL for additional graphic capabilities. This operates by saving a data file at assigned time intervals and the data can later be used for plotting. The iSALEplot

program has the advantage of operating independently from KFIX and plots can be made to specification post-simulation.

3.4 Code Validation

We conducted a series of simple test problems with the KFIX-LPL code. The test problems serve to validate the usefulness of KFIX-LPL at solving geologic two-phase flow problems such as ejecta particles falling through the atmosphere.

3.4.1 Stokes Flow in Air

We modeled a simple scenario of particle fall under gravity through a tank of air in order to test the ability of KFIX-LPL to reproduce Stokes flow. The fall velocities of 50 µm spherules with a density of 2.777 g/cm^3 were tracked as they settled through a 10×10 square mesh (Δx = 1 m) of isothermal (273 K) air with an exponential pressure gradient (although little change occurs between sea level and 10 m altitude). We used the momentum exchange function of Harlow and Amsden (1975), but included only the viscous term in order to limit the model to viscous flow. Both spherule and air phases are initially at rest, but the spherules quickly accelerate to a constant velocity of 22 cm/s (Figure 10). The Stokes velocity for spherical particles of this size and density falling through air at 273 K with a viscosity of 1.74E-4 g cm^{-1} s^{-1} under standard gravity is 22 cm/s and the model agrees with viscous flow theory.

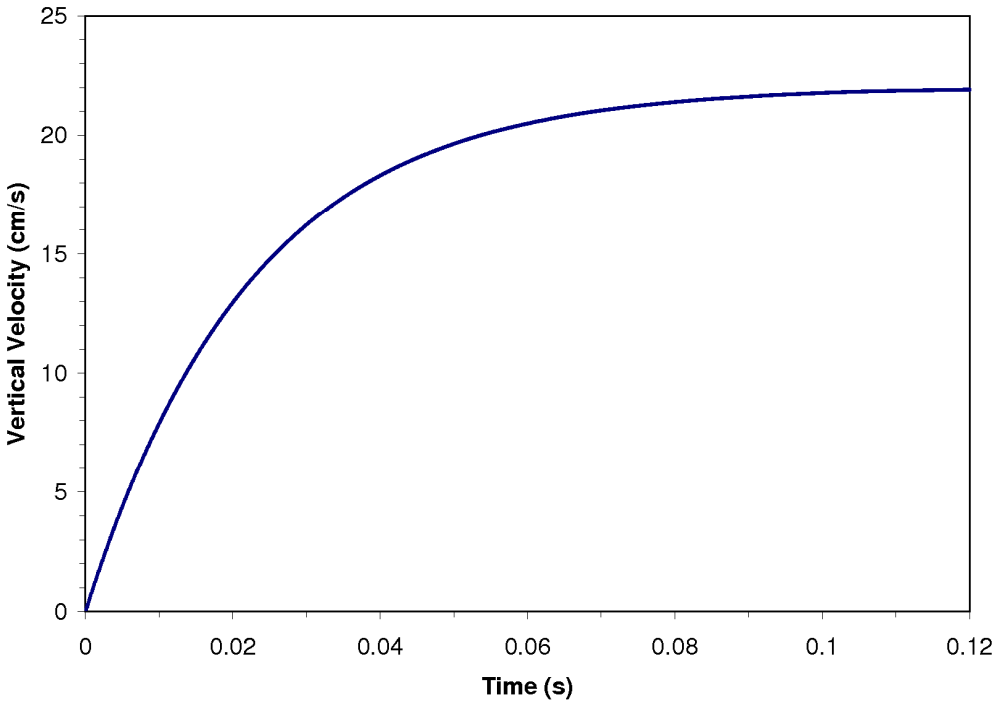

Figure 10. Vertical velocity of 50 µm spherical particles as a function of time in the middle of a 10×10 m^2 square mesh of 273 K air at sea level. In order to remove any component of turbulent flow, the drag equation in KFIX includes only the viscous term in order to test that KFIX models Stokes flow (22 cm/s for these input parameters) correctly.

3.4.2 Equilibrium Pressure Distribution

Using an identical model set-up as in the Stokes flow test, we also tested the stability of imposing an exponential pressure gradient on air. The model results (Figure 11) show that the pressure gradient is indeed at equilibrium and does not readjust upon starting the simulation. In any computational cell, there are some small oscillations but

there is no net change in pressure over time. Additionally, the oscillations are a product of the specified convergence criterion: the stricter the threshold for convergence, the smaller the amplitude of the air oscillations.

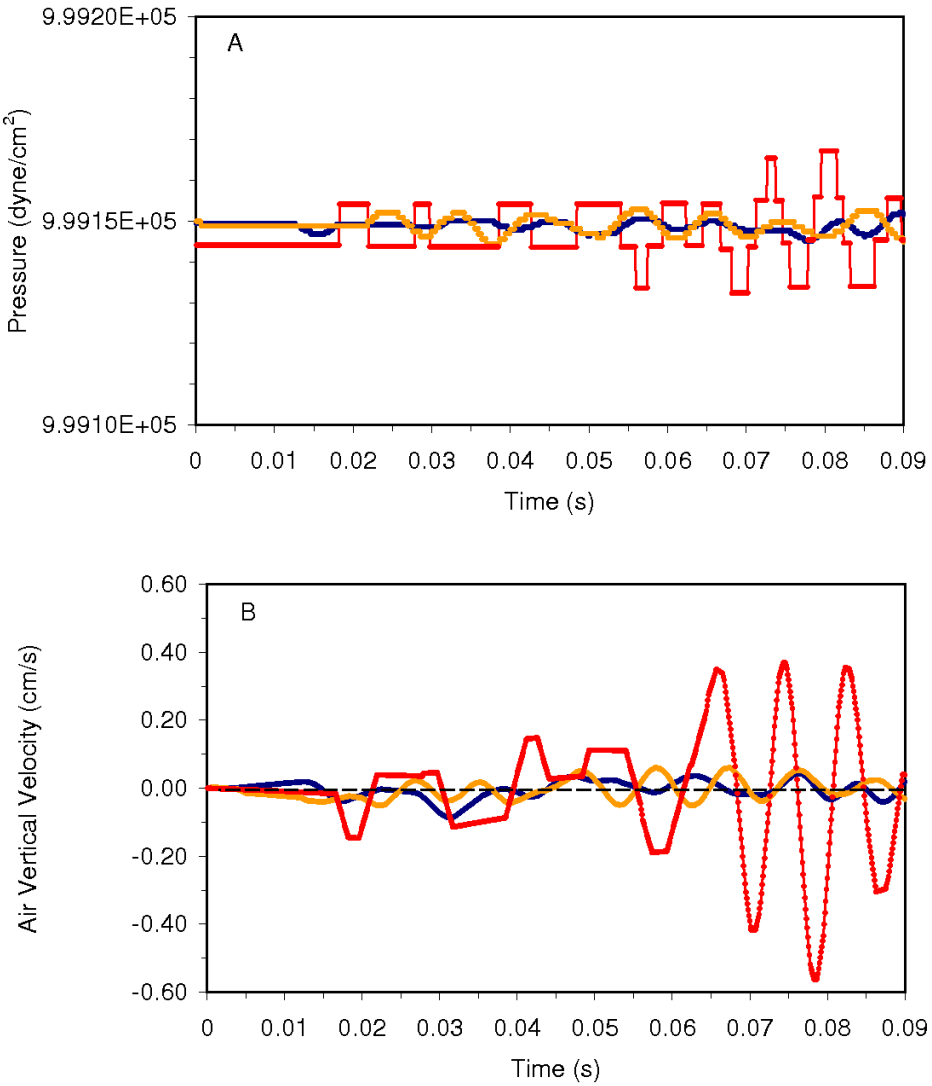

Figure 11. (a) Pressure oscillations and (b) air velocity oscillations as a function of time for a 10×10 (Δx = 1 m) isothermal (273 K) atmosphere with standard gravity. The amplitude of the oscillation depends on the convergence criterion (1E-5 = red, 1E-6 = orange, 5E-7 = blue). Upward velocities are negative.

3.4.3 Energy Balance

The atmospheric reentry of ejecta delivers a large quantity of energy to the atmosphere and it is important that the models maintain energy conservation. Due to the hypersonic velocities of reentry, a small time step is required in our simulations so even small errors in the energy balance can build up substantially over the course of spherule reentry. We track kinetic, gravitational potential, and internal energies for both phases in all cells. At the end of each computational cycle KFIX-LPL compares the total energy in the mesh with the expected total energy. The expected total energy is calculated as the initial energy in the mesh, plus energy added by spherule reentry, and minus energy removed by thermal radiation. If the code is otherwise functioning properly, poor energy conservation can be improved by tightening the convergence criterion employed by the pressure iteration at the heart of KFIX-LPL.

CHAPTER 4

THE CHICXULUB EJECTA MODEL

4.1 Introduction

Previous studies of the deposition of Chicxulub impact plume ejecta and its atmospheric consequences on the end-Cretaceous environment (i.e. Alvarez et al., 1995; Durda and Kring, 2004; Kring and Durda, 2002; Melosh et al., 1990; Toon et al., 1997) treated ejecta transport to the Earth's surface simply as particles settling through an unaltered atmospheric column following ballistic delivery to the upper atmosphere. However, at great distances from Chicxulub where the global K-Pg ejecta layer is found, the ejecta reenters the atmosphere at high speeds (5-10 km/s), delivering a large quantity of energy to the atmosphere and exerting large forces on the air molecules during deceleration. Decelerating spherules both heat and displace air leading to an altered atmospheric density and temperature structure. Any changes to the atmosphere in turn affects the settling of particles by modifying both their terminal velocities, as well as the conditions required for density current formation.

A numerical model is required that treats the particles and air as two fluid phases that can exchange mass, momentum, and energy across the particle surfaces. The model must accommodate accurate drag, heat transfer, and thermal radiation transport functions for the ranges of velocities, flow regimes, and mean free paths experienced by the spherules during descent through the atmosphere. With a model capable of these spherule-air

interactions, KFIX-LPL, we can study how the atmosphere's temperature and density distribution is altered, which is essential for evaluating post-impact atmospheric chemistry and ejecta sedimentation mechanics, including how fast the ejecta is deposited and in what flow regime.

In this chapter we present a general model for atmospheric reentry of Chicxulub ejecta from the impact plume and describe the interactions between the falling ejecta and the Earth's atmosphere. Although impact plume material may be launched ballistically from the impact site, the descent of condensed spherules through the atmosphere is modified by interactions with both the air and other spherules and is far from a ballistic process. We also hypothesize that ejecta-atmosphere interactions explain two enigmas observed at distal K-Pg boundary localities: the uniform thickness of the ejecta layer and the presence of shocked quartz in these high-energy ejecta deposits.

4.2 Model Setup

We modeled the atmospheric reentry of Chicxulub impact ejecta and the subsequent deposition of ejecta through the Earth's atmosphere using the KFIX-LPL two-phase fluid flow code. For the Chicxulub problem, the two phases are impact ejecta spherules and air. The properties of each phase are described in detail in Chapter 3, where the air phase has the average properties of the Earth's atmosphere and the ejecta phase is dispersed into spherical droplets with the average properties of Chicxulub spherules. The initial KFIX-LPL model mesh approximates a 150-km high slice of isothermal

Earth's atmosphere with standard gravity and an exponential pressure gradient. The left and right mesh boundaries are periodic, the bottom boundary (at the ground) is free slip, and the top boundary is an inflow boundary, into which the spherules are injected. The models presented in this chapter use a mesh 600 cells high and 120 cells wide (30-km-wide mesh), which represent our highest resolution (250 m) models to date.

250 μm basaltic spherules, representing the average size and composition of spherules in the global K-Pg ejecta layer (Smit, 1999), are injected uniformly across the top of the model atmosphere at 45 degrees and at 8 km/s. In reality, ejecta from the impact plume would enter the atmosphere at a range of angles and velocities. All particles in a single computational cell must be the same size and velocity and so we use average values for distal Chicxulub ejecta. The mass flux of spherules approximates the ballistic atmospheric reentry calculations by Melosh (1990) as a triangular pulse lasting for one hour and peaking after 10 minutes, where the total mass of spherules ejected per unit area is equal to the average spherule mass density observed at distal localities (0.5 g/cm^2) according to Smit (1999). As they decelerate in the atmosphere, the spherules dissipate their heat according to a complete thermal radiation model which includes the effects of optical opacity for both phases.

4.3 Model Results

The spherules streak through the upper atmosphere, initially at 8 km/s, but decelerating rapidly due to drag as denser air is encountered at lower altitudes. The spherules

reach terminal velocity at ~70 km in altitude (Figure 12). A layer of spherules accumulates at this altitude, which becomes denser as more spherules enter the atmosphere and thickens at the rate of the spherule's terminal velocity (Figure 13). If spherule reentry is uniform across the top of the atmosphere, as it is in our nominal Chicxulub model, then the resulting cloud below is also laterally uniform in density, assuming the layer is stable. If the layer is unstable, due to sufficient density contrast with the underlying spherule-free air, then turbulent density currents can form and the particles concentrate into descending plumes (density current formation will be discussed in the next chapter). The spherules decelerate predominately in the vertical direction; thus a large portion of the horizontal velocity component remains after the initial deceleration and the spherules in the cloud flow horizontally at ~5 km/s at the top of the cloud, slowing as the particles continue to settle through the atmosphere. The air in the spherule cloud is accelerated to horizontal velocities of up to ~5 km/s due to momentum exchange with the spherules. Thus, spherule reentry induces high horizontal winds in the mesosphere.

Although the atmosphere initially has an exponential pressure gradient, the injection of spherules at hypervelocities compresses the atmosphere (Figure 14) resulting in a more rarefied upper atmosphere and a denser lower atmosphere (Figure 15). The altered density structure affects the fall of subsequent spherules, both in the upper atmosphere where spherules encounter fewer obstacles/less drag and in the lower atmosphere, where the spherules have lower terminal velocities through the denser air and instability is easier to initiate.

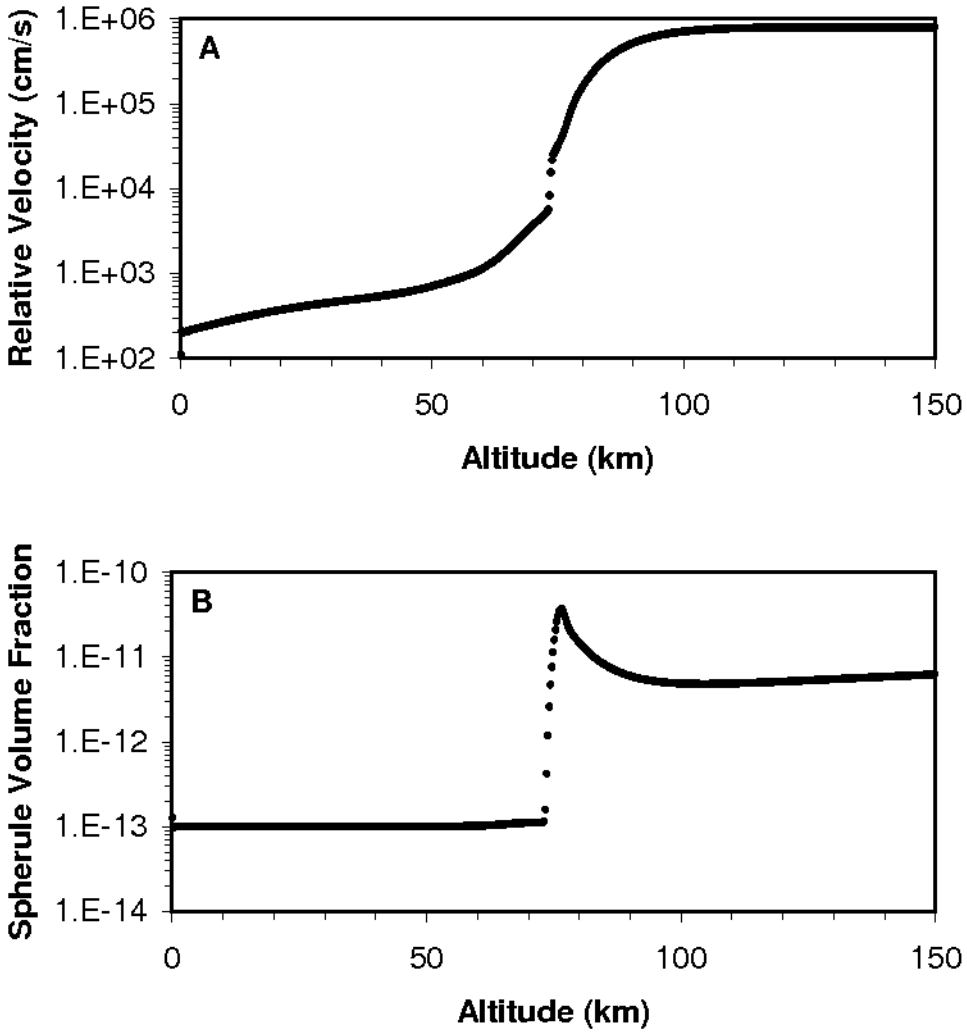

Figure 12. The relative velocity between phases and the volume fraction of spherules as a function of altitude after 1 minute of Chicxulub spherule reentry. The spherules decelerate to their fall velocities at ~70 km in altitude, as illustrated by the increase in spherule concentration at this altitude.

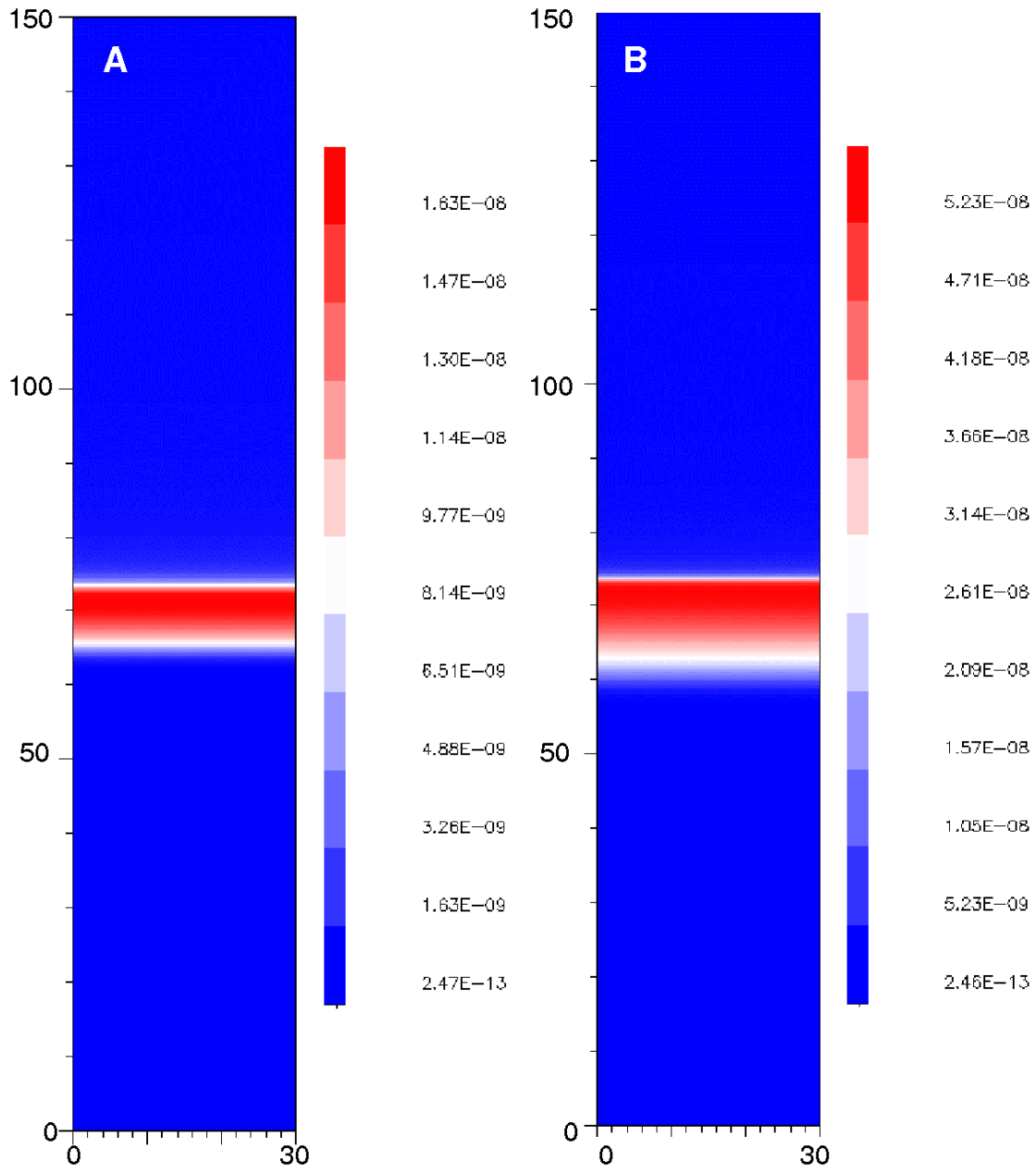

Figure 13. Contour plot showing the macroscopic density (g/cm^3) of spherules in the model atmosphere (a) at 5 min and (b) at 10 min. Axes are in kilometers. Note different contour legends.

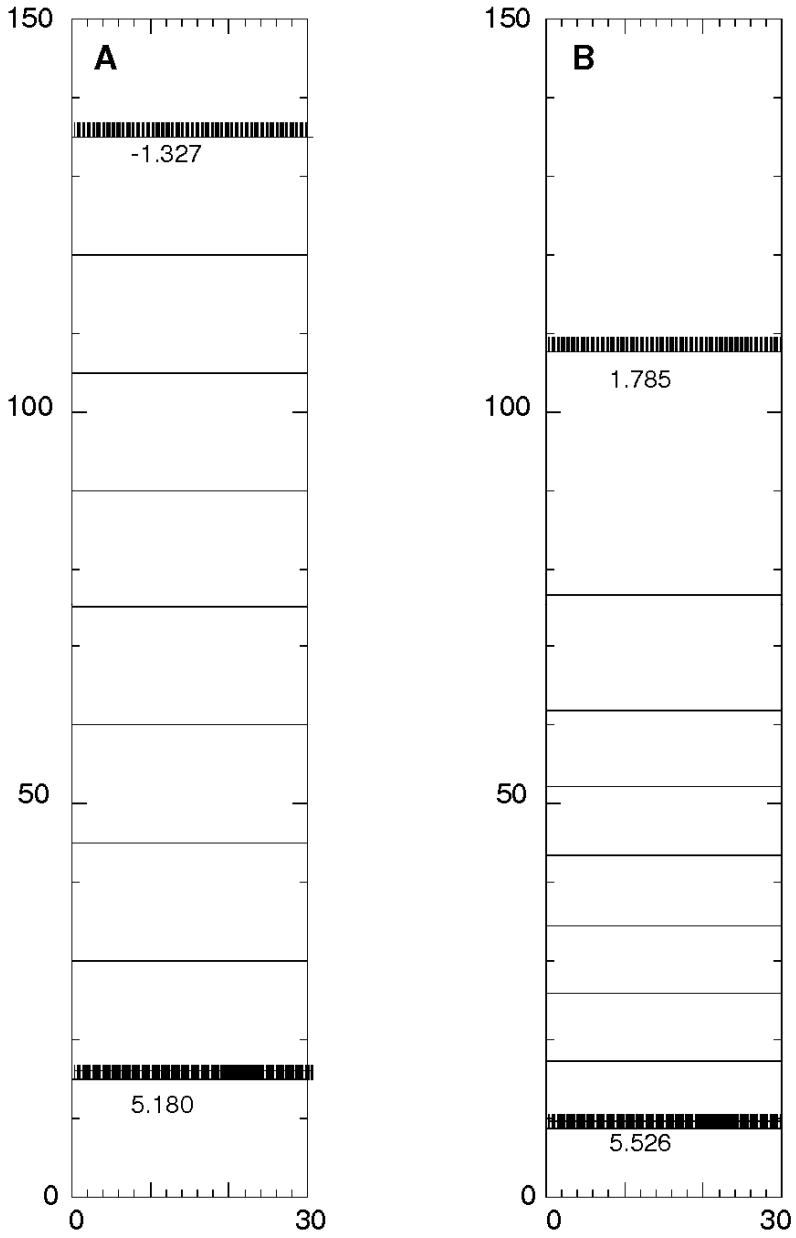

Figure 14. Log pressure (dyne/cm^2) contours in the model atmosphere (a) at 0 min (prior to spherule reentry) and (b) at 10 minutes (maximum mass flux of spherules). Note the even spacing of contours for the initial atmosphere with an exponential pressure gradient as compared with the compressed atmosphere. Axes are in kilometers.

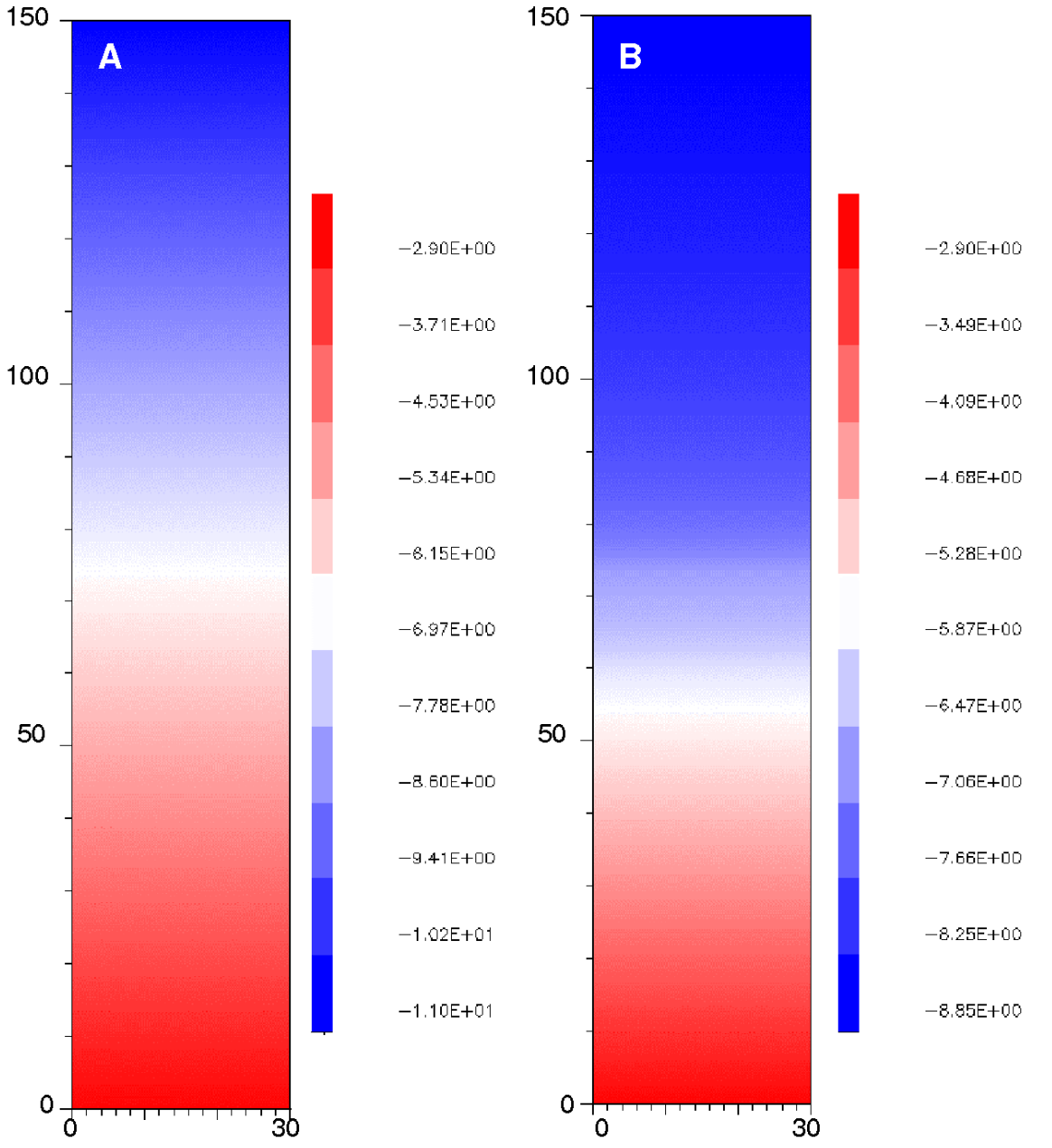

Figure 15. Contours of log macroscopic air density (g/cm^3) in the model atmosphere (a) at 0 min (prior to spherule reentry) and (b) at 10 minutes (maximum spherule mass flux) showing compression of the atmosphere from the initial exponential pressure gradient as reentry progresses. Axes are in kilometers. Note different contour legends.

The deceleration of particles from high velocity results in the conversion of a large quantity of kinetic energy into thermal energy. If the spherule phase was unable to dissipate this heat, the spherules would become so hot that they would ablate entirely. There is no evidence for this in the global K-Pg deposits where spherule preserve a relict crystalline texture and spherical shape—evidence against complete remelting during reentry. The use of a thermal radiation model in KFIX-LPL allows the spherules to radiate heat according to their temperature and the efficiency of this depends on particle size. Because the spherules are small and have a high surface area to volume ratio, they can radiate their heat efficiently. At the start of the model, the decelerating spherules reach maximum temperatures of ~1600 K (Figure 16). Over the first few minutes of reentry, the maximum spherule temperature decreases to ~1300 K where it remains fairly constant for the remaining duration of spherule reentry. Without considering atmospheric interactions, it would be assumed that the spherules would all experience the same maximum temperature because they are injected with identical size and energy throughout the simulation. However, when atmospheric interactions are considered, the compression of the atmosphere alters spherule deceleration and decreases the peak temperatures because decelerating spherules encounter less atmosphere. Once the atmosphere is compressed, the temperatures remain fairly constant, as can be seen in contour plots (Figure 17) where the altitude range in which the spherules are hot and the temperatures within this region are maintained throughout the remainder of spherule reentry.

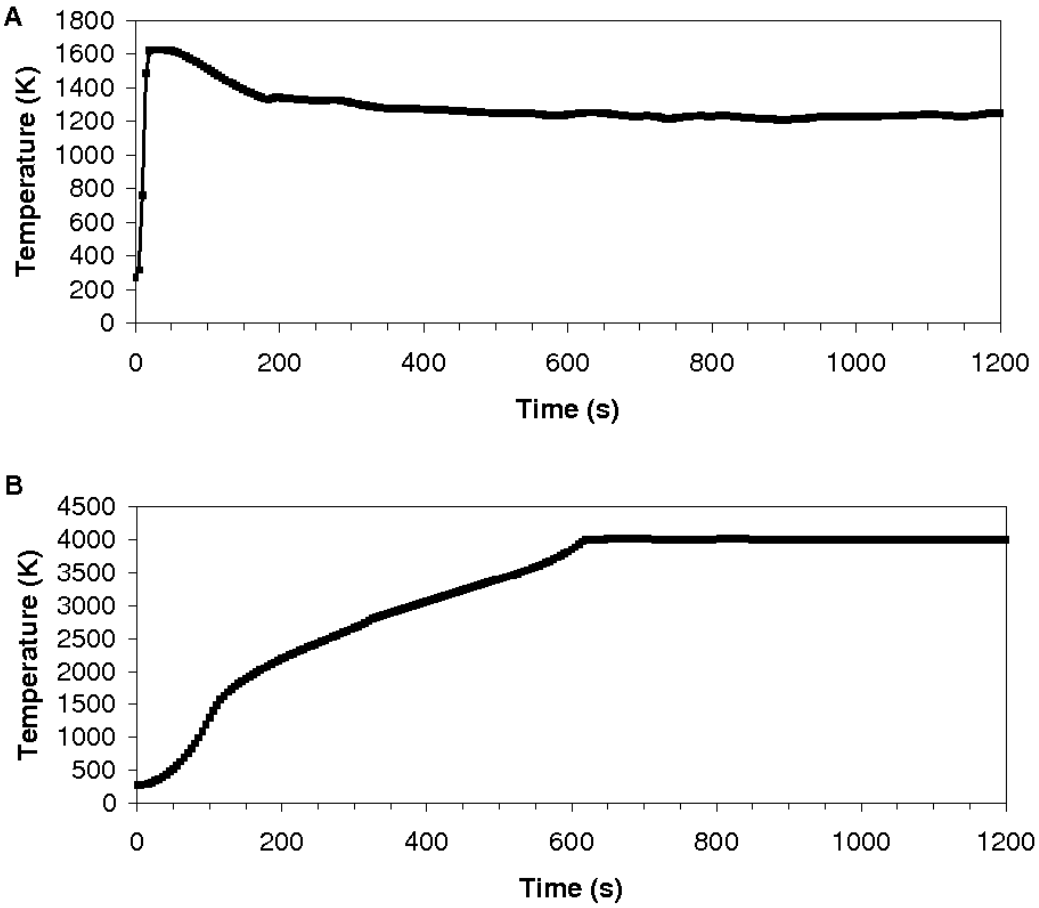

Figure 16. (a) Maximum spherule temperature and (b) maximum air temperature in the model atmosphere as a function of time. Peak particle injection occurs at 600 s.

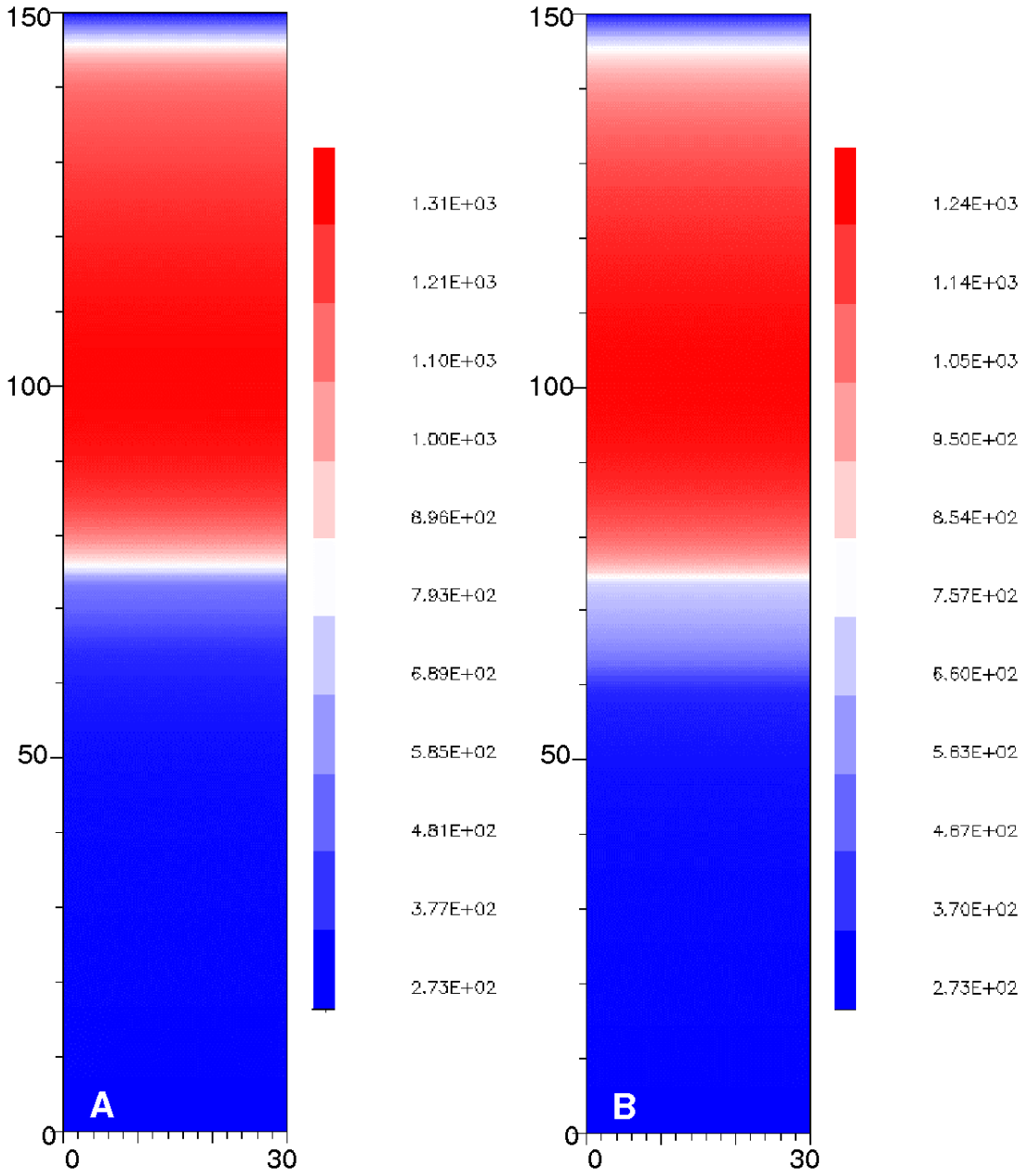

Figure 17. Spherule temperature (K) contour plot (a) after 5 min and (b) after 10 min showing the presence of hot spherules decelerating through the upper atmosphere and the decrease in peak temperature due to alteration of the upper atmosphere's density structure. The band of spherules below 70 km is cooler, grading to unheated atmosphere below. Axes are in kilometers. Note different contour legends.

The air in the upper atmosphere also heats up, due to frictional and conductive exchange with the spherule phase. Unlike the spherules, greenhouse gases are not blackbodies and absorb/emit infrared radiation over a narrow part of the spectrum, not at all frequencies like solid blackbodies. A greenhouse gas molecule emits thermal radiation in all directions, some of which may be reabsorbed by other gas species. Thus, air is not as readily able to radiate its heat as thermal radiation so its temperature continues to increase (Figure 18), reaching >3000 K just 10 minutes into spherule reentry and eventually reaching temperatures at which gas species begin to dissociate and ionize. Although there is some pressure dependence, O_2 dissociates at >2000 K, N_2 dissociates at >3000 K, and the dissociated atoms are ionized at >6000 K (Hansen, 1958). The thermodynamic behavior of air in the upper atmosphere at high temperatures, including dissociation and ionization effects is described by Hansen (1958). The air below the spherule layer remains cool and isothermal.

4.4 Ejecta Distribution: Patchy or Continuous?

In distal K-Pg boundary sites >7000 km from Chicxulub, the thickness of the ejecta layer is fairly uniform at 2-3 mm (Smit, 1999), at least in the most undisturbed localities. Unlike ejecta deposits closer to the crater, which contain ejecta curtain material and decrease in thickness as a function of distance from the crater, the distal impact plume ejecta deposits show no such trends in thickness. Why is the global K-Pg boundary layer uniform in thickness regardless of distance from Chicxulub?

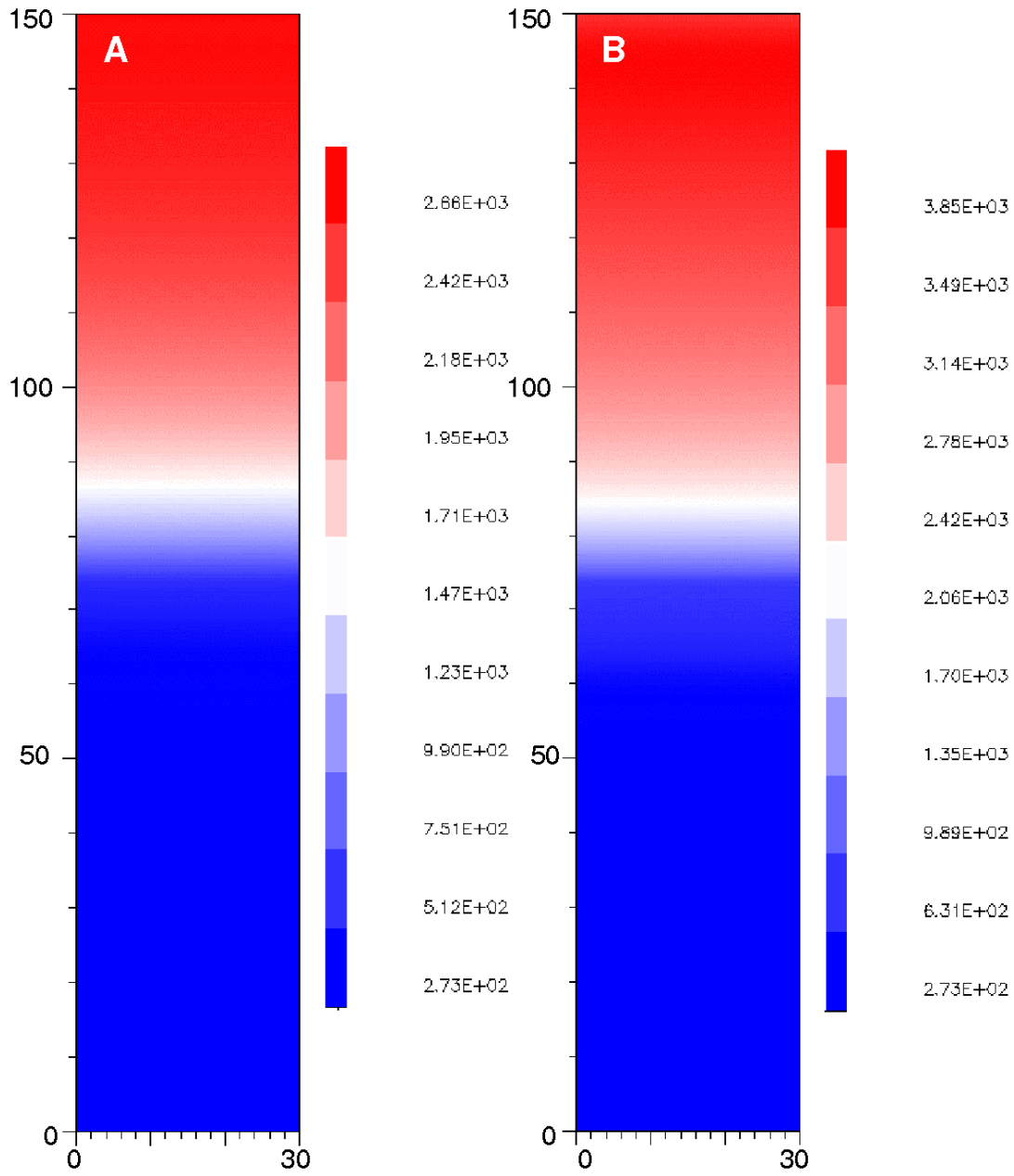

Figure 18. Air temperature (K) contour plots of the model atmosphere (a) at 5 minutes and (b) at 10 minutes showing the heating of the upper atmosphere above 70 km as spherule reentry mass flux increases. The lower atmosphere remains cool regardless of the flux of decelerating spherules above. Axes are in kilometers. Note different contour legends.

Secondly, the global layer is uniform in thickness regardless of geographic location, which is also problematic given our current understanding of cratering mechanics. Studies of ejecta on airless bodies as well as from explosion craters suggest a non-uniform distribution of ejecta by impact cratering processes along a path equidistant from the crater. The most distal ejecta observed on other planets are crater rays, which are ephemeral bright albedo features forming radial streaks from fresh craters. Rayed craters have been found on all airless bodies to date (Melosh, 1989) and include the lunar crater Tycho, whose rays cross most of the visible hemisphere of the Moon (Figure 19). Photographs of the expanding impact plume from nuclear explosion craters (Glasstone and Dolan, 1977, Figs. 2.18, 2.32) show patches of hotter and cooler areas, suggesting ejecta travelling at variable velocities and thus non-uniform expansion of the impact plume. Although the origin of crater rays remains unclear (Are they depositional or erosional features?), as does the scaling of nuclear explosions to a Chicxulub-sized impact, there seems to be something intrinsically non-uniform about the transport of impact plume material on airless bodies. However, there is no evidence for rays or any other kind of clumping of ejecta in the distal Chicxulub deposits. Can atmospheric interactions with ejecta reconcile a heterogeneous distribution of ejecta into the top of the atmosphere with a uniform deposit on the ground?

Figure 19. The Tycho crater on the moon and its bright rays. Lick Observatory Photo.

To test this hypothesis, we modeled a scenario in which spherules reenter the atmosphere across only one-half of the model mesh and observe whether this distribution holds and the particles are deposited only on one side of the mesh, or whether lateral redistribution of ejecta occurs during transport through the atmosphere. We inject 250 µm spherules at double the mass fluxes employed in the nominal simulation (uniform spherule reentry across the width of the mesh) so the total mass of injected material is the

same for both models. In the partial-reentry case, the spherules reenter the atmosphere vertical at 8 km/s so that any horizontal movement of ejecta must be attributable to atmospheric interactions, not the original horizontal velocity component. The models presented here are at lower resolution (5 km), which is much too coarse to resolve the exact behavior of the settling spherules, in particular density current formation. However, the resolution is sufficient to illustrate the general influence of atmosphere-spherule interactions on the ejecta redistribution. Because the coarser resolution shortens run times, the models shown here use wider computational meshes (100 km wide, 150 km tall)

Initially, the particles decelerate vertically to their terminal velocities and accumulate in a layer on one side of the mesh according to the reentry distribution. The injection of high velocity ejecta on only one side of the mesh results in one side of the atmosphere becoming more compressed than the undisturbed side and a pressure gradient develops between the two sides of the model atmosphere. At the altitude at which spherules accumulate (~70 km), the air is denser on the side of the mesh with spherule reentry (not to mention the additional density of the spherules) than the spherule-free side. The spherules spread horizontally across the pressure gradient (Figure 20), producing an increasingly uniform cloud of spherules despite the non-uniform inflow above. In higher resolution runs (not shown here because they use narrower meshes that are not very illustrative), lateral density currents appear to form and spread the spherules even more effectively. This effect has not yet been explored in detail because high resolution runs on wider meshes (i.e. 100 km wide as in lower-resolution runs) are needed.

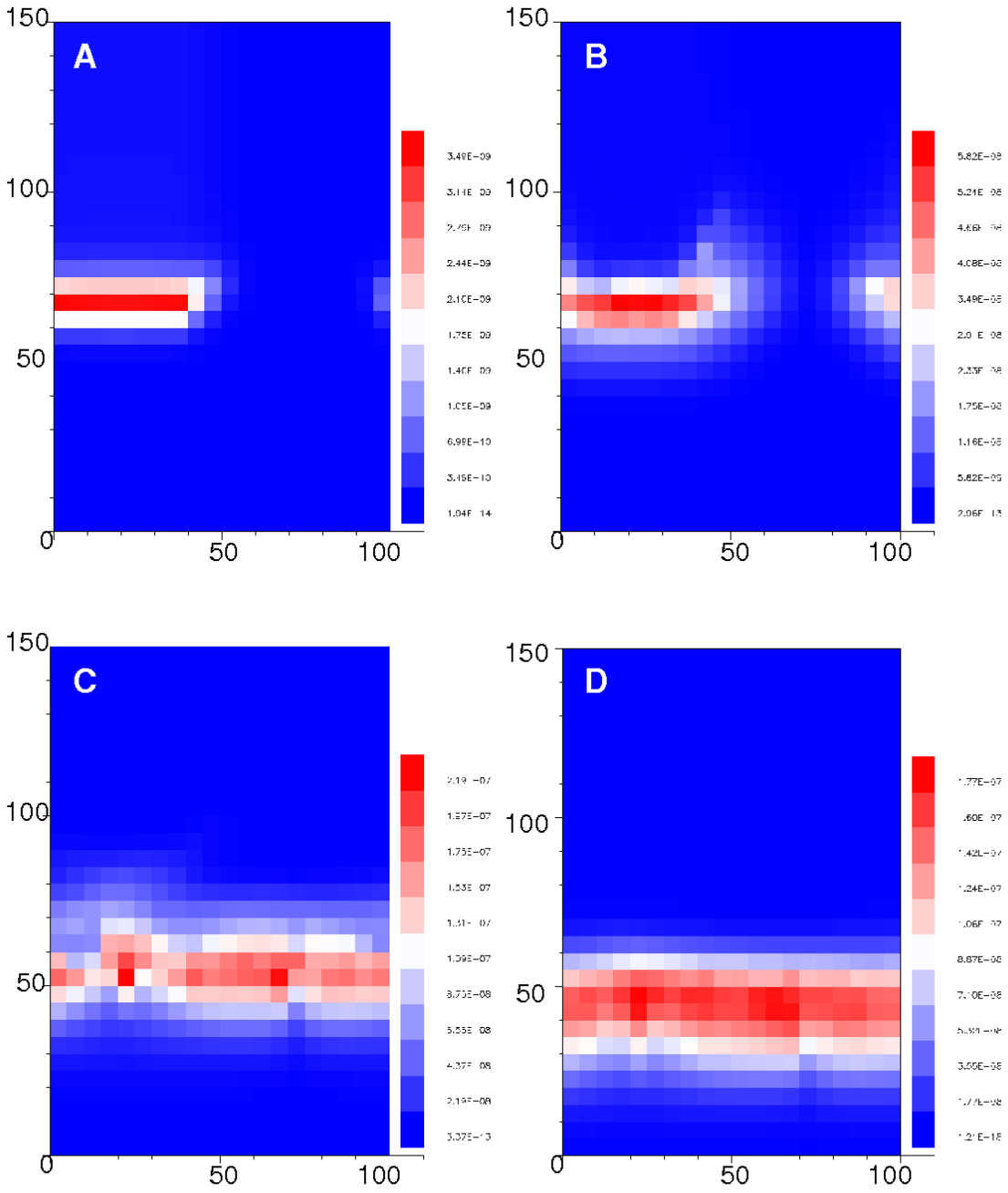

Figure 20. Macroscopic spherule density (g/cm^3) after (a) 2 min, (b) 10 min, (c) 60 min, and (d) 100 min in a model of vertical spherule reentry across only the left half of the mesh. Axes are in kilometers, resolution is 5 km, and left and right boundaries are periodic. Note different contour legends.

4.5 The Shocked Quartz Enigma

Although the discovery of shocked quartz, in addition to the extraterrestrial geochemical signature, was proof for the meteorite impact hypothesis, there are several reasons why the presence of shocked quartz in the global K-Pg layer is surprising (Alvarez et al., 1995): (1) The iridium, spherules, and Ni-bearing spinels of the global boundary layer originate from the hot impact plume which consists of melted and vaporized target and projectile material, conditions not conducive to shocked quartz survival. (2) The distribution of shocked quartz appears to be asymmetric (Alvarez et al., 1995) and the size of shocked quartz grain varies with distance from the crater (Croskell et al., 2002), despite the fairly uniform thickness and properties of the global K-Pg boundary layer. (3) Finally, the shocked quartz is found in even the most distal deposits, despite the high velocities required for transport to such great distances and the fact that either the shocked pressures required for ejection (Alvarez et al., 1995) or heating following atmospheric reentry (Croskell et al., 2002) at those velocities would lead to annealing of shock features. Recent models of Chicxulub ejecta formation and transport from the impact event suggest that basement material, which is the source for shocked quartz and zircon grains, is ejected at velocities <3 km/s and would be unable to reach distal locations (Artemieva and Morgan, 2008).

Alvarez et al. (1995) invoked a third ejection process, a “warm fireball”, in addition to the impact plume (“hot fireball”) and ejecta curtain to explain the shocked quartz enigma. Artemieva and Morgan (2008) proposed a non-ballistic mechanism for shocked

quartz dispersal to distal locations via “skidding” where the hot upper atmosphere expands laterally and allows the particles to “float” (Colgate and Petschek, 1985) around the globe.

Our models suggest a simple mechanism for the transport of lower velocity ejecta radially outward from the impact crater. The oblique reentry of ballistic ejecta from the impact plume creates strong winds in the atmosphere between 50-70 km in altitude, due to the remaining horizontal velocity component following vertical deceleration through the upper atmosphere. Faster materials are ejected from the target earlier, thus setting the atmosphere in motion before or as the shocked mineral grains reach it. If the shocked minerals reach these altitudes, they would be swept away by the outward atmospheric flow, accelerating with increasing distance from the crater as the average velocity of the reentering spherules increases. The larger shocked quartz grains would settle through the horizontally flowing spherule layer faster than smaller grains and the average grain size would decrease with increasing distance from Chicxulub.

4.6 Conclusions

The deposition of Chicxulub impact plume ejecta to form the global K-Pg boundary layer cannot be described by the passive settling of particles through the atmosphere. In fact, the relationship between the ejecta and the atmosphere is a dynamical one. Hypervelocity spherule reentry compresses and heats the upper atmosphere and generates high horizontal winds if reentry is oblique. The spherules themselves heat up, accumu-

late in a layer at ~70 km in altitude, and settle either individually or collectively in a flow regime controlled by the altered atmospheric structure and the density of the particle layer. Ejecta-atmosphere interactions may explain why the K-Pg boundary is uniform in thickness in distal localities regardless of distance from Chicxulub and why low-velocity shocked quartz and other mineral grains are found in the deposit of high-velocity impact plume ejecta. Although KFIX-LPL is a purely physical model (no chemistry), understanding the evolution of the atmospheric temperature and pressure structure over the course of spherule reentry is essential for evaluating perturbations of atmospheric chemistry following the Chicxulub impact and assessing their environmental effects.

CHAPTER 5

VERTICAL DENSITY CURRENTS: IMPLICATIONS FOR SEDIMENTATION AT THE K-PG BOUNDARY

5.1 Introduction

Fine sediment is sometimes deposited more rapidly and turbulently than the settling of individual particles would allow. This enigma is illustrated by volcanic tephra-fall layers in marine sediments, which display characteristics inconsistent with deposition by passive settling through the ocean column such as sharp basal contacts and high contents of juvenile volcanic material (Bradley, 1965; Carey, 1997; Carey and Sigurdsson, 1980; Sigurdsson et al., 1980). Measurements of tephra fall in the ocean following the 1991 eruption of Mount Pinatubo yielded settling rates two to three orders of magnitude greater than the predicted Stokes law velocity (Wiesner et al., 1995). Carey (1997) performed a series of tephra-fall experiments where tephra of a given size fraction were dropped at a constant mass flux into a tank filled with water. Initially the tephra velocities were consistent with Stokes flow settling of individual particles. As the experiments progressed, the concentration of particles near the surface and the thickness of this layer increased until the layer became unstable and, accompanied by a tenfold increase in velocity, the tephra particles were rapidly transported by density currents to the bottom of the tank.

Carey thus proposed that rapid deposition of tephra-fall layers is due to transport through the ocean column by vertical density currents. Experiments into stratified envi-

ronments with varying salinity (Manville and Wilson, 2004) further supported this claim and qualitatively agreed with other experimental studies of vertical density current formation involving a pulse of fine particles falling into a fluid (Bradley, 1965, 1969). Generally stated, if the mass flux of small particles is sufficiently high, a fluid medium (water, air, etc.) can be loaded to the point where the density of the particle-fluid layer exceeds the density of the fluid below. The particle layer then becomes unstable, density currents form and the particles fall collectively, rather than individually.

In addition to volcanic eruptions, meteorite impacts also produce large quantities of fine material which can be preserved as distinct layers in the Earth's stratigraphy. The best-known of these impact layers is at the Cretaceous-Paleogene (K-Pg) boundary (65 Ma) and is associated with the end-Cretaceous mass extinction event. Linked to the 180-km Chicxulub crater on the Yucatán peninsula, the K-Pg boundary impact layer is found worldwide and, in most distal localities, consists of a 2-3 mm layer composed primarily of altered impact spherules with a 250-µm average size (Smit, 1999). From impact cratering theory, it is known that the Chicxulub impact would have produced an impact plume composed of melted and vaporized target and projectile material (Melosh, 1989; Vickery, 1986). The impact plume would have expanded globally and condensed to form spherical particles (Melosh and Vickery, 1991) which then reentered the atmosphere (if traveling slower than the Earth's escape velocity). Less clear, however, are the mechanical style and timescale of spherule settling through the Earth's atmosphere, crucial parameters for modeling the environmental effects of Chicxulub.

Previous calculations (Alvarez et al., 1995; Kring and Durda, 2002; Melosh et al., 1990) assume the spherules settled through the atmosphere as individual particles. However, if atmospheric loading was sufficient to trigger instabilities, vertical density currents must be considered as a viable transport mechanism, delivering spherules to the Earth's surface more rapidly and chaotically than previously assumed. Such transport would be further modified by accompanying winds, water currents, etc. prior to deposition to form the K-Pg boundary layer.

Understanding the mechanics of K-Pg spherule transport through the atmosphere requires a means to evaluate instability as well as a numerical tool to model the complex scenario of hypervelocity atmospheric reentry of impact spherules. In this Chapter we explore density current formation in geologic systems analytically and numerically. A criterion for the onset of turbulent instability in an incompressible fluid is presented and is applied successfully to previous experimental results of Carey (1997). Furthermore, we have implemented a numerical tool, KFIX-LPL, to model turbulent instability growth. Models of the test case of tephra fall in water are validated against both the instability criterion and experimental constraints. Simulations of atmospheric loading of K-Pg impact spherules from the Chicxulub impact and comparisons with criteria for instability in a *compressible* fluid suggest density currents did indeed form, transporting particles collectively through the lower atmosphere to the Earth's surface, rather than calmer settling of individual particles.

5.2 Analytical Criteria for an Incompressible Fluid

Consider a single small spherical particle of diameter d and density ρ_p falling under gravity g through a fluid of viscosity η and lower density ρ_f. If viscous forces dominate, the flow is in the laminar regime and the particle's terminal velocity is given by Stokes' law (Stokes, 1851):

$$v_s = \frac{(\rho_p - \rho_f)gd^2}{18\eta} \qquad [5.1]$$

Now consider a layer of thickness h containing a mixture of particles and fluid overlying a layer of particle-poor fluid. The difference between the density ρ of the particle layer and that of the particle-poor fluid ρ_o ($\approx\rho_f$) is equal to $(1-\theta)(\rho_p-\rho_f)$ where θ is the volume fraction of water. If the particles are diffuse, Stokes law applies and the particles settle individually by passive settling. However, if the density of the particle-laden layer exceeds the density of the fluid below, any small wavelike disturbance of the interface is unstable and the instability will propagate downwards. The tendency for a particle-bearing layer of fluid to form density currents or be subject to settling of individual particles can be expressed by the dimensionless number B, which relates the timescale of individual particle settling by Stokes flow, τ_s, to the timescale of instability growth, τ_i:

$$B = \frac{\tau_s}{\tau_i} \qquad [5.2]$$

If the rate of individual particle settling exceeds the rate of instability growth (B<1), the particles will settle at Stokes velocity before any instabilities develop. If the rate of instability growth is greater (B>1), the particle-laden layer is unstable and density currents will form.

If both individual particle settling and instability formation are in the laminar flow regime, the following criterion for laminar instability applies:

$$B_l = \frac{h^2(1-\theta)}{d^2} \qquad [5.3]$$

which is similar to criteria proposed by Marsh (1988) and Boothroyd (1971). Carey (1997) used this criterion to evaluate density current formation conditions in his tephra fall experiments. Its use, however, did not give an adequate representation of when instability actually occurred because the criterion was inappropriately applied to the experimental instabilities: The Reynolds number of the developing plumes in the experiments is large, invalidating Carey's assumption of a viscosity-dominated instability. Neither water nor air is sufficiently viscous for laminar instability initiation. Any instability is instead *turbulent* and the Marsh criterion does not apply.

Turbulent flow of a body can be expressed by momentum balance conditions, where $\dot{\delta}$ is the instability growth rate and δ is the amplitude of the instability, such that the driving force (weight) of the flow, $\rho_f \dot{\delta}^2$, is equal to the turbulent pressure induced by the flow, $(\rho - \rho_f)g\delta = (1-\theta)(\rho_p - \rho_f)g\delta$, and the viscosity of the fluid can be ignored. For a scenario where individual particle settling is in the laminar flow regime (Stokes flow settling) and density current formation is in the turbulent flow regime, we can define a new instability criterion:

$$B = \frac{9h\eta}{d^2}\sqrt{\frac{(1-\theta)}{\rho_f(\rho_p - \rho_f)\delta g}} \qquad [5.4]$$

This is the appropriate criterion for the Carey tephra-fall experiments, which yield *B* values close to one at the observed onset of instability. It is also the relevant criterion for other geologic scenarios involving loading of a low viscosity incompressible fluid with fine particles. It is expected from this criterion that either increasing the thickness or particle volume fraction of the particle-laden layer will make the layer increasingly unstable, whereas increasing the particle size or density favors stability and the settling of individual particles. A more detailed derivation of these criteria can be found in Appendix A.

5.3 Numerical Modeling of the Carey Experiments

Modeling the deposition of spherical particles through a fluid medium requires a two-phase flow code, which can accurately handle the transfer of mass, momentum and energy between particles and fluid in both laminar and turbulent flow regimes. Based on the original KACHINA code (Amsden and Harlow, 1975), KFIX-LPL is a version of the KFIX code (Rivard and Torrey, 1978), which we have adapted to simulate tephra fall in a water tank and impact ejecta fall in the atmosphere. The finite-difference code models two-dimensional, two-phase fluid flow, permitting examination of the interactions between two fluid phases, which in this case represent the particles (tephra or ejecta) and the medium (water or air).

The KFIX-LPL tephra fall simulations replicate the experimental setup of Carey (1997) as closely as possible. The initial mesh consists of a two-dimensional “tank” of

freshwater 70 cm high and 30 cm wide. KFIX-LPL is currently a two-dimensional code, but for this problem the third dimension is not required because the tephra is added uniformly to the top of the tank and hence instability formation depends only on the layer thickness. The water phase is modeled as a compressible fluid, although the compressibility of water is very small such that density variations in the tank are minor. The fluid phase has the properties of freshwater, including a density of 1 g/cm^3 and a viscosity of 0.01 $g\ cm^{-1}\ s^{-1}$. The left, right, and bottom mesh boundaries are free slip, representing conditions at the edges of the tank. The top boundary is an inflow boundary into which the tephra are uniformly introduced.

Tephra particles are added to the top of the mesh with a fixed mass flux of 0.17 $g/cm^2/hr$, which was the mass flux in Carey's experiments and is within the range of distal tephra mass fluxes (0.09-0.22 g/cm^2) measured for the 1980 Mount St. Helens eruption (Sarna-Wojcicki et al., 1981; Scheidegger et al., 1982). The modeled particles are uniform in size and density, in contrast to the real Pinatubo tephra used in Carey's experiments, which consisted of a mixture of vesicular glass shards, mineral crystals (plagioclase, hornblende, Fe-Ti oxides), and lithic fragments and were heterogeneous in size, shape and composition. Because KFIX-LPL can only accommodate a single particle type within a computational cell, each particle is approximated as a sphere with a density of 2.34 g/cm^3 based on the mean density of Pinatubo tephra (Wiesner et al., 1995) and a diameter reflecting the average of each experiment's tephra size range. Experiment 96-1 used 32-64 µm tephra and experiment 96-5 used 20-32 µm tephra (Carey, 1997) and our numerical simulations of these experiments use 48 µm and 26 µm particles respec-

tively. Additional simulations were run with other particle sizes up to 64 µm to further validate our model against the turbulent instability criterion.

Simulations were run at resolutions of 1 cm (30cm x 70 cm tank), 0.5 cm (30 cm x 30 cm tank), and 0.25 cm (30 cm x 30 cm tank). For a given particle size, individual tephra particles settle at the same Stokes velocity regardless of resolution and development of density currents occurs at roughly the same time in all resolutions. Smaller cell sizes, however, allow better resolution of (1) the onset of instability at smaller amplitudes which permits more precise determination of the time of onset for a given instability amplitude and layer thickness and (2) the morphology of the growing plumes. The simulations presented here use 0.25 cm resolution, which is sufficient to resolve instabilities ≥3 cm in amplitude for the range of tephra sizes explored.

The 48 µm simulation proceeds as follows (Figure 21): As the particles are added to the top of the mesh, initially they fall through the water at a constant velocity of 0.17 cm/s, which coincides with the predicted Stokes velocity. The individually settling particles form a horizontal layer at top of the tank which thickens with time at the rate of the Stokes velocity. After 30 s, the bottom of the particle-laden layer, which is now 6 cm thick (24 cells/layer thickness for the highest resolution simulations), begins to develop an irregular surface and the particle-laden fluid begins to accelerate. After 60 s, at a layer thickness of 10 cm, the amplitude of the developing instability is ~3 cm and the particles continue to accelerate downwards. Morphologically, some plumes have bulbous heads while others taper to a point and look similar to those observed in the experiments (Figure 22). As the model progresses, the plumes coalesce to form two main descending

flows. The descending particle-laden plumes displace the particle-poor fluid below, generating a clockwise return flow of water and resulting in the lateral migration of the plumes. The particles incorporated in the density currents undergo a fairly constant acceleration of ~0.02 cm/s^2 (Figure 23), reaching velocities of 2 cm/s after ~2.5 minutes and continuing to increase.

Density currents evolve similarly in the 26 µm simulation (Figure 24), except the growth of an instability of a given amplitude requires half as much time. A horizontal particle-laden layer forms and grows at the rate of 0.05 cm/s, the Stokes settling velocity of these smaller particles. When the layer reaches 1 cm in thickness after 15 s, its base begins to become unstable. The amplitude of the instability reaches 3 cm after 30 s. The rate of acceleration is the same as the previous model (0.02 cm/s^2) and also fairly constant. Particle velocities of 2 cm/s are attained after ~2 min.

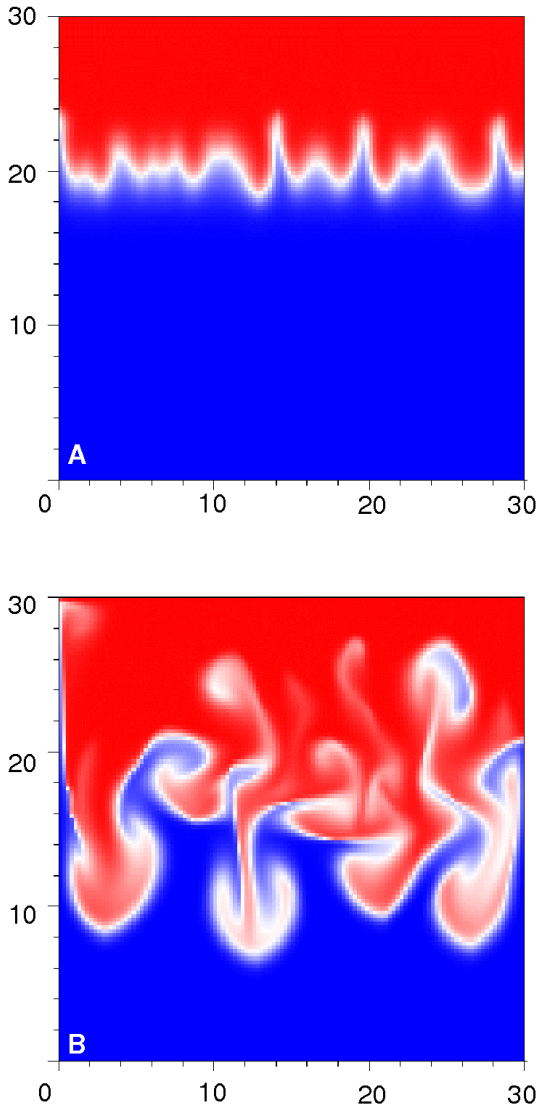

Figure 21. Macroscopic tephra density contours from a numerical simulation of tephra fall in water for 48-µm tephra in a 30 cm × 30 cm tank. Warmer colors indicate higher tephra concentrations. The amplitude of the growing instability reaches ~3 cm after 60 s (a) when the particle-laden layer is ~10 cm thick. The instabilities grow to form density currents with typical morphologies, as evident after 90 s (b). Model resolution is 0.25 cm and this model uses a 30 cm x 30 cm mesh representing the top half of Carey's experimental water tank.

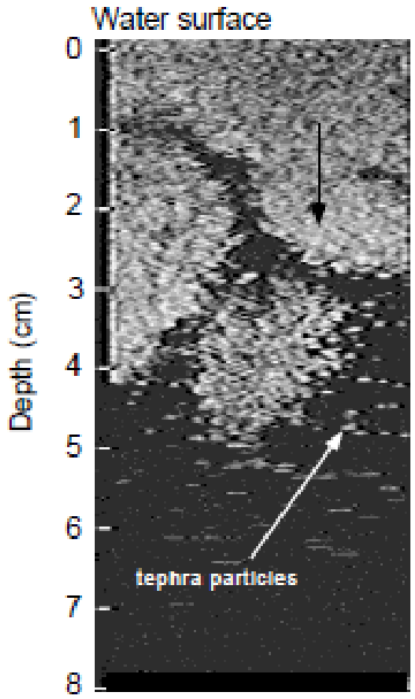

Figure 22. Ultrasound image of vertical density current development in a tephra fall experiment. The experiment number and time of shown ultrasound frame are not specified. From Carey (1997).

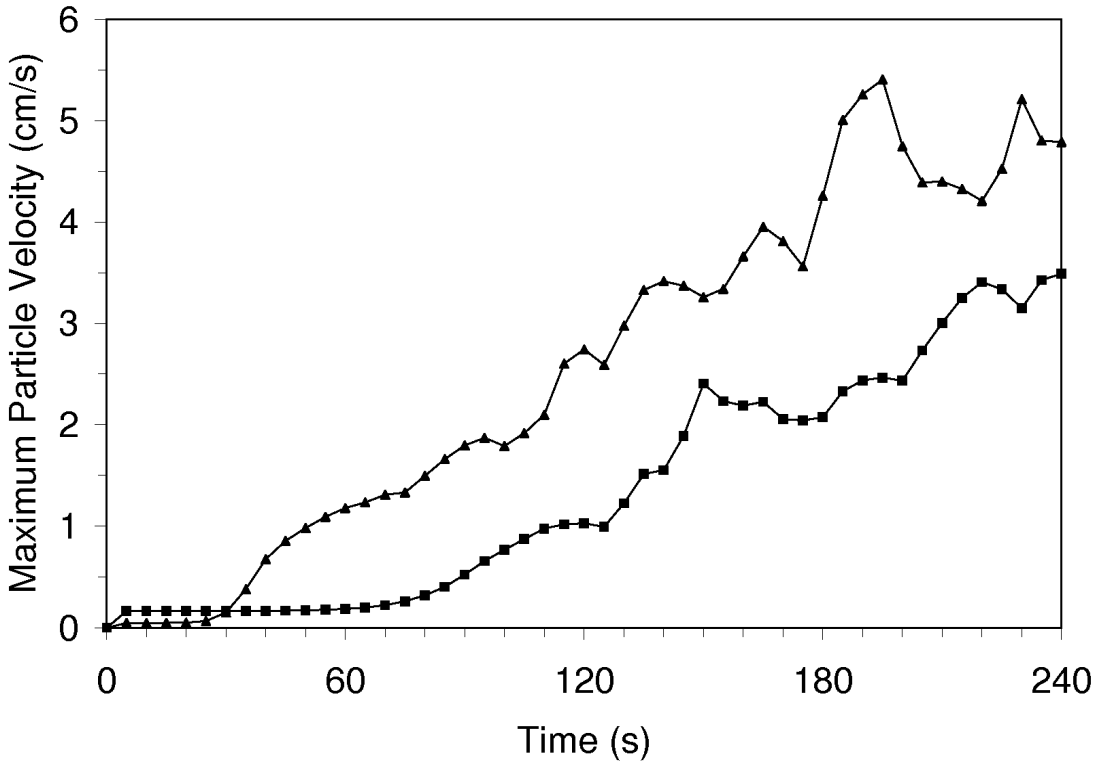

Figure 23. Maximum velocity of tephra particles as a function of time for 48 µm tephra (squares) and 26 µm tephra (triangles). The particles initially fall through the water tank at their Stokes velocities, but accelerate following the onset of instability.

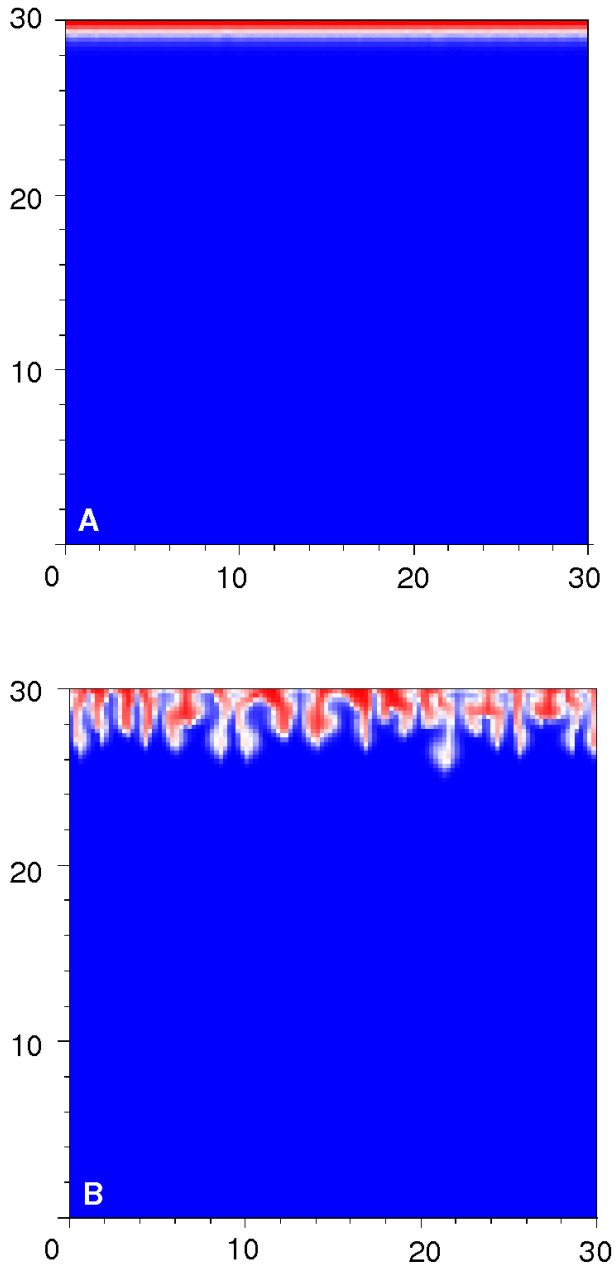

Figure 24. Macroscopic tephra density contours from a numerical simulation of tephra fall in water for 26-μm tephra in a 30 cm × 30 cm tank. Warmer colors indicate higher tephra concentrations. The particle layer becomes unstable after only 15 s (a) when the particle-laden layer is ~1 cm thick (indicated by density variations observed across the base of the layer that are not fully resolved at this resolution) and the instability reaches 3 cm in amplitude after 30 s (b). Model resolution is 0.25 cm.

The KFIX-LPL models agree with Carey's (1997) tephra fall experiments in which instability onset was imaged after approximately one minute in experiment 96-1 and approximately 30 s in experiment 96-5. In the former, velocities jumped from 0.2 cm/s as the particles settled individually to 2 cm/s following density current development and in the latter, a similar velocity increase was seen despite a smaller stokes settling velocity. Additional numerical simulations using other particle sizes reinforce the relationship between particle size and layer instability, where smaller particles result in less time (and thus thinner layer thickness) required for instability (

Table **1**). Increasing the flux of particles to the surface also increasingly promotes instability in our simulations. Such instability trends obey the turbulent instability criterion with instability developing for B>1, as we will discuss later.

a (cm)	1-θ	h (cm)	Onset Time (s)	B
0.0013	4.10E-04	1.33	27	5.72
0.0016	2.71E-04	2.39	32	5.51
0.0020	1.73E-04	5.13	44	6.06
0.0024	1.20E-04	9.39	56	6.42
0.0028	8.83E-05	16.44	72	7.08
0.0032	6.76E-05	29.82	100	8.60

Table 1. Results from KFIX-LPL tephra fall simulations of various particle radii showing the time it takes for an 3 cm-amplitude instability to develop and the B criterion at that time as calculated from equation 5.4.

5.4 Numerical Modeling of Chicxulub Ejecta Deposition

Having achieved agreement between numerical simulations and previous experimental observations for the problem of tephra deposition through a water column, KFIX-LPL was next adapted for the more complex scenario of atmospheric reentry of distal ejecta from the Chicxulub impact. Like the Carey experiment simulations, spherical particles are injected into the top of a "tank" of fluid medium, but in this case the medium is air and the tank is the scale of the Earth's atmosphere (top of model mesh is 150 km in altitude). The initial mesh approximates the Earth's atmosphere with an exponential pressure gradient and the thermodynamic properties of air, assuming ideal gas behavior. The pressure decreases with increasing height according to the expression:

$$P = P_0 e^{-gz/RT} \qquad [5.5]$$

where P is pressure, P_0 is pressure at sea level, z is altitude, T is temperature and R is the molecular gas constant for air. The model assumes an initially isothermal temperature atmosphere, which is not correct at high altitudes, but the temperatures attained in the upper atmosphere during ejecta reentry dwarf the normal upper atmospheric temperature gradient. The initial isothermal assumption simplifies evaluation of instability formation against an analytical criterion, as will be discussed later.

250-μm spherical particles are injected into the top of the model atmosphere at 8 km/s, which is the average speed of spherules reentering the atmosphere from the ex-

panding impact plume (Melosh et al., 1990), and at an angle of 45º. Rather than a constant flux of particles, the Chicxulub impact spherules would have reentered the atmosphere as a pulse of material, which decays with time. The mass flux of particles employed in the model is based on previous calculations (Melosh et al., 1990), where the total mass of injected particles is equal to the mass of spherules observed in the K-Pg boundary which consists of 20,000 spherules (250 µm mean size) per square centimeter (Smit, 1999). The particle phase is modeled as a simple incompressible fluid with the properties of basaltic glass. The KFIX-LPL models for ejecta reentry employ a drag coefficient which accommodates free molecular flow, in addition to laminar and turbulent flow. This is necessary because particles falling through the thin upper atmosphere at hypervelocity speeds are in the free molecular flow regime. The model also accommodates the large amount of atmospheric heating caused by spherule deceleration, including conductive and convective heat transfer between the two phases at all relevant flow regimes and the dissipation of heat via thermal radiation. The particles enter the atmosphere as an hour-long triangular pulse which peaks after 10 minutes.

In the model simulation, the spherules enter the thin upper atmosphere at hypersonic velocities. As the spherules encounter denser atmosphere, the increased drag decelerates the spherules and leads to compression of the atmosphere. The spherules accumulate at ~70 km in altitude and continue to fall at their terminal velocities (~10 m/s). A spherule-laden band of air forms at the altitude of accumulation, which also marks an unusually steep pressure gradient due to mass loading in the layer by the particles. The ejecta particles, upon deceleration and radiation of their heat, attain maximum tempera-

tures of 1600 K. Transfer of some of this thermal energy to the air, which is unable to efficiently dissipate its heat, results in the upper atmosphere heating up to >3000 K over the course of spherule reentry. However, the air below the particle layer remains cool. With increasing time, the density of the particle-laden band increases and the layer thickens downwards at the rate of the settling velocity. After ~30 minutes, the base of the layer begins to destabilize resulting in well-formed density currents (Figure 25). After 40 minutes, spherules are falling collectively in plumes with maximum velocities of ~20 m/s and the plumes displace the air below producing a return flow travelling upwards at 10-20 m/s. The descending plumes slow as they penetrate into denser atmosphere. Continuing injection of impact material at the top of the atmosphere over the next hour continues to feed the density currents.

The density currents initiate at the edges of the mesh and we are unsure at this time of the reason and the possibility of numerical artifact cannot be entirely ruled out. This is particularly anomalous because the periodic boundaries employed on the left and right sides of the mesh have not shown evidence for any numerical problems except at the onset of instability. Similar behavior at the mesh edges is the observed in Chicxulub ejecta reentry simulations employing a wider mesh (<50 km) than the one shown in **Error! Reference source not found.**, including identical times of onset. It is possible an even wider mesh is required to eliminate the edge effects. If so, the narrow mesh may be imposing an artificial wavelength upon instability formation.

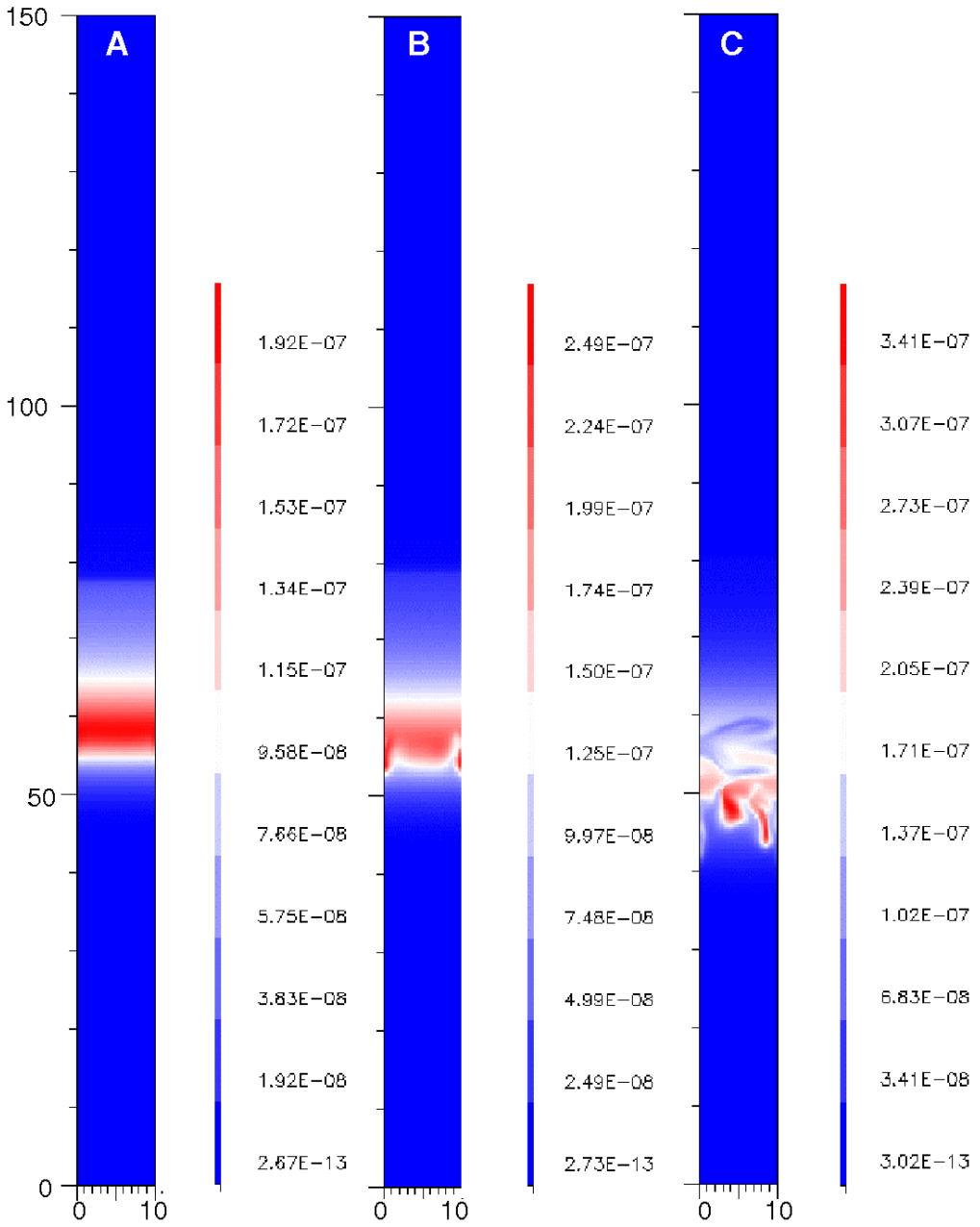

Figure 25. Density current onset and propagation in a simulation of average Chicxulub ejecta reentry at 45 degrees into a 150 km high and 10 km wide slice of atmosphere, as shown in contour plots of macroscopic spherule density (g/cm^3) after (a) 30 minutes, (b) 35 minutes, and (c) 55 minutes. Model resolution is 250 m. Models employing wider meshes (<50 km) at this resolution show similar instability onset, but were not run to the fully development of plumes.

Running on a single processor on a Mac Pro with quad-core Intel Xeon 3.2 GHz processors (KFIX-LPL is not currently parallelized), each additional 5 cells of width for a mesh 600 cells high with 250 m resolution adds ~2 days to the computing time of a 4,000 s simulation. Due to time constraints of this thesis, we were limited to run times of ~2 weeks (1 month maximum), which prevented modeling instability formation on meshes >50 km and also prevented modeling the complete fall of spherules to the ground, which requires the model be run to ~10,000 s. The simulation shown in **Error! Reference source not found.** was chosen because it ran to the end of spherule reentry to the upper atmosphere and full development of density currents; simulations with wider meshes were stopped shortly after instability onset (~2,000 s) due to time constraints.

We suspect the anomalous instability initiation at the mesh boundaries may be a resolution effect as we have not yet conducted resolution tests to determine the minimum required cell dimension in order to accurately resolve the wavelength of the instability. However, we are less concerned with the morphology and evolution of density currents at this stage, but simply seek to answer the question of whether the spherule-laden layer accumulating in the atmosphere following Chicxulub became destabilized into vertical density currents. The KFIX-LPL models of spherule reentry yield the properties of the particle-laden layer and the ambient air through time and allow us to evaluate whether instability is expected. If conditions favor instability, the modeled instability onset reflects real driving forces, despite any un-real preference in location.

Additional simulations varying the spherule reentry input parameters show that increasing the spherule mass flux (Figure 26) to the upper atmosphere or decreasing the

spherule size decreases the time of instability onset, similar to the tephra case. These observations agree with expectation from the analytical criterion for instability in an incompressible fluid, which will be introduced in the next section, and support a real origin for the instabilities versus numerical artifact. In one simulation employing smaller particles (125 µm), density currents do not initiate at the edges indicating either the mesh width or resolution is insufficient for simulations with larger particles and thicker particle layers. Vertical spherule reentry also shortens the time required for density current formation.

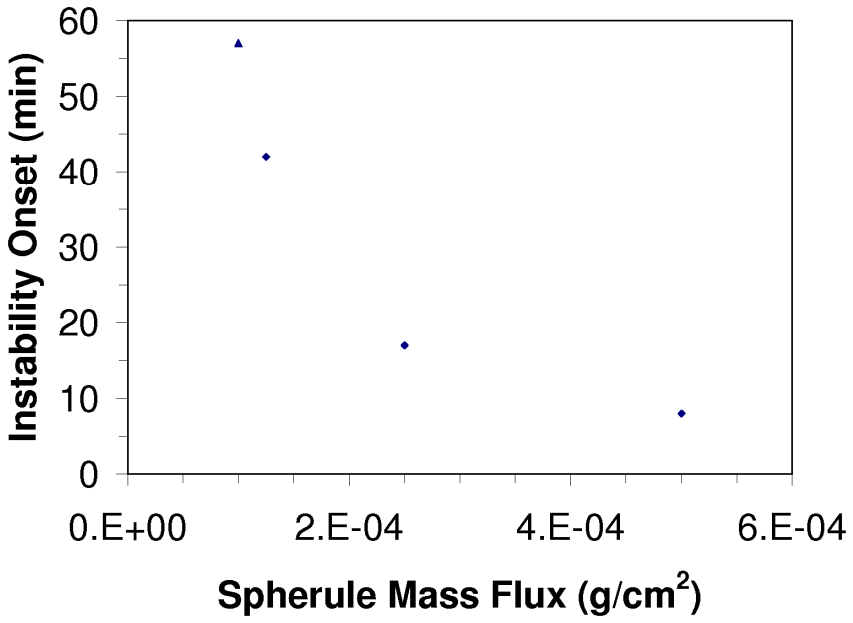

Figure 26. The time of instability onset for a series of 250 µm spherule reentry simulations at 45° where the spherule mass flux to the top of the atmosphere is constant throughout the duration of the simulation. Time of onset is defined by an instability amplitude of ~1 km. Simulations use 250 m (4 cells/onset amplitude) resolution with the exception of one (triangle), which uses 500 m (2 cells/onset amplitude).

5.5 Discussion

In both the KFIX-LPL models of tephra fall through a small water tank and impact spherule sedimentation through the Earth's atmosphere, the fluid medium is loaded to the point of instability resulting in the formation of vertical density currents, which transport the particles collectively faster than if the particles settled individually. Comparisons with observational data from Carey's (1997) tephra fall experiments serve to validate the ability of KFIX-LPL to successfully model turbulent instability growth. Simulations of two Carey experiments closely match the experimental observations, including general time of instability onset, resulting increase in particle velocity, and morphology of the particle-laden plumes. The B values calculated from equation 5.4 for the onset of instability observed in each of the tephra fall simulations are all greater than 5 and are consistent with functional behavior of the analytical criterion (Figure 27), where an increased particle size requires increased layer thickness and/or layer particle concentration for instability. The increasing divergence from B=5 at larger particle sizes is likely reflective of larger particles not falling individually in purely Stokes flow, as our criterion assumes, but rather having an increasingly turbulent velocity component.

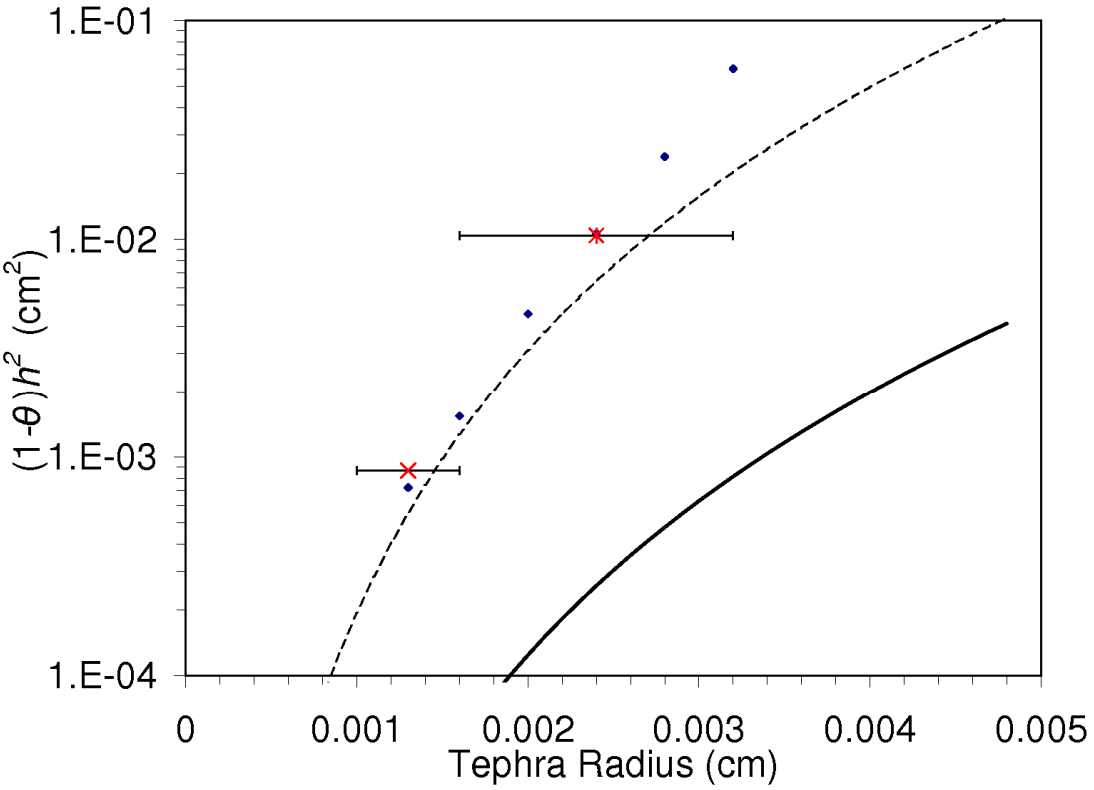

Figure 27. Comparison of instability onset in KFIX-LPL models (diamonds) and Carey tephra-fall experiments (stars) for various tephra radii with the analytical criterion for the onset of turbulent instability. The solid line represents B=1 and the dotted line represents B=5. Note that models agree with experiments and neither models nor experiments become unstable at B<1, as expected from the criterion. Horizontal error bars on experiment data points show the range of particle sizes used in the experiments. Onset of instability is defined as the time at which a growing instability reaches 3 cm in amplitude.

The B values calculated for the two Carey experiments closely match the models and also exceed 5. There is some error in calculating the instability criterion for the experiments, as the method of identifying instability onset was less precise than the numerical models allow. Carey visualized density current formation using an ultrasound probe positioned at a depth of 7 cm that only imaged a small area near the top of the tank. He approximated the instability onset based on measurements of particle velocities and

the distribution of imaged particles, not the growing amplitude of the irregular interface between the layer and the underlying fluid. The precise onset of instability, defined as the time when the base of the originally horizontal particle-laden layer becomes irregularly wavy to some amplitude, may not have been observable with this experimental setup. Carey would have only observed instability once the change in settling mode became evident in the ultrasound images (measurable change in velocity, observable reorganization of particles into density currents). We estimate the amplitude of instability at the recorded onset in the experiments to be ~3 cm, at which point the increase in particle velocities and collective grouping of particles should be reasonably observable, as evident from comparing the onset times in
Table 1 to the particle fall velocities plotted in Figure 23. For consistency, the same amplitude is used for the instability onset threshold in evaluating the numerical simulations.

Assessing the instability criterion for the numerical models is more precise than the experiments because we are able to track velocity and density variations throughout the tank in detail. However, the modeled B values are all greater than one (~5-8). This may be partially due to the homogeneity of the particle-laden layer, which has fewer disturbances at the lower interface than in the actual experiment (where there is some heterogeneity in tephra size, shape, density, etc.), resulting in a delay in the numerical triggering of density current formation. The criterion itself may also not be good to such constant factors when applied to our models. Furthermore, the amplitude of the instability near the time of onset may not being fully resolved in the highest resolution (0.25 cm)

simulations, particularly when the particle layer is thin and instability wavelength small. However, the modeled density current formation matches well with Carey's experiments suggesting that the delay in instability onset beyond the mathematical point of instability is inherent to the process. What is more important is that the modeled particle-laden layers reach instability only at B>1 and not in the zone of stability (B<1). The modeled instabilities are therefore physically meaningful and develop as expected from turbulent instability theory and experimental observations; they are not numerical artifacts.

Despite a much larger scale and far more complicated set of input parameters, the Chicxulub ejecta model is qualitatively similar to the tephra-fall models. Like the tephra models, particles accumulate in a layer of density ρ overlying a denser medium of density ρ_o ($\approx\rho_f$) (the denser lower atmosphere in the Chicxulub case) and initially settle at their individual terminal velocities. Eventually, critical density and/or thickness of the particle-laden layer is achieved and the bottom of the layer becomes unstable, allowing particles to fall collectively in density currents at higher velocities. Evaluating instability formation, however, is more difficult. The small-scale tephra-fall models can be directly compared to experimental observations, but there is no observational data on density current formation due to atmospheric reentry of impact ejecta. It is also more difficult to evaluate the modeled instabilities analytically due to the complexities of the problem: The particles enter the atmosphere at hypersonic speeds and deliver a large quantity of energy to the model mesh; both the particles and air are heated to some degree; the particles reenter the atmosphere at an angle, not vertically (although we model both oblique and vertical cases); finally, a large range of air densities are involved and a

parcel of air in a growing vertical instability will compress adiabatically as the instability's amplitude increases.

The simple criterion for turbulent instability (Equation 5.4) is inadequate to evaluate density current formation in the atmosphere because air is compressible: density and temperature changes due to adiabatic compression must be considered. In addition, temperature gradients are created due to conversion of kinetic energy to heat as the particles slow and a hot particle-laden layer of air will be more buoyant than a cool layer of equivalent thickness and macroscopic density. Incorporating atmospheric compression yields a set of new criteria for instability in a compressible fluid (see Appendix B for full derivation), which is applicable to both viscous and turbulent instability formation. All three criteria must be satisfied for vertical density current formation.

1) The overlying particle-laden layer must be denser than the underlying medium:

$$\left(\rho - \rho_o\right) > 0 \qquad [5.6]$$

2) Any excursion at the base of the layer will oscillate and not develop into finite-amplitude density currents unless:

$$\left\{ \frac{\theta}{\gamma}\rho - \left(1 + \frac{R}{g}\frac{dT}{dZ}\right)\rho_o \right\} > 0 \qquad [5.7]$$

3) The timescale of instability growth τ must be shorter than the time it takes a particle to cross the layer thickness h at its terminal velocity v_t (B>>1):

$$B = \frac{h/v_t}{\tau} \qquad [5.8]$$

The terminal velocity v_t of a particle of radius a is defined as a function of its Stokes, v_s , and inertial (turbulent), v_i , velocities:

$$v_t = \frac{v_i^2}{2v_s}\left[\sqrt{1+4\frac{v_s^2}{v_i^2}}-1\right] \qquad [5.9]$$

where

$$v_s = \frac{2}{9}\frac{(\rho_p - \rho_o)a^2 g}{\eta} \qquad [5.10]$$

$$v_i = \sqrt{\frac{16}{3}\left(\frac{\rho_p - \rho_o}{\rho_o}\right)ag} \qquad [5.11]$$

These equations are very approximate when the air density is low since the instability criterion assumes a simple drag coefficient which includes only Stokes and turbulent flow, not free molecular flow in the upper atmosphere. Thus, for comparison of the model instabilities with the analytical criteria we use the computed terminal velocity from the model which uses a more accurate drag coefficient, rather than using v_t as defined in equation 5.9.

The timescale of instability growth τ is a function of the two limiting timescales for viscous flow, τ_v , and inertial (turbulent) flow, τ_i , where value D is found by dividing equation 5.7 by twice the atmospheric scale height:

$$\tau = \frac{\tau_v + \sqrt{\tau_v^2 + \tau_i^2}}{2} \qquad [5.12]$$

where

$$\tau_v = \frac{6\eta}{(\rho - \rho_o)g\delta + Dg\delta^2} \qquad [5.13]$$

$$\tau_i = \sqrt{\frac{\rho_o \delta}{(\rho - \rho_o)g + Dg\delta}} \qquad [5.14]$$

We tracked the values of the three instability criteria throughout the Chicxulub simulation as the particle-laden layer thickened and increased in density. For simplicity, we assume the ambient temperature gradient at base of the particle layer is zero (as it is initially). This is not entirely correct, but the base of the particle layer does not experience a large increase in temperature as compared with the top of the particle layer and the atmosphere above. Because oblique spherule reentry delays the onset of instability—likely because remnant horizontal velocities in the particle layer following spherule deceleration act to shear the top of any developing instability, an effect not included in our criteria—we evaluate instability onset for a model of vertical spherule reentry. In this model, the base of the particle layer develops an instability with an amplitude of 1 km after ~20 minutes, at which point the particle layer is 14 km thick and has a maximum volume fraction of spherules of ~7E-8 and an air density of ~4E-7 g/cm^3 just below the layer. The fall velocity of particles in the layer is ~10 m/s. Criterion 5.6 is satisfied

throughout the simulation because the particle layer is always denser than the underlying air. Criterion 5.7 is negative at the start of the simulation, but becomes positive after ~15 minutes, not long before instability is first observed. Criterion 5.8 is >10 near the beginning of the simulation and >100 by the time density currents initiate. Thus, the controlling criterion is not whether there is a density contrast favoring development of an excursion or whether the rate of instability growth exceeds the terminal velocity; rather, any excursion will oscillate until the criterion regarding adiabatic compression of the excursion is met. Only once all three criteria are satisfied do density currents initiate in our models.

The *B* values calculated from our models are closest to the limiting case of viscous particle settling and turbulent instability growth. It may seem counterintuitive that particles at 70 km in altitude would be falling in the Stokes regime, but the combination of a small Reynolds number, *Re*, and small Mach number, *M*, within the particle layer result in a large drag coefficient of ~100 at this altitude (Figure 28). This is a consequence of the long mean free path and the fact that this region is in the Knudsen free molecular flow regime. Thus, the terminal velocity of a particle within the layer is twice the Stokes flow velocity (v_s~5 m/s), rather than falling turbulently at much higher velocities (~200 m/s). The fact that the particles are falling in the viscous regime is favorable to instability development as the time required to cross the layer thickness is less than for turbulent flow.

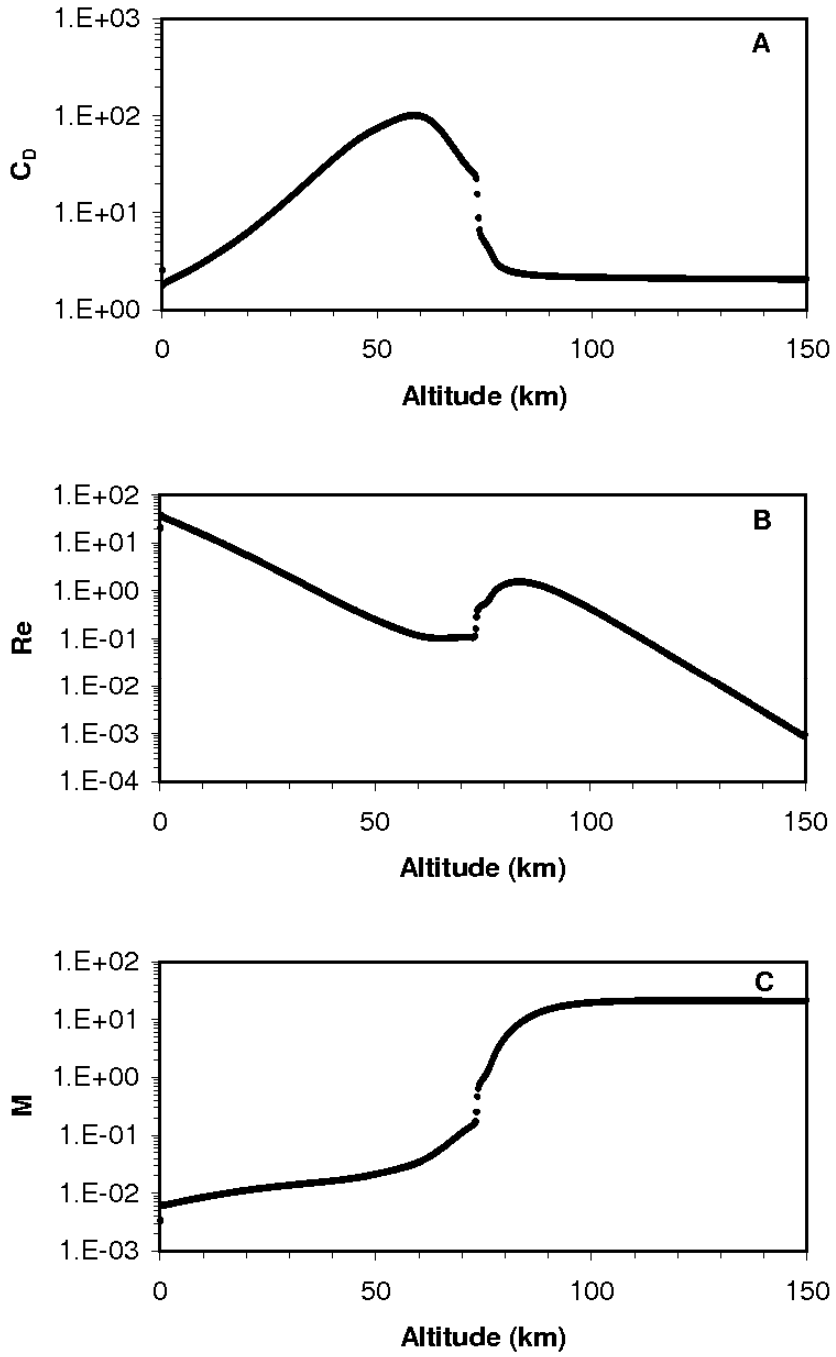

Figure 28. Drag coefficient C_D, Reynolds number *Re*, and Mach number *M*, as a function of altitude after 1 minute of Chicxulub spherule reentry, illustrating the behavior of the drag coefficient in the region below ~70 km in altitude where the spherules accumulate after decelerating to their terminal velocities.

A more rigorous assessment of instability development for the Chicxulub ejecta settling models requires modifications to the generalized instability criteria to reflect the variations of properties within the spherule layer. Such additions include the complete drag coefficient treating free molecular flow and inclusion of property gradients across the thickness of the particle layer because the layer does not have constant density, temperature, spherule volume fraction, etc. The temperature gradient in the ambient air below the spherule layer, which we ignored for simplicity, must also be considered in more detail. Increased model resolution is also needed to fully resolve density current onset and the anomalous boundary effects at the time of onset must be removed in order to ensure that the modeled instabilities are real.

5.6 Conclusion

Nipkow (1920) established that annual blooms of diatoms are represented by laminated varves on lake bottoms, despite the fact that the settling time of an individual diatom might exceed a year (Bradley, 1965). This led Bradley (1965; 1969) to propose that vertical density currents might be responsible for not only the enhanced transport of diatoms to the bottoms of lakes, but also rapid sedimentation in other geologic systems where a high mass flux of small particles enters a fluid medium. The models presented here reinforce the conclusions of experimentalists (Carey, 1997; Manville and Wilson, 2004) that vertical density current formation is a viable explanation for rapid transport of volcanic ash to the seafloor. Furthermore, our models suggest that the large flux of tiny

spherical particles into the upper atmosphere following the Chicxulub impact event led to the development of density currents in the atmosphere and deposition of the global K-Pg boundary layer from particle-laden plumes on a scale of hours. Finally, the criteria presented here for instability growth in a nearly incompressible fluid, such as water, and in a compressible fluid, such as air, supply a means by which both viscous and turbulent instability might be evaluated in other geologic systems.

CHAPTER 6

SELF-SHIELDING OF THERMAL RADIATION BY CHICXULUB IMPACT EJECTA: FIRESTORM OR FIZZLE?

6.1 Introduction

The hypervelocity atmospheric reentry of impact ejecta, which were eventually deposited to form the global 2-3 mm-thick layer at the Cretaceous-Paleogene (K-Pg) boundary, released a large quantity of energy into the atmosphere. The fate of this energy is less clear: did enough reach the surface to be a major contributor to the end-Cretaceous mass extinctions? Soot discovered within the K-Pg boundary sequence at several localities around the world (Wolbach et al., 1990; Wolbach et al., 1988; Wolbach et al., 1985) suggested that impact ejecta from the Chicxulub crater emitted sufficient thermal radiation while decelerating through the Earth's atmosphere to ignite global wildfires (Melosh et al., 1990). Additionally, differential survival patterns observed in the terrestrial fossil record across the K-Pg boundary appear consistent with a large thermal pulse. Animals' ability to seek shelter from the thermal radiation and subsequent fires correlates with increased survival rates (Robertson et al., 2004b). Previous calculations of the expected thermal radiation at the ground produced by the ballistic reentry of ejecta (Kring and Durda, 2002; Melosh et al., 1990; Toon et al., 1997) lend further support for a large thermal pulse causing global wildfires and other biologic destruction. These studies estimate a pulse of thermal radiation on the order of 10 kW/m^2 at the sur-

face for >20 min, which is presumed to be near the lower limit of forest fire ignition (Melosh et al., 1990).

The post-Chicxulub global wildfire hypothesis has faced criticism. Measurements from non-marine North American localities show lower than background concentrations of charcoal at the K-Pg boundary, suggesting there were no distinctive forest fires on the continent (Belcher et al., 2005; Belcher et al., 2003). Robertson et al. (2004a) argue that this is in fact evidence for global wildfires, as such intense fires would lead to the complete combustion of any biomass. However, there is not a complete lack of charcoal and experiments on the irradiation of wood (Belcher et al., 2005) indicate that some charcoal would remain after an impact-induced thermal pulse. Jones & Lim (2000) argue, based on biodegradation evidence in charcoal fragments, for a time lag between the plant deaths and later preservation in wildfires as charcoal. However, the K-Pg deposits, which include soot and fossil charcoal, were deposited in less than a day. Other controversy exists surrounding the origin of the soot. Elevated levels of aciniform soot within the K-Pg deposits were initially interpreted as products of wildfires initiated before all the ejecta had settled based on carbon isotopes and the presence of the polyaromatic hydrocarbon retene, which are both consistent with woody biomass combustion (Wolbach et al., 1990; Wolbach et al., 1988; Wolbach et al., 1985). Subsequent studies argued that the source material of the soot is not biomass, but rather fossil carbon from the target rock at Chicxulub (Belcher et al., 2005; Belcher et al., 2003; Harvey et al., 2008). Harvey et al. (2008) discovered elevated levels of carbon cenospheres in various K-Pg North American localities, which are thought to be formed solely by the incomplete combustion

of fossil hydrocarbons, and suggested that their abundance is consistent with impact into an organic carbon-rich target sequence.

Melosh et al. (1990) estimated that the atmospheric reentry of the K-Pg boundary ejecta at 5-10 km/s would be accompanied by a total energy of 1.3-5 × 10^8 J/m^2 over the entire globe. Because the impact plume ejecta is initially launched by the impact with a range of angles and velocities, the ejecta—and hence energy—will be delivered over a period of 1-2 hours, resulting in rates of power deposition peaking at 50 kW/m^2 world-wide. Melosh et al. (1990) base their calculation on the theory of thermal radiation from the atmospheric reentry of micrometeorites (Whipple, 1950); assuming half the energy is radiated upwards to space and that some fraction is absorbed in the atmosphere by green-house gases, they estimate that a third of the total thermal power reaches the ground. Subsequent studies (Durda and Kring, 2004; Kring and Durda, 2002; Toon et al., 1997) present different estimates of the global ejecta distribution and energy flux delivered to the atmosphere from the Chicxulub impact, but also calculate the thermal radiation reach-ing the ground assuming that absorption by greenhouse gases is the only limitation to energy transmission. Given the solar thermal power delivered to the top of the atmos-phere (1.4 kW/m^2 maximum), there is no question that ejecta reentry delivered enough energy to potentially cause significant environmental disturbance. However, calculating what fraction penetrates to the ground and what fraction escapes to space is more compli-cated than has previously been presumed. Recent modeling (Goldin and Melosh, 2007) shows that impact ejecta settles through the mesosphere in an increasingly dense cloud in which the optical mean free path is reduced. Consideration of particle interactions with

the thermal radiation, in addition to air interactions, is essential for calculating the thermal irradiance reaching the Earth's surface because some of the energy radiated by falling ejecta is reabsorbed by previously-decelerated particles and greenhouse gases.

We present a new numerical model of the atmospheric reentry of Chicxulub ejecta that introduces a more complete calculation of thermal radiation than previous studies. Not only does this model calculate the descent of ejecta through the atmospheric column so the optical opacity of particles can be determined at any time, but it includes optical opacity in computing the emission and absorption of thermal radiation. Understanding how the energy delivery to the upper atmosphere relates to thermal radiation transmission to the ground allows us to better constrain the validity of the global impact wildfire hypothesis for Chicxulub.

6.2 Numerical Modeling

Numerical modeling of atmospheric reentry of Chicxulub ejecta and the resulting thermal radiation transfer used KFIX-LPL, a two-dimensional, two-phase fluid flow code. Based on KFIX (Rivard and Torrey, 1978), which is itself a variant of KACHINA (Amsden and Harlow, 1975), KFIX-LPL is adapted for the problem of impact ejecta sedimentation through the Earth's atmosphere. It uses an eulerian, finite-difference technique where a model mesh is composed of discrete cells, each of which contains some volume fraction of each distinct phase. The two phases can interact, exchanging mass, momentum, and energy within each cell and phases can also move between cells.

Several key modifications to the code are crucial for calculating the thermal effects of ejecta reentry. Modeling the deceleration of particles through the atmosphere requires accurate drag coefficients, which is complicated by the fact that most of the deceleration occurs in the upper atmosphere where the mean free path is much larger than the particles' diameter and the gas cannot be treated as a continuum. Similarly, spherule temperature, which is central to any thermal radiation calculation, requires an accurate calculation of heat transfer between phases in the non-continuum flow of the upper atmosphere. We incorporated both drag coefficient and heat transfer functions (Melosh and Goldin, 2008) into KFIX-LPL. These coefficients apply over a wide range of flow regimes (free molecular flow to semi-continuous flow to the continuum limit of Stokes flow). KFIX-LPL also includes a thermal radiation calculation which uses a diffusion approximation for radiation transport (based on Zel'dovich and Raizer, 1967) where each phase has its own absorptive properties. The algorithm computes the instantaneous thermal radiation balance from the spherule and air temperatures, densities, and absorption coefficients and is described in more detail in Chapter 7 and Appendix C.

For a terrestrial impact, the two phases are air, for which perfect gas behavior is assumed, and impact spherules, which are treated as a simple incompressible fluid dispersed into droplets of uniform size. The initial mesh approximates a 150-km high slice of undisturbed Earth's atmosphere with an exponential pressure gradient, constant temperature (normal temperature variations in the upper atmosphere are insignificant compared to those produced by ejecta reentry), standard gravity, and zero initial velocities. The left and right mesh boundaries are periodic and the lower boundary (at the ground) is

free slip. The upper boundary is an inflow boundary through which we inject the impact spherules. The radiation model employs periodic boundaries on the left and right, a fixed temperature boundary (273 K) on the bottom, and a 100% absorptive boundary on the top (i.e. any thermal radiation reaching the top of the model atmosphere freely escapes to space). The model resolution is 250 m, which we have determined—via testing resolutions ≥125 m (Appendix D)—to sufficiently resolve variations in mean free path throughout the model atmosphere and yield a resolution-independent solution for the surface irradiance.

Because the simulation begins when spherules first enter the atmosphere, not at ejection from the impact site itself, the model inputs rely on the current understanding of the global transport of Chicxulub ejecta and observations of the K-Pg boundary layer. The following describes our nominal Chicxulub ejecta reentry model: Assuming properties of average distal K-Pg ejecta (see Smit, 1999), the spherule phase is modeled as 250-µm spherical particles with the properties of basaltic glass. The particles are injected into the model atmosphere at 8 km/s and at a 45º angle of incidence. In actuality, the ejecta reentering the atmosphere at any location would do so with a range of particle sizes, velocities, and trajectories. KFIX-LPL is limited to single values for these parameters so we use average values for Chicxulub. With these simplifications, each spherule enters the atmosphere with the same kinetic energy throughout the simulation. However, the total rate of energy delivery is not constant because the number of spherules added at any time is varied.

The rate of atmospheric reentry depends of the mechanics of the expanding impact plume, which contains ejecta travelling at the high velocities required to reach the most distal localities. This material is ejected at a range of initial velocities and angles (Melosh et al., 1990), which, assuming ballistic expansion, results in the ejecta arriving at a given distance over a period of time. The rate of ejecta mass deposition to the upper atmosphere through time was calculated by Melosh et al. (1990) as a pulse of material which arrives over a few hours. We approximate the injection of ejecta spherules to the atmosphere as a triangular pulse (Figure 29), where the mass flux increases linearly to a maximum value after some number of minutes and then decreases linearly over the remaining duration of the pulse. The total spherule density injected into our model atmosphere is 0.5 g/cm^2, which is derived from the 20,000 spherules/cm^2 observed in the most undisturbed distal K-Pg localities (Smit, 1999). In subsequent simulations, we vary the dimensions of the triangle to examine the relationship between the mass flux (and hence energy flux) added to the atmosphere and the resulting thermal radiation reaching the ground.

6.3 Model Results

For a nominal Chicxulub scenario, impact spherules reenter the atmosphere over the course of one hour, reaching maximum mass flux after 10 minutes. As the ejecta spherules encounter increasingly denser atmosphere and increasing drag, they decelerate.

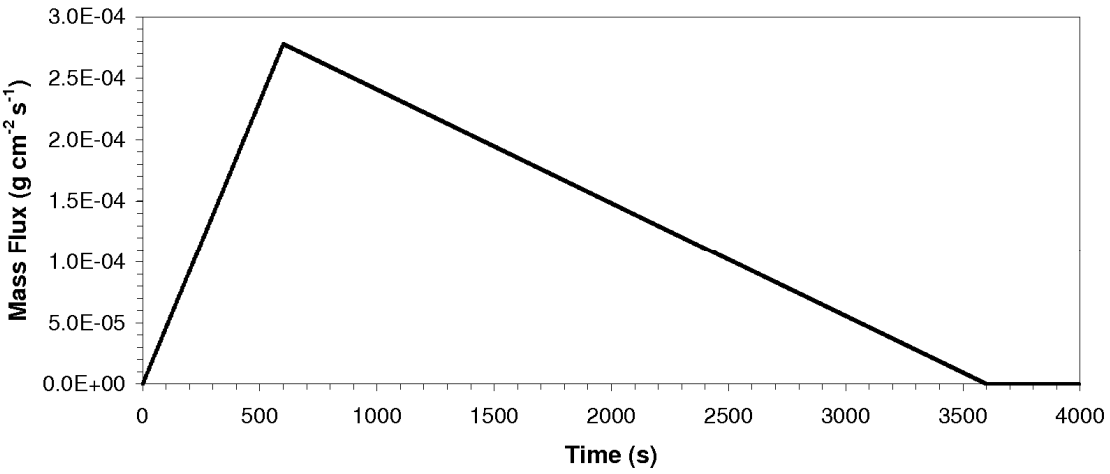

Figure 29. Mass flux of spherules per unit area injected into the top of the model atmosphere. Our nominal Chicxulub model assumes spherule reentry lasts 60 minutes and peaks after 10 minutes, depositing a total spherule mass density of 0.5 g/cm^2.

The loss of kinetic energy heats the spherules to ~1600 K maximum, decreasing to ~1200 K due to compression of the upper atmosphere by ejecta reentry. This heat is efficiently radiated from the small particles at infrared wavelengths. The surrounding air is also heated through frictional exchange with the spherules. The air in the upper atmosphere does not radiate this heat as readily as the particles and thus the air temperature continues to increase, exceeding 3000 K by the end of spherule reentry. The decelerating spherules eventually reach their terminal velocities at ~70 km in altitude and continue to settle towards the ground. A cloud of settling spherules accumulates below this altitude and becomes increasingly opaque, partially blocking thermal radiation emitted from the decelerating spherules higher in the atmosphere. In our nominal calculations we assume that the upward thermal radiation reaching the top of the mesh escapes freely to space.

The irradiance at both the top and bottom of the model atmosphere was calculated over the duration of spherule reentry (

Figure 30). At any time, the upward flux of thermal radiation is proportional to the mass flux of spherules injected into the mesh, increasing linearly to a maximum of ~25 kW/m^2 after 10 minutes and decreasing linearly over the remaining duration of spherule reentry. The flux of thermal radiation reaching the ground, however, does not so clearly reflect the energy input above. The flux initially increases linearly, but the rate of the thermal radiation flux increase soon declines. The flux reaches a plateau after ~8 minutes at a maximum of only ~6 kW/m^2. The mass flux continues to increase to a maximum after 10 minutes, at which time the irradiance at the surface has already begun to decrease. After 10 minutes, when the mass flux of spherules steadily decreases, the radiation flux to the ground rapidly decreases in a nonlinear fashion. The maximum flux of thermal radiation reaching the ground is only one-fourth of the maximum flux to space and the high fluxes (exceeding peak solar irradiance of ~700 W/m^2 at the surface, assuming 50% absorption of the solar flux reaching the top of the atmosphere) are maintained over half the length of time of spherule reentry. The surface irradiance is a nonlinear function of time, suggesting control by factors other than the energy flux to the upper atmosphere.

The lower magnitude of the peak flux and shorter duration of fluxes exceeding normal solar values indicate that the transmission of downward thermal radiation is limited while upwards radiation flows freely to space. In the thin air of the upper atmosphere, the optical mean free path is so long that thermal radiation encounters few obstacles. The downward flux, however, must penetrate increasingly dense atmosphere containing absorptive greenhouse gases and previously entered spherules. Models compar-

ing ejecta reentry into an atmosphere void of absorptive gases to our nominal Chicxulub simulation show significant absorption of thermal radiation by greenhouse gases (Figure 30). Assuming an identical pulse of spherules into the upper atmosphere, the maximum flux of thermal radiation reaching the ground doubles (~13 kW/m^2) if the atmosphere contains no greenhouse gases. However, this is still less than the ~25 kW/m^2 reaching the top of our model atmosphere and the duration of high fluxes is still half that of the sky.

The other source of opacity is the concentration of spherules. Figure 31 shows the mean free path and the flux of thermal radiation with respect to altitude at two different times in the model. After 5 minutes, the following patterns are observed: Mean free paths in the upper atmosphere are relatively long (~10^8 cm) as the air is thin, although there is some opacity contributed by the diffuse rain of decelerating spherules. At ~70 km in altitude, there is a decrease in mean free path (~10^6 cm) coinciding with increased spherule density. The mean free path sharply increases at the base of the spherule layer to ~10^9 cm where the air is still quite thin and devoid of spherules. The mean free path then steadily decreases to ~10^6 cm at the ground due to increased opacity of greenhouse gases in the denser air. At this time, the flux of thermal radiation to space is ~12.5 kW/m^2 and the flux to the ground is ~5 kW/m^2. At 10 minutes, the spherule cloud is denser, reducing mean free paths further over a larger altitude range. At this time, the spherule mass flux peaks at twice that of the previous example. Although the radiation flux to space also doubles (~25 kW/m^2), the radiation at the ground increases very little

with a major truncation of downward thermal radiation occurring at the top of the optically opaque spherule layer.

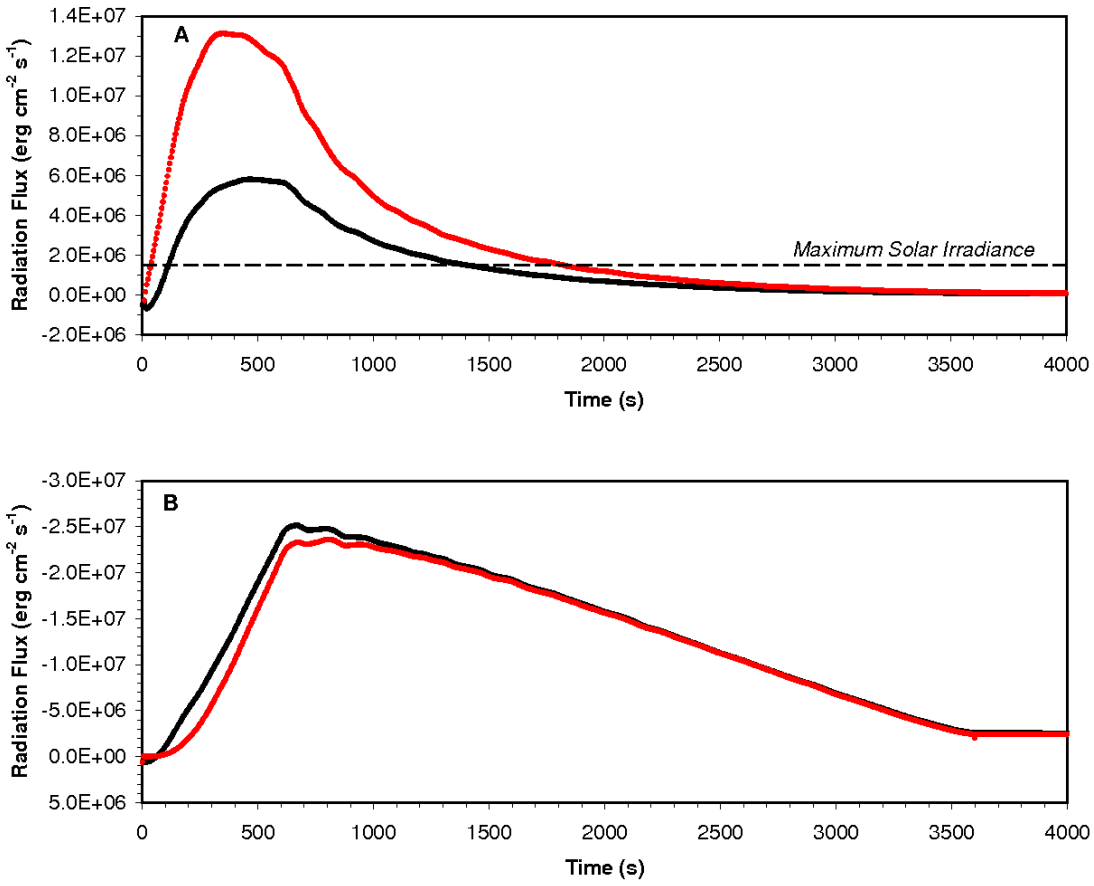

Figure 30. Thermal radiation flux at the ground (a) and to space (b) as a function of time for the nominal Chicxulub model where the atmosphere contains absorbing greenhouse gases (black) and where the atmosphere has no absorption by the gas phase (red). The dotted line represents the maximum solar irradiance at the top of the atmosphere (~1.4 kW/m^2); this value is variable at the ground depending on atmospheric absorption, etc. (average ~0.7 kW/m^2). Upward fluxes are negative.

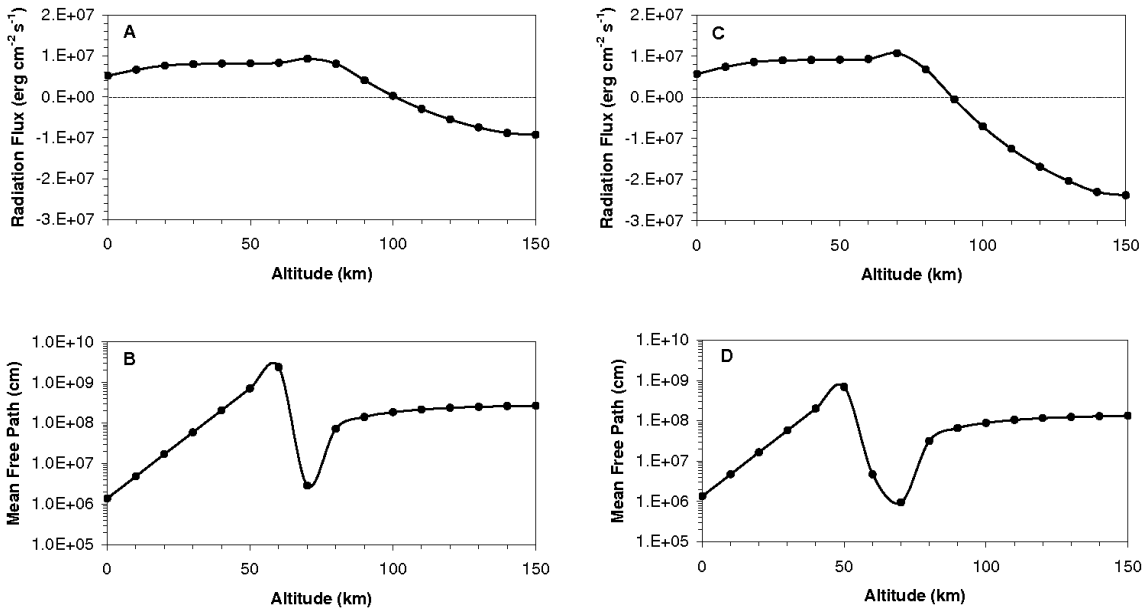

Figure 31. The average thermal radiation flux per unit area throughout the height of the model atmosphere for the nominal Chicxulub ejecta reentry model at (a) 5 minutes and (c) 10 minutes, which is the time of peak mass flux. Positive values denote downward fluxes and negative values denote upward fluxes. The average mean free path throughout the height of the model atmosphere at (b) 5 minutes and (d) 10 minutes.

The spherule opacity in the mesosphere limits the proportion of energy added to the upper atmosphere that reaches the ground. It is logical to expect that, if maximum spherule mass fluxes are attained earlier when the spherule cloud below is less dense, then higher fluxes would reach the ground. We tested this with a series of models (

Figure 32) in which the time required to obtain peak spherule reentry is varied. Because the duration of spherule reentry (60 min) and the total added spherule mass (0.5 g/cm^2) are the same, the peak mass flux is unchanged, but the mass of spherules already in the atmosphere during peak mass spherule flux varies depending on how long the reentry has proceeded. As expected, the earlier that peak spherule flux occurs, the more thermal radiation reaches the ground. Increasing to peak spherule reentry over 5 minutes results in a maximum surface irradiance of 8.5 kW/m^2. Immediately injecting spherules into the atmosphere at the maximum rate when there is no spherule cloud present increases surface fluxes to ~12 kW/m^2-- approximately half of that upwards to space, as expected if the other half is absorbed by greenhouse gases. Although thermal radiation fluxes are increased by shifting peak spherule reentry to earlier times, the thermal pulse's duration is reduced. A more rapid increase in the mass flux of spherules not only corresponds with a more rapid increase in the thermal radiation emitted from the reentering spherules, but also corresponds with an enhanced rate of accumulation of decelerated spherules below. The optical opacity of the spherule cloud increases more rapidly leading to a more rapid decrease of thermal radiation reaching the ground, despite the same total thermal energy being deposited in the upper atmosphere. We conducted additional tests, in which duration of spherule reentry, total spherule mass, spherule size, reentry velocity, and reentry angle were varied (see Chapter 7) and similar trends in the resulting surface irradiance resulted: increasing the energy deposition into the upper atmosphere is accompanied by strengthened absorption by spherules in the lower atmosphere.

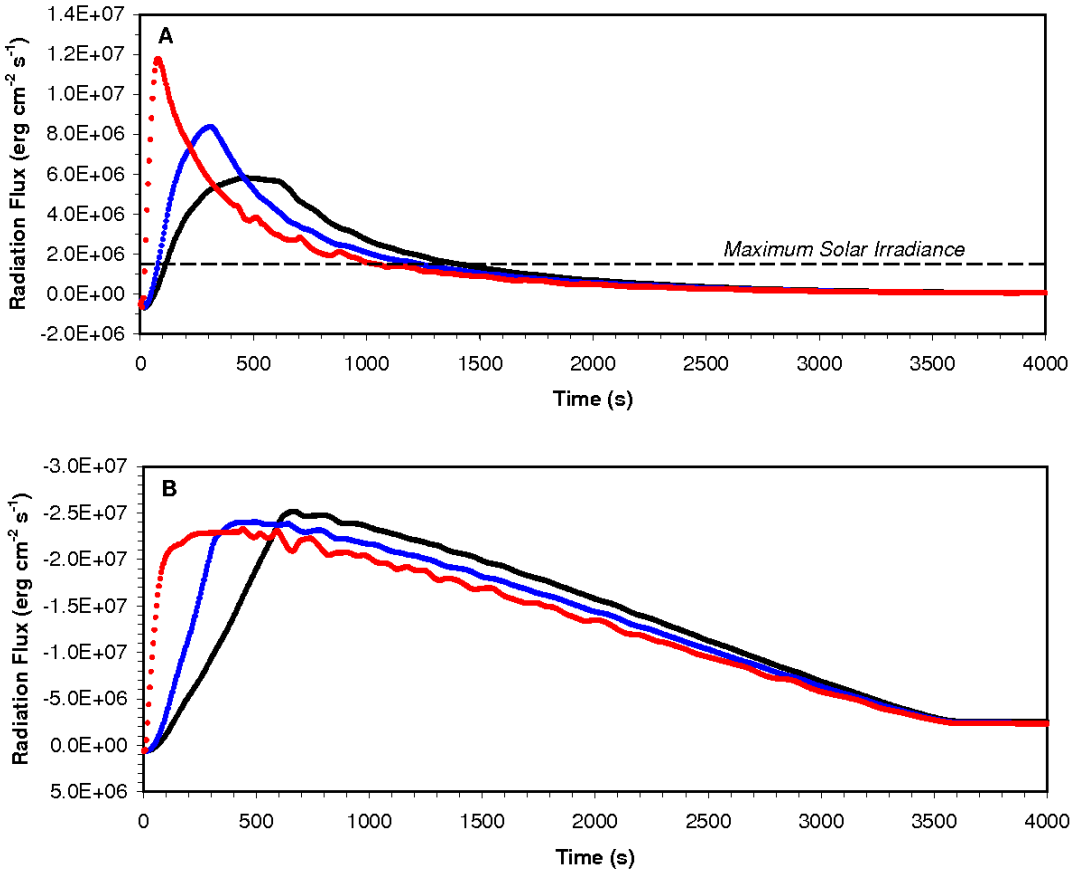

Figure 32. Thermal radiation flux per unit area (a) reaching the ground and (b) escaping to space for a series of models varying the time required to achieve peak spherule mass flux. In all models spherule reentry lasts for 60 min and the total mass of spherules added is 0.5 g/cm^2 (identical power deposition). Results for increasing to peak mass flux after 0 minutes (red), 5 minutes (blue), and 10 minutes (black). Upward fluxes are negative.

6.4 The Self-Shielding Effect

Our simulations of Chicxulub distal ejecta reentry into the Earth's atmosphere demonstrate that the quantity of thermal radiation reaching the surface is not a simple function of the energy injected into the upper atmosphere. The spherules themselves limit the amount of thermal radiation reaching ground. If it is assumed that 50% of thermal radiation from a single falling spherule is emitted upwards and 50% is emitted downwards and that the atmosphere is empty of any other absorptive species, the ground receives an equal dose of thermal radiation as escapes to space. Of course, the atmosphere is not devoid of absorptive gases such as CO_2 and H_2O vapor. The air in the upper atmosphere is so thin that greenhouse gases have little effect on the upward radiation; however, the density of air increases exponentially towards the ground and our models show that ~50% of the thermal radiation reaching the lower atmosphere is absorbed by greenhouse gases. If gas absorption was the only factor limiting transmission of downward thermal radiation, the thermal radiation reaching the ground at any time should be directly proportional to the energy injection to the upper atmosphere. Our models show that not only are maximum radiation fluxes at the ground less than half of that escaping to space, but proportionally less thermal radiation reaches the ground as reentry progresses.

Previous studies considered that spherules were solely thermal radiation producers. However, after losing their initial velocities and radiating their heat, the spherules remain in the atmosphere for several more hours as they slowly settle to the ground and the opacity of the cloud of settling spherules below 70 km in altitude increases with each

added spherule. The thermal radiation emitted downwards from the decelerating spherules in the upper atmosphere encounters an increasingly opaque zone as the total mass of material injected into the atmosphere increases. The same spherules that deliver energy to the atmosphere in the form of thermal radiation later act to shield that radiation from subsequent reentering spherules. 'Self-shielding' by the spherules thus limits both the magnitude and duration of the thermal radiation pulse reaching the Earth's surface, an effect that becomes stronger with time. The rates at which spherules are injected into the atmosphere may vary, but this not only affects the rate of energy deposition to the atmosphere; it also affects the rate of particle accumulation lower in the atmosphere and hence the strength of self-shielding. The peak flux of thermal radiation to the ground may be enhanced by increasing the energy flux to the upper atmosphere, but so is the effect of self-shielding and high irradiances cannot be sustained over as long a duration of time.

6.5 Self-Shielding: Global Wildfire Suppressant?

Compared with previous calculations, which did not consider self-shielding by the spherules, our models predict both a weaker and shorter pulse of thermal radiation at the ground. This has important implications for assessing the global wildfire hypothesis. Ignition of wood occurs when volatiles are produced at a rate sufficient to form a flammable mixture with the surrounding air (Simms, 1962). If the intensity of thermal radiation is high enough, a flame can form spontaneously in the volatile mixture and jump down to the wood's surface (*spontaneous ignition*); at lower radiation intensities volatiles

can be ignited by an independent source (*piloted ignition*) (Simms, 1962). Lightning has been proposed as a possible ignition source for impacts due the buildup of static energy following dust particulate loading of the atmosphere (Durda and Kring, 2004; Wolbach et al., 1990). The critical intensity at which dry wood will ignite has been determined experimentally to be 29.3 kW/m^2 for spontaneous ignition and 12.5 kW/m^2 for piloted ignition (Simms and Law, 1967). Although some experiments show little variation in critical intensity amongst tree species (Lawson and Simms, 1952), moisture content increases the critical intensity (Simms, 1960, 1963; Simms and Law, 1967) for both types of ignition (although there is little effect at <40% moisture for piloted ignition; (Simms and Law, 1967)) and increased material density also results in an increased critical intensity for piloted ignition (Simms, 1963).

Previous Chicxulub thermal radiation calculations considered the minimum requirement for piloted ignition to be 12.5 kW/m^2 over a duration exceeding 20 minutes (Kring and Durda, 2002; Melosh et al., 1990; Toon et al., 1997), a requirement met by supposed prolonged pulses of thermal radiation on the order of 10 kW/m^2. However, taking into account the opacity contribution of the spherules themselves, our models predict a pulse that may exceed the solar norm for >20 minutes, but certainly does not sustain fluxes >10 kW/m^2 for more than a few minutes (only if the high spherule fluxes occur early in the reentry). In addition, the critical intensity for ignition is a theoretical minimum; actual ignition intensities obtained experimentally often exceeds the critical intensity because wood has a limited supply of volatiles which may be depleted by the long duration of heating (Simms, 1962) or stripped away by wind (Durda and Kring,

2004). More realistic thermal radiation intensities required for piloted ignition of wood have been estimated to be 20 kW/m^2 for 30 minutes (Yang et al., 2003) and 20 kW/m^2 for 20 minutes (Durda and Kring, 2004), both of which make ignition even less likely at our modeled irradiances.

The reduced thermal pulse at the ground does not preclude ignition of all vegetation types. Lichen, grass, and pine needles may ignite at intensities as low as 8 kW/m^2 for exposure times of <1 minute (Anderson, 1970), so it is possible that some types of biomass may have ignited and eventually spread to the forests. Additionally, there is another type of impact plume ejecta, fine dust, which may act against the self-shielding of spherules and inflict a greater proportion of the energy deposited in the upper atmosphere upon the surface.

6.6 Fine Dust: Banking for a Firestorm?

Although self-shielding may limit the radiation reaching the ground directly, the surface thermal irradiation may be exacerbated if the impact ejecta include more than just 250 μm spherules. Submicron dust has long been suspected to play a role in the impact process, and, if it accompanies the spherules, it may substantially increase the thermal radiation reaching the surface. Although such dust is not directly observed in even the best-preserved K-Pg boundary deposits, a matrix of clay surrounding the spherules may account for an equal volume of material that may represent this ejecta faction. Sulfur-rich aerosols may also contribute to this opacity source (Pierazzo et al., 2003).

Thermodynamic studies of SiO_2 show that, of the material vaporized by the impact, about half of the mass fails to condense into liquid droplets because of the rapid adiabatic expansion of the vapor plume (Melosh, 2007). When this uncondensed gas, traveling with the spherules, encounters the top of the atmosphere, it decelerates quickly and condenses into a silicate "smoke" of sub-micron particles (Nuth and Donn, 1983; Nuth and Ferguson, 2006). Because of their small sizes, the particles in this smoke are more than 250 times more opaque, per unit mass, than the spherules themselves.

This opaque smoke layer generates a hot cap to the atmosphere that is easily penetrated by the larger spherules, but not by thermal radiation. Because the smoke opacity is so high, our numerical code would not converge in reasonable time when such a layer is explicitly added to the simulation. However, changing the upper radiation boundary condition from free streaming to total reflection accurately approximates the effect of this layer. Because this approximation neglects the internal energy of the smoke layer itself, this is actually a mild *underestimate* of the thermal radiation originating in this layer.

The reflected thermal radiation does not all reach the ground: Absorption by both the accumulated spherule layer below and gases in the lower atmosphere both reduce the surface flux. However, the "banking" effect of this high opaque layer increases the thermal flux to 19 kW/m^2 maximum and >10 kW/m^2 for >20 minutes, for a stronger and longer pulse as compared to the nominal case (Figure 33). This may be sufficient to ignite woody biomass in addition to less-dense vegetation.

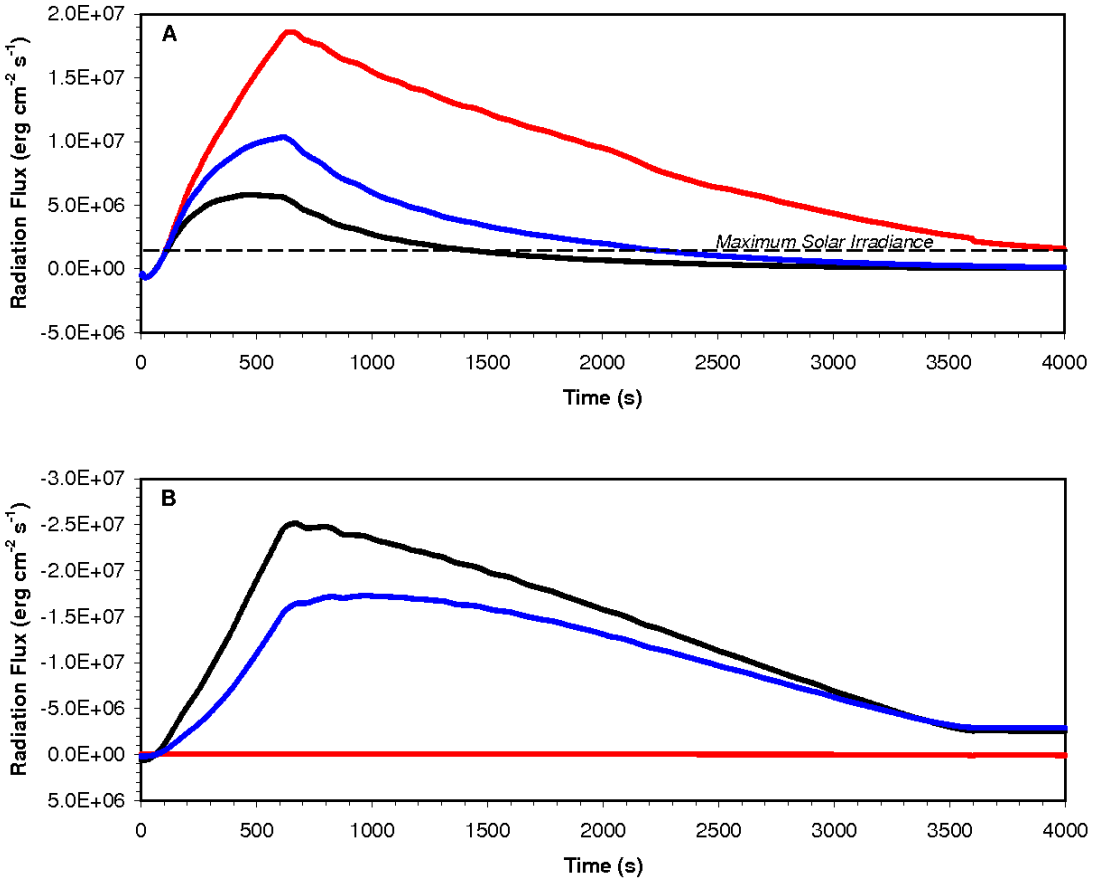

Figure 33. Thermal radiation flux at the ground (a) and to space (b) for the nominal Chicxulub pulse of ejecta if the upper model boundary transmits all radiation to space (black), reflects 50% (blue), or reflects 100% (red). Upward fluxes are negative.

It is possible that the larger spherules drag some portion of the dust downwards and determining the effect of fine dust on thermal radiation transfer may not be as simple as described above. Unfortunately, KFIX-LPL cannot accommodate multiple particle sizes in a single cell and the physical interactions between dust and spherules cannot

modeled at this time. Using a reflective upper boundary yields an upper limit of a dust cap; a realistic Chicxulub model will require both better-constrained dust volume estimates and consideration of dust-spherule interactions in the upper atmosphere.

6.7 The Thermal-Sheltering Hypothesis

Understanding the effects of a thermal pulse following Chicxulub on terrestrial organisms is quite complex due the wide variety of skin properties, internal physiologies, and insulating covers like fur and feathers. Human skin is essentially a blackbody at the wavelengths of infrared radiation, absorbing 97% of radiant heat from sources <1500º C (Hymes et al., 1996). Complete epidermal necrosis occurs when the skin reaches a temperature of 52º C (Moritz and Henriques Jr, 1947). At a radiation intensity of 10 kW/m^2, unbearable pain occurs after 5 seconds and there is a 50% probability of death after a 100s exposure time (Hymes et al., 1996). In a more general model applicable to animals of different dermal thicknesses, Adair (in press) suggests that, at 6 kW/m^2 radiation intensities, skin will cross the necrosis threshold over the outer 1 mm after 20 seconds and over the outer 5 mm after 2 minutes. The epidermis is often important structurally for larger animals such as elephants and would be sensitive to thermal damage (Adair, in press). A 2-minute pulse of fluxes ~6 kW/m^2 seems quite plausible from our model results and may have been lethal to the thick-skinned dinosaurs, in addition to smaller thinner-skinned animals.

6.8 Conclusions

The same tiny particles that deposit a large amount of energy as they reenter the atmosphere at hypersonic speeds later, as they settle through the lower atmosphere, act to limit the transmission of thermal radiation to the ground. This self-shielding weakens the flux of thermal radiation reaching the Earth's surface and the effect strengthens as more spherules accumulate in the atmosphere. If spherules are the only type of ejecta entering the atmosphere, the resulting thermal pulse exceeds normal solar fluxes for less than half of the duration of spherule reentry and peaks at 6-12 kW/m^2. Given that previous calculations were already at the lower limit of wildfires, it seems unlikely that this thermal radiation intensity is sufficient to ignite most forms of biomass, particularly because the self-shielding by spherules makes sustaining a large thermal pulse difficult. However, the shortened pulse still attains fluxes 5-15 times the normal solar irradiance, if only for a few minutes, which may ignite non-woody vegetation such as grass, pine needles, fallen leaves, etc. and dry the forests making them more susceptible to fires. Additionally, ~7 kW/m^2 is analogous to an oven set to 'broil' and even a short thermal pulse of these magnitudes will have deleterious biologic effects on living animals. A few minutes at this intensity might cause enough dermal damage to be lethal to even the largest animals.

If spherules are the only type of ejecta reentering the atmosphere from the impact plume, our models suggest that the atmospheric reentry of ejecta shielded the planet from much of the damaging thermal energy and suppressed a global firestorm. However, an equal volume of submicron dust accompanying the spherules would act as an opaque cap

in the upper atmosphere, reflecting much of the upward thermal radiation downwards and increasing the magnitude and duration of high thermal fluxes at the surface to the lower limits of forest fire ignition.

Our models treat the spherules as perfectly opaque (blackbody absorbers/emitters), but, if the spherules are glassy and quite transparent to the infrared radiation, the self-shielding effect is prevented (Adair, in press). However, a nearly transparent spherule (ε=0.05) cannot emit its thermal energy as efficiently and would reach temperatures >3000 K leading to ablation upon atmospheric reentry, inconsistent with preservation of spherules and their crystalline structures at K-Pg boundary localities. Another mechanism to override spherule self-shielding is a heterogeneous distribution of distal ejecta by impact plume expansion (Kring and Durda, 2002) which might leave clear windows through the mesosphere with few spherules through which downwards thermal radiation may be concentrated.

CHAPTER 7

THERMAL RADIATION FROM THE ATMOSPHERIC REENTRY OF IMPACT EJECTA

7.1 Introduction

From July 16 through July 22, 2004, the world watched as pieces of the comet Shoemaker-Levy 9 (SL9) collided with Jupiter. It was the first observed collision between two planetary bodies and presented a unique opportunity not only to observe the impact cratering process, but also to study the effects of a rapid deposition of energy into a planetary atmosphere. As each fragment of the 1.5-km diameter comet crashed into Jupiter, telescopes on Earth viewing at infrared wavelengths detected a sequence of three flashes. The typical light curve for an SL9 event had two subtle and brief peaks followed by a third peak, which was brightest and longest-lasting (Graham et al., 1995; Nicholson et al., 1995; Zahnle, 1996). The first peak represented the entry of the cometary fragment into Jupiter's atmosphere culminating in the explosion of the fragment, the second peak represented the formation and expansion of a hot impact plume, and the third peak represented the impact plume falling back into the Jovian atmosphere (Graham et al., 1995; Nicholson et al., 1995; Zahnle, 1996). The third peak was typically first detected ~5 minutes after impact and endured for another 10-15 minutes (Hammel et al., 1995) as the plume ejecta descended into the atmosphere. The plume material fell from heights of up to 3000 km and at velocities of 10-12 km/s (Hammel et al., 1995) over a radius >18,000 km from the impact site (McGregor et al., 1996).

The most spectacular flash was not from the collisions of the cometary fragments or the resulting fireballs of melted and vaporized ejecta; rather, it was what happened *after* each impact event that put on the big show. Traveling at hypersonic speeds and carrying a large fraction of the impact energy (20-40%, Zahnle, 1996), the SL9 impact plume ejecta emitted a large amount of energy as infrared thermal radiation over an area wider than Earth and showed the world that thermal radiation from the atmospheric reentry of impact ejecta is an important consequence of impacts into planets with atmospheres.

*****

On the last day of the Cretaceous, 65 million years ago, a ~10-km diameter bolide collided with the submerged carbonate platform of the Yucatán peninsula creating a ~180-km diameter crater and transporting ejecta around the globe. The ejecta deposit at the Cretaceous-Paleogene (K-Pg) boundary was first discovered by Alvarez et al. (1980), who, based on elevated levels of iridium, proposed that a giant impact was responsible for the end-Cretaceous mass extinction. The subsequent search for the source of the impact ejecta led to the discovery of the now-buried Chicxulub crater (Hildebrand et al., 1991).

Chicxulub ejecta deposits have been found at the K-Pg boundary at sites around the world. At distal sites greater than 7000 km from the Chicxulub crater, the thickness of the ejecta layer is a fairly uniform 2-3 mm and is composed primarily of densely packed spherules (or *microkrystites* due to their relict crystalline texture) with a mean size of 250 µm (Smit, 1999). The extraterrestrial signature of the spherules' composition,

such as iridium enrichment and Ni-rich spinels, indicates an origin from the impact plume (Ebel and Grossman, 2005; Kyte and Smit, 1986), which was originally composed of a mixture of vaporized and melted projectile and target materials (Melosh, 1989). It is believed that the spherules condensed from the impact plume as it expanded and cooled and reentered the atmosphere on ballistic trajectories (Melosh and Vickery, 1991). Projectile-enriched ejecta is also found in localities more proximal to Chicxulub, but here interpretation is complicated by additional projectile-poor ejecta curtain material in the K-Pg deposits. In this study, we are concerned with only the impact plume material, which contained most of the energy of the impact (Melosh, 1989) and deposited this energy in the atmosphere at hypersonic velocities. A 3-mm thick ejecta layer may not seem like much, but the total mass of spherules corresponding to a global 3-mm thick layer, assuming atmospheric reentry at 5-10 km/s, would deposit a total energy of 1.3-5 × 10^{15} J/m^2 in the atmosphere[3] (Melosh et al., 1990). Much of this would be radiated from the spherules during deceleration in the atmosphere producing a thermal pulse, much like what was observed following the impact of SL9 into Jupiter.

Although some of this energy would be radiated to space, like the thermal radiation detected from SL9, some proportion would be radiated towards the ground and, as we saw in Chapter 6, understanding the magnitude and duration of such a thermal pulse at the Earth's surface has important environmental implications. Reports of soot within

[3] The Melosh et al. (1990) energy and thermal radiation calculations were based on the thickness of the ejecta layer (3 mm) and assume the total volume of the ejecta layer is composed of 500 µm spherules. Our study uses more recent data on spherule concentration (20,000 spherules/cm^2) and average spherule size (250 µm) from the most undisturbed distal K-Pg localities to date (Smit 1999). Our models deposit ~50% less energy dispersed into spherules of half the size as the Melosh et al. calculations.

K-Pg boundary ejecta deposits (Wolbach et al., 1990; Wolbach et al., 1988; Wolbach et al., 1985) are interpreted by some as evidence for global wildfires triggered by such a thermal pulse (Melosh et al., 1990; Robertson et al., 2004; Wolbach et al., 1990). The differential survival of species in the terrestrial fossil record is also consistent with the ability of animals to seek shelter from an extreme thermal pulse (Robertson et al., 2004). The potential for severe thermal damage to the biosphere underscores the need to understand the production and fate of thermal radiation from the atmospheric reentry of impact ejecta.

There have been several attempts to quantify the thermal pulse received by the Earth's surface following Chicxulub. Calculations by Melosh et al. (1990) predicted a power deposition to the atmosphere on the order of 50 kW/m^2 over one or two hours, most of which would be radiated as thermal energy at temperatures between 1000 and 1500 K. They predicted that a third of this thermal energy would reach the surface; the rest would be either absorbed by the atmosphere or radiated upwards to space. Toon et al. (1997) calculated, for a Chicxulub-sized impact, a thermal pulse at the surface exceeding 10 kW/m^2 for >20 minutes globally. Other calculations (Durda and Kring, 2004; Kring and Durda, 2002) suggest a heterogeneous distribution of impact plume ejecta, but still predict >10 kW/m^2 at the surface for >20 minutes over much of the globe.

These calculations all use different approaches to compute the rate of spherule reentry from a ballistically expanding impact plume and the resulting energy deposition to the atmosphere, but all employ the same simplified approach to thermal radiation: half is radiated upwards and lost to space and some portion of the remaining downward radia-

tion is absorbed in the lower atmosphere by greenhouse gases. While the presence of the spherule layer at the K-Pg boundary is evidence for the large amount of energy that was deposited in the atmosphere during reentry, the fate of that energy is more complicated. In Chapter 6, we showed that the spherules themselves, in addition to greenhouse gases, absorb a significant portion of the downwards thermal radiation as they slowly settle through the lower atmosphere. In this chapter, we explore in detail the effect of self-shielding by spherules as a mechanism limiting the thermal effects at the Earth's surface. We present a series of numerical models of atmospheric ejecta reentry in which both the rate of energy deposition to the atmosphere and the properties of the spherules are varied in order to assess the roles that spherules, air, and interactions between them play in the transfer of thermal radiation through the atmosphere. The focus of this study is Chicxulub, due to the important environmental implications and the wealth of information about its ejecta deposits, but the trends discussed here can be applied to other large impacts into planets with atmospheres.

7.2 Thermal Radiation Theory and Numerical Approach

Thermal radiation is electromagnetic energy emitted as photons from the surface of an object due to its temperature. Although we commonly hear about the thermal radiation from hot objects, such as the sun (or, in this case, hot ejecta particles), all matter emits thermal radiation at all temperatures, at all frequencies, and at all times (Bohren and Clothiaux, 2006). Both the amount of energy radiated from a body ($\sim T^4$) and the

wavelength associated with the maximum emitted intensity (λ_{max}(nm) = 2.897 × 10^6 /T(K)) depend on the body's temperature. The maximum amount of thermal radiation possible for a given temperature is the *black-body radiation*. Likewise, a body that radiates the maximum possible intensity of radiation for every wavelength at a given temperature according to the Planck function and completely absorbs all incident radiation is called a *black body*. This is an idealization and the absorption and emission of thermal radiation by real bodies is always less than this. The spectral *emissivity*, ε, is the fraction of energy emitted by a body compared to a black-body, which is multiplied by the Planck function to yield the *radiance* (per unit frequency). The spectral *absorptance*, α, of a body is the fraction of energy that is absorbed and is, by Kirchoff's law, equal to the emissivity for a given temperature and frequency.

Integrating the spectral radiance as defined by the Planck Function over all frequencies and over a hemispherical area yields the *irradiance* (or thermal radiation flux density), $\boldsymbol{S}$ (W/m^2), which is the power per unit area at some location and at a direction normal to a defined surface. For a black body, which emits and absorbs radiation isotropically, the irradiance at a given temperature, T, is defined by the Stefan-Boltzmann Law:

$$\boldsymbol{S} = \sigma T^4 \qquad [7.1]$$

where σ is the Stefan-Boltzmann constant (5.671 × 10^{-8} W m^{-2} K^{-4}).

Radiative transfer in the atmosphere is generally either from solar (short-wave) photons emitted from the Sun's photosphere or from thermal (long-wave) photons emitted by the atmosphere or ground (Andrews, 2000; Seinfeld and Pandis, 1998). The radia-

tion emitted by the Sun's photosphere, which spans wavelengths between 0.1-4 µm (ultraviolet, visible, infrared) approximates that of a black body at ~6000 K where the maximum intensity occurs in the visible portion of the spectrum (~0.5 µm). The Earth's surface approximates a black body at ~300 K, emitting radiation in the invisible infrared portion of the spectrum with a dominant wavelength of ~10 µm. Because the irradiance increases as a function of T^4, the sun radiates almost 2×10^5 times more energy per unit area than the Earth.

Now consider a single spherical particle entering the atmosphere with hypersonic velocity, decelerating, heating up in excess of 1000 K, and emitting that energy as infrared thermal radiation. If we assume that the particle behaves like a black body ($\varepsilon = \alpha = 1$), then the thermal radiation flux from the hot particle is approximated by the Stefan-Boltzmann Law. If we assume the particle emits energy isotropically, then half of the thermal radiation is emitted upward and the rest is emitted down towards the ground.

In an atmosphere void of absorptive gaseous species, this would be the end of the calculation and all of the thermal energy radiated downwards would reach the surface. However, absorbing greenhouse gases exist which reduce the downward thermal radiation, particularly at certain wavelengths. Infrared absorption is strong in bands around 2.7 µm, 6.3 µm, and 16 µm due to water vapor and 43 µm and 15 µm due to carbon dioxide (Andrews, 2000). Absorption by ozone occurs in a narrow band around 9.6 µm (ozone absorption is mostly important for ultraviolet and visible radiation). A radiation temperature of 1000-2000 K would have a dominant wavelength of ~1.5-3 µm, at a frequency range in which absorption by H_2O and CO_2 is significant.

For a single particle, or for a dispersed group of particles such that the mean free path through them is long, it is sufficient to only consider the particles as black body emitters. However, as Kirchoff's Law states, a particle with a certain emissivity has the same absorptivity and if the particles are densely packed and the mean free path reduced, the thermal radiation emitted from one particle might encounter another particle and be reabsorbed or reflected. Our KFIX-LPL models of Chicxulub ejecta reentry show that the spherules accumulate in an increasingly dense cloud at ~70 km in altitude after losing their initial high velocities. The downward thermal radiation from the decelerating spherules in the upper atmosphere will be increasingly absorbed by the settling spherules below. Thus, the contribution of opacity from both greenhouse gases and the spherules must be considered in a radiative transfer model. This makes the problem computationally much more difficult and requires a numerical model to compute the transfer of thermal radiation through the atmosphere following a large impact.

7.2.1 Thermal Radiation Model

We couple a thermal radiative transfer model, which calculates the radiation energy density throughout the model atmosphere, to the KFIX-LPL model for ejecta reentry. The thermal radiation model (see Appendix C) uses a diffusion approximation for radiative transport (based on Zel'dovich and Raizer, 1967) which yields a relation between the radiation flux density $\boldsymbol{S}$ and the gradient of thermal energy density U:

$$S = \frac{-c}{3\kappa}\nabla U = \frac{-lc}{3}\nabla U \qquad [7.2]$$

where κ is the optical opacity and $l = 1/\kappa$ is the optical mean free path.

The spherules are distinguished from the air, as they are in KFIX-LPL, and each phase has a separate radiation absorption coefficient which contributes to the overall opacity in any computational cell. We assume liquid or solid mafic silicate droplets are nearly perfect absorbers of thermal radiation at infrared frequencies and approximate their emissivity as 1, although this coefficient can also be varied if the particles are more transparent to thermal radiation. The volume fraction of air, θ, and the volume fraction of spherules, 1-θ, are computed in KFIX-LPL for each computational cell. Since we are assuming that the spherules are black-body emitters/absorbers, only their cross-sectional surface area, which radiation travelling in some direction would encounter, contributes to their opacity. The opacity κ_s (g/cm^2) of spherules of radius a in a single cell is

$$\kappa_s = \frac{3(1-\theta)}{4a} \qquad [7.3]$$

The opacity of the air can be approximated using averages over the spectral line population. A "Rosseland mean opacity" is defined as the opacity of a gas at a given composition, temperature, and density averaged over the range of wavelengths of the thermal radiation being absorbed and scattered (Ridpath, 1997). It assumes the incident thermal radiation is in thermal equilibrium with the gas (has a blackbody spectrum) and is useful for calculating the total energy absorbed over all wavelengths, such as in stellar interior calculations or other problems of radiation hydrodynamics. In the diffusion regime, we can replace the complex opacity spectrum of a gas by this single average, which yields the correct radiative energy transport and momentum balance (Mihalas and Weibel-Mihalas, 1999). A Rosseland mean opacity for air was computed using modern

tropical atmospheric absorption profiles (Goody, 1964). The absorption by greenhouse gases is fixed for a given frequency, but the blackbody spectrum of the emitted thermal radiation changes as a function of spherule temperature-- according to the Planck Function-- and so the Rosseland mean opacity also depends on temperature. The average opacity of air κ_a (g/cm^2) is calculated to be

$$\kappa_a = \frac{\rho_a \theta}{(1200 + 3.1\times10^{-4} T_{\max}{}^2)} \qquad [7.4]$$

where ρ_a is the air density (g/cm^3) and T_{max} is the radiating temperature of the spherules in Kelvins. This approximation allows us to ignore the wavelength dependence of the thermal radiation and simply calculate the total absorption by the air phase at all wavelengths. Differences in greenhouse gas content between the modern and late Cretaceous atmosphere, variations in water content at different latitudes and for different seasons, local weather and clouds, and possible contributions by impact-produced greenhouse gases were not considered. A better understanding of the ranges of absorbing gas concentrations following Chicxulub is needed for a more realistic Rosseland mean opacity.

The thermal radiation model permits four types of boundary conditions, which can be imposed on any boundary of the model mesh. These include (1) a fixed temperature boundary where the energy density on the boundary is equal to the Planck energy density for a specified temperature, (2) a fixed radiation flux boundary where the gradient of the energy density is held constant, (3) a reflection boundary which ranges from 100% reflection at all frequencies to 100% absorption at all frequencies, and (4) periodic boundaries.

The radiation model was implemented in KFIX-LPL. The routine is called at the end of each computation cycle, at which point it computes the instantaneous thermal radiation balance using the temperatures and densities of both spherule and air phases. A solution for the diffusion approximation of radiative transport (Zel'dovich and Raizer, 1967) is attained via a successive over-relaxation technique (Press et al., 1996 p.860) in which the radiation energy densities of all the cells in the mesh are recalculated iteratively until a solution converges to the desired accuracy. This solver can be quite computationally expensive because higher resolution requires more iterations for convergence. An alternate radiation solver using a multi-grid algorithm (Press et al., 1996 p.869), in which the radiation field is determined over a succession of increasingly finer meshes, has also been developed. This solver requires a square mesh, which also is computationally expensive at the resolution required for the Chicxulub reentry problem. If ejecta reentry is homogenous across the top of the model mesh, a tall skinny mesh is sufficient and the successive over-relaxation algorithm is preferred. However, the multi-grid solver may be preferable in other problems where a wider mesh is needed.

The radiation model and KFIX-LPL are coupled in the energy balance, which accounts for the energy gained by absorption or lost by emission by each phase in each cell for each computational cycle.

7.3 Modeling

We modeled the thermal radiation transfer throughout the atmosphere for the duration of atmospheric spherule reentry. The initial mesh approximates a 150-km high slice of normal Earth's atmosphere with an exponential pressure gradient, average properties of air, and ideal gas law behavior. For simplicity, the initial atmosphere is also assumed to be isothermal (273 K). Spherical particles of some size are injected uniformly across the top of our model atmosphere at some angle and velocity. The spherules have the properties of basaltic glass (approximately the average composition of Chicxulub spherules) and are treated as a simple incompressible fluid dispersed into discrete spherical droplets. The spherules are injected with a mass flux rate that can vary with time according to the desired model of reentry from the expanding impact plume.

The physical model employs periodic boundary conditions on the left and right mesh boundaries, a free slip boundary on the bottom (ground) and an inflow boundary on the top into which the spherules are injected. The radiation model also employs periodic boundaries on the left and right sides. The bottom of the mesh has a fixed temperature boundary (273 K) to approximate conditions at the surface and the top of the mesh has a boundary that is 100% absorptive (all incident thermal radiation is removed from the mesh, i.e. 'lost to space'). Due to the periodic boundaries and the fact that spherules are injected uniformly across the top of the mesh, the radiation solution is not dependent on the width of the mesh and it is sufficient to use a mesh only a few cells wide. The models presented in this study use a mesh 600 cells high and 5 cells wide with a resolution of 250 m, which has been determined to be sufficient to resolve density (and hence opacity) variations across the mesh and yield an accurate solution for the surface irradiance (Ap-

pendix D). Each model was run out to 4000 s, which required ~2 days of computing time on a Mac Pro machine with 3.2 GHz quad-core Intel Xeon processors.

The thermal energy radiated from a black-body emitter is strongly dependent on the radiating temperature. Accurately calculating the maximum spherule temperature requires an understanding of how the spherules decelerate (drag coefficient) and how heat is exchanged between phases via frictional heating or conduction (heat transfer coefficients). KFIX-LPL includes algorithms for computing the drag coefficient and heat transfer for flow conditions encountered by ejecta, which range from reentry into the thin upper atmosphere at high velocities (free molecular flow) to settling through the denser lower atmosphere (Stokes/turbulent flow). For a complete description of these terms see Chapter 3 and Melosh and Goldin (2008).

In our simulations we increase and then decrease the rate of spherule mass flux reentry linearly. The mass flux as a function of time plots as a triangle, where the base of the triangle is the total duration of spherule reentry and the height of the triangle is the peak spherule flux. The triangle's area represents the total mass of spherules injected into the model atmosphere (for Chicxulub, this is equal to the mass of spherules deposited at the K-Pg boundary). For a triangle of a given height and width, the slopes on either side of the peak flux represent the rate at which the mass flux increases and then decreases and depend on the time at which the peak flux occurs. Employing this simple triangular pulse of spherules allows us to easily change the dimensions of the pulse and examine the effect on the thermal pulse at the Earth's surface. In addition to changing the number of spherules injected into the atmosphere at any time, we can vary properties

affecting the energy delivered by individual spherules such as the reentry velocity and angle as well as spherule size.

We compare each model to a nominal Chicxulub run (see Chapter 6) in which a total mass density of 0.5 g/cm^2 of 250-µm spherules (average mass and size of spherules in the K-Pg distal ejecta deposits; Smit, 1999) reenters the model atmosphere at 8 km/s (average reentry velocity; Melosh et al., 1990) obliquely at 45 degrees. Ejecta reentry lasts for one hour with maximum spherule flux at 10 minutes—a triangle pulse which roughly approximates the pattern of ballistic reentry calculated by Melosh et al. (1990) where the area of the triangle is the mass density of spherules at the most undisturbed localities according to Smit (1999).

7.4 Model Results from Ejecta Reentry Scenarios

For a simulation of Chicxulub-sized spherules reentering the atmosphere at 8 km/s (the nominal Chicxulub model presented in Chapter 6), the spherules streak into the upper atmosphere at hypersonic velocities, decelerating due to drag in the increasingly dense air. The spherules decelerate to terminal velocity at ~70 km in altitude and continue to settle towards the ground. Because drag forces act primarily in the vertical direction, if the spherules enter the atmosphere obliquely much of the horizontal velocity component of the original high velocities will remain. In this case, the zone of spherule accumulation below 70 km experiences strong horizontal winds on the order of several

kilometers per second while the spherules are much more slowly settling downwards under gravity.

As the spherules decelerate, kinetic energy is converted to heat and this heat is efficiently radiated from the surface area of the spherules as infrared radiation. The spherules reach a maximum temperatures of 1600 K initially, but peak spherule temperatures decline to ~1250 K after ~10 minutes and then slowly increase to ~1300 K over the remainder of spherule reentry. This variation is due to spherule-air interactions in the upper atmosphere: friction between the spherules and air compresses the upper atmosphere and changes in the density structure of the upper atmosphere in turn affects the deceleration of subsequent spherules. Some of the thermal energy is transferred to the air via conduction, and because air is not able to readily radiate its heat, the temperature of the upper atmosphere increases throughout spherule reentry reaching temperatures in excess of 3000 K.

The spherules, however, are able to radiate their heat as infrared radiation. 1300-1600 K is near the melting point of the mafic spherules (>1473 K, depending on composition), but because the ratio of surface area to volume is high for small particles, the spherules will not retain such high temperatures very long and very little mass is expected to be lost via ablation. The preservation of spinel and feldspar crystallites, which are products of condensation in the impact plume, are evidence against complete remelting of spherules during atmospheric transport and agree with the peak temperatures in the KFIX-LPL models. The spherules are assumed to be black bodies and the emission of thermal radiation from the hot spherules is a function of their radiating temperature as

described by the Stefan-Boltzmann Law. Part of the thermal radiation escapes to space, part is absorbed by greenhouse gases in the lower atmosphere, part is absorbed by previously injected spherules settling below 70 km in altitude, and the remaining downward thermal radiation reaches the Earth's surface.

Varying the input parameters shows the effect that each of these parameters has on the strength of self-shielding by spherules and on the proportion of the thermal radiation emitted by the decelerating spherules that reaches the Earth's surface. The surface irradiance is determined by the balance between the rate at which energy is deposited into the upper atmosphere and the rate at which the thermal radiation is absorbed by greenhouse gases and the spherules below.

7.4.1 Time to Peak Flux

Holding the duration of spherule reentry (60 min) and total mass of spherules (0.5 g/cm^2) constant, we first vary the time at which peak spherule mass flux occurs. Because the width and area of the reentry triangle are constant, the height of the triangle—peak mass flux—is constant as well. The earlier peak flux occurs, the faster spherule mass flux increases prior to peak flux and the slower spherule mass flux declines afterwards. This scenario was introduced in section 6.3 and is now explored in more detail.

Five simulations, ranging from reentry initiating at peak mass flux and slowly building up to peak mass flux after 50 minutes, were compared (Figure 34). Despite identical magnitudes of peak mass flux in all simulations, the peak thermal radiation flux

at the ground is dependent on how quickly that peak mass flux is attained. The surface receives a thermal radiation dose up to ~12 kW/m^2 if spherule reentry begins immediately at maximum mass flux. If the time to peak spherule reentry is 10 minutes, at which point one-sixth of the total spherule mass has entered the atmosphere, the maximum thermal flux at the ground is halved to ~6 kW/m^2. For an even later occurrence of peak mass flux (>10 min), although this is less physically plausible based on impact plume expansion models (Kring and Durda, 2002; Melosh et al., 1990), the surface irradiance is further reduced. The slower the increase in mass flux to the atmosphere, the greater the opacity contribution by spherules at any given mass flux, the greater the effect of self shielding, and the smaller the fraction of thermal energy reaching the Earth's surface.

Unlike at the ground, where the thermal pulse is truncated in both magnitude and duration by spherule self-shielding, the thermal radiation pulse exiting the top of the model atmosphere is approximately half the power deposition in the upper atmosphere. The peak flux to space is 22.5 kW/m^2 if peak spherule reentry begins immediately and is equivalent to 50% of the peak energy flux. The radiation flux to space increases slightly to ~28 kW/m^2 if peak mass flux occurs at 50 minutes. This is explained by half of the downwards thermal radiation absorbed by the shielding spherules below being reradiated upward. The strength of the self shielding effect determines how much excess thermal radiation will escape to space.

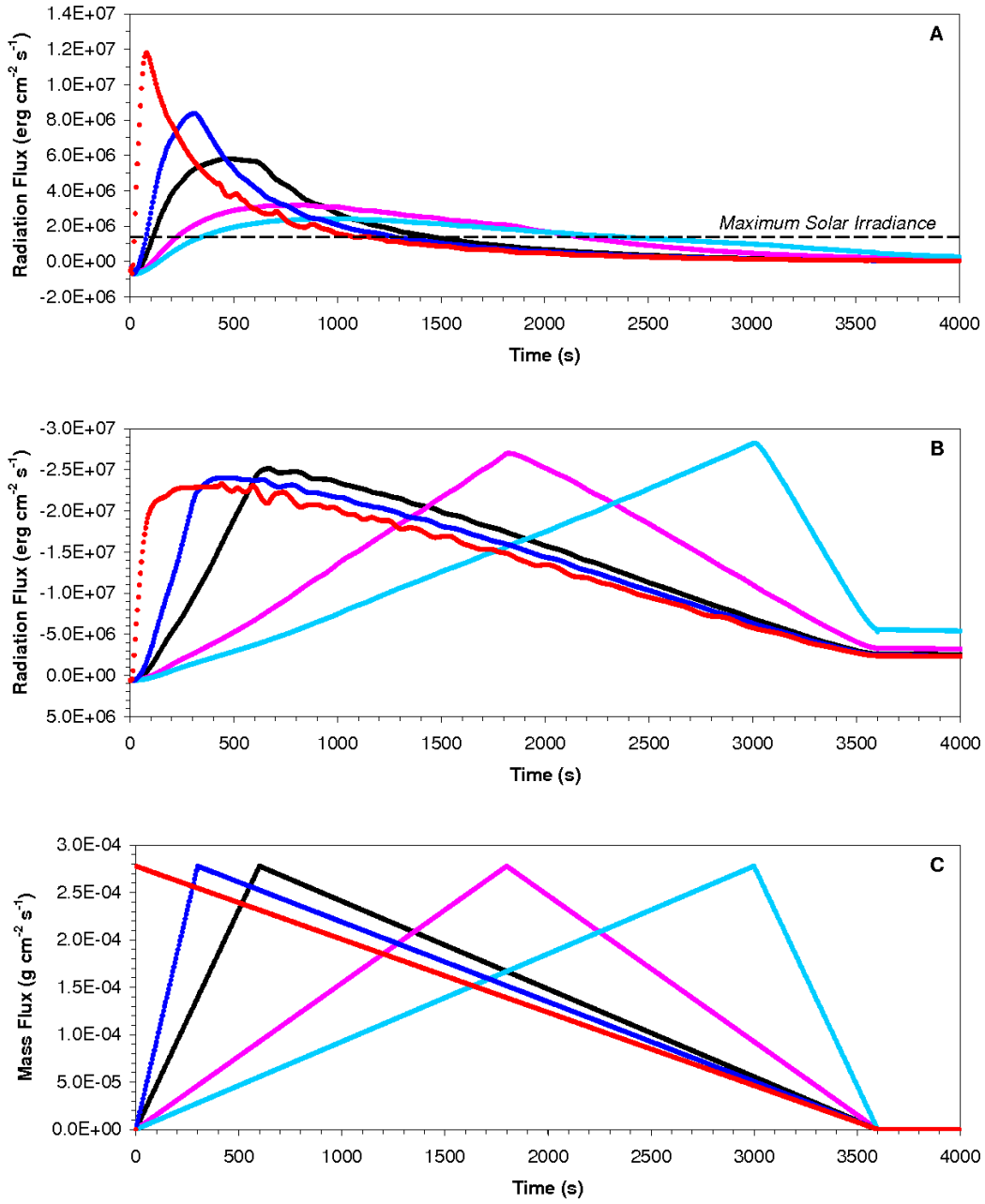

Figure 34. Irradiance as a function of time at the ground (a) and to space (b) if the time to peak spherule mass flux is varied while holding the total duration and spherule mass constant (c). Peak mass flux occurs after 0 min (red), 5 min (blue), 10 min (black= nominal Chicxulub run), 30 min (pink), and 50 min (light blue). Upward radiation fluxes are negative.

7.4.2 Duration of Spherule Reentry

Although previous calculations of ballistic impact plume expansion predict spherule reentry over one hour or more, a characteristic time interval of ~20 minutes has been suggested for the delivery of the bulk of the spherules (Melosh et al., 1990; Toon et al., 1997). Assuming constant total spherule mass (0.5 g/cm^2) and time of peak spherule reentry (10 min), the total duration of the pulse was varied between 15 minutes and 2 hours (Figure 35). Because the same spherule mass is delivered to the atmosphere in every simulation, shortening the duration of reentry increases the peak mass flux and the slopes of the mass flux triangle. The peak mass flux in the 15-minute long spherule pulse is four times greater than that of the hour-long pulse. Quadrupling the power deposition to the upper atmosphere results in quadrupling the thermal energy radiated upwards to space (~100 kW/m^2 vs. ~25 kW/m^2). However, only twice as much thermal radiation reaches the ground (~13 kW/m^2 vs. ~6 kW/m^2). Peak radiation flux at the ground occurs earlier for shorter, stronger spherule pulses despite the fact that peak spherule flux occurs at the same time in all simulations. At the time of peak spherule mass flux, 4 times more spherules have entered the atmosphere in a 15 minute pulse versus a 60 minute pulse, and the shielding effect of the spherules is much stronger.

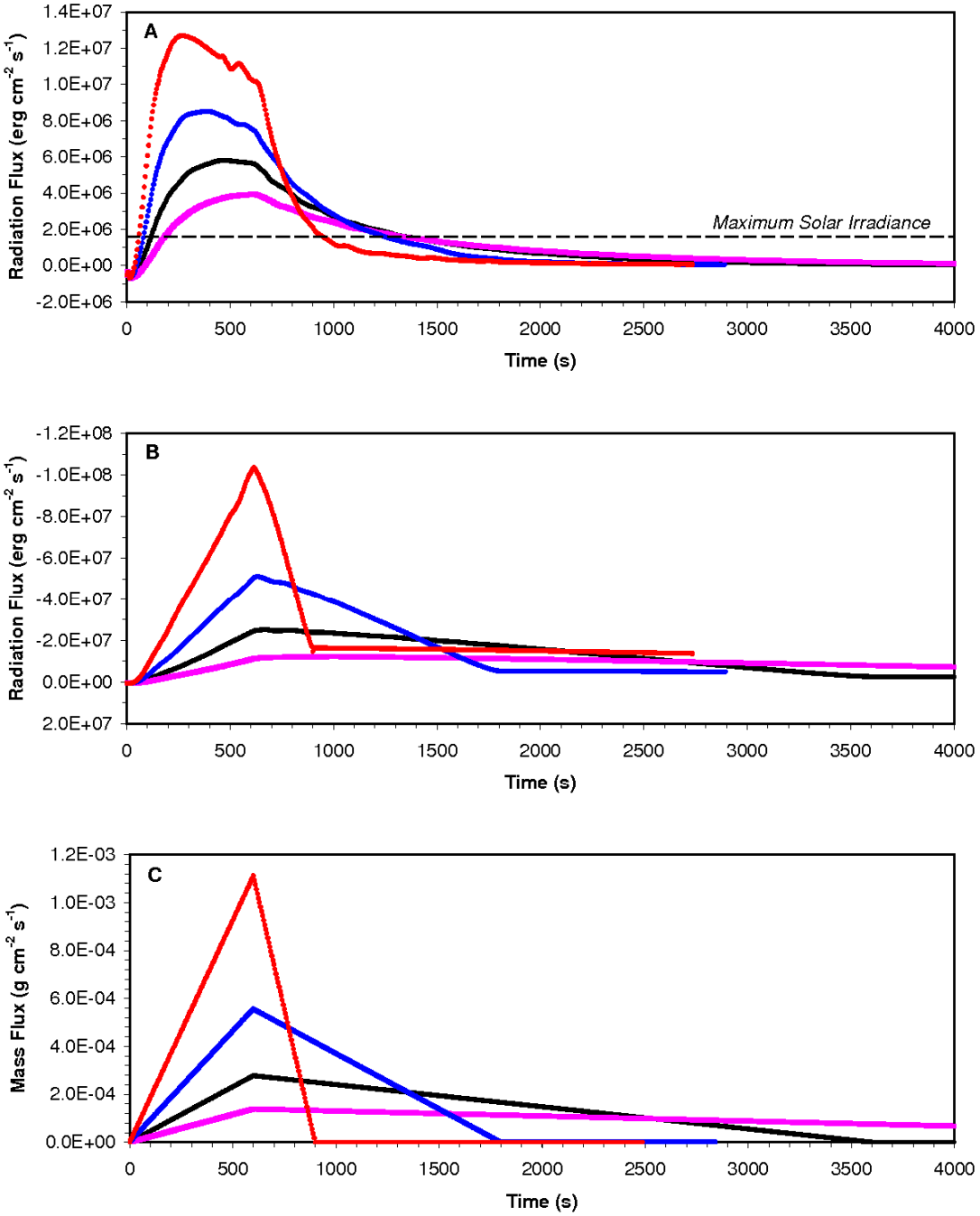

Figure 35. Flux of thermal radiation at the ground (a) and to space (b) where the duration of spherule reentry is varied: 15 min (red), 20 min (blue), 60 min (black), and 120 min (pink). The spherule mass flux to the upper atmosphere (c) is determined assuming constant total mass of spherules and time of peak reentry. Upwards radiation fluxes are negative.

7.4.3 Total Spherule Mass

For Chicxulub, the total amount of spherules which reenter the atmosphere is constrained by the spherule content of K-Pg boundary deposits which is fairly uniform at distal localities (Smit, 1999). It has been suggested that parts of the globe, such as areas more proximal to Chicxulub or the antipode, would have received more impact plume ejecta (Kring and Durda, 2002; Melosh et al., 1990). In addition, impacts of different sizes would eject various volumes of impact plume material so it is important to consider the effect that the total spherule mass density, which relates directly to the total energy density deposited in the upper atmosphere, has on the thermal pulse at the ground. The total spherule mass density was varied between 0.25 g/cm^2 and 2.0 g/cm^2, assuming constant duration of reentry (60 min) and time of peak reentry (10 min) (Figure 36). Hence, we varied the area of the "reentry triangle" while keeping its width constant, which implies that the height (maximum flux) and slopes (flux increase and decrease) change proportionally.

Until the decline of spherule reentry (>10 min), the thermal radiation fluxes to space and to the surface look nearly identical to those of the reentry duration tests. This is to be expected because the mass fluxes in both sets of tests are identical until peak reentry. After reentry, the rate at which spherule flux decreases is different because the decline of spherules is fixed to 50 minutes in these simulations, whereas it varies in the previous set of simulations. Comparison of Figure 35 and Figure 36 permits examination of the effect of spherule flux decline on the thermal pulse at the ground.

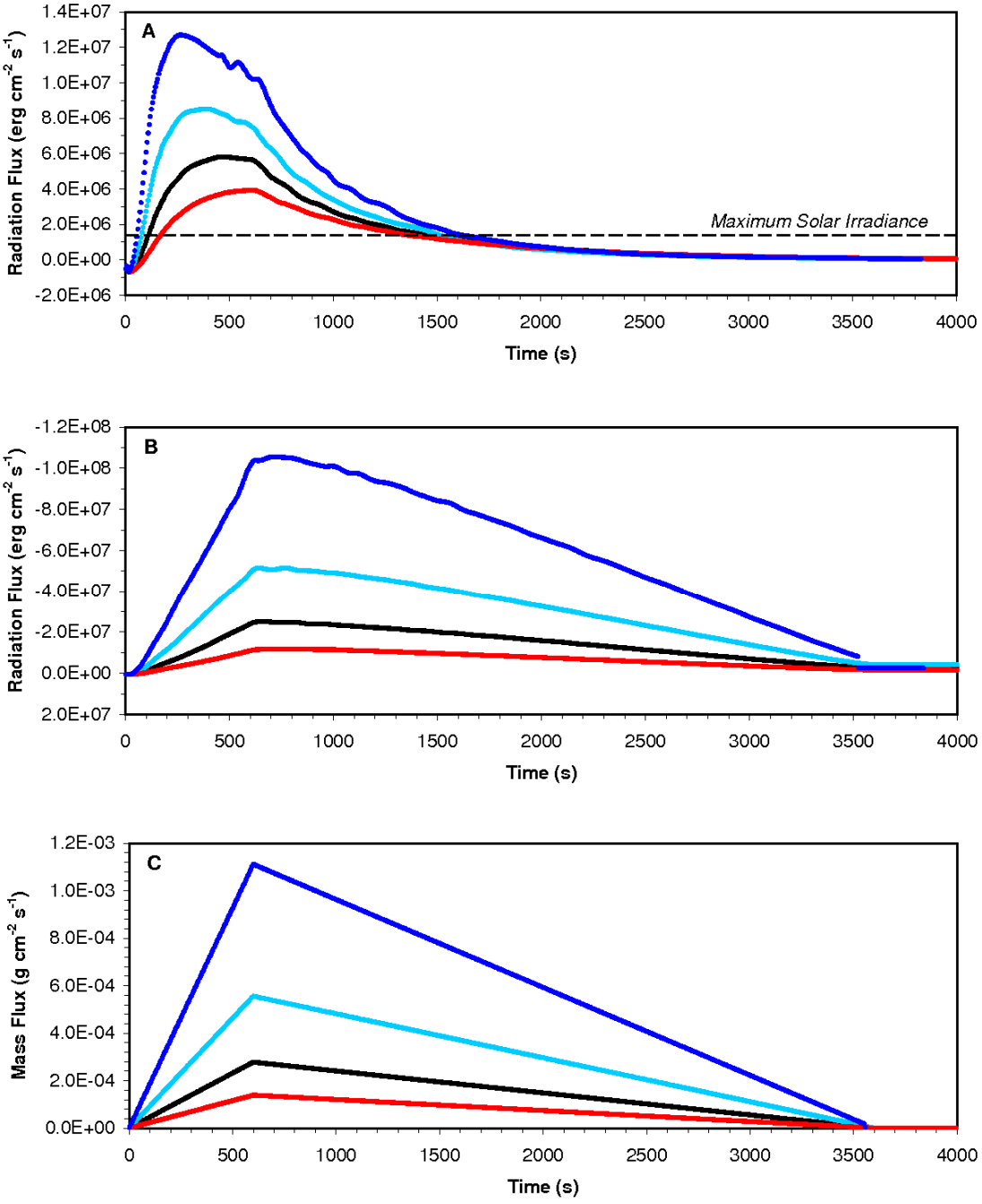

Figure 36. Thermal radiation flux at the surface (a) and to space (b) for spherule reentry mass fluxes (c) in which the total mass density of spherules injected into the atmosphere is varied: 2.0 g/cm^2 (blue), 1.0 g/cm^2 (light blue), 0.5 g/cm^2 (black), and 0.25 g/cm^2 (red). The duration of reentry and time of peak reentry is held constant. Upward fluxes are negative.

7.4.4 Spherule Size

Up to this point, we have assumed uniform 250 µm spherules (125 µm radius), which is the average spherule size in distal K-Pg localities (Smit, 1999). There is some natural variation in spherule sizes in the K-Pg ejecta deposits (<1 mm, (Smit, 1999)), which we are unable to model due to the inability of KFIX-LPL to handle different sized particles in the same computational cell. Spherule condensation models suggest that the characteristic spherule size is a function of impactor size (Melosh and Vickery, 1991). Not only is it important to consider the effect of spherule size on the thermal pulse for Chicxulub, but also for other impacts where different spherule size distributions may be produced. Changing the spherule size has two important consequences for the resulting thermal pulse at the ground: the radiating temperature changes (bigger spherules become hotter upon reentry and radiate more heat per spherule, although there are fewer spherules overall) and the opacity contribution of the spherules changes (the same volume of larger spherules contributes less opacity than that of smaller spherules).

We conducted a series of simulations with the same spherule mass flux for all runs (1 hour duration, peak flux after 10 minutes, 0.5 g/cm^2 total mass density), but varying the particle radius between 62.5 µm and 500 µm (Figure 37). Because the mass flux and reentry velocity is constant, the power deposition to the upper atmosphere at any time is the same for the entire set of simulations. Despite this, increasing the particle size leads to increased irradiance at the surface and decreased irradiance to space. For exam-

ple, 9 kW/m^2 of thermal radiation reaches the ground and 17 kW/m^2 escape to space when 1-mm sized spherules are used, in contrast to 6 kW/m^2 and 25 kW/m^2 for average Chicxulub 250-µm sized spherules. In addition, increasing the particle size shifts the peak irradiance at the ground towards the time of peak mass flux, causing the shape of the ground irradiance with respect to time to approach that of the power deposition to the atmosphere.

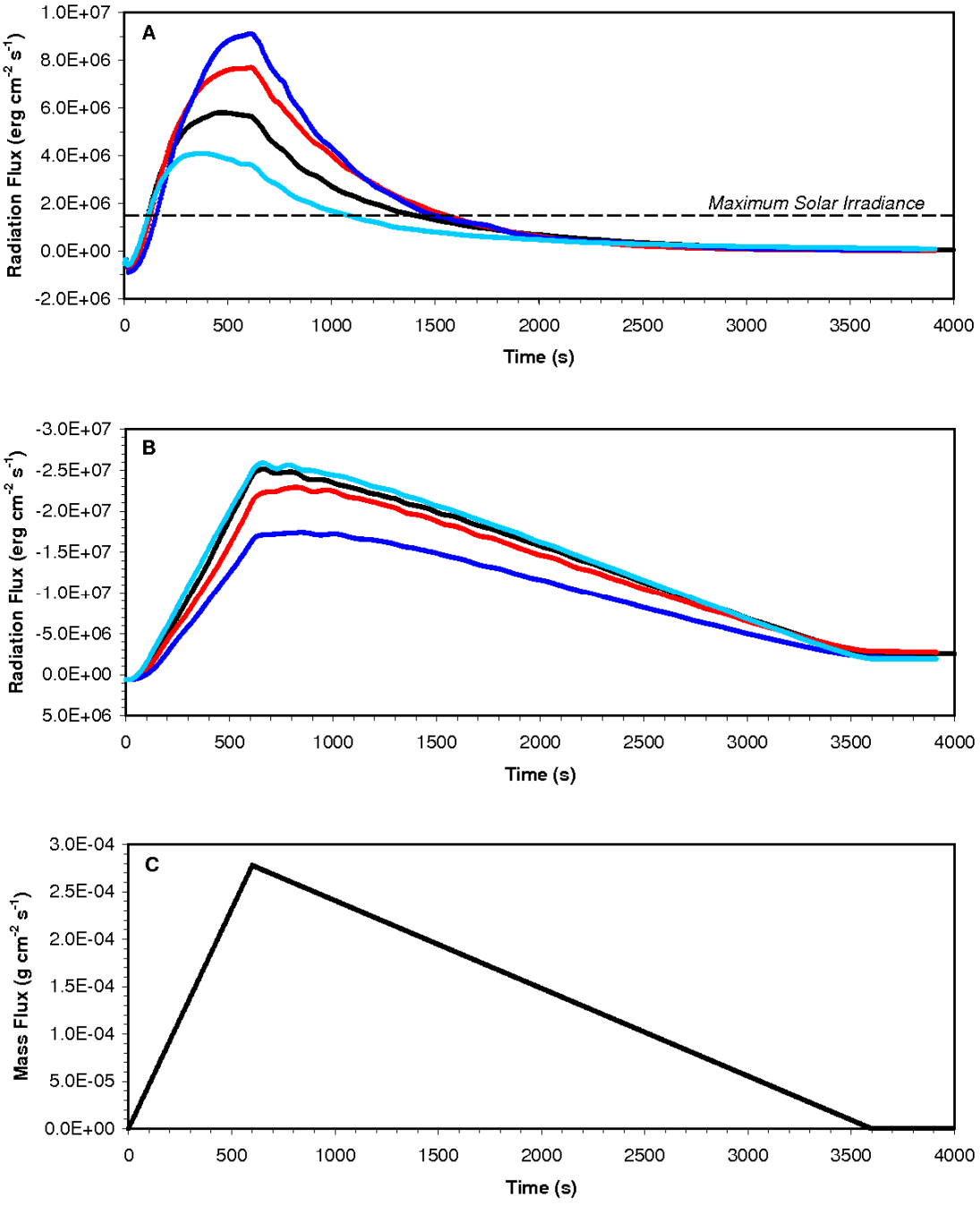

Figure 37. Thermal irradiance at the ground (a) and to space (b) as a function of time due to atmospheric reentry of particles with radii 62.5 µm (light blue), 125 µm (black), 250 µm (red), and 500 µm (blue). The mass flux throughout spherule reentry (c) is identical in all simulations. Upward radiation fluxes are negative.

7.4.5 Reentry Angle

Since all the spherules in a single computational cell must move uniformly, we are limited to a single angle of spherule reentry. However, impact plume ejecta is launched with a range of initial angles and ballistically reenters the atmosphere with the same range of angles (Melosh et al., 1990) due to conservation of angular momentum. In the simulations presented thus far, we assumed spherule entered at 45º. An additional set of simulations, which varied the reentry angle with respect to the horizontal from 90º to 30º (Figure 38), explored the effect that the incidence of spherule reentry has on the thermal pulse at the ground. While the peak surface irradiance from the nominal Chicxulub simulation with 45º reentry is ~6 kW/m^2, that for vertical reentry is ~13 kW/m^2. Steeper reentry angles also result in a thermal pulse at the ground which exceeds the maximum solar flux for a longer time interval, although the effects of self shielding are still evident. The thermal radiation flux to space more than doubles (~65 kW/m^2 vs. 25 kW/m^2) if vertical reentry is used. The steeper the angle of reentry, the greater the thermal pulse to both ends of the atmosphere.

Despite identical energy deposition in all simulations, the proportion of a spherule's kinetic energy that is converted to thermal energy depends on the reentry angle. The drag forces acting on a falling spherule decelerate the spherule's vertical velocity. Spherules that reenter the atmosphere obliquely retain most of the horizontal component

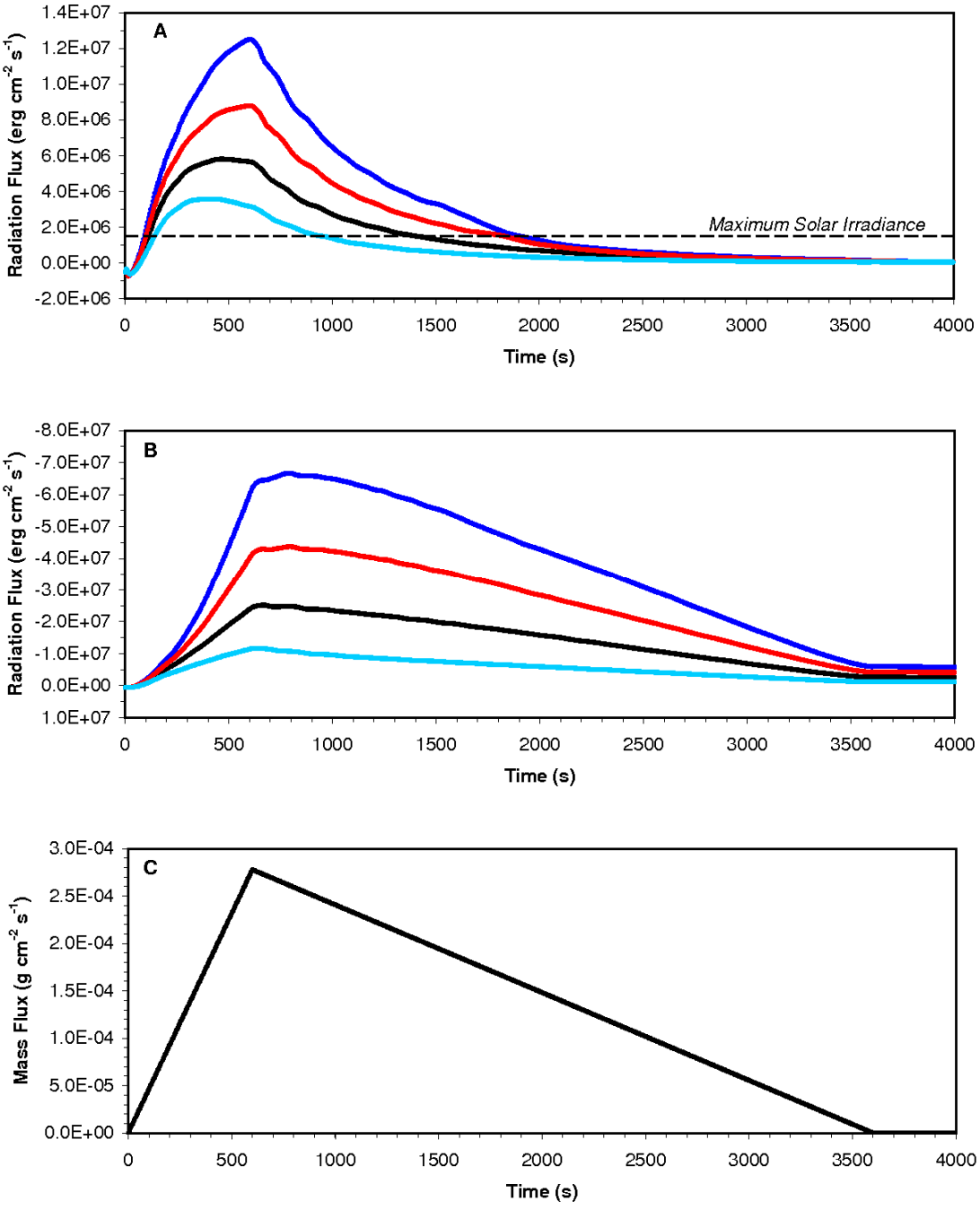

Figure 38. Thermal radiation flux at the ground (a) and to space (b) for model simulations where the spherules reenter at 30º (light blue), 45º (black), 60º (red), and 90º (blue) angles to the horizontal. The mass flux of spherules throughout the duration of reentry (c) is identical for all simulations. Upward radiation fluxes are negative.

of their velocity upon reaching their terminal vertical velocities because the upper atmospheric gases are accelerated by the horizontal component of the entry velocity. The smaller the vertical velocity component, the lower the radiating temperature and emission of thermal radiation. However, because the mass flux of spherules is unchanged between simulations, the number of spherules in the atmosphere at any time is constant for all reentry angles and the resulting opacities are similar. A more oblique reentry angle decreases the thermal energy radiated from the vertical deceleration of the spherules, but the absorption of that energy is the same regardless of angle. The reduction of irradiance at the ground and to space in more oblique instances is proportional to the reduction in thermal energy. The duration of the thermal pulse at the ground is reduced because the strengthening self-shielding effect increasingly dominates the thermal energy flux for lower reentry angles.

7.4.6 Reentry Velocity

In addition to reentering at a range of angles, impact plume ejecta also arrives at the top of the atmosphere with a range of velocities. Melosh et al. (1990) suggest that, of the material which does not exceed the Earth's escape velocity (11.8 km/s), most of the impact plume ejecta would reenter the atmosphere at velocities in the range of 5-10 km/s. In addition to velocity variations inferred from ejecta plume theory, the presence of shocked quartz within the K-Pg distal ejecta deposits indicates the presence of lower velocity material (Alvarez et al., 1995) which was somehow incorporated into the impact

plume deposits. An average velocity of 8 km/s, which represents the Earth's circular orbital velocity (Toon et al., 1997), was used in all previous simulations and here we compare those results to those of slower reentry velocities, assuming the same nominal Chicxulub spherule mass pulse to the upper atmosphere. Simulations were conducted for both 45º reentry (Figure 39) as well as vertical reentry (Figure 40) in order to maximize thermal energy production for an individual spherule. Higher reentry velocity results in a larger thermal radiation flux both to space and at the ground. As expected, vertical reentry results in increased fluxes as compared with oblique reentry at the same velocity. Again, the different irradiances can be explained by considering the conversion of kinetic energy to thermal energy during reentry. The faster a spherule reenters the atmosphere, the more kinetic energy it has, the hotter its radiating temperature will be, and the greater the emission of thermal radiation from its surface. Reducing the reentry velocity from 8 km/s to 5 km/s (both at 45º) results in a 40% decrease in power deposition to the atmosphere, a drop in peak radiating temperatures from 1600 K to 1100 K, and a decrease in peak surface irradiance from ~6 kW/m^2 to ~2 kW/m^2. Since spherule mass flux and spherule size are the same in all simulations, the opacity contribution by the spherules and thus the strength of self-shielding is the same throughout the period of spherule reentry.

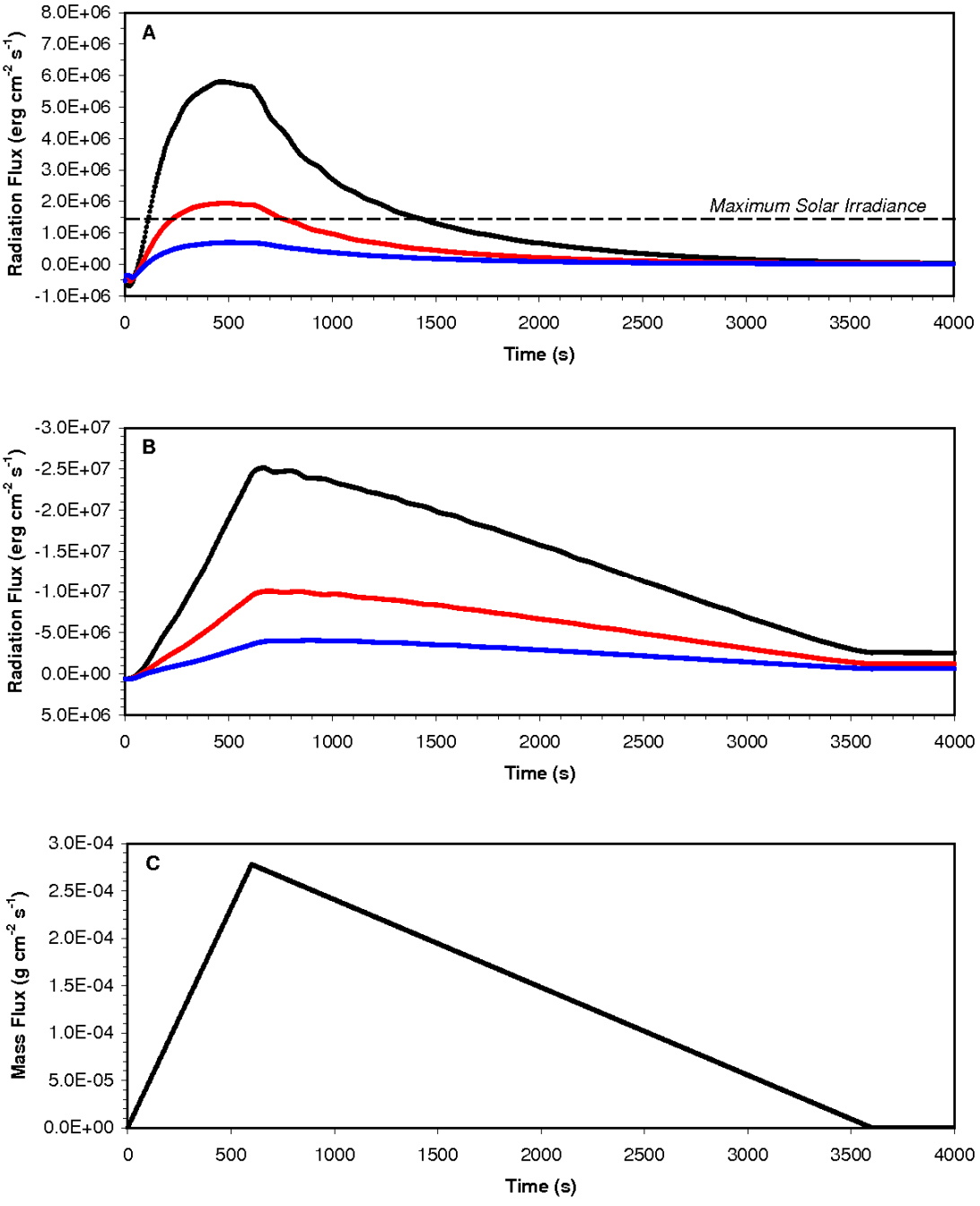

Figure 39. Thermal radiation flux at the surface (a) and to space (b) for 45º spherule reentry at 3 km/s (blue), 5 km/s (red), and 8 km/s (black). The mass flux of spherules is the same for all simulations (c) as is spherule diameter (250 µm). Upward radiation fluxes are negative.

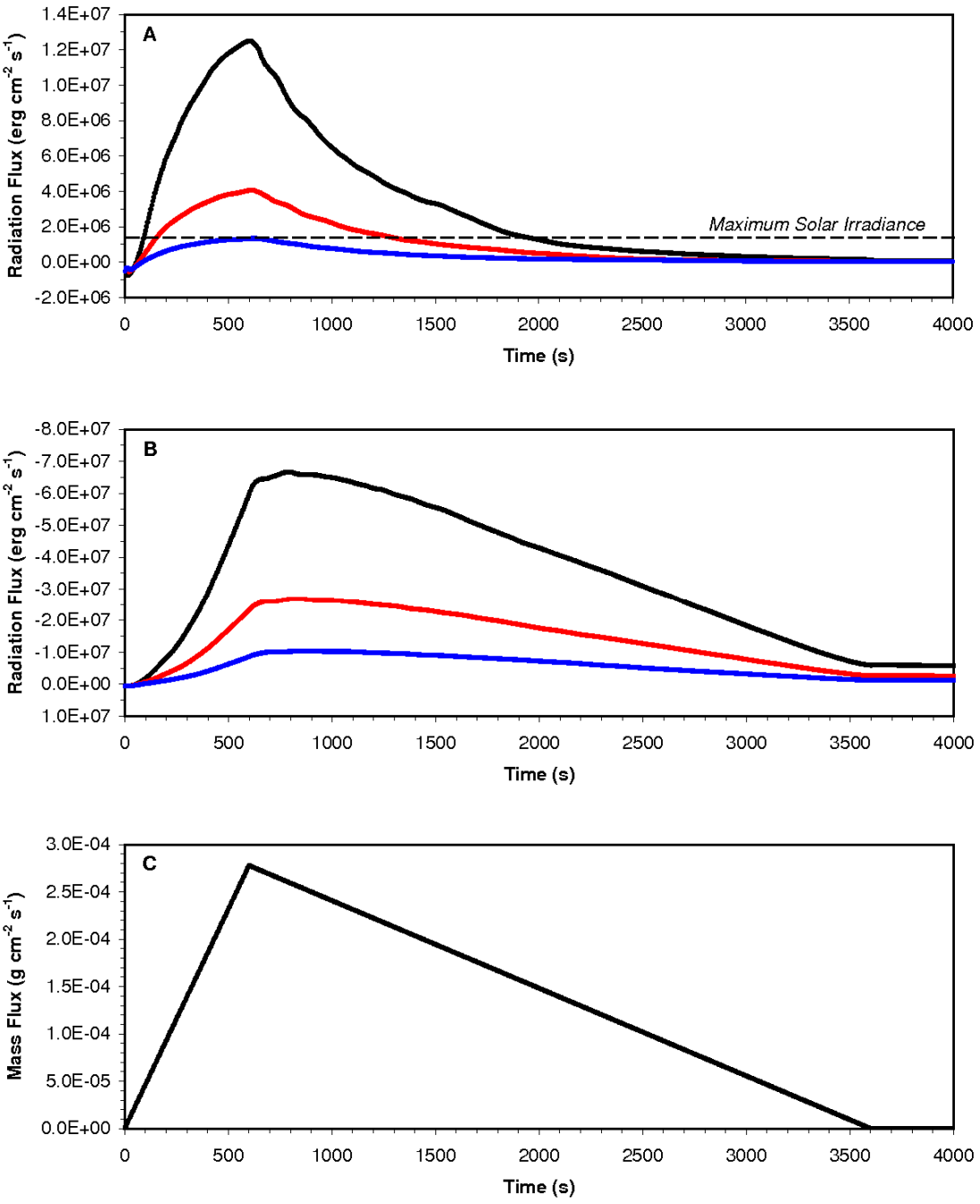

Figure 40. Thermal radiation flux at the surface (a) and to space (b) for 90º (vertical) spherule reentry at 3 km/s (blue), 5 km/s (red), and 8 km/s (black). The mass flux of spherules is the same for all simulations (c), as is spherule diameter (250 µm). Upward radiation fluxes are negative.

7.4.7 Spherule Emissivity

It has been argued (Adair, in press) that the Chicxulub impact spherules had glassy translucent textures after cooling in the atmosphere following heating during deceleration to a molten state. However, in contrast to the glassy microtektites found at sites more proximal to Chicxulub, the spherules (microkrystites) found at distal K-Pg boundary sites display a relict crystalline texture (Smit, 1999). If the crystalline texture is primary, this suggests that the spherules did not completely melt during reentry, but instead cooled slowly in the expanding impact plume and were not completely glassy at any point during atmospheric descent. Also, the spherules have a mafic composition (Smit, 1999) which would limit their translucence even if originally glassy. However, it is important to explore how the particles' deviation from black bodies ($\varepsilon < 1$) affects the thermal radiative transfer from impact ejecta reentry.

We conducted a series of models with the nominal Chicxulub pulse of ejecta in which we varied the emissivity of the spherule phase (Figure 41). Lower spherule emissivity leads to greater thermal radiation fluxes at the ground and lower fluxes to space. Additionally the thermal pulse at the ground endures for a longer period of time and more closely reflects the power deposition to the upper atmosphere. Compared with the half-hour thermal pulse peaking at 6 kW/m^2 if the spherules behave like black bodies, surface irradiance exceeds solar values for ~50 minutes with a maximum of 11 kW/m^2 if $\varepsilon = 0.25$ and ~60 minutes with a maximum of 17 kW/m^2 if $\varepsilon = 0.05$. The translucent spherules absorb less incident thermal radiation and the self-shielding effect is weakened.

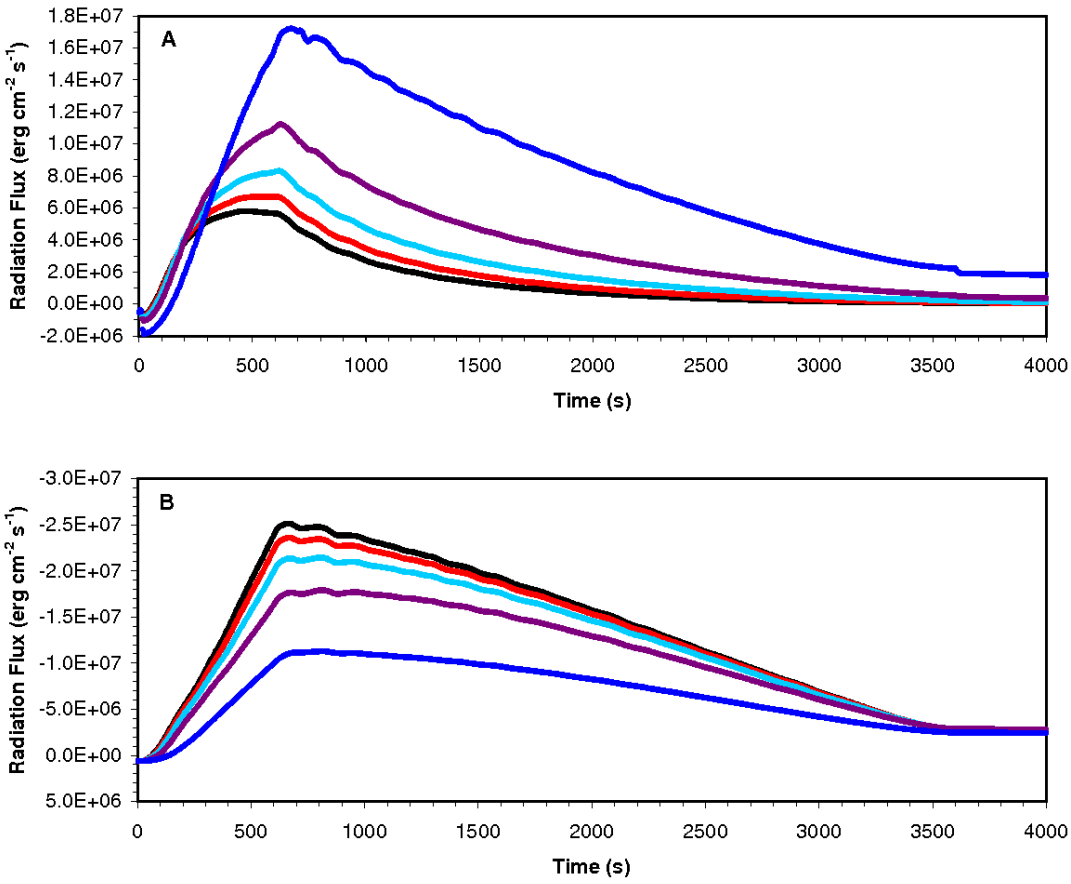

Figure 41. Flux of thermal radiation at the ground (a) and to space (b) for nominal Chicxulub spherule reentry at 45º where the emissivity coefficient is varied between the black body absorption/emission and almost complete transparency: 1.0 (black), 0.75 (red), 0.5 (light blue), 0.25 (purple), 0.05 (blue). Upward radiation fluxes are negative.

A translucent spherule may absorb less incident radiation, but it also emits its thermal energy less efficiently and, as a result, the spherules become hotter. In contrast to maximum spherule temperatures of 1200-1600 K for black-body 250 μm spherules, temperatures reach 1700-2200 K for $\varepsilon = 0.25$ and 2500-3300 K for $\varepsilon = 0.05$. At such high temperatures, ablation of spherule mass may be significant.

7.5 The Role of Opacity in Surface Irradiance

Varying the rate and manner in which spherules reenter the atmosphere alters the flux of downward thermal radiation reaching the ground as well as that of the upward radiation escaping to space. Modifying reentry parameters changes the rate of energy deposition in the upper atmosphere and the resulting rate of thermal radiation emission from the decelerating spherules. However, differences in thermal radiation production do not entirely explain differences in the transfer of that thermal radiation throughout the height the atmosphere, particularly to the surface. If the spherules are black-body emitters and radiate half of their thermal energy upwards and half downwards and the atmosphere contains no absorptive species, then the thermal pulse at the top and bottom of the atmosphere should be identical and equal to half the energy pulse delivered by the spherules. While the top of the atmosphere in our KFIX-LPL simulations receives an irradiance equal to approximately half of the energy flux, the ground receives a thermal pulse

that is truncated in both magnitude and duration as compared to the energy pulse from spherule reentry. The proportion of downward thermal radiation that is absorbed increases with time.

Unlike the upward flux of thermal radiation to space, which encounters few obstacles in the thin upper atmosphere in which the mean free path is long, the downward flux encounters (1) increasingly dense atmosphere containing absorbing greenhouse gas species and (2) the cloud of decelerated spherules below 70 km in altitude. The flux of thermal radiation that reaches the surface is a function of the power deposition in the upper atmosphere and the rate at which the downward thermal radiation is absorbed or reflected by gases and other spherules. In our impact ejecta simulations, we treat spherule reentry as a pulse in which the rate of spherule mass flux to the atmosphere increases and then decreases. Both the rate of energy deposition and the strength of absorption by spherules are varied with respect to time. In order to isolate the contributions of absorption by greenhouse gases and self-shielding by spherules to the surface irradiance, we conducted a series of simulations in which the rate of spherule reentry is held constant for the entire 4000 s simulation. Although the spherule mass fluxes are within the ranges of our variable-inflow Chicxulub models, the total spherule mass deposited in these simulations is not necessarily comparable to Chicxulub. The purpose of the constant-inflow runs is to isolate the self-shielding effect.

The power deposition to the upper atmosphere is constant and the irradiance emitted from the decelerating spherules is also constant. According to previous methods of determining the thermal radiation from ejecta reentry (i.e. Melosh et al., 1990), this

would result in constant irradiance to space equaling half the power input in the upper atmosphere and a constant irradiance to the ground equaling, perhaps, a third of the power input after the absorption of some constant fraction by greenhouse gases. As our model results show (Figure 42), the flux of thermal radiation at the ground decreases with time, and the decrease is more pronounced for greater mass fluxes. Regardless of the magnitude of spherule mass flux, the radiation flux at the ground in every simulation converges upon sub-solar irradiance levels. Although the flux to space more closely reflects the constant power deposition to the upper atmosphere, the increasingly truncated downward flux results in stronger than predicted upward fluxes, and the irradiance escaping to space increases gradually with time.

7.5.1 Absorption by Air

Modeling spherule reentry at constant mass flux allows us to quantify the absorption of thermal radiation by greenhouse gases in the atmosphere. We modeled spherule reentry with a constant mass flux (10^{-4} g cm^{-2} s^{-1}) into an atmosphere with average grey-body absorption by greenhouse gases (see Appendix C) and into an atmosphere without any absorbing species. The 250-µm spherules travelling at 8 km/s reenter the atmosphere vertically in order to maximize thermal radiation emission from the decelerating spherules and eliminate the added complication of remnant horizontal velocity in the spherule cloud. We then compared the fraction of the kinetic energy flux deposited in the upper atmosphere that reaches the ground or is lost to space (Figure 43). For a nonabsorbing

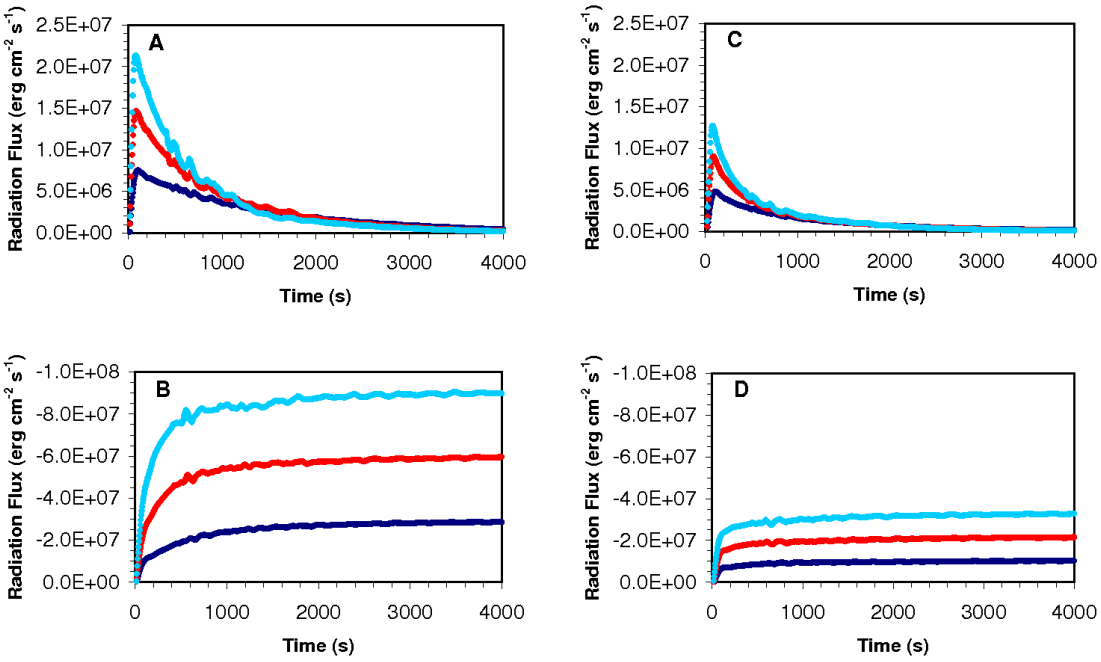

Figure 42. Radiation flux at the ground (a) and to space (b) for vertical spherule reentry and radiation flux at the ground (c) and to space (d) for 45° reentry. The mass flux of spherules reentering the atmosphere is constant: 1E-4 g cm^{-2} s^{-1} (dark blue), 2E-4 g cm^{-2} s^{-1} (red), 3E-4 g cm^{-2} s^{-1} (blue).

atmosphere, initially ~55% of the kinetic energy flux reaches the ground and this declines with time, dipping below 10% after 30 minutes. For an average absorbing atmosphere, only 25% of the energy flux reaches the ground as thermal radiation, falling to 6% after 30 minutes. Comparing the surface irradiance for the absorbing atmosphere model to that of the non-absorbing model yields the proportion of downward thermal radiation that is blocked from reaching the surface by greenhouse gas opacity. Near the beginning of the model, 60% of the downward thermal radiation is absorbed by greenhouse gases and this

decreases to a fairly constant 35% absorption by the end of spherule reentry. The fraction of the energy flux that reaches space as thermal radiation increases to 90% by the end of spherule reentry, far more than the 50% expected by models that do not include optical opacity. The radiation flux to space is similar for both models, but the fraction of the energy exiting the model atmosphere as upward radiation is higher for an absorbing atmosphere.

The proportion of downward thermal radiation absorbed by gases is not constant, but decreases gradually with time. The gas opacity in KFIX-LPL is a function of the radiating temperature of the spherules, which varies from 1600-1300 K throughout the coarse of spherule reentry due to the varying degree of atmospheric compression. On average ~40% of the downward thermal radiation is blocked by greenhouse gases, although a little less is transmitted to the ground early in the simulation and a little more towards the end. Some of the blocked downward thermal radiation is absorbed and some is reflected upwards, which explains why the presence of greenhouse gases in the lower atmosphere leads to enhanced thermal radiation flux to space, particularly near the beginning of spherule reentry when the effect of gas opacity is strongest. Changes in the degree of gas absorption, however, does not explain the sharp decrease in surface irradiance as compared with the constant energy flux to the upper atmosphere. If greenhouse gases were the only limiting species, then the fraction of thermal radiation reaching the ground should *increase* with time as the gas absorption weakens. Additionally, the model without gas opacity shows a thermal pulse at the ground that also decreases with time. This suggests that, while greenhouse gas opacity may prevent 40-50% of the thermal radiation

Figure 43. The fraction of the kinetic energy flux deposited by spherules (vertical reentry) in the upper atmosphere that reaches (a) the ground and (b) space as thermal radiation. An atmosphere void of any absorptive species (red) is compared with an average Earth's atmosphere with absorbing greenhouse gases (dark blue). (c) The fraction of downward thermal radiation absorbed by gases. (d) The shortest mean free path for both types of atmosphere, which lies within the spherule cloud settling through the mesosphere. The shortest mean free path is determined from average mean free paths at 10 km altitude intervals. The actual shortest mean free path may be in a cell between these intervals and the jagged plot due to this incomplete sampling.

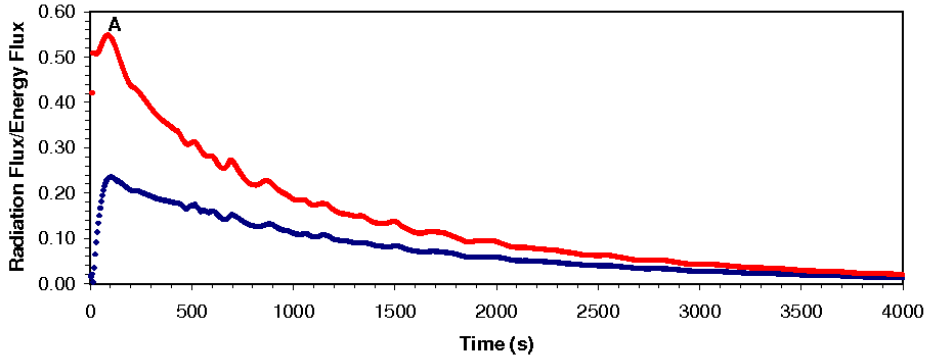
A
Radiation Flux/Energy Flux
0.60
0.50
0.40
0.30
0.20
0.10
0.00
0
500
1000
1500
2000
2500
3000
3500
4000
Time (s)

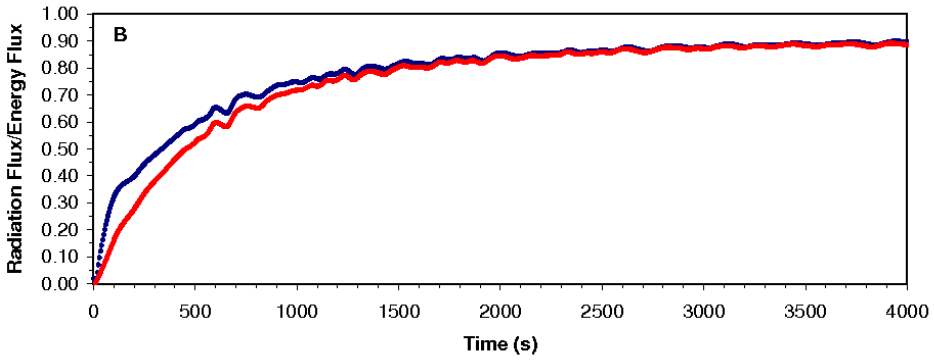
B
Radiation Flux/Energy Flux
1.00
0.90
0.80
0.70
0.60
0.50
0.40
0.30
0.20
0.10
0.00
0
500
1000
1500
2000
2500
3000
3500
4000
Time (s)

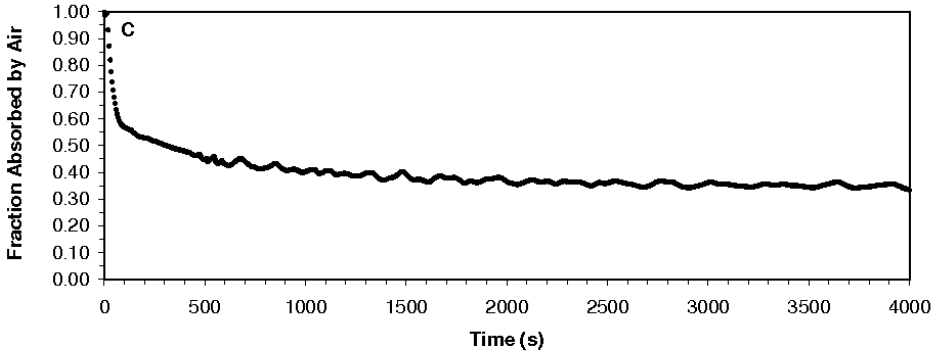
C
Fraction Absorbed by Air
1.00
0.90
0.80
0.70
0.60
0.50
0.40
0.30
0.20
0.10
0.00
0
500
1000
1500
2000
2500
3000
3500
4000
Time (s)

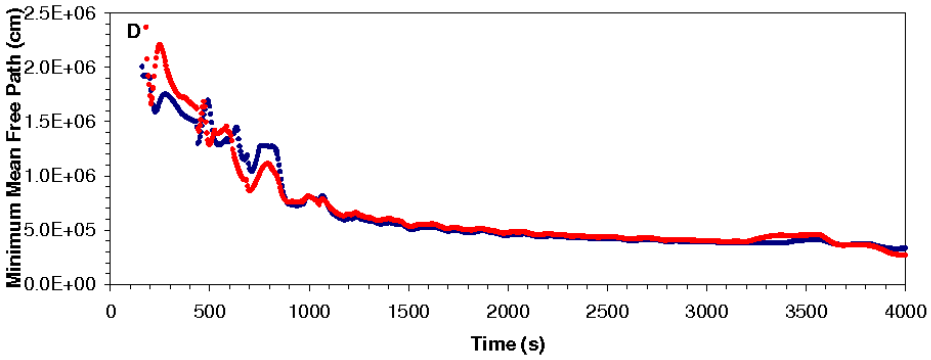
D
Minimum Mean Free Path (cm)
2.5E+06
2.0E+06
1.5E+06
1.0E+06
5.0E+05
0.0E+00
0
500
1000
1500
2000
2500
3000
3500
4000
Time (s)

in the lower atmosphere from reaching the ground, the main effect of gas opacity is to roughly halve the magnitude of downward thermal radiation throughout reentry, but not limit the duration of the strong thermal pulse. In fact, while the absorption by gases weakens slightly with time, the minimum mean free path for both atmospheres decreases and this is controlled not by greenhouse gases but by the increasing concentration of spherules in the mesosphere.

7.5.2 Absorption by Spherules

If we compare the fraction of the energy flux deposited in the upper atmosphere that reaches the ground as thermal radiation for several different constant rates of spherule reentry (Figure 44), it is apparent that increasing the rate of spherule injection also increases the rate at which the downward thermal radiation is absorbed. For all vertical simulations, initially 25% of the energy flux reaches the ground, 30% reaches space and the rest is presumably absorbed by greenhouse gases. If a more realistic 45º reentry is assumed, the maximum fraction of the energy flux is only ~15% at the ground and ~20% to space. Despite the constant rate of energy deposition in the upper atmosphere, and the gradually weakening absorption by greenhouse gases, the thermal radiation flux reaching the ground in all simulations decreases and the flux to space increases. After 1 hour of spherule reentry, almost all of the thermal energy emitted by the spherules is escaping to space with just a few percent reaching the surface regardless of the mass flux to the upper atmosphere.

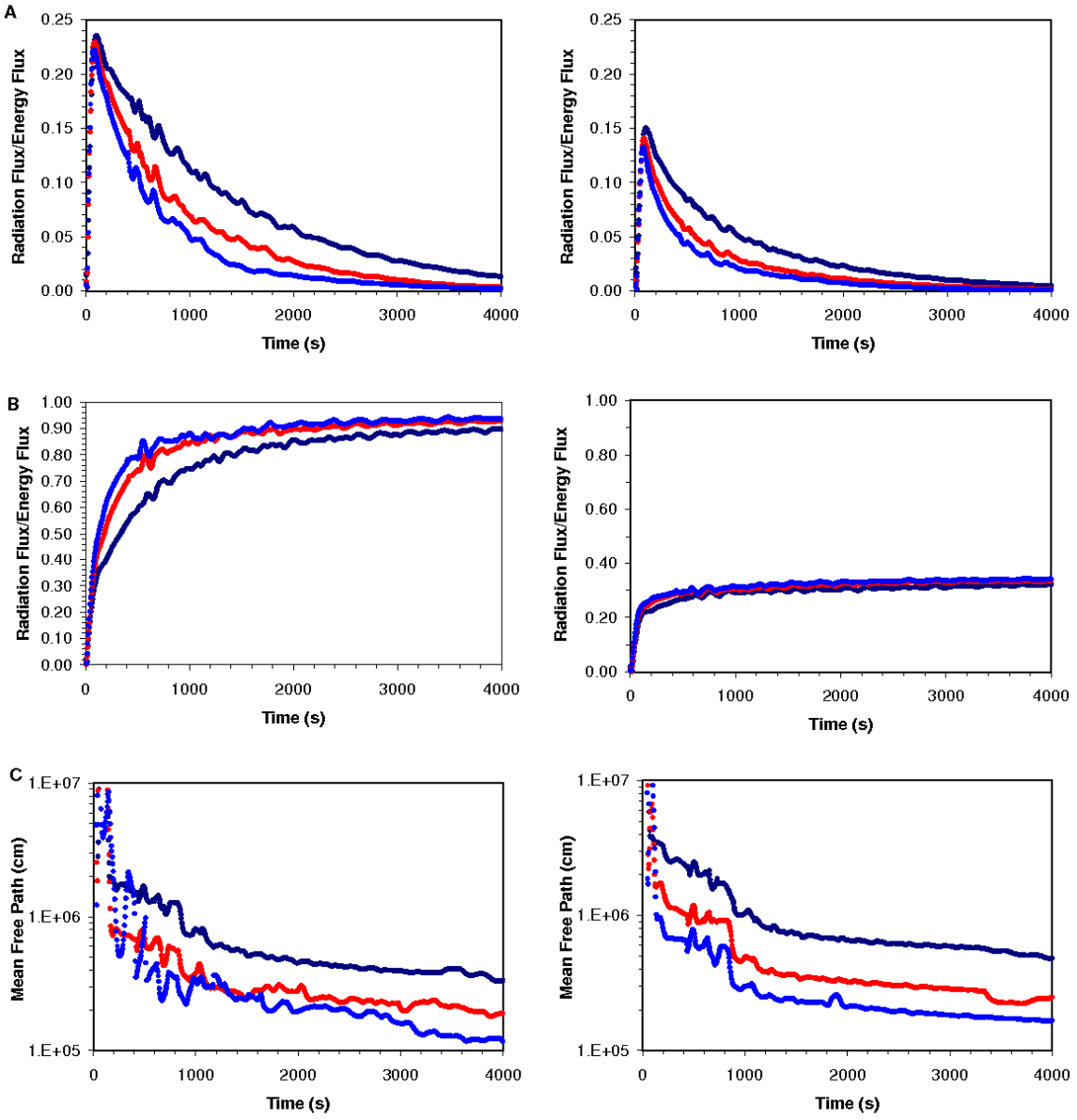

Figure 44. Fraction of the kinetic energy flux delivered to the upper atmosphere by spherules that reaches the ground (a) and space (b) as thermal radiation. The minimum mean free path in the model atmosphere (c) reflects the increasing opacity of the spherule cloud with increasing time. Models with constant spherule mass fluxes of 1E-4 g cm^{-2} s^{-1} (dark blue), 2E-4 g cm^{-2} s^{-1} (red), and 3E-4 g cm^{-2} s^{-1} (blue) for both vertical (left column) and oblique 45º (right column) reentry.

The spherule opacity contribution to a single computational cell is a function of the number of spherules in the cell and the cross-sectional area of each spherule. Thus, the higher the flux of spherules to the upper atmosphere, the greater the spherule opacity contribution, the shorter the mean free path through the spherule cloud, and the greater the fraction of downward thermal radiation that is prevented from reaching the ground. In the constant flux simulations, the minimum mean free path, which is at an altitude coinciding with the densest part of the spherule cloud, decreases with time as the spherule cloud becomes denser. Although the spherules are added to the atmosphere at a constant rate, the minimum mean free path through the spherule cloud decreases nonlinearly. This is due to the complex nature of particle-air interactions in the accumulation of spherules in the cloud and emphasizes why a numerical model is needed to accurately compute the density of the spherule cloud. Two runs with identical spherule mass fluxes, but different reentry angles have similar minimum mean free paths (a little shorter for vertical reentry because the spherule cloud is a little less densely packed if some horizontal velocity is retained) which explains the similar rates of absorption with respect to time.

7.5.3 Thermal Radiation Transfer through the Atmospheric Column

Thus far we have considered just the thermal radiation reaching the top and bottom of our atmosphere. To fully understand the effect of opacity, both from greenhouse gases and spherules, the transfer of thermal radiation and the variations in opacity throughout the height of the atmosphere are compared (

Figure **45**) at different times in a simulation of vertical spherule reentry at constant mass flux.

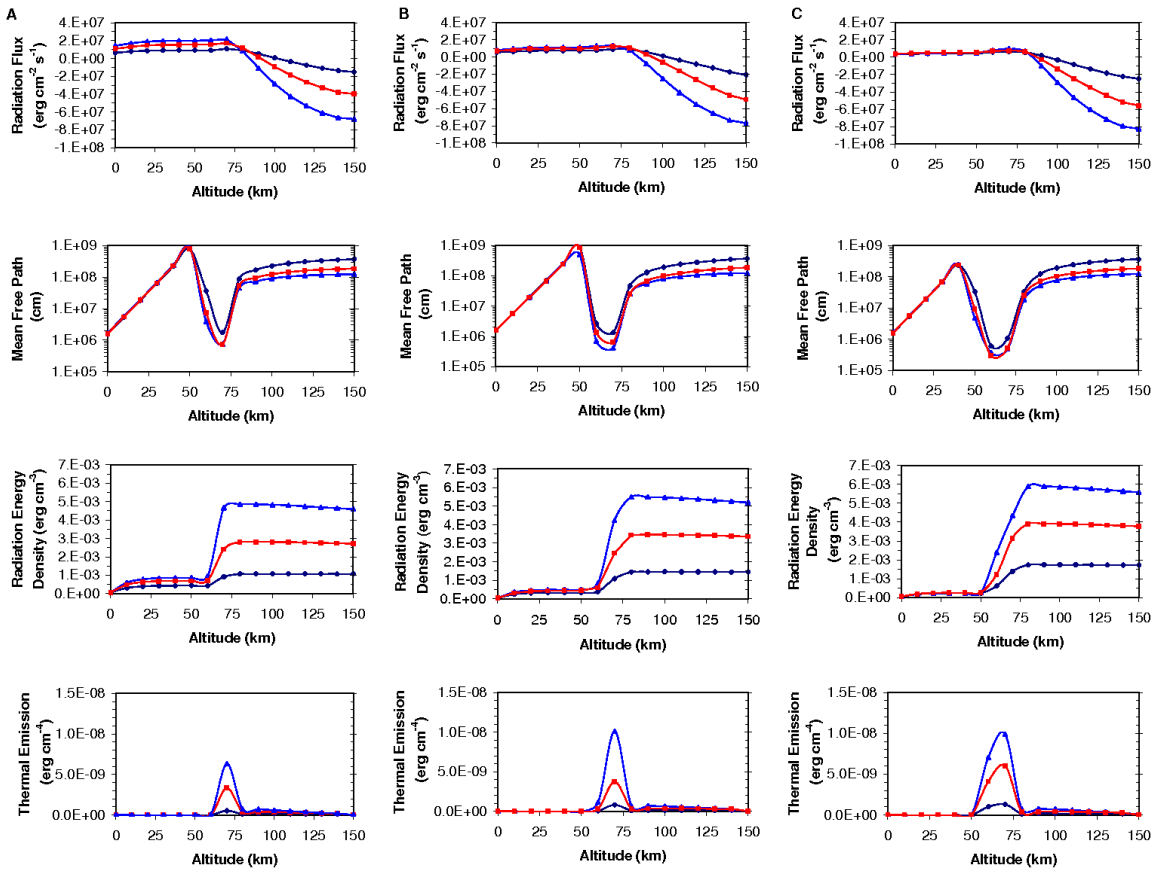

Figure 45. Thermal radiation flux, mean free path, radiation energy density, and thermal emission vs. altitude after (a) 5 minutes, (b) 10 minutes, and (c) 20 minutes of vertical spherule reentry at constant mass flux (1E-4 g cm^{-2} s^{-1} = dark blue, 2E-4 g cm^{-2} s^{-1} = red, 3E-4 g cm^{-2} s^{-1} = blue). Upward radiation fluxes are negative.

The upper atmosphere is thin and largely void of greenhouse gases, although there is some opacity contribution by the rain of decelerating spherules. The higher the mass flux of spherules, the shorter the mean free path through the upper atmosphere. Because the mass flux in each simulation is constant, the opacity in the upper atmosphere is constant with respect to time. The lower atmosphere is void of spherules, so only greenhouse gases contribute to the opacity. As the density of the atmosphere increases exponentially with decreasing altitude, the mean free path is shorter closer to the ground and gas absorption is stronger. The density structure of the lower atmosphere is unaffected by the spherule reentry above, and so the opacity is independent of spherule mass flux and time, at least until the settling spherules reach the lower atmosphere.

For reentry at a constant mass flux, both the opacity in the lower atmosphere and that of the upper atmosphere are largely constant as reentry progresses and absorption of thermal radiation in these regions should also be constant. However, in the middle of our model atmosphere at ~70 km in altitude, the decelerated spherules accumulate and here the opacity is not constant. As more spherules decelerate in the upper atmosphere the spherule cloud below becomes denser and broader and the mean free path over this region decreases.

The flux of downward thermal radiation does not echo that of the upward thermal radiation. The downward thermal radiation is truncated at the top of the spherule layer, and this effect increases with time. In contrast, the upward thermal radiation quite freely exits to space and the flux to space increases with time, as some of the downward thermal radiation is reflected upwards by opaque species. Instead of the distribution of radiation

energy density being equal throughout the atmosphere, the radiation energy density drops sharply below the spherule cloud.

7.6 Conclusions

As we observed in the impact of comet SL9 with Jupiter, ejecta emits a substantial quantity of thermal radiation when reentering the atmosphere at hypervelocities from the expanding impact plume. However, understanding the fate of that energy is more complicated than previous workers have assumed. Not only must absorption by gases be considered, but the spherules themselves act to shield the surface from a fraction of the downward thermal radiation, a fraction that increases with time. Absorption by both phases must be considered in any impact ejecta reentry model in order to predict the flux of thermal radiation both to the ground and to space. Although there is some variation in gas absorption due to changes in the spherule radiation temperature as reentry progresses, approximately 40-50% of the thermal radiation is absorbed by greenhouse gases. The proportion absorbed by spherules is much more variable, increasing with time as a function of the rate of spherule reentry. We varied spherule reentry input parameters and our models show that the thermal pulse at the surface, to space, or anywhere else in the atmosphere is determined by the energy flux delivered to the upper atmosphere, the strength of self shielding by spherules, and absorption by greenhouse gases. Gas absorption is approximately constant, but changing the input parameters alters the emission of thermal radiation in the upper atmosphere, absorption below, or both:

(1) Emission and absorption by spherules change in the same direction. Modifying duration of spherule reentry, temporal variations in spherule reentry rate, and the total added mass of spherules alter not only the energy deposition to the upper atmosphere (the production of thermal radiation), but also the opacity of the spherule cloud below 70 km (the absorption of thermal radiation). A higher rate of spherule reentry will initially lead to higher fluxes at the ground, but the opacity of the spherule cloud will also increase at a higher rate resulting in stronger self shielding and increased truncation of the thermal pulse at the ground.

(2) Emission and absorption by spherules change in opposite directions. Modifying spherule size or emissivity for the same spherule reentry pulse changes the opacity of the spherule layer, but does not change the energy deposition to the atmosphere. For the same mass of larger spherules, incident thermal radiation encounters less cross-sectional area and the effect of self-shielding is weaker. Likewise, transparent spherules transmit more incident thermal radiation and also weaken the effect of self shielding. However, both increasing the particle size and decreasing the emissivity ($\varepsilon<1$) of the spherules increases the peak spherule temperatures and lengthens their cooling time and ablation must be considered.

(3) Emission changes, but absorption stays the same. Modifying the angle or velocity at which spherules reenter the atmosphere does not change the rate of spherule addition to the upper atmosphere, but does alter the thermal energy emitted from each spherule. For steeper reentry angles or higher velocities, the thermal energy emission by

decelerating spherules is increased, but the self-shielding by the spherule cloud is nearly unchanged.

Although our models, in contrast to previous calculations of spherule reentry, include absorption by spherules and a more rigorous treatment of absorption by greenhouse gases, there are other sources of optical opacity, particularly at the regional scale, that must be considered in any complete model of thermal radiation following a large impact event. In the lower atmosphere, we assume a clear sky with average greenhouse gas content, but do not consider the effect of weather. Water droplets and ice crystals in clouds in the lower atmosphere possess absorption bands over much of the infrared spectrum (Seinfeld and Pandis, 1998) and would reduce downward thermal radiation reaching the Earth's surface as a function of the optical thickness of the cloud layer. The energy required to evaporate a cloud with column density typical of tropical clouds is comparable to the total thermal energy reaching the cloud top during Chicxulub ejecta reentry (Melosh et al., 1990) and the ground beneath would be shielded from damaging irradiances. Small particulate matter in the lower atmosphere such as smog, dust, and soot (either from preexisting or impact-generated wildfires) would also add to the opacity of the lower atmosphere and block downward radiation. In addition to the impact spherules, the reentry of the impact plume may inject some quantity of submicron dust (Melosh, 2007; Nuth and Donn, 1983; Nuth and Ferguson, 2006), water vapor (Pope et al., 1994) and sulfur-rich aerosols (Pierazzo et al., 2003). This would serve as an opaque cap to the upper atmosphere and reflect/absorb upward thermal radiation, decreasing the radiation flux to space, but increasing the surface irradiance (see Chapter 6).

Finally, our models assume a fixed temperature radiation boundary condition at the ground, but the surface of the Earth is heterogeneous in how the ground interacts with downward radiation. An ocean or lake surface, wet swampland, sandy desert, grassland, rocky craton, vegetation-sheltered forest floor, etc. all reflect and absorb incident radiation differently. Subsequent modeling work will explore how varying the lower boundary condition affects the radiation energy density at the Earth's surface.

CHAPTER 8

CONCLUSIONS AND FUTURE WORK

The sedimentation of the global K-Pg boundary layer was fast, furious, and deadly. The Chicxulub ejecta spherules travelling in the impact plume at hypersonic velocities deposited a large quantity of energy in the upper atmosphere, heating both air and spherules, altering both the mechanical style of spherule descent and the structure of the atmosphere, and releasing a potentially lethal pulse of thermal radiation upon the surface. Our models show that atmospheric interactions between air and ejecta during K-Pg boundary layer deposition factored heavily in the fate of the ejecta and life on Earth. The main results of the modeling work presented in this thesis show how atmospheric interactions with falling ejecta affect (1) the mechanics of ejecta sedimentation and (2) the environmental consequences of Chicxulub.

8.1 Ejecta Sedimentation Mechanics

The deposition of ejecta spherules through the Earth's atmosphere cannot be described by the Stokes flow settling of individual particles at their terminal velocities. Spherule loading of the mesosphere at ~70 km in altitude leads to turbulent instability and vertical density currents transport the spherules convectively as plumes. It is a similar phenomenon as found in other natural systems, such as tephra fall in water, where fine particles are added to a fluid medium at a high flux. We can assess density current for-

mation both analytically with our derived criteria for instability onset and numerically with KFIX-LPL. The formation of plumes has important implications for the total time required to deposit the K-Pg boundary and the style of deposition. Our models only include transport through air and several local and regional phenomena including wind and other local weather, waves, ocean currents, and settling through a deep water column, affect the final sedimentation of the K-Pg boundary layer as observed in the rock record today.

Atmospheric interactions with decelerating ejecta lead to compression of the upper atmosphere and the development of pressure gradients if the distribution of ejecta across the top of the atmosphere is patchy. The decelerated spherules spread laterally across these pressure gradients leading to a uniform deposit on the ground despite a non-uniform entry into the upper atmosphere.

Horizontal winds up to 5 km/s are generated within the spherule layer due to remnant horizontal velocities following oblique atmospheric reentry. Such winds may transport low velocity mineral grains radially away from Chicxulub and explain why shocked quartz grains are found within the impact plume ejecta material. In addition, heating of the air above the spherule layer may lead to debris floating (Artemieva and Morgan, 2008; Colgate and Petschek, 1985) and lateral spread of small grains around the globe. Debris floating is not observed in our current models, but these models only include spherule-sized particles and future work will examine the transport of smaller particles through a spherule-altered atmosphere. This will test whether small shocked mineral grains are carried laterally by the buoyant hot upper atmosphere.

8.2 Environmental Effects

Reentry of Chicxulub spherules at 8 km/s and at 45° and the subsequent deceleration in the atmosphere heats the particles to 1300-1600 K and this heat is radiated from the spherules' surfaces as infrared thermal radiation. The downward thermal radiation is modified by absorption by both absorptive greenhouse gas species in the air and previously decelerated spherules settling lower in the atmosphere. This self-shielding effect limits both the magnitude and duration of the pulse of high thermal irradiances reaching the Earth's surface. The flux of thermal radiation reaching the ground is a function of not only the emission of thermal radiation from decelerating spherules in the upper atmosphere, but also the strength of the self shielding effect which is a function of the concentration of spherules drifting lower in the atmosphere.

Although a pulse above solar values for ~30 minutes and peaking at 6 kW/m^2, as predicted by our nominal Chicxulub model, is sufficient to cause significant dermal damage (even to large animals), this is below the lower limit for piloted ignition of most woody biomasses. Without a mechanism to override self-shielding by spherules, support for the global wildfire hypothesis is weakened. However, the presence of a hot opaque dust cap in the upper atmosphere, either as submicron dust condensed from the impact plume or as sulfur-aerosols will reflect enough thermal radiation downwards to ignite fires across the Earth.

8.3 Future Directions

8.3.1 Chicxulub

The work presented here focuses mainly on the first hour or two of spherule reentry and the changes to the atmosphere that occur during this time. Future models will track the deposition of ejecta to the ground to obtain the time required for complete deposition of the layer. This has been modeled at coarser resolutions showing the deposition of ejecta over several hours, but resolution <250 m is required to resolve density current formation and adequately model the descent of ejecta in plumes through the lower atmosphere.

We modeled the role submicron dust may play in radiation transport with a crude approximation where we use a reflective upper boundary to our mesh. Future work will model the descent of fine dust particles through the atmosphere to determine how deep in the atmosphere the dust penetrates, when the dust is deposited relative to the spherules, and how different volumes of dust affect the environment. We also plan to examine the transport of fine particles in the lower atmosphere, like soot from impact-generated wildfires to test whether the soot is lofted high enough in the atmosphere to spread globally.

At sites of intermediate distance (2000-4000 km) from the crater in continental North America, the Chicxulub impact ejecta consists of two layers: In addition to the ~3 mm-thick upper layer containing the Iridium anomaly and spherules, there is a lower, thicker (i.e. ~2 cm-thick in Raton Basin, NM) layer consisting of mainly terrestrial clay-

stone (Smit, 1999). It has been suggested that the upper layer is equivalent to the distal fireball layer and the lower layer represents material from the ejecta curtain, but the mechanics of producing two distinct layers is unclear. The dual-layer stratigraphy has led to the argument of a second impact event, but it is also possible that atmospheric interactions can explain the emplacement of two distinct ejecta layers. Deposits from the ejecta curtain are expected to extend to the intermediate distances where the double layer is observed. We can model this by injecting an initial brief injection of terrestrial ejecta into our model atmosphere in addition to the more prolonged flux of fireball material. Preliminary KFIX-LPL models with an older version of the code (without the full radiation model and corrected drag coefficients) showed that compression of the atmosphere by the terrestrial material alters the structure of the atmosphere causing the fireball material to fall separately and resulting in the deposition of two distinct layers. Currently KFIX-LPL is sensitive to injection at the large mass fluxes of the ejecta curtain, but future models work with the updated version of KFIX-LPL at higher resolution will explore the atmospheric effects of two distinct pulses of material to the upper atmosphere and also resolve any density current formation, which was observed to occur in both particle layers in our preliminary models.

KFIX-LPL does not include chemistry, but the results from our models provide the pressures and temperatures throughout the atmosphere and through time and yield initial conditions for the chemical reactions that occurred following the Chicxulub impact. Betty Pierazzo has recently adapted the general circulation model WACCM, which includes atmospheric chemistry, for use in modeling atmospheric and climatic perturba-

tions following a large impact event and future collaboration will lead to an increased understanding of environmental effects such as acid rain production, sulfur aerosol formation, and climatically active gases such as CO_2, H_2O, NO_x and SO_x.

8.3.2 Impacts on Earth and Beyond

The K-Pg boundary layer is not the only impact spherule layer found in the stratigraphic record and this work can be expanded to explore spherule deposition through the atmosphere from impacts of various sizes on Earth as well as on other planets, such as Mars. Several spherule deposits have been identified in the Archean, with thicknesses as large as hundreds of centimeter and spherules as large as 2 mm in diameter. Although many of these spherule beds are interpreted as high energy deposits that have been heavily reworked (Bruce Simonson, pers. comm.), if an estimate of spherule mass density can be derived we can model the deposition of spherules from large Archean impacts. This is an interesting exercise because the anoxic Archean atmosphere was quite different from the modern atmosphere. Similarly, we can model the deposition of impact ejecta through the atmospheres of other planets, such as Mars and Titan.

8.3.3 Multiphase Geologic Flows

As the models of tephra fall experiments show, KFIX-LPL is a useful tool for use with two-phase geologic flows. Essentially, the Chicxulub models presented here are

simply an extreme example of sedimentation and the same numerical technique can be applied to more “normal” forms of sedimentation, including ash fall out through the atmosphere, turbidites, debris flows, etc. The complete treatment of thermal radiation in KFIX-LPL, unlike other flow codes in use for such geologic flows, is particularly useful for modeling hot flows, such as pyroclastic flows or volcanic plumes.

APPENDIX A

TURBULENT INSTABILITY CRITERION FOR AN INCOMPRESSIBLE FLUID

Using the Stokes velocity and momentum balance conditions, we can derive criteria for both laminar and turbulent instability in an incompressible fluid. First consider the settling of an individual spherical particle (Figure 46) of diameter d and density ρ_p falling in the laminar flow regime under gravity g through a fluid of viscosity η and lesser density ρ_f. The particle's terminal velocity is given by Stokes law:

$$v_s = \frac{(\rho_p - \rho_f)gd^2}{18\eta} \qquad [1]$$

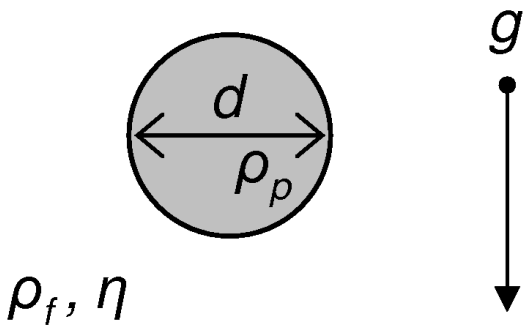

Figure 46. Cartoon illustrating a single spherical particle falling through an incompressible fluid medium.

Now consider a layer of thickness h containing a particle-fluid mixture overlying a layer of particle-poor fluid (Figure 47). The difference between the density ρ of the particle layer and that of the particle-poor fluid below ρ_o ($\approx\rho_f$) is equal to $(1-\theta)(\rho_p-\rho_f)$ where θ is the volume fraction of water. If the particles are diffuse, Stokes law applies and the particles settle individually by passive settling. However, if the density of the particle-laden layer exceeds the density of the fluid below, any small wavelike disturbance (amplitude δ) of the interface is unstable. The tendency for a particle-bearing layer of fluid to form density currents or be subject to settling of individual particles can be expressed by the dimensionless number B, which relates the timescale of individual particle settling by Stokes flow, τ_s, to the timescale of instability growth, τ_i:

$$B = \frac{\tau_s}{\tau_i} \qquad [2]$$

For B<1 the particle-laden layer is stable and particles settle individually, whereas for B>1 the layer is unstable and density currents may form.

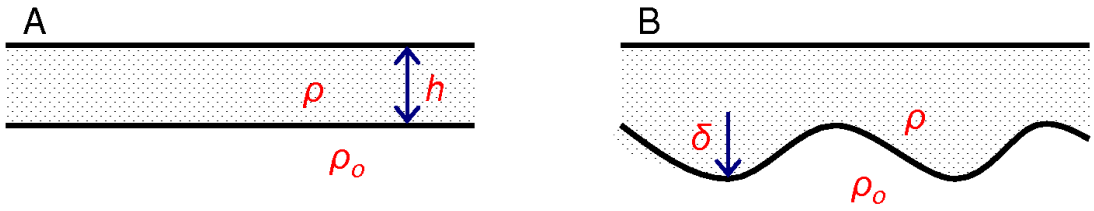

Figure 47. Cartoon illustrating (a) a particle-laden layer ($\rho = (1-\theta)\rho_p + \theta\rho_f$) overlying a particle-poor fluid ($\rho_o = \rho_f$) and (b) an instability of some amplitude forming at the base of the particle-laden layer.

The time required for a particle to settle individually through a layer of thickness *h* is shown from [1] to be

$$t_s = \frac{18h\eta}{(\rho_p - \rho_f)gd^2} \qquad [3]$$

If the flow regime for instability formation is also laminar, the instability growth rate, $\dot{\delta}$, is defined by the Stokes velocity for the particle-fluid mixture:

$$\dot{\delta} = \frac{(\rho_p - \rho_f)gh\delta}{18\eta} \qquad [4]$$

where δ is the amplitude of the growing instability. Rewriting [4] yields an expression for the time required for a viscous instability to grow to a certain amplitude:

$$t_i = \frac{18\eta}{(\rho_p - \rho_f)gh} \qquad [5]$$

Therefore, if both individual particle settling and instability formation are in the laminar flow regime, the instability criterion for laminar instability can be defined as

$$B_l = \frac{h^2\,(1-\theta)}{d^2} \qquad [6]$$

and instability depends only on the layer thickness, particle size and particle concentration, not the fluid viscosity. This is similar to the criterion proposed by Marsh (1988).

Turbulent flow of a body can be expressed by momentum balance conditions, such that the driving force (weight) of the flow, $\rho_f\dot{\delta}^2$, is equal to the turbulent pressure induced by the flow, $(\rho - \rho_f)g\delta$, and the viscosity of the fluid can be ignored. The rate of

instability growth to a given amplitude and the timescale of that growth can be written for turbulent instability:

$$\dot{\delta} = \sqrt{\frac{(\rho - \rho_f) g \delta}{\rho_f}} \qquad [7]$$

$$t_i = 2\sqrt{\frac{\rho_f \delta}{(\rho_p - \rho_f)(1-\theta) g}} \qquad [8]$$

For a scenario such as the Carey tephra-fall experiments where settling of individual particles is in the laminar regime and density current formation is in the turbulent flow regime, the ratio of [3] and [8] yields a new instability criterion:

$$B = \frac{9h\eta}{d^2}\sqrt{\frac{1-\theta}{\rho_f(\rho_p - \rho_f)\delta g}} \qquad [9]$$

This criterion is sufficient to evaluate instability onset in an incompressible fluid where particles settle in the Stokes regime and instability growth is in the turbulent (inertial) flow regime.

APPENDIX B

INSTABILITY CRITERIA FOR A COMPRESSIBLE FLUID

We derive a set of three criteria for the onset of density currents in a compressible medium for both the viscous (Stokes) and turbulent (inertial) flow regimes. The criteria are tailored for scenarios involving particle fall through air, which is assumed to behave like an ideal gas. All three criteria must be met in order for a density current to propagate from the base of a particle-laden layer into the particle-poor air below.

Consider a layer of thickness h composed of a mixture of spherical particles of radius a and air, the base of which has a density ρ, temperature T, pressure P, and void fraction (of air) θ (Figure 48). The ambient air just beneath the particle layer, which consists of the gas phase only, has a density ρ_o, temperature T_o, and pressure P_o. Now suppose that an vertical instability initiates at the base of the particle layer as a finite excursion of amplitude δ. When a parcel of air of volume V is brought to lower altitude, it compresses according to the ideal gas law to volume V'. Thus, the particle-laden air at the bottom of the excursion has a different density ρ', temperature T', pressure P', and void fraction θ'. The ambient air at the level of the excursion is also at a higher pressure as compared to that at the base of the particle layer and can be described by density ρ_o', temperature T_o', and pressure P_o'.

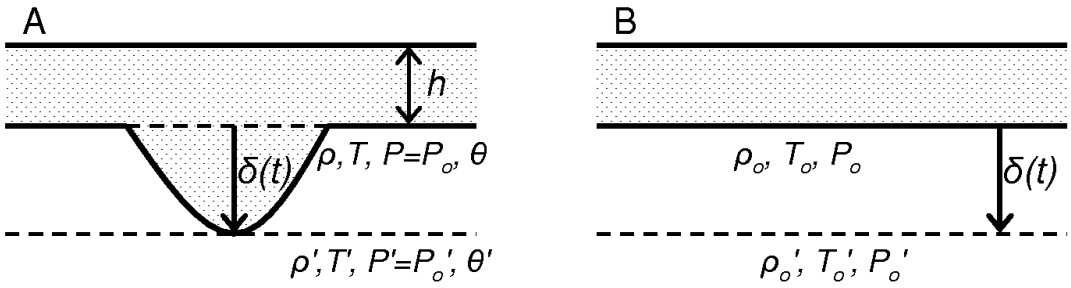

Figure 48. Cartoon illustrating the macroscopic properties of (a) the particle-air mixture and (b) the ambient (particle-poor) air at the top (base of the particle layer) and bottom of an excursion of some finite amplitude.

If the condition at the top of the excursion is known, then we can solve for the condition at the bottom of the excursion in terms of the known parameters. This is simple for the ambient atmosphere, which is void of particles. Using the perfect gas law $P_o = \rho_o R T_0$ (or $P_o' = \rho_o' R' T_0'$), where R is the specific gas constant for air, the hydrostatic equation $\frac{dP}{dZ} = \rho g$, and the thermal gradient in the ambient air $\frac{dT}{dZ}$, we can solve for the ambient density at the bottom of the excursion ρ_o':

$$\rho_0' = \frac{P_0 + \rho_o g \delta}{R\,(T_o - \frac{dT}{dZ}\delta)} \qquad [1]$$

where to the first order in δ we can approximate the density as ρ_o rather than ρ_o' or $\frac{1}{2}(\rho_o - \rho_o')$. Substituting for ρ_o and using the ambient atmospheric scale height, $H_{scale} = RT_o / g$, this becomes

$$\rho_0' = \rho_o \left[1 + \left(1 + \frac{R}{g}\frac{dT}{dZ} \right) \frac{\delta}{H_{scale}} \right] \qquad [2]$$

to the first order in δ.

It is more complex to solve for ρ', the increase in macroscopic density of the particle-laden air, upon a shift from $\delta = 0$ to δ. We assume that the initial volume fraction of gas is θ, the spherical droplets are incompressible, and that the gas is perfect. We also assume that the pressures at the top and bottom of the excursion are equal to the ambient pressures at those levels ($P = P_o$ and $P' = P_o' = P_o + \rho_o g\delta$). However, we do not assume that the temperature of the spherule-laden cloud is ambient because for impact ejecta studies an instability criterion is required where the gas in the particle layer may be hotter than the surrounding air due to the presence of hot particles. If we consider a fixed volume of gas V that undergoes an adiabatic compression to V' upon this shift from $\delta = 0$ to δ, the macroscopic densities are

$$\rho = (1-\theta)\rho_p + \theta\rho_g \qquad [3]$$

$$\rho' = (1-\theta')\rho_p + \theta'\rho_g' \qquad [4]$$

where ρ_p is the microscopic density of the particles and ρ_g is the initial microscopic density of the gas, which compresses to ρ_g'. Due to mass conservation in adiabatic compression, the initial and final masses of the liquid and the gas in the parcel of air must be equal and the ratio of parcel volumes is

$$\frac{V'}{V} = \frac{(1-\theta)\rho_p}{(1-\theta')\rho_p} = \frac{\theta\rho_g}{\theta'\rho_g'} \qquad [5]$$

from which we can derive the ratio of microscopic gas densities:

$$\frac{\rho_g}{\rho_g'} = \frac{(1/\theta - 1)}{(1/\theta' - 1)} \qquad [6]$$

From this equation we can determine the remaining unknown, θ', in terms of θ and re-write [4].

$$\theta' = \frac{\theta}{\theta + (1-\theta)\,\rho_g'/\rho_g} \qquad [7]$$

$$\rho' = \left[\frac{\rho_g'/\rho_g}{\theta + (1-\theta)\,\rho_g'/\rho_g} \right] \left[(1-\theta)\rho_p + \theta\rho_g \right] = \left[\frac{1}{1+\theta\left(\rho_g/\rho_g' - 1\right)} \right] \rho \qquad [8]$$

For small δ and assuming adiabatic, not isothermal, compression, the ratio of microscopic gas densities can be expanded to the first order in δ as

$$\frac{\rho_g}{\rho_g'} = \left(\frac{P_o}{P_o'} \right)^{1/\gamma} = \left(\frac{P_o}{P_o + \rho_o g \delta} \right)^{1/\gamma} \approx 1 - \frac{\rho_o g}{P_o} \frac{1}{\gamma} \delta \qquad [9]$$

where γ is the ratio of specific heats for air. Substituting this ratio into [8], along with the ideal gas law and scale height relations, yields

$$\rho' = \left(1 + \frac{\theta}{\gamma} \frac{\delta}{H_{scale}} \right) \rho \qquad [10]$$

where H_{scale} is computed in the ambient atmosphere because that is where the pressure differential is determined.

The driving stress of the instability is the pressure (the weight of the air-particle mixture) at the bottom of the excursion. Because the density changes across the amplitude of the instability due to the compressibility of air, the driving stress is approximated by the average weight of the excursion:

$$\sigma_{drive} = \left[\tfrac{1}{2}(\rho - \rho_o) + \tfrac{1}{2}(\rho' - \rho_o') \right] g \delta \qquad [11]$$

Substituting equations [2] and [10], yields an expression for the driving force in terms of the initial particle layer and ambient air parameters only:

$$\sigma_{drive} = \left[\left(\rho - \rho_o\right) + \left\{ \frac{\theta}{\gamma}\rho - \left(1 + \frac{R}{g}\frac{dT}{dZ}\right)\rho_o \right\} \frac{\delta}{2H_{scale}} \right] g\delta \quad [12]$$

where we can define the second term of the driving stress as *D*:

$$D = \left\{ \frac{\theta}{\gamma}\rho - \left(1 + \frac{R}{g}\frac{dT}{dZ}\right)\rho_o \right\} \frac{\delta}{2H_{scale}} \quad [13]$$

If we are considering only terms of order δ, the D term can be ignored and we need only consider the density anomaly at one level. However, in order to guard against an oscillatory solution, a real density current requires that the whole expression be >0. For D>0, as δ increases the density current becomes more unstable. Thus, from [12], two instability criteria are defined:

$$\left(\rho - \rho_o\right) > 0 \quad [14]$$

$$\left\{ \frac{\theta}{\gamma}\rho - \left(1 + \frac{R}{g}\frac{dT}{dZ}\right)\rho_o \right\} > 0 \quad [15]$$

The first criterion simply states that the overlying layer must be denser than the medium below in order for any excursion to initiate, which also applies for instability in an incompressible fluid. If a density anomaly is present, but the second criterion is not satisfied, then the layer will oscillate and the density current will be unable to grow in amplitude. The second criterion applies only for compressible gas.

According to Newtonian mechanics, the driving force must equal the drag force resisting the instability propagation. Balancing these two forces allows us to derive the

rate of instability growth and compare this to the rate at which the particles fall individually. The resisting stress can be defined using a generalized drag equation that encompasses both viscous and turbulent drag:

$$\sigma_{resist} = \tfrac{1}{2}\rho_0 C_D \dot{\delta}^2 \qquad [16]$$

where $\dot{\delta}$ is the rate of instability growth and C_D is the drag coefficient, which can be expressed, according to Harlow and Amsden (1975) as

$$C_D \cong \frac{12\eta}{\rho_o L \nu} + \frac{1}{2} \qquad [17]$$

This expression for the drag coefficient is approximate and does not incorporate free molecular flow, a correction which is needed to more rigorously assess the Chicxulub problem. The dynamic viscosity, η, of the air depends on its temperature. Choosing a length scale L equivalent to the instability amplitude, δ, and setting the velocity equal to the instability growth rate $\dot{\delta}$, we can balance the driving and resisting stresses:

$$\left[(\rho - \rho_o) + D\delta\right] g\delta = \tfrac{1}{2}\rho_0 \left(\frac{12\eta}{\rho_o \delta \dot{\delta}} + \frac{1}{2} \right) \dot{\delta}^2 \qquad [18]$$

Expanding this,

$$(\rho - \rho_o) g\delta + Dg\delta^2 = \frac{6\eta}{\delta}\dot{\delta} + \frac{1}{4}\rho_0 \dot{\delta}^2 \qquad [19]$$

Solving this nonlinear differential equation yields two complex solutions, one for $\dot{\delta} > 0$ and the other for $\dot{\delta} < 0$, and the timescale of growth depends on the scale of the initial

perturbation. To a crude order of magnitude, we can replace $\dot{\delta}$ by the length scale δ divided by the instability timescale τ and solve the algebraic equation

$$(\rho - \rho_o)g\delta + Dg\delta^2 = \frac{6\eta}{\tau} + \frac{1}{4}\rho_0 \frac{\delta^2}{\tau^2} \qquad [20]$$

which can also be written by dividing the right hand side of the equation by the left hand side:

$$1 = \frac{1}{\tau}\left(\frac{6\eta}{(\rho - \rho_o)g\delta + Dg\delta^2}\right) + \frac{1}{4\tau^2}\left(\frac{\rho_o\delta}{(\rho - \rho_o)g + Dg\delta}\right) \qquad [21]$$

We can define from this expression two limiting timescales, the first for viscous flow τ_v and the second for inertial flow τ_i:

$$\tau_v = \frac{6\eta}{(\rho - \rho_o)g\delta + Dg\delta^2} \qquad [22]$$

$$\tau_i = \sqrt{\frac{\rho_o\delta}{(\rho - \rho_o)g + Dg\delta}} \qquad [23]$$

Substituting these timescales into [21] yields a quadratic formula with only one positive solution:

$$\tau = \frac{\tau_v + \sqrt{\tau_v^2 + \tau_i^2}}{2} \qquad [24]$$

If viscosity dominates then $\tau = \tau_v$ and if the viscosity is zero then $\tau = \tau_i/2$.

In order for a density current to form, the timescale of the layer instability growth must exceed the time it takes for a particle to fall individually through the layer of thickness h at terminal velocity. Using the same drag coefficient as before, we equate the weight of the particle, $\frac{4}{3}\pi(\rho_p - \rho_o)a^3 g$, to the drag force, $\frac{\pi}{2}\rho_o a^2 C_D v_t^2$, and solve for the

terminal velocity v_t as a function of Stokes velocity v_s and inertial (turbulent) viscosity v_i where a is the particle radius:

$$\nu_t = \frac{\nu_i^2}{2\nu_s}\left[\sqrt{1+4\frac{\nu_s^2}{\nu_i^2}}-1\right] \quad [25]$$

$$\nu_s = \frac{2}{9}\frac{(\rho_p-\rho_o)a^2 g}{\eta} \quad [26]$$

$$\nu_i = \sqrt{\frac{16}{3}\left(\frac{\rho_p-\rho_o}{\rho_o}\right)ag} \quad [27]$$

The dimensionless instability criterion for an incompressible medium, *B*, is the particle fall time across the layer divided by the layer instability time:

$$B = \frac{h/\nu_t}{\tau} \quad [28]$$

If B>>1 then layer instability favors the formation of density currents, but if B<1 layer instability does not have sufficient time to form and the particles settle individually at their fall velocity rather than collectively in plumes.

There are three limiting cases for the combinations of settling and instability flow regimes:

(1) Stokes settling, viscous density currents

$$B_{sv} = \frac{h}{\tau_v \nu_s} = \frac{3}{4}\left(\frac{(\rho-\rho_o)+D\delta}{\rho_p-\rho_o}\right)\frac{h\delta}{a^2} \quad [29]$$

When *D* is zero, the term in parentheses is just the particle volume fraction and the expression reduces to an expression similar to the criterion for viscous instability in an incompressible fluid derived in Appendix A.

(2) Stokes settling, turbulent density currents

$$B_{si} = \frac{h}{(\tau_i/2)v_s} = \frac{9\eta h}{a^2(\rho_p - \rho_o)}\sqrt{\frac{1}{g\delta}\left(\frac{\rho - \rho_o}{\rho_o} + \frac{B\delta}{\rho_o}\right)} \qquad [30]$$

(3) Turbulent settling, turbulent density currents

$$B_{ii} = \frac{h}{(\tau_i/2)v_i} = \frac{h\sqrt{3}}{2}\sqrt{\frac{1}{a\delta}\left(\frac{(\rho - \rho_o) + D\delta}{(\rho_p - \rho_o)}\right)} \qquad [31]$$

APPENDIX C

THERMAL RADIATION ADDITIONS TO THE KFIX TWO-FLUID HYDRODYNAMIC MODEL

Author's Note: The following was provided by Jay Melosh and describes the fundamental equations used to calculate thermal radiation transfer in Melosh's thermal radiation model, which was implemented by the author into KFIX-LPL.

1. Fundamentals of Radiative Transport in the Diffusion Approximation

The fundamental quantity in any thermal radiation problem is the radiation intensity, I (**r**,**n**,ν,t) dA dΩ dν dt. It represents the amount of energy passing through area dA perpendicular to a unit vector **n** in the direction of motion, centered about point **r**, within solid angle $d\Omega = \sin\theta\, d\theta\, d\phi$ and frequency interval dν between time t and t + dt. It is measured in units of J/m^2-sr-Hz-sec. The form of the radiation field can vary from a narrow cone centered around solid angle $\mathbf{n}_0$, in which case $I = I_0\, \delta(\mathbf{n}\text{-}\mathbf{n}_0)$, where δ is the Dirac delta function, to an isotropic blackbody radiation field. The radiation intensity is frequently decomposed into various moment distributions for practical computations (Mihalas and Weibel-Mihalas, 1999).

The fundamental equation of radiation transport is derived from an accounting of the energy either gained or lost from a narrow cone of radiation propagating in direction **n** and within solid angle dΩ. The equation is written as:

$$\frac{1}{c}\frac{\partial I}{\partial t} + \mathbf{n}\,\mathrm{g}\nabla\, I = \kappa(I_p - I) \qquad [1]$$

where c is the speed of light, κ is an absorption coefficient (units length^{-1}) and I_p is a source term that generally represents interaction with matter in thermal equilibrium at a given location **r**. Although this equation looks very simple, its actual use in computations is very difficult because it is inherently non-local: Radiation can propagate long distances from one region to another, which is not easy to account for with differential equations. A simpler relation is derived by integrating this equation over the entire range of solid angle dΩ:

$$\frac{\partial U}{\partial t} + \nabla \cdot \mathbf{S} = c\kappa(U_p - U) \qquad [2]$$

where the energy density U and net flux vector **S** are defined as:

$$\begin{aligned} U &= \frac{1}{c}\int I \, d\Omega, \\ \mathbf{S} &= \int I \, \mathbf{n} \, d\Omega \end{aligned} \qquad [3]$$

The net flux **S** vanishes in an isotropic radiation field. The energy density U has units of energy/volume, while net flux **S** has units of energy/area-time.

The local interaction with matter often produces an isotropic radiation energy density U_p, given by the Planck function at the local temperature T,

$$U_p = \frac{4\,\sigma T^4}{c} \qquad [4]$$

where σ is the Stefan-Boltzmann constant.

Equation (2) is thus essentially an equation of continuity for the radiation field and represents local conservation of radiant energy. Although the integration of equation (1) over angles discards a great deal of information about the radiation intensity, the remain-

ing piece does express the overall energy balance. The total energy $q(\mathbf{r})$ lost or gained per unit volume at any position $\mathbf{r}$ is given by the divergence of the flux

$$q = \nabla \cdot \mathbf{S} = c\,\kappa\,(U_p - U) \qquad [5]$$

Because of the integration over angles, equation (2) only captures a portion of the full angular dependence of I embodied in (1). U and $\mathbf{S}$ are often described as the first two "moments" of I over solid angle. In particular, equation (2) does not discriminate between a narrow beam of radiation and a broad flow in the same direction: Such discrimination requires the definition of an infinite number of higher moments.

The quantities appearing in equations (1) through (3) depend implicitly on frequency ν. However, in this work we adopt the gray-body approximation in which all quantities are integrated over frequency. This integration creates particular problems for the opacity κ, which is often a strong function of frequency in the Earth's atmosphere due to infrared absorptions by atmospheric gases. In this case the opacity we use will always be understood to be the Rosseland mean (Mihalas and Weibel-Mihalas, 1999), which attempts to create a useful gray-body approximation by weighting frequencies of low absorption more heavily than those of strong absorption.

Another important, but usually excellent, approximation is to assume that the radiation field is quasi-static, so that the time derivatives in equations (1) and (2) can be dropped. In coupling thermal radiation transport to hydrodynamics this is valid when material velocities are much smaller than the velocity of light. The radiation field then establishes its own equilibrium on a time scale much shorter than the fluid flow because the velocity of light is so high compared with material motions. The radiation field is

then determined by the distribution of material and its temperature at any given time, so that all of the time dependence is contained in the source term on the right hand side of the equation. Similarly, we ignore the momentum of the radiation field in comparison to the momentum of the material, and so do not need to modify the overall momentum balance to account for the thermal radiation. Only the energy is affected by emission and absorption of radiation in this approximation.

The diffusion approximation retains only the first two moments of *I*. In this case the frequency-independent *I* is completely determined by the two quantities *U* and **S** (Zel'dovich and Raizer, 1967 p. 144ff):

$$I(\mathbf{n},\mathbf{r},t) = \frac{1}{4\pi}\left[c\,U + 3\,\mathbf{n}\,\mathbf{g}\mathbf{S}\right] \qquad [6]$$

Because both *U* and **S** are moments computed from equation (3), they do not, themselves, contain any dependence on angle: All of the angular dependence is now explicit in the **n** vector present in this equation. The angular dependence of *I* is thus severely restricted by this approximation. Although *U* and **S** do not depend on angle, they may still be functions of position.

If we consider a plane perpendicular to the direction of the net flux vector at some point **r**, then divide space into a hemisphere on the side receiving the flux and a hemisphere on the side transmitting the flux, the net flux can be divided into two contributions, the dominant one traveling into the forward hemisphere and a smaller one traveling backward into the rear hemisphere. These two fluxes are computed by integrating equation (6) separately over the forward and backward hemispheres:

$$S_{+} = \frac{c\,U}{4} + \frac{S}{2}$$
$$S_{-} = \frac{c\,U}{4} - \frac{S}{2} \qquad [7]$$

The difference of these two hemispheric fluxes, S_+ - S_-, equals the magnitude of the net flux $S = |\mathbf{S}|$. Although the mean energy density U cancels out of the net flux, it still contributes to the total energy flux traveling either along the direction of the net flux vector or against it.

Clearly, S_- can never be less than zero, so the maximum net flux in this approximation is $S = c\,U/2$. Care must be taken in numerical computations that this limit is not exceeded, which may happen near a sharp boundary between a region of large opacity and a region with small opacity. Physically, of course, S can be as large as $c\,U$, which occurs when all photons travel in the same direction and the distribution of I is that of a narrow cone of radiation.

In our approximation to the radiation field, we assume that equation (6) fully describes I. A unidirectional beam of radiation thus cannot be represented well by this approximation, although deviations are often stated not to be serious in practical problems (Zel'dovich and Raizer, 1967). This situation sometimes leads to awkwardness in the boundary conditions, especially where the radiation propagates into a region of very low opacity, so care must be taken to make sure that the results are physically meaningful.

The diffusion approximation is derived from the second moment of equation (1) with respect to solid angle (Zel'dovich and Raizer, 1967 p.145). Thus, equation (1) is

multiplied by **n** and integrated over dΩ. On he right hand side the integral over I_p vanishes when the radiation arises from matter in thermal equilibrium because I_p is isotropic in this case. The second term on the right is $-\kappa \mathbf{S}$, by definition (3). On the left side the gradient of the isotropic factor *U* in equation (6) produces the numerical factor c/3 times the gradient, while the flux term from equation (6) vanishes because it contains an odd number of factors of **n**. The result is a relation between flux **S** and the gradient of the thermal energy density:

$$\mathbf{S} = -\frac{c}{3\kappa}\nabla U = -\frac{l\,c}{3}\nabla U \qquad [8]$$

where $l = 1/\kappa$ is the mean free path of the radiation. Note that the negative sign here is essential to ensure that energy travels from regions of high radiation density to regions of low density.

The success of equation (8), and thus the validity of the diffusion approximation, depends on the validity of equation (6) as an approximation to the full radiation intensity field. In general, a radiation field cannot be fully described by equation (6). In this case, however, the diffusion approximation may still be valid so long as the net flux is small compared to the energy density, $c\,U << S$.

Putting all these approximations together, equations (8), (2) and the quasi-static assumption yield the fundamental equation of radiation transport in the diffusion approximation:

$$\frac{1}{3}\nabla\mathrm{g}\left(l\,\nabla U\right) = \frac{1}{l}\left(U - U_p\right) = -\frac{q}{c} \qquad [9]$$

We presume that the mean free path l is a function of position and so keep it inside the divergence term.

In this approximation energy is transported from one region to another by thermal radiation. The radiation mean free path, however, is not negligibly small so that energy can move some distance, although transport distances must be short in comparison to the largest scales in the problem. The radiation field U thus has a local component U_p as well as contributions from more distant regions. Although this is a moderately drastic approximation, we do not take the next step commonly employed in modeling stellar interiors, in which U is set *equal* to the local blackbody energy density U_p at every position (this is the approximation of LTE, or Local Thermodynamic Equilibrium). The LTE approximation essentially assumes that the radiation mean free path is negligibly small. In this limit equation (8) reduces to the heat conduction equation with a temperature dependent conductivity, and (9) becomes the equation for conductive heat transfer.

2. Boundary Conditions to the Fundamental Equation

The elliptic partial differential equations defined by equation (7) are not complete in themselves: To solve practical problems boundary conditions must also be specified. Our implementation in KFIX permits four different classes of boundary condition, each of which may be imposed on one side of our square mesh.

Most of these conditions are fairly simple, mathematically. Thus, one can specify a fixed temperature at a boundary. In this case the energy density on the boundary is just equal to the Planck energy density, equation (4), at the boundary temperature T_b, $U_p(T_b)$.

A slightly more complicated boundary condition is a fixed radiant energy flux normal to a boundary. In this case equation (8) fixes the gradient $\mathbf{n} \cdot \nabla U$, where $\mathbf{n}$ is a unit vector normal to the boundary. We also implement periodic boundary conditions, such that the radiant energy density U on one boundary is equal to that of the opposite.

The most complex, but useful, boundary condition specifies a reflection coefficient R for radiant energy at the boundary. In conjunction with R one must also specify a boundary temperature T_b. R varies from 1, which implies perfect, mirror-like reflection at all frequencies, to 0, which implies perfect blackbody absorption. Unfortunately, this does not translate into a simple condition on U or its derivative, but an algebraic relation between the two. The case $R = 1$ is the simplest limit. Perfect reflection means no energy gradient at the surface, so the condition is simply $\mathbf{n} \cdot \nabla U = 0$. However, when $R \neq 1$, radiant energy arrives at the surface with a flux S_{in} and leaves with a flux S_{out}. We assume that a fraction $R\,S_{in}$ is reflected from the surface. However, by Kirchhoff's laws, the surface also loses thermal radiation at a rate given by $(1-R)\,\sigma\,T_b^4$, so that $S_{out} = R\,S_{in} + (1-R)\,\sigma\,T_b^4$. Using equations (7) and (8), we have:

$$\begin{aligned} S_{out} &= \frac{c\,U}{4} - \frac{l\,c}{6}\,\mathbf{n} \cdot \nabla U \\ S_{in} &= \frac{c\,U}{4} + \frac{l\,c}{6}\,\mathbf{n} \cdot \nabla U \end{aligned} \qquad [10]$$

Solving these equations for the gradient of U, we obtain the relation:

$$\mathbf{n} \cdot \nabla U = \frac{3}{2l}\left(\frac{1-R}{1+R}\right)\left[U - U_p(T_b)\right] \qquad [11]$$

Which has all the correct properties in the limits of *R*. Although this is a bit more complex to impose than the other relations, it is nevertheless mathematically tractable.

3. Interaction of Radiation with Matter in KFIX

KFIX permits both liquid and gas to be both present in each cell. The relative volume of gas to liquid is determined by the local "void" fraction, ϕ. At the infrared frequencies at which most heat is lost from reentering ejecta, liquid or solid silicate drops are nearly perfect absorbers, and so we approximate their emissivity as 1.

Liquid or solid silicate is assumed to be in the form of spherical drops of radius *a*. In this case the opacity κ_L due to absorption or emission from the drops is given by

$$\kappa_L = \frac{3(1-\phi)}{4a} \qquad [12]$$

where the drops are assumed to be black body emitters/absorbers, so only their projected surface area contributes to the opacity.

Gaseous absorption coefficients are estimated from averages over the spectral line populations. A very useful such average is the Rosseland mean opacity (Mihalas and Weibel-Mihalas, 1999), which is generally cited on a per unit mass basis, and so must be multiplied by gas density to obtain opacities per unit volume. Furthermore, because the spectral lines are fixed in frequency, while the blackbody spectrum changes shape with changing temperature, the Rosseland mean also depends on temperature. A Rosseland mean opacity for air was computed using atmospheric absorption profiles for sea level

and 11 km in altitude (Goody, 1964). The average opacity of air κ_G (g/cm^2) is calculated to be

$$\kappa_G = \frac{\rho_G \theta}{(1200 + 3.1\times10^{-4} T_{\max}{}^2)} \qquad [13]$$

where ρ_a is the air density (g/cm^3) and T_{max} is the radiating temperature of the spherules in Kelvins. This approximation allows us to ignore the wavelength dependence of the thermal radiation.

The average opacity is the sum of the liquid and gas opacity. The mean free path l of radiation in the presence of both liquid and gas is the inverse of this sum,

$$l = \frac{1}{\kappa_G + \kappa_L} \qquad [14]$$

When matter absorbs radiation it adds energy. Similarly, when matter emits radiation its energy decreases. The overall energy balance for the gas and liquid thus acquires two new terms that account for this exchange. Writing the energy balance on a per unit volume basis, we have

$$\begin{aligned} \rho_G \frac{dE_G}{dt} &= \{\text{non radiative terms}\} + c\,\kappa_G \left[U - U_p(T_G)\right] \\ \rho_L \frac{dE_L}{dt} &= \{\text{non radiative terms}\} + c\,\kappa_L \left[U - U_p(T_L)\right] \end{aligned} \qquad [15]$$

where ρ_G and ρ_L are the macroscopic densities of the gas and liquid, respectively, while E_G and E_L are the specific internal energies (per unit mass) of the two substances. The Planck energy density U_p is determined from the local gas and liquid temperatures T_G and T_L by equation (4) while U is computed from equation (9) in conjunction with the boundary conditions. Notice that the source term for the radiative equilibrium in equation (9)

must equal the sum of the two terms on the right hand side of the equations above to maintain overall energy balance. The precise form of equation (9) when both liquid and gas are present is thus:

$$\frac{1}{3}\nabla\left(l\,\nabla U\right)-\frac{U}{l}=-\left[\kappa_G U_p(T_G)+\kappa_L U_p(T_L)\right] \qquad [16]$$

The gas and liquid thus maintain separate balances with the radiation field, mediated by their different opacities.

APPENDIX D

RESOLUTION AND CONVERGENCE TESTS FOR THE THERMAL RADIATION CALCULATION IN KFIX-LPL

Correctly solving for the flux of thermal radiation at the Earth's surface in the KFIX-LPL model requires a cell size sufficient to resolve the gradients in material density (or mean free path) throughout the mesh. This is particularly true in the region of atmosphere around 70 km in altitude where the spherules accumulate after losing their initial high velocities and reaching their fall velocities. Not only is the transition from the base of the spherule cloud to the empty atmosphere below quite sharp, but the thickness of the densest part of the spherule cloud during the first several minutes of a simulation (when maximum fluxes at the ground are maintained) can be < 1 km in thickness. If the model fails to resolve spherule density variations across the spherule cloud, particularly if the resolution is on the order of the thickness of the spherule cloud, then the region of high opacity is too broad resulting in over-absorption of thermal radiation and underestimating fluxes at the ground.

A complication that arises with increasing resolution is that it requires an increasing number of iterations for the successive overrelaxation radiation algorithm to solve for a radiation energy field which meets a specified convergence criteria. It is preferable to cap the maximum iterations permitted by the radiation solver for each computational time step in order to keep run times reasonable. However, for a given resolution, using too few iterations per cycle also leads to underestimates of fluxes at the ground. The following resolution and iteration tests were conducted to determine the minimum resolution

and number of radiation solver iterations needed to resolve the thermal radiation flux at the ground to within a couple percent accuracy:

1) Resolution tests for cell sizes between 2.5 km and 250 m with radiation solver iterations capped at 9000 (Figure 49). This iteration limit is sufficient to fully converge runs at the courser resolutions, but it is apparent that 2.5 km is a poor choice of resolution as it underestimates peak radiation fluxes by 50% compared to 250 m.

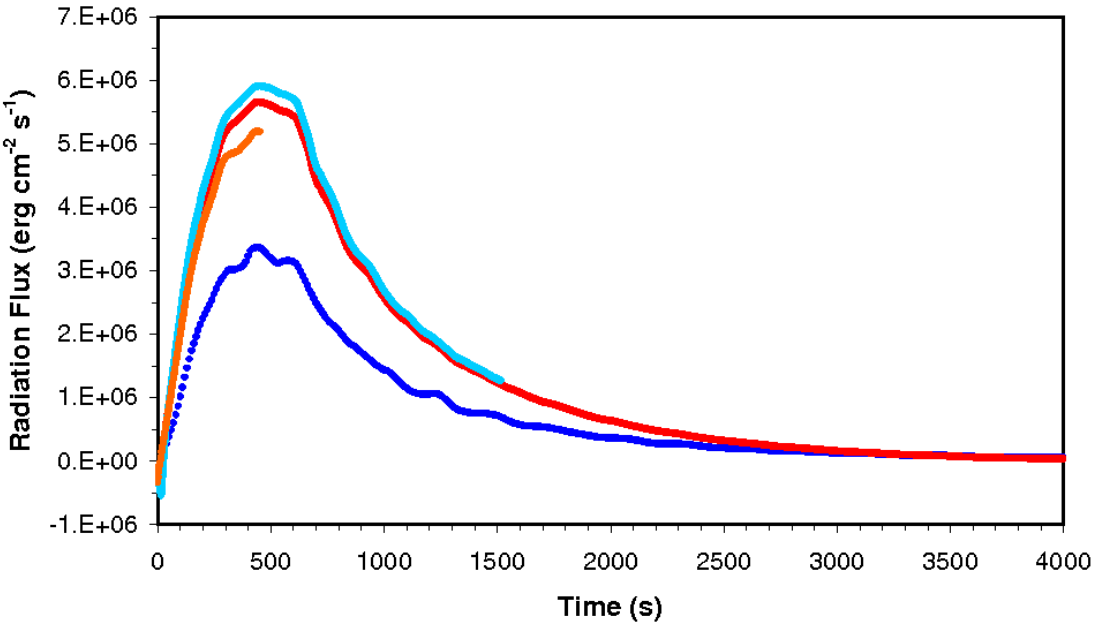

Figure 49. Surface irradiance of thermal radiation for models of nominal Chicxulub ejecta reentry with resolutions of 2.5 km (blue), 1 km (orange), (500 m) red, and 250 m (light blue). The radiation solver is limited to 9000 iterations in all simulations.

2) Radiation solver iteration tests where iterations are capped at between 100 and 9000 iterations for a resolution of 500 m (Figure 50). The results for 9000, 1000, and 500 iterations are all in good agreement, suggesting 500 iterations yields a good solution for this resolution (<1% error). Capping iterations at 100, however, underestimates peak fluxes at the ground by 5% and is especially poor at calculating the initial rise in thermal radiation over the first few minutes of spherule reentry.

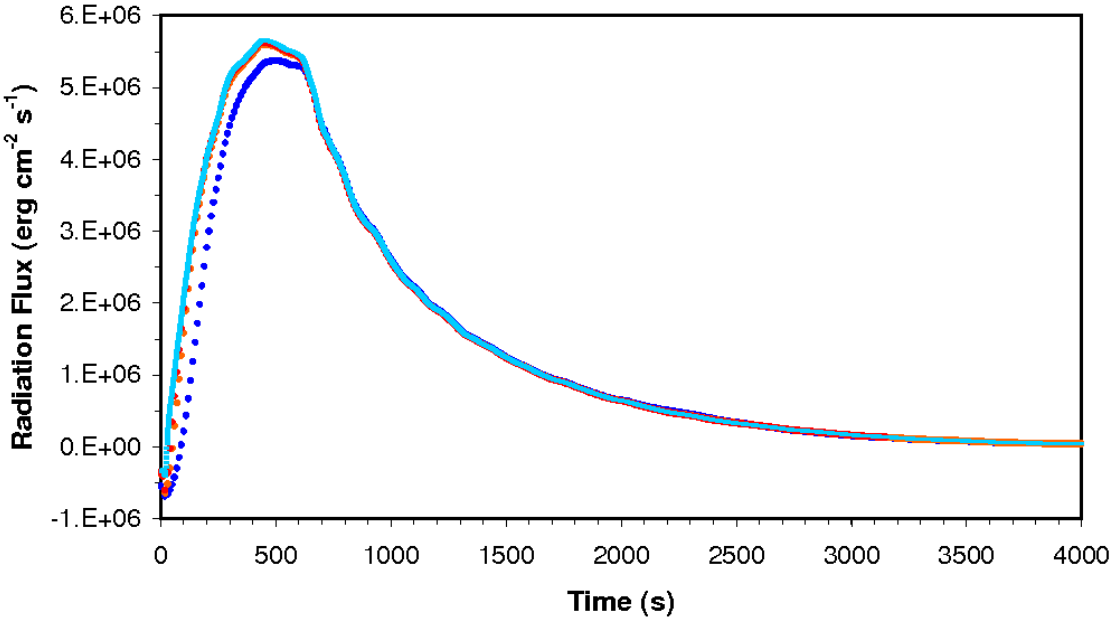

Figure 50. Surface irradiance for models of nominal Chicxulub reentry employing 500 m resolution where the number of iterations the radiation solver is permitted to make is varied: 100 (blue), 500 (orange), 1000 (red), 9000 (light blue).

3) Resolution Tests for cell sizes between 125 m and 500 m with a radiation solver limit of 500 iterations (Figure 51). Agreement in peak fluxes at the surface for the two highest resolutions indicates that 250 m is an adequate resolution for accurate calculation of surface irradiance. A model with 50 m resolution was also run out to ~10 minutes and reached a lower peak flux at a later time than the other models. This is likely due to the 500 iteration cap being insufficient to reach a good solution at such a high resolution, not the resolution itself being too low.

4) Comparison of results between a maximum radiation iteration limit of 500 versus 9000 for a resolution of 250 m (Figure 52). Peak fluxes reaching the ground are underestimated if iterations are capped at 500 by <2 %. Although it would be more accurate to allow the radiation solver to iterate longer, a small amount of error is acceptable for the purposes of the studies presented in Chapters 6 and 7. It should be stressed that capping the number of iterations allowed by the numerical radiation solver *underestimates* thermal radiation fluxes and so we will not *overestimate* the environmental effects of the thermal radiation pulse due to the small error imposed by the iteration limit.

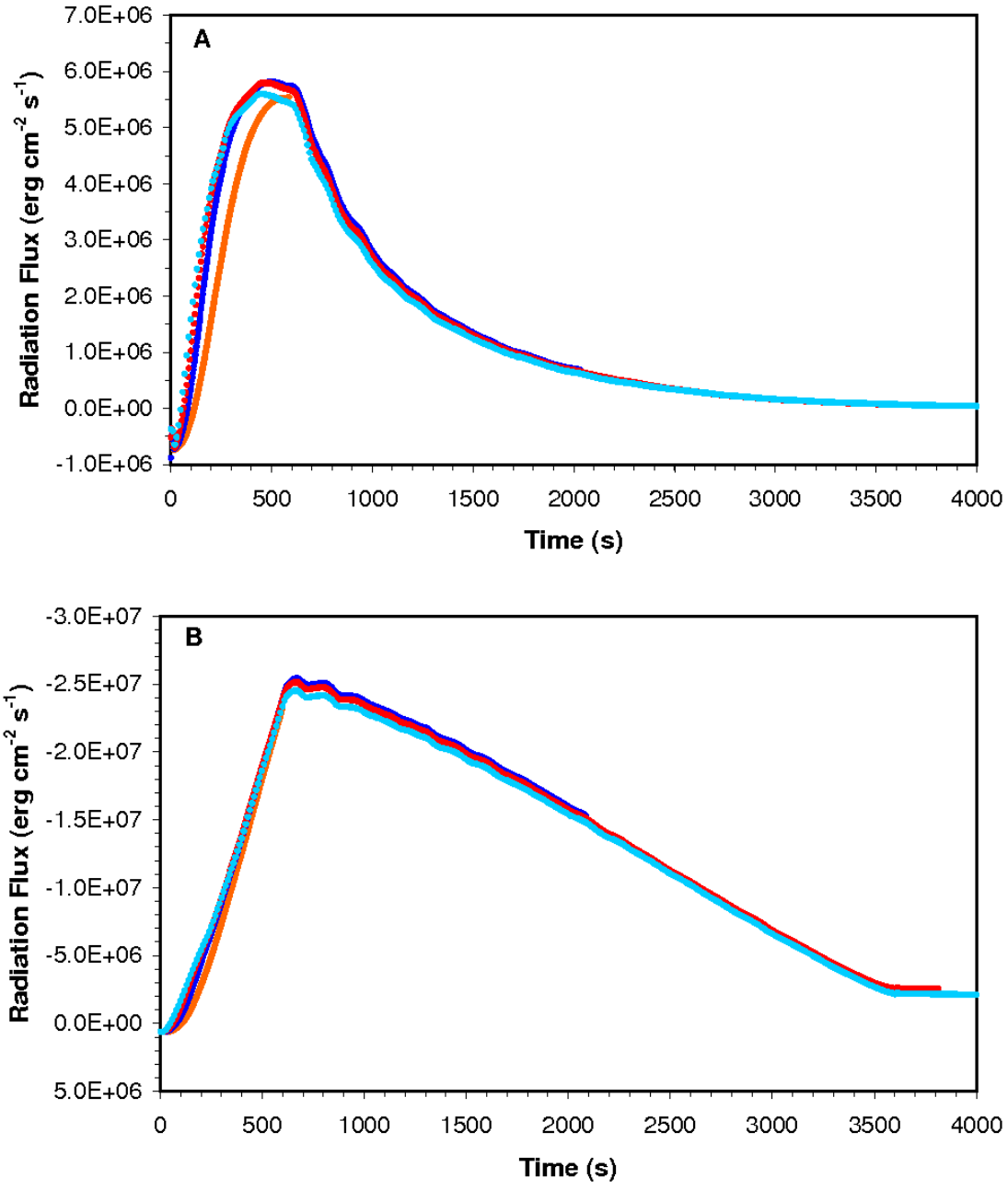

Figure 51. Thermal radiation flux at the surface (a) and to space (b) for models of nominal Chicxulub ejecta reentry where the radiation solver is limited to 500 iterations and model resolution is 50 m (orange), 125 m (blue), 250 m (red), and 500 m (light blue). The 500 iteration cap is insufficient for 50 m resolution.

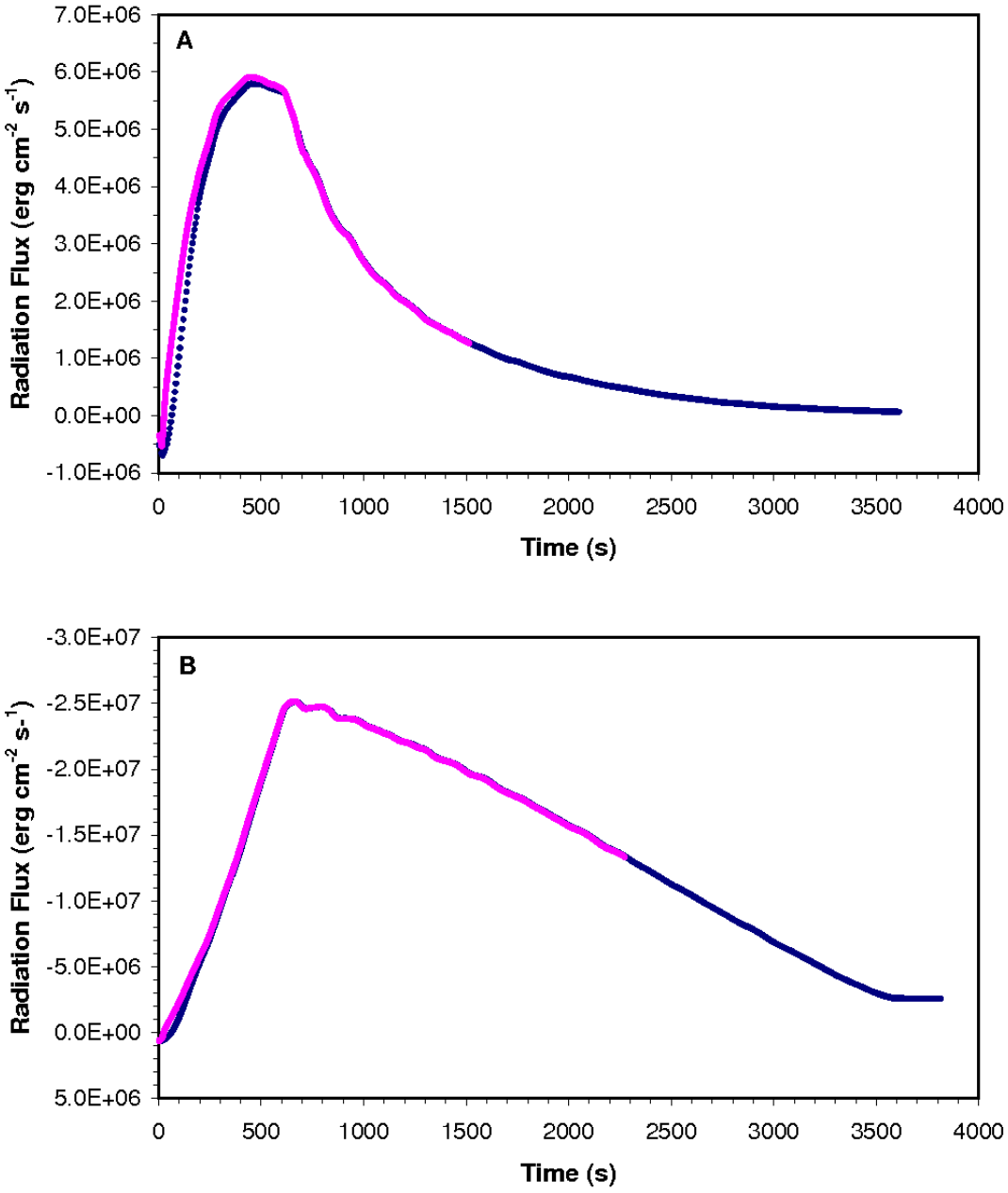

Figure 52. Thermal radiation flux at the ground (a) and to space (b) for 250m-resolution simulations of our nominal Chicxulub ejecta reentry scenario where the radiation solver is capped at 500 (blue) and 9000 (pink) iterations.

REFERENCES

ADAIR R. K. (in press) Wildfires and animal extinctions at the Cretaceous/Tertiary Boundary. *Physical Review E*.

ALVAREZ L. W., ALVAREZ W., ASARO F. and MICHEL H. V. (1980) Extraterrestrial Cause for the Cretaceous-Tertiary Extinction. *Science* **208**, 1095-1108.

ALVAREZ W., ALVAREZ L. W., ASARO F. and MICHEL H. V. (1979) Anomalous iridium levels at the Cretaceous/Tertiary boundary at Gubbio, Italy: Negative results of tests for a supernova origin. In *Cretaceous/Tertiary Boundary Events Symposium, v. 2* (eds. W. K. Christensen and T. Birkelund), pp. 69, Copenhagen.

ALVAREZ W., ALVAREZ L. W., ASARO F. and MICHEL H. V. (1984) The End of the Cretaceous: Sharp Boundary or Gradual Transition? *Science* **223**, 1183-1186.

ALVAREZ W., CLAEYS P. and KIEFFER SUSAN W. (1995) Emplacement of Cretaceous-Tertiary boundary shocked quartz from Chicxulub Crater. *Science* **269**, 930-935.

AMSDEN A. A. and HARLOW F. H. (1975) KACHINA: An Eulerian Computer Program for Multifield Flows. In *Report LA-NUREG-5680*. Los Alamos Scientific Laboratory, Los Alamos.

ANDERS E. and GREVESSE N. (1989) Abundances of the elements- Meteoritic and solar. *Geochimica et Cosmochimica Acta* **53**, 198-200.

ANDERSON H. E. (1970) Forest fuel ignitibility. *Fire Technology* **6**, 312-319.

ANDREWS D. G. (2000) *An Introduction to Atmospheric Physics*. Cambridge University Press, New York. pp. 229.

ARCHIBALD J. D. and BRYANT L. J. (1990) Differential Cretaceous/Tertiary extinctions of nonmarine vertebrates; evidence from northeastern Montana. In *Global Catastrophes in Earth History* (eds. V. L. Sharpton and P. D. Ward), pp. 549–562. Geological Society of America Special Paper 247.

ARTEMIEVA N. A. and MORGAN J. (2008) Possible Mechanisms of the Chicxulub Distal Ejecta Emplacement. In *39th Lunar and Planetary Science Conference*, #1581.

BARKER J. L. and ANDERS E. (1968) Accretion rate of cosmic matter from iridium and osmium contents of deep-sea sediments. *Geochimica et Cosmochimica Acta* **32**(6), 627-645.

BASS J. D. (1995) Elasticity of minerals, glasses, and melts. In *Mineral Physics and Crystallography: A Handbook of Physical Constants* (ed. T. Ahrens), pp. 45–63.

BECKER L., POREDA R. J., BUNCH T. E. (2000) The origin of fullerenes in the 65 myr old Cretaceous/ Tertiary boundary. In *31st Lunar and Planetary Science Conference*.

BELCHER C. M., COLLINSON M. E. and SCOTT A. C. (2005) Constraints on the thermal energy released from the Chicxulub impactor; new evidence from multi-method charcoal analysis. *Journal of the Geological Society of London* **162**, 591-602.

BELCHER C. M., COLLINSON M. E., SWEET A. R., HILDEBRAND A. R. and SCOTT A. C. (2003) Fireball passes and nothing burns; the role of thermal radiation in the Cretaceous-Tertiary event; evidence from the charcoal record of North America. *Geology* **31**, 1061-1064.

BIRKELUND T. and HAKANSSON E. (1982) The terminal Cretaceous extinction in Boreal shelf seas—A multicausal event. In *Geological implications of impacts of large asteroids and comets on the Earth* (eds. L. T. Silver and P. H. Schultz), pp. 373–384. Geological Society of America Special Paper 190.

BOHOR B. F., FOORD E. E., MODRESKI P. J. and TRIPLEHORN D. M. (1984) Mineralogic Evidence for an Impact Event at the Cretaceous-Tertiary Boundary. *Science* **224**, 867-869.

BOHOR B. F. and GLASS B. P. (1995) Origin and diagenesis of K/ T impact spherules, from Haiti to Wyoming and beyond. *Meteoritics* **30**, 182-198.

BOHOR B. F., MODRESKI P. J. and FOORD E. E. (1987) Shocked Quartz in the Cretaceous-Tertiary Boundary Clays: Evidence for a Global Distribution. *Science* **236**, 705-709.

BOHREN C. F. and CLOTHIAUX E. (2006) *Fundamentals of Atmospheric Radiation: An Introduction with 400 Problems*. Wiley-VCH, Weinheim. pp. 472.

BOOTHROYD R. G. (1971) *Flowing Gas-Solid Suspension*. Chapman and Hall, London.

BRADLEY W. H. (1965) Vertical density currents. *Science* **150**, 1423-1428.

BRADLEY W. H. (1969) Vertical density currents; Part 2. *Limnology and Oceanography* **14**, 1-3.

BRETT R. (1992) The Cretaceous-Tertiary extinction- A lethal mechanism involving anhydrite target rocks. *Geochimica et Cosmochimica Acta* **56**, 3603-3606.

BROWNLEE D. E. (1985) Cosmic Dust: Collection and Research. *Annual Reviews in Earth and Planetary Sciences* **13**, 147-173.

BYERLY G. R. and LOWE D. R. (1994) Spinel from Archean impact spherules. *Geochimica et Cosmochimica Acta* **58**, 3469-3486.

CAREY S. (1997) Influence of convective sedimentation on the formation of widespread tephra fall layers in the deep sea. *Geology* **25**, 839-842.

CAREY S. N. and SIGURDSSON H. (1980) The Roseau ash; deep-sea tephra deposits from a major eruption on Dominica, Lesser Antilles arc.; Explosive volcanism in island arcs. *Journal of Volcanology and Geothermal Research* **7**, 67-86.

CARLSON D. J. and HOGLUND R. F. (1964) Particle Drag and Heat Transfer in Rocket Nozzles. *AIAA Journal* **2**, 1980-1984.

CAVIN L. (2001) Effects of the Cretaceous-Tertiary boundary event on bony fishes. In *Geological and biological effects of impact events*, pp. 141–158. Springer-Verlag, Berlin.

CHEN G., TYBURCZY J. A. and AHRENS T. J. (1994) Shock-induced devolatilization of calcium sulfate and implications for KT extinctions. *Earth and Planetary Science Letters* **128**, 615-628.

CLAEYS P., KIESSLING W. and ALVAREZ W. (2002) Distribution of Chicxulub ejecta at the Cretaceous-Tertiary boundary. In *Geological Society of America Special Paper 356* (eds. C. Koeberl and K. G. MacLeod), pp. 55–68.

CLAUSER C. and HUENGES E. (1995) Thermal conductivity of rocks and minerals. In *Rock Physics and Phase Relations: A Handbook of Physical Constants* (ed. T. Ahrens), pp. 105–126.

COLGATE S. A. and PETSCHEK A. G. (1985) Cometary impacts and global distributions of resulting debris by floating. In *Report LA-UR-84-3911*. Los Alamos National Laboratory, Los Alamos.

COURTILLOT V., VANDAMME D., BESSE J., JAEGER J. J. and JAVOY M. (1990) Deccan volcanism at the Cretaceous–Tertiary boundary; data and inferences. In *Global Catastrophes in Earth History* (eds. V. L. Sharpton and P. D. Ward), pp. 577–583.

COURTILLOT V. E. (1990) A volcanic eruption. *Scientific American* **263**, 85-92.

COVEY C., GHAN S. J., WALTON J. J. and WEISSMAN P. R. (1990) Global environmental effects of impact-generated aerosols: results from a general circulation model. In *Global Catastrophes in Earth History* (eds. V. L. Sharpton and P. D. Ward), pp. 263-270. Geological Society of America Special Paper 247.

COVEY C., THOMPSON S. L., WEISSMAN P. R. and MACCRACKEN M. C. (1994) Global climatic effects of atmospheric dust from an asteroid or comet impact on Earth. *Global and Planetary Change* **9**, 263-273.

CROSKELL M., WARNER M. and MORGAN J. (2002) Annealing of shocked quartz during atmospheric re-entry. *Geophysical Research Letters* **29**, 1940-1944.

CROWE C. T. (1967) Drag Coefficient of Particles in a Rocket Nozzle. *AIAA Journal* **5**, 1021-1022.

CRUTZEN P. J. and BIRKS J. W. (1982) The atmosphere after a nuclear war: Twilight at noon. *Ambio* **11**, 114-125.

CULVER S. J. (2003) Benthic foraminifera across the Cretaceous-Tertiary (KT) boundary: a review. *Marine Micropaleontology* **47**, 177-226.

CUVIER G. and BRONGNIART A. (1811) Essai sur la geographie mineralogique des environs de Paris: Memoires de la Classe de Sciences Mathematiques et Physiques de l'Institut Imperial de France 1810. 1-278.

D'HALLOY J. J. O. (1822) The systematic classification of geologic formations. *Annales des Mines* **7**, 353-376.

D'HONDT S., PILSON M. E. Q., SIGURDSSON H., HANSON A. K. and CAREY S. (1994) Surface-water acidification and extinction at the Cretaceous-Tertiary boundary. *Geology* **22**, 983-986.

DARWIN C. (1859) *On the Origin of Species by Natural Selection*. John Murray, London. pp. 490.

DREW D. A. (1983) Mathematical Modeling of Two-Phase Flow. *Annual Reviews in Fluid Mechanics* **15**, 261-291.

DURDA D. D. and KRING D. A. (2004) Ignition threshold for impact-generated fires. *Journal of Geophysical Research* **109**, E08004, doi:10.1029/2004JE002279.

EBEL D. S. and GROSSMAN L. (1999) Condensation in a Model Chicxulub Fireball. In *29th Lunar and Planetary Science Conference #1906*.

EBEL D. S. and GROSSMAN L. (2005) Spinel-bearing spherules condensed from the Chicxulub impact-vapor plume. *Geology* **33**, 293-296.

EMILIANI C., KRAUS E. B. and SHOEMAKER E. M. (1981) Sudden death at the end of Mesozoic. *Earth and Planetary Science Letters* **55**, 317-334.

FLESSA K. W. (1990) The “facts” of mass extinctions. In *Global Catastrophes in Earth History* (eds. V. L. Sharpton and P. D. Ward), pp. 1–7. Geological Society of America Special Paper 247.

FRENCH B. M. (1998) Traces of Catastrophe: A Handbook of Shock-Metamorphic Effects in Terrestrial Meteorite Impact Structures, pp. 120. Technical Report, LPI Contribution 954.

GAYRAUD J., ROBIN E., ROCCHIA R. and FROGET L. (1996) Formation conditions of oxidized Ni-rich spinel and their relevance to the K/T boundary event. In *The Cretaceous-Tertiary Event and Other Catastrophes in Earth History* (eds. G. Ryder, D. Fastovsky and S. Gartner), pp. 425-444. Geological Society of America Special Paper 307.

GLASS B. P. (1990) Tektites and microtektites: key facts and inferences. *Tectonophysics* **171**, 393-404.

GLASS B. P. and BURNS C. A. (1988) Microkrystites: A new term for impact-produced glassy spherules containing primary crystallites: Houston, Texas. In *18th Lunar and Planetary Science Conference*, pp. 455–458.

GLASSTONE S. and DOLAN P. J. (1977) *The Effects of Nuclear Weapons, 3rd ed*. US Departments of Defense and Energy, Wahington DC. pp. 653.

GOLDIN T. J. and MELOSH H. J. (2007) Interactions Between Chicxulub Ejecta and the Atmosphere: The Deposition of the K/T Double Layer. In *38th Lunar and Planetary Science Conference*, pp. 2114, #1338.

GOODY R. M. (1964) *Atmospheric radiation, Vol. 1: Theoretical basis*. Clarendon Press. pp. 435.

GRAHAM J. R., DE PATER I., JERNIGAN J. G., LIU M. C. and BROWN M. E. (1995) The Fragment R Collision: WM Keck Telescope Observations of SL9. *Science* **267**, 1320-1323.

GRESHAKE A., KLOECK W., ARNDT P., MAETZ M., FLYNN G. J., BAJT S. and BISCHOFF A. (1998) Heating experiments simulating atmospheric entry heating of micrometeorites: Clues to their parent body sources. *Meteoritics and Planetary Science* **33**, 267-290.

HAMMEL H. B., BEEBE R. F., INGERSOLL A. P., ORTON G. S., SIMON A. A., CHODAS P., CLARKE J. T., DE JONG E., DOWLING T. E. (1995) HST imaging of atmospheric phenomena created by the impact of comet Shoemaker-Levy 9. *Science* **267**, 1288-1296.

HANSEN F. C. (1958) Approximations for the thermodynamic and transport properties of high-temperature air. National Advisory Committee for Aeronautics Technical Note 4150 (NASA-TN-4150).

HARVEY M. C., BRASSELL S. C., BELCHER C. M. and MONTANARI A. (2008) Combustion of fossil organic matter at the Cretaceous-Paleogene (K-P) boundary. *Geology* **36**, 355-358.

HAY W. W. (1960) The Cretaceous-Tertiary boundary in the Tampico Embayment. In *21st International Geological Congress, Part 5*, pp. 70-77, Copenhagen.

HILDEBRAND A. R., PENFIELD G. T., KRING D. A., PILKINGTON M., CAMARGO ZANOGUERA A., JACOBSEN S. B. and BOYNTON W. V. (1991) Chicxulub Crater; a possible Cretaceous/Tertiary boundary impact crater on the Yucatan Peninsula, Mexico. *Geology* **19**, 867-871.

HSU K. J., HE Q., MCKENZIE J. A., WEISSERT H., PERCH-NIELSEN K., OBERHANSLI H., KELTS K., LABRECQUE J., TAUXE L. and KRAHENBUHL U. (1982) Mass Mortality and Its Environmental and Evolutionary Consequences. *Science* **216**, 249-256.

HUBER B. T., MACLEOD K. G. and NORRIS R. D. (2002) Abrupt extinction and subsequent reworking of Cretaceous planktonic Foraminifera across the Cretaceous-Tertiary boundary: Evidence from the subtropical North Atlantic. In *Catastrophic Events and Mass Extinctions: Impacts and Beyond* (eds. C. Koeberl and K. G. MacLeod), pp. 277-290. Geological Society of America Special Paper 356.

HYMES I., BOYDELL W. and PRESCOTT B. (1996) *Thermal Radiation: Physiological and Pathological Effects*. Institution of Chemical Engineers (IChemE). pp. 130.

IVANOV B. A., BADUKOV D. D., YAKOVLEV O. I., GERASIMOV M. V., DIKOV Y. P., POPE K. O. and OCAMPO A. C. (1996) Degassing of sedimentary rocks due to Chicxulub impact: Hydrocode and physical simulations. In *The Cretaceous–Tertiary*

Event and Other Catastrophes in Earth History (eds. G. Ryder, D. E. Fastovsky and S. Gartner), pp. 125–139. Geological Society of America Special Paper 307.

IVANY L. C. and SALAWITCH R. J. (1993) Carbon isotopic evidence for biomass burning at the K-T boundary. *Geology* **21**, 487-490.

IZETT G. A. (1987) Authigenic "spherules" in KT boundary sediments at Caravaca, Spain, and Raton Basin, Colorado and New Mexico, may not be impact derived. *Bulletin of the Geological Society of America* **99**, 78-86.

IZETT G. A. (1990) The Cretaceous/ Tertiary boundary interval, Raton Basin, Colorado and New Mexico, and its content of shock-metamorphosed minerals; evidence relevant to the K/ T boundary impact-extinction theory. *Special Paper Geological Society of America* **249**.

JABLONSKI D. (1986) Causes and consequences of mass extinctions: a comparative approach. In *Dynamics of Extinction* (ed. D. K. Elliott), pp. 183–229. Wiley, New York.

JABLONSKI D. (1991) Extinctions: A Paleontological Perspective. *Science* **253**, 754-757.

JABLONSKI D. (1996) Mass extinctions: Persistent problems and new directions. In *The Cretaceous-Tertiary Event and Other Catastrophes in Earth History* (eds. G. Ryder, D. Fastovsky and S. Gartner), pp. 1-7. Geological Society of America Special Paper #307.

JOHNSON K. R. and HICKEY L. J. (1990) Megafloral change across the Cretaceous/Tertiary boundary in the northern Great Plains and Rocky Mountains, USA. In *Global Catastrophes in Earth History* (eds. V. L. Sharpton and P. D. Ward), pp. 433-444. Geological Society of America Special Paper 247.

JONES T. P. and LIM B. (2000) Extraterrestrial impacts and wildfires.; Fire and the palaeoenvironment. *Palaeogeography, Palaeoclimatology, Palaeoecology* **164**, 57-66.

KAIHO K. (1992) A low extinction rate of intermediate-water benthic foraminifera at the Cretaceous/Tertiary boundary. *Marine Micropaleontology* **43**, 229-259.

KAUFFMAN E. G. (1988) Stepwise Mass Extinctions. In *Paleontology and Evolution: Extinction Events* (eds. M. Lamolda, E. G. Kauffman and O. H. Walliser), pp. 58-71. Revista Espanola de Paleotologia, Special Issue.

KELLER G. (1988) Biotic turnover in benthic foraminifera across the Cretaceous/Tertiary boundary at El Kef, Tunisia. *Palaeogeography, palaeoclimatology, palaeoecology* **66**, 153-171.

KELLER G. R., BARRERA E., SCHMITZ B. and MATTSON E. (1993) Gradual mass extinction, species survivorship, and long-term environmental changes across the Cretaceous-Tertiary boundary in high latitudes. *Bulletin of the Geological Society of America* **105**, 979-997.

KIESSLING W. and CLAEYS P. (2002) A geographic database to the KT boundary. In *Impact Studies Series: Geological and Biological Effects of Impact Events* (eds. E. Buffetaut and C. Koeberl), pp. 83-140. Springer-Verlag, Berlin.

KOCH C. F. (1991) Species extinctions across the Cretaceous-Tertiary boundary: Observed patterns versus predicted sampling effects, stepwise or otherwise? *Historical Biology* **5**, 355-361.

KRING D. A. (2003) Environmental Consequences of Impact Cratering Events as a Function of Ambient Conditions on Earth. *Astrobiology* **3**, 133-152.

KRING D. A. and DURDA D. D. (2002) Trajectories and distribution of material ejected from the Chicxulub impact crater; implications for postimpact wildfires. *Journal of Geophysical Research, E, Planets* **107**, 6.1-6.22.

KYTE F. T., BOHOR B. F., TRIPLEHORN D. M. and SCHMITZ B. (1990) Comments and Replies on" Origin of microlayering in worldwide distributed Ir-rich marine Cretaceous/Tertiary boundary clays". *Geology* **18**, 87-94.

KYTE F. T. and SMIT J. (1986) Regional variations in spinel compositions; an important key to the Cretaceous/Tertiary event. *Geology* **14**, 485-487.

LAWSON D. I. and SIMMS D. L. (1952) The ignition of wood by radiation. *British Journal of Applied Physics* **3**, 288-292.

LEWIS J. S., WATKINS G. H., HARTMAN H. and PRINN R. G. (1982) Chemical consequences of major impact events on earth. In *Geological implications of impacts of large asteroids and comets on the earth* (eds. L. T. Silver and P. H. Schultz), pp. 215-221. Geological Society of America Special Paper 190.

LILES D. R. (1981) Two-Phase Flow. *Los Alamos Science* **3**, 26-35.

LOPEZ-RAMOS E. (1975) Geological summary of the Yucatan Peninsula. In *The Ocean Basins and Margins, Volume 3: The Gulf of Mexico and the Caribbean* (eds. A. E. M. Nairn and F. G. Stehli), pp. 257-282. Plenum, New York.

LUDER T., BENZ W. and STOCKER T. F. (2002) Modeling long-term climatic effects of impacts: First results. In *Catastrophic Events and Mass Extinctions: Impacts and Beyond* (eds. C. Koeberl and K. G. MacLeod), pp. 717-729. Geological Society of America Special Paper 356.

MANABE S. and WETHERALD R. T. (1967) Thermal Equilibrium of the Atmosphere with a Given Distribution of Relative Humidity. *Journal of the Atmospheric Sciences* **24**, 241-259.

MANVILLE V. and WILSON C. J. N. (2004) Vertical density currents; a review of their potential role in the deposition and interpretation of deep-sea ash layers. *Journal of the Geological Society of London* **161**, 947-958.

MARSH B. D. (1988) Crystal capture, sorting, and retention in convecting magma. *Geological Society of America Bulletin* **100**, 1720-1737.

MARSHALL C. R. and WARD P. D. (1996) Sudden and Gradual Molluscan Extinctions in the Latest Cretaceous of Western European Tethys. *Science* **274**, 1360.

MCGREGOR P. J., NICHOLSON P. D. and ALLEN M. G. (1996) CASPIR Observations of the Collision of Comet Shoemaker–Levy 9 with Jupiter. *Icarus* **121**(2), 361-388.

MELOSH H. J. (1989) *Impact cratering: A geologic process*. Oxford University Press, New York. pp. 245.

MELOSH H. J. (2007) A Hydrocode Equation of State for SiO2. *Meteoritics and Planetary Sciences* **42**, 2079-2098.

MELOSH H. J. and GOLDIN T. J. (2008) Heat and Drag Coefficients for Reentry of Impact Ejecta. In *39th Lunar and Planetary Science Conference*, #2457.

MELOSH H. J., SCHNEIDER N. M., ZAHNLE K. J. and LATHAM D. (1990) Ignition of global wildfires at the Cretaceous/ Tertiary boundary. *Nature* **343**, 251-254.

MELOSH H. J. and VICKERY A. M. (1991) Melt droplet formation in energetic impact events. *Nature* **350**, 494-497.

MIHALAS D. and WEIBEL-MIHALAS B. (1999) *Foundations of Radiation Hydrodynamics*. Dover, New York. pp. 718.

MONTANARI A., HAY R. L., ALVAREZ W., ASARO F., MICHEL H. V., ALVAREZ L. W. and SMIT J. (1983) Spheroids at the Cretaceous-Tertiary boundary are altered impact droplets of basaltic composition. *Geology* **11**, 668-671.

MORITZ A. R. and HENRIQUES JR F. C. (1947) Studies of Thermal Injury: II. The Relative Importance of Time and Surface Temperature in the Causation of Cutaneous Burns. *The American Journal of Pathology* **23**, 695-720.

NICHOLS D. J. (2007) Selected plant microfossil records of the terminal Cretaceous event in terrestrial rocks, western North America. *Palaeogeography, Palaeoclimatology, Palaeoecology* **255**, 22-34.

NICHOLS D. J. and FLEMING R. F. (1990) Plant microfossil record of the terminal Cretaceous event in the western United States and Canada. In *Global Catastrophes in Earth History* (eds. V. L. Sharpton and P. D. Ward), pp. 445-455. Geological Society of America Special Paper 247.

NICHOLSON P. D., GIERASCH P. J., HAYWARD T. L., MCGHEE C. A., MOERSCH J. E., SQUYRES S. W., VAN CLEVE J., MATTHEWS K., NEUGEBAUER G. and SHUPE D. (1995) Palomar observations of the R impact of comet Shoemaker-Levy 9: I. Light curves. *Geophysical Research Letters* **22**, 1613–1616.

NIPKOW F. (1920) Vorläufige Mitteilungen über Untersuchungen des Schlammabsatzes im Zürichsee *Schweizer Zeitschrift fur Hydrobiologie* **1**, 100-122.

NUTH J. A. and DONN B. (1983) Laboratory studies of the condensation and properties of amorphous silicate smokes. *Journal of Geophysical Research* **88, Suppl.**, A847-A852.

NUTH J. A. and FERGUSON F. T. (2006) Silicates do nucleate in oxygen-rich circumstellar outflows: New vapor pressure data for SiO. *Astrophysical Journal* **649**, 1178-1183.

O'KEEFE J. D. and AHRENS T. J. (1982) Interaction of the Cretaceous/Tertiary bolide with the atmosphere, ocean, and solid Earth. In *Geological implications of impacts of large asteroids and comets on Earth* (eds. L. T. Silver and P. H. Schultz), pp. 103-120. Geological Society of America Special Paper 190.

OBERBECK V. R. (1975) The role of ballistic erosion and sedimentation in lunar stratigraphy. *Reviews of Geophysics* **13**, 337-362.

OBERBECK V. R., MORRISON R. H. and HÖRZ F. (1975) Transport and emplacement of crater and basin deposits. *Earth, Moon, and Planets* **13**, 9-26.

PATANKAR S. V. (1980) *Numerical Heat Transfer and Fluid Flow*. McGraw-Hill, New York. pp. 197.

PEARSON D. A., SCHAEFER T., JOHNSON K. R. and NICHOLS D. J. (2001) Palynologically calibrated vertebrate record from North Dakota consistent with abrupt dinosaur extinction at the Cretaceous-Tertiary boundary. *Geology* **29**, 39-42.

PENFIELD G. T. and CAMARGO Z. A. (1981) Definition of a major igneous zone in the central Yucatan platform with aeromagnetics and gravity. In *Society of Exploration Geophysicists 51st Annual International Meeting*, pp. 37. Society of Exploration Geophysicists, Los Angeles.

PIERAZZO E. (1997) The Chicxulub Impact Event and the Environmental Catastrophe at the end of the Cretaceous. PhD thesis. University of Arizona, Tucson.

PIERAZZO E. (2005) Assessing Atmospheric Water Injection from Oceanic Impacts. In *36th Annual Lunar and Planetary Science Conference* #1987.

PIERAZZO E., HAHMANN A. N. and SLOAN L. C. (2003) Chicxulub and climate: Radiative perturbations of impact-produced S-bearing gases. *Astrobiology* **3**, 99-118.

PIERAZZO E., KRING D. A. and MELOSH H. J. (1998) Hydrocode simulation of the Chicxulub impact event and the production of climatically active gases. *Journal of Geophysical Research* **103**, 28607-28625.

POLLACK J. B., TOON O. B., ACKERMAN T. P., MCKAY C. P. and TURCO R. P. (1983) Environmental Effects of an Impact-Generated Dust Cloud: Implications for the Cretaceous-Tertiary Extinctions. *Science* **219**, 287-289.

POPE K. O. (2002) Impact dust not the cause of the Cretaceous-Tertiary mass extinction. *Geology* **30**, 99-102.

POPE K. O., BAINES K. H., OCAMPO A. C. and IVANOV B. A. (1994) Impact winter and the Cretaceous/Tertiary extinctions: Results of a Chicxulub asteroid impact model. *Earth and Planetary Science Letters* **128**, 719-725.

POPE K. O., BAINES K. H., OCAMPO A. C. and IVANOV B. A. (1997) Energy, volatile production, and climatic effects of the Chicxulub Cretaceous/Tertiary impact. *Journal of Geophysical Research* **102**, 21645–21664.

PRESS W. H., TEUKOLSKY S. A., VETTERLING W. T. and FLANNERY B. P. (1996) *Numerical recipes in Fortran 77: the art of scientific computing*. Cambridge University Press, New York. pp. 963.

PRINN R. and FEGLEY B. (1987) Bolide impacts, acid rain, and biospheric traumas at the Cretaceous-Tertiary boundary. *Earth and Planetary Science Letters* **83**, 1-15.

PUESCHEL R. F., RUSSELL P. B., ALLEN D. A., FERRY G. V., SNETSINGER K. G., LIVINGSTON J. M. and VERMA S. (1994) Physical and optical properties of the Pinatubo volcanic aerosol: Aircraft observations with impactors and a sun-tracking photometer. *Journal of Geophysical Research. D. Atmospheres* **99**, 12915-12922.

RAINWATER E. H. (1960) Paleocene of the Gulf Coastal Plain of the United States of America. In *21st International Geological Congress, Part 5*, pp. 97-116, Copenhagen.

RAUP D. M. (1989) The case for extraterrestrial causes of extinction. *Philosophical Transactions of the Royal Society of London* **B325**, 421-435.

RAUP D. M. and SEPKOSKI J. J. (1984) Periodicity of Extinctions in the Geologic Past. *Proceedings of the National Academy of Sciences* **81**, 801-805.

RIDPATH I. (1997) *A Dictionary of Astronomy*. Oxford University Press.

RIVARD W. W. and TORREY M. D. (1978) KFIX: A Program for Transient Two Dimensional Two Fluid Flow. In *Report LA-NUREG-6623*. Los Alamos Scientific Laboratory, Los Alamos.

ROBERTSON D. S., MCKENNA M. C., TOON O. B., HOPE S. and LILLEGRAVEN J. A. (2004a) Fireball passes and nothing burns—The role of thermal radiation in the Cretaceous-Tertiary event: Evidence from the charcoal record of North America: Comment and Reply: COMMENT. *Geology: Online Forum*, e50.

ROBERTSON D. S., MCKENNA M. C., TOON O. B., HOPE S. and LILLEGRAVEN J. A. (2004b) Survival in the first hours of the Cenozoic. *Geological Society of America Bulletin* **116**, 760-768.

ROBIN E., BOCLET D., BONTE P., FROGET L., JEHANNO C. and ROCCHIA R. (1991) The stratigraphic distribution of Ni-rich spinels in cretaceous-tertiary boundary rocks at El Kef(Tunisia), Caravaca(Spain) and Hole 761 C(Leg 122). *Earth and planetary science letters* **107**, 715-721.

ROBIN E., BONTE P., FROGET L., JEHANNO C. and ROCCHIA R. (1992) Formation of spinels in cosmic objects during atmospheric entry: a clue to the Cretaceous-Tertiary boundary event. *Earth and planetary science letters* **108**, 181-190.

RYDER G. (1996) The Unique Significance and Origin of the Cretaceous-Tertiary Boundary: Historical Context and Burdens of Proof. In *The Cretaceous-Tertiary Event*

and Other Catastrophes in Earth History (eds. R. G., F. D. and G. S.), pp. 31-38. Geological Society of America Special Paper #307.

SARNA-WOJCICKI A., SHIPLEY S., WAITT R. B., DZURISIN D. and WOOD S. (1981) Aerial distribution, thickness, mass, volume and grain size of air-fall ash from the six major eruptions of 1980. In *U. S. Geological Survey Professional Paper*, pp. 577-600.

SCHEIDEGGER K. F., FEDERMAN A. N. and TALLMAN A. M. (1982) Compositional heterogeneity of tephras from the 1980 eruptions of Mount St. Helens. *Journal of Geophysical Research* **87**, 10861-10881.

SCHMITZ B. (1988) Origin of microlayering in worldwide distributed Ir-rich marine Cretaceous/Tertiary boundary clays. *Geology* **16**, 1068-1072.

SCHULTZ P. H. and D'HONDT S. L. (1996) Cretaceous-Tertiary (Chicxulub) impact angle and its consequences. *Geology* **24**, 963-967.

SEINFELD J. H. and PANDIS S. N. (1998) *Atmospheric Chemistry and Physics: From Air Pollution to Climate Change*. John Wiley & Sons, New York. pp. 1326.

SEPKOSKI J. J. (1993) Ten years in the library: new data confirm paleontological patterns. *Paleobiology* **19**, 43-51.

SEPKOSKI J. J. and KOCH C. F. (1996) Evaluating paleontological data relating to bio-events. In *Global Events and Event Stratigraphy in the Phanerozoic* (ed. O. H. Walliser), pp. 21-34. Springer, Berlin.

SHEEHAN P. M. and FASTOVSKY D. E. (1992) Major extinctions of land-dwelling vertebrates at the Cretaceous-Tertiary boundary, eastern Montana. *Geology* **20**, 556-560.

SIGNOR P. W. and LIPPS J. H. (1982) Sampling bias, gradual extinction and catastrophes in the fossil record. *Geological Society of America Special Paper* **190**, 291-296.

SIGURDSSON H., BONTE P., TURPIN L., CHAUSSIDON M., METRICH N., STEINBERG M., PRADEL P. and D'HONDT S. (1991) Geochemical constraints on source region of Cretaceous/Tertiary impact glasses. *Nature* **353**, 839-842.

SIGURDSSON H., D'HONDT S. and CAREY S. (1992) The impact of the Cretaceous/Tertiary bolide on evaporite terrane and generation of major sulfuric acid aerosol. *Earth and planetary science letters* **109**, 543-559.

SIMMS D. L. (1960) Ignition of cellulosic materials by radiation. *Combustion and Flame* **4**, 293-300.

SIMMS D. L. (1962) Damage to cellulosic solids by thermal radiation. *Combustion and Flame* **6**, 303-317.

SIMMS D. L. (1963) On the Pilot Ignition of Wood by Radiation. *Combustion and Flame* **7**, 253-261.

SIMMS D. L. and LAW M. (1967) The ignition of wet and dry wood by radiation. *Combustion and Flame* **11**, 377-388.

SIMONSON B. M. and GLASS B. P. (2004) Spherule layers; records of ancient impacts. *Annual Review of Earth and Planetary Sciences* **32**, 329-361.

SIMONSON B. M. and HARNIK P. (2000) Have distal impact ejecta changed through geologic time? *Geology* **28**, 975-978.

SIRET D. and ROBIN E. (2003) Spinel Formation in an Impact Plume: A Thermodynamic Approach. In *34th Lunar and Planetary Science Conference #1865*.

SLEEP N. H., ZAHNLE K. J., KASTING J. F. and MOROWITZ H. J. (1989) Annihilation of ecosystems by large asteroid impacts on the early Earth. *Nature* **342**, 139-142.

SLOAN R. E., RIGBY J. K., VAN VALEN L. M. and GABRIEL D. (1986) Gradual Dinosaur Extinction and Simultaneous Ungulate Radiation in the Hell Creek Formation. *Science* **232**, 629-633.

SMIT J. (1979) The Cretaceous/Tertiary transition in the Barranco del Gredero, Spain. In *Cretaceous/Tertiary Boundary Events Symposium, v. 2* (eds. W. K. Christensen and T. Birkelund), pp. 156-163, Copenhagen.

SMIT J. (1999) The global stratigraphy of the Cretaceous-Tertiary boundary impact ejecta. *Annual Review of Earth and Planetary Sciences* **27**, 75-113.

SMIT J., ALVAREZ W., MONTANARI A., SWINBURNE N., VAN KEMPEN T. M., KLAVER G. T. and LUSTENHOUWER W. J. (1992a) "Tektites" and microkrystites at the Cretaceous Tertiary boundary; two strewn fields, one crater?. *Proceedings of the Lunar and Planetary Science Conference* **22**, 87-100.

SMIT J., GRAJALES M., ALVAREZ W., SWINBURNE N. H. M. and MONTANARI A. (1992b) Sedimentology and biostratigraphy of Cretaceous-Tertiary impact-tsunami wave deposits in NE Mexico and Texas. Geological Society of America annual meeting. *Abstracts with Programs Geological Society of America* **24**, 355.

SMIT J., KELLER G., ZARGOUNI F., RAZGALLAH S., SHIMI M. and BEN A. O. (1997) The El Kef sections and sampling procedures. *Marine Micropaleontology* **29**, 69–72.

SMIT J. and KLAVER G. (1981) Sanidine spherules at the Cretaceous–Tertiary boundary indicate a large impact event. *Nature* **292**, 47-49.

SMIT J. and KYTE F. T. (1984) Siderophile-rich magnetic spheroids from the Cretaceous–Tertiary Boundary in Umbria, Italy. *Nature* **310**, 403-405.

SPICER R. A. and SHACKLETON N. J. (1989) Plants at the Cretaceous-Tertiary Boundary. *Philosophical Transactions of the Royal Society of London B* **325**, 291-305.

STOKES G. G. (1851) On the effect of the internal friction of fluids on the motion pendulum. *Transaction of Cambridge Philosophical Society* **9**, 8-149.

TAKATA T. and AHRENS T. J. (1994) Numerical Simulation of Impact Cratering at Chicxulub and the Possible Causes of KT Catastrophe. In *New Developments Regarding the KT Event and Other Catastrophes in Earth History, LPI Contribution 825*, pp. 125. Lunar and Planetary Institute, Houston, Texas.

THIERSTEIN H. R. (1982) Terminal Cretaceous plankton extinctions- A critical assessment. In *Geological implications of impacts of large asteroids and comets on the earth* (eds. L. T. Silver and P. H. Schultz), pp. 385-399. Geological Society of America Special Paper 190.

THOMAS E. (1990) Late Cretaceous-early Eocene mass extinctions in the deep sea. In *Global Catastrophes in Earth History* (eds. V. L. Sharpton and P. D. Ward), pp. 481–496. Geological Society of America Special Paper 247.

TOON O. B., POLLACK J. B., ACKERMAN T. P., TURCO R. P., MCKAY C. P. and LIU M. S. (1982) Evolution of an impact-generated dust cloud and its effects on the atmosphere. In *Geological implications of impacts of large asteroids and comets on the earth* (eds. L. T. Silver and P. H. Schultz), pp. 187-200. Geological Society of America Special Paper 190.

TOON O. B., ZAHNLE K., MORRISON D., TURCO R. P. and COVEY C. (1997) Environmental perturbations caused by the impacts of asteroids and comets. *Reviews of Geophysics* **35**, 41-78.

TRAVIS J. R., HARLOW F. H. and AMSDEN A. A. (1975) Numerical calculation of two-phase flows. In *Report LA-5942-MS*. Los Alamos National Laboratory, Los Alamos.

TSCHUDY R. H., PILLMORE C. L., ORTH C. J., GILMORE J. S. and KNIGHT J. D. (1984) Disruption of the Terrestrial Plant Ecosystem at the Cretaceous-Tertiary Boundary, Western Interior. *Science* **225**, 1030-1032.

TSCHUDY R. H. and TSCHUDY B. D. (1986) Extinction and survival of plant life following the Cretaceous/Tertiary boundary event, Western Interior, North America. *Geology* **14**, 667-670.

TURCO R. P., TOON O. B., PARK C., WHITTEN R. C., POLLACK J. B. and NOERDLINGER P. (1982) An analysis of the physical, chemical, optical, and historical impacts of the 1908 Tunguska meteor fall. *Icarus* **50**, 1-52.

U.S. Standard Atmosphere (1976), pp. 227. National Oceanic and Atmospheric Administration, NOAA-S/T 76-1562.

VAJDA V. and MCLOUGHLIN S. (2004) Fungal Proliferation at the Cretaceous-Tertiary Boundary. *Science* **303**, 1489.

VAJDA V., RAINE J. I. and HOLLIS C. J. (2001) Indication of Global Deforestation at the Cretaceous-Tertiary Boundary by New Zealand Fern Spike. *Science* **294**, 1700-1702.

VICKERY A. (1986) Effect of an impact-generated gas cloud on the acceleration of solid ejecta. *Journal of Geophysical Research* **91**, 14139-14160.

VOGT P. R. and HOLDEN J. C. (1979) The end-Cretaceous extinctions: a study of the multiple working hypotheses method gone mad. In *Cretaceous/Tertiary Boundary Events Symposium, v. 2* (eds. W. K. Christensen and T. Birkelund), pp. 49, Copenhagen.

WALTER M. J. and TRØNNES R. G. (2004) Early Earth differentiation. *Earth and Planetary Science Letters* **225**, 253-269.

WARD P., WIEDMANN J. and MOUNT J. F. (1986) Maastrichtian molluscan biostratigraphy and extinction patterns in a Cretaceous/Tertiary boundary section exposed at Zumaya, Spain. *Geology* **14**, 899-903.

WARD P. D. (1990) The Cretaceous/Tertiary extinctions in the marine realm: a 1990 perspective. In *Global Catastrophes in Earth History* (eds. V. L. Sharpton and P. D. Ward), pp. 425-432. Geologic Society of America Special Paper 247.

WARD W. C., KELLER G., STINNESBECK W. and ADATTE T. (1995) Yucatan subsurface stratigraphy; implications and constraints for the Chicxulub impact. *Geology* **23**, 873-876.

WHIPPLE F. L. (1950) The Theory of Micro-Meteorites. Part I. In an Isothermal Atmosphere. *Proceedings of the National Academy of Sciences* **36(**, 687-695.

WIESNER M. G., WANG Y. and ZHENG L. (1995) Fallout of volcanic ash to the deep South China Sea induced by the 1991 eruption of Mount Pinatubo (Philippines). *Geology* **23**, 885-888.

WOLBACH W. S., GILMOUR I. and ANDERS E. (1990) Major wildfires at the Cretaceous/ Tertiary boundary. In *Global catastrophes in Earth history* (eds. V. L. Sharpton and P. D. Ward), pp. 391-400. Geological Society of America Special Paper.

WOLBACH W. S., GILMOUR I., ANDERS E., ORTH C. J. and BROOKS R. R. (1988) Global fire at the Cretaceous-Tertiary boundary. *Nature (London)* **334**, 665-669.

WOLBACH W. S., LEWIS R. S. and ANDERS E. (1985) Cretaceous extinctions; evidence for wildfires and search for meteoritic material. *Science* **230**, 167-170.

YANG L., CHEN X., ZHOU X. and FAN W. (2003) The pyrolysis and ignition of charring materials under an external heat flux. *Combustion and Flame* **133**, 407-413.

ZAHNLE K. (1996) Dynamics and chemistry of SL9 plumes. In *The Collision of Comet Shoemaker-Levy 9 and Jupiter* (eds. K. S. Noll, H. A. Weaver and P. D. Feldman), pp. 183-212. Cambridge University Press.

ZAHNLE K. J. (1990) Atmospheric chemistry by large impacts. In *Global Catastrophes in Earth History* (eds. V. L. Sharpton and P. Ward), pp. 271–288. Geological Society of America Special Paper 247.

ZEL'DOVICH Y. B. and RAIZER Y. P. (1967) *Physics of Shock Waves and High-Temperature Hydrodynamic Phenomena*. Academic Press, New York. pp. 705.